Solubility and Diffusivity of Water in Lunar Basalt, and Chemical Zonation in Olivine-Hosted Melt Inclusions

Thesis by
Megan Eve Newcombe

In Partial Fulfillment of the Requirements for the degree
of
Doctor of Philosophy

CALIFORNIA INSTITUTE OF TECHNOLOGY
Pasadena, California
2016
(Defended 9th December, 2015)

This thesis is dedicated to Lesley Newcombe, whose wild imagination never ceases to inspire me, and Jeremy Newcombe, who always asks the best questions.

ACKNOWLEDGEMENTS

Firstly, I would like to thank my advisor, Edward Stolper. Thank you, Ed, for your kindness over the past six years. I'm grateful for all of the times you've stayed up late to work on one of my abstracts, called to tell me about an idea you had, and found time to meet me even during your busiest weeks. I'm also grateful for your eternal optimism and encouragement as I learned to embrace the many little failures required to become a scientist, and for your enthusiasm on the days when things went well.

I would like to thank my thesis committee: Paul Asimow, John Eiler, George Rossman, and David Stevenson. It's been a complete thrill to work with a group of people who so genuinely love science. Thanks in particular to George for his lab superpowers and Saturday conversations; to John for his valuable and succinct career advice (and for being the Will Ferrell of PRG); to Dave for his mathematical prowess and the best chalk talk I have ever seen; and to Paul for teaching me Thermodynamics and for calling me late on a weekday night in the January of 2009 to tell me I'd got in to Caltech (me: 'You're joking…'; Paul: 'I'm not in the habit of making long-distance phone calls as practical jokes.').

I'm incredibly grateful to Mike Baker, John Beckett, and Sally Newman for training me to be an experimental petrologist, for keeping me safe in the lab, and for improving my fashion sense along the way (I hear utility belts are in again this year). Many thanks are due to Yunbin Guan and Chi Ma for helping me to get the absolute best out of the SIMS and the electron microprobe. Thanks also to Alex Brett for working so hard during their Summer Undergraduate Research Fellowship—many of the solubility experiments presented in Chapter 2 of this thesis were produced and analyzed by Alex. I'd also like to thank my 3rd floor office mates Cam Macris, Maryjo Brounce, Paula Antoshechkina, Steve Chemtob, and Melanie Channon for sharing their knowledge and laughs. Marion Le Voyer, Sarah Lambart, Alessandro Fabbrizio, and Jed Mosenfelder have been great collaborators, mentors, and friends. I've also learned a lot from conference and email interactions with Alberto Saal and Youxue Zhang. I'm grateful to Janice Grancich for her kindness and amazing efficiency.

I'd like to give a shout-out to my wonderful Pit cohort: Joel Scheingross, Paul Magyar, Alison Piasecki, Erika Swanson, Jeff Marlow, and Daniel Stolper. Thanks for helping me to settle in to this country and for all the adventures—from Japanese hot springs to the Adelaide Hostel to ACM100...

My housemates have literally kept me alive while I have written this thesis. I'm so grateful to April Vos, Eyrún Eyjólfsdóttir, Cindy Wang, and Fernando Pastawski for being my Caltech family. Thank you for your support and company over countless cups of tea, and thank you for not letting me starve this past month!

I would never have made it to Caltech without the love and support of my parents. Thank you so much for always encouraging me to explore. No matter how much I gloated about the sunshine, I never stopped missing home. Thanks also to my talented sister, Grace, for understanding me so well and for diverting our parents' attention away from my own lack of a proper job by choosing to be a professional medieval minstrel.

Last but not least, I would like to thank Pratyush Tiwary, who took me out for shepherd's pie five years ago when I was feeling homesick, and who has been there for me ever since.

ABSTRACT

I report the solubility and diffusivity of water in lunar basalt and an iron-free basaltic analogue at 1 atm and 1350 °C. Such parameters are critical for understanding the degassing histories of lunar pyroclastic glasses. Solubility experiments have been conducted over a range of fO_2 conditions from three log units below to five log units above the iron-wüstite buffer (IW) and over a range of pH_2/pH_2O from 0.03 to 24. Quenched experimental glasses were analyzed by Fourier transform infrared spectroscopy (FTIR) and secondary ionization mass spectrometry (SIMS) and were found to contain up to ~420 ppm water. Results demonstrate that, under the conditions of our experiments: (1) hydroxyl is the only H-bearing species detected by FTIR; (2) the solubility of water is proportional to the square root of pH_2O in the furnace atmosphere and is independent of fO_2 and pH_2/pH_2O; (3) the solubility of water is very similar in both melt compositions; (4) the concentration of H_2 in our iron-free experiments is <3 ppm, even at oxygen fugacities as low as IW-2.3 and pH_2/pH_2O as high as 24; and (5) SIMS analyses of water in iron-rich glasses equilibrated under variable fO_2 conditions can be strongly influenced by matrix effects, even when the concentrations of water in the glasses are low. Our results can be used to constrain the entrapment pressure of the lunar melt inclusions of Hauri et al. (2011).

Diffusion experiments were conducted over a range of fO_2 conditions from IW-2.2 to IW+6.7 and over a range of pH_2/pH_2O from nominally zero to ~10. The water concentrations measured in our quenched experimental glasses by SIMS and FTIR vary from a few ppm to ~430 ppm. Water concentration gradients are well described by models in which the diffusivity of water (D^*_{water}) is assumed to be constant. The relationship between D^*_{water} and water concentration is well described by a modified speciation model (Ni et al. 2012) in which both molecular water and hydroxyl are allowed to diffuse. The success of this modified speciation model for describing our results suggests that we have resolved the diffusivity of hydroxyl in basaltic melt for the first time. Best-fit values of D^*_{water} for our experiments on lunar basalt vary within a factor of ~2 over a range of pH_2/pH_2O from 0.007 to 9.7, a range of fO_2 from IW-2.2 to IW+4.9, and a water concentration range from ~80 ppm to ~280 ppm. The relative insensitivity of our best-fit values of D^*_{water} to variations in pH_2 suggests that H_2 diffusion was not significant during degassing of the lunar glasses of Saal et al. (2008). D^*_{water} during dehydration and hydration in H_2/CO_2 gas mixtures are approximately the same, which supports an equilibrium boundary condition for these experiments. However, dehydration experiments into CO_2 and CO/CO_2 gas mixtures leave some scope for the importance of kinetics during dehydration into H-free environments. The value of D^*_{water} chosen by Saal et al. (2008) for modeling the diffusive degassing of the lunar volcanic glasses is within a factor of three of our measured value in our lunar basaltic melt at 1350 °C.

In Chapter 4 of this thesis, I document significant zonation in major, minor, trace, and volatile elements in naturally glassy olivine-hosted melt inclusions from the Siqueiros Fracture Zone and the Galapagos Islands. Components with a higher concentration in the host olivine than in the melt (MgO, FeO, Cr_2O_3, and MnO) are depleted at the edges of the zoned melt inclusions relative to their centers, whereas except for CaO, H_2O, and F, components with a lower concentration in the host olivine than in the melt (Al_2O_3, SiO_2, Na_2O, K_2O, TiO_2, S, and Cl) are enriched near the melt inclusion edges. This zonation is due to formation of an olivine-depleted boundary layer in the adjacent melt in response to cooling and crystallization of olivine on the walls of the melt inclusions concurrent with diffusive propagation of the boundary layer toward the inclusion center.

Concentration profiles of some components in the melt inclusions exhibit multicomponent diffusion effects such as uphill diffusion (CaO, FeO) or slowing of the diffusion of typically

rapidly diffusing components (Na_2O, K_2O) by coupling to slow diffusing components such as SiO_2 and Al_2O_3. Concentrations of H_2O and F decrease towards the edges of some of the Siqueiros melt inclusions, suggesting either that these components have been lost from the inclusions into the host olivine late in their cooling histories and/or that these components are exhibiting multicomponent diffusion effects.

A model has been developed of the time-dependent evolution of MgO concentration profiles in melt inclusions due to simultaneous depletion of MgO at the inclusion walls due to olivine growth and diffusion of MgO in the melt inclusions in response to this depletion. Observed concentration profiles were fit to this model to constrain their thermal histories. Cooling rates determined by a single-stage linear cooling model are 150–13,000 °C hr^{-1} from the liquidus down to ~1000 °C, consistent with previously determined cooling rates for basaltic glasses; compositional trends with melt inclusion size observed in the Siqueiros melt inclusions are described well by this simple single-stage linear cooling model. Despite the overall success of the modeling of MgO concentration profiles using a single-stage cooling history, MgO concentration profiles in some melt inclusions are better fit by a two-stage cooling history with a slower-cooling first stage followed by a faster-cooling second stage; the inferred total duration of cooling from the liquidus down to ~1000 °C is 40 s to just over one hour.

Based on our observations and models, compositions of zoned melt inclusions (even if measured at the centers of the inclusions) will typically have been diffusively fractionated relative to the initially trapped melt; for such inclusions, the initial composition cannot be simply reconstructed based on olivine-addition calculations, so caution should be exercised in application of such reconstructions to correct for post-entrapment crystallization of olivine on inclusion walls. Off-center analyses of a melt inclusion can also give results significantly fractionated relative to simple olivine crystallization.

All melt inclusions from the Siqueiros and Galapagos sample suites exhibit zoning profiles, and this feature may be nearly universal in glassy, olivine-hosted inclusions. If so, zoning profiles in melt inclusions could be widely useful to constrain late-stage syneruptive processes and as natural diffusion experiments.

TABLE OF CONTENTS

C h a p t e r 1

INTRODUCTION

The main body of this thesis is composed of two projects I completed during my time at Caltech: Chapters 2 and 3 describe an experimental investigation of the solubility and diffusivity of water in basaltic melts; and in Chapter 4, I document chemical zonation in olivine-hosted melt inclusions and I describe a model with which the thermal histories of olivine-hosted melt inclusions may be determined from the shapes of concentration gradients of MgO within the inclusions. In Appendix III of the thesis, I include a paper published in *Science* on which I am a co-author (Stolper et al. 2013), concerning the petrogenesis of alkaline rock "Jake_M" which was discovered and characterized by the Curiosity rover (MSL) in Gale Crater, Mars. My contribution to this study was to assess the viability of a number of potential parental magmas to Jake_M by modeling fractional crystallization of a series of trial parental compositions over a range of pressures and water contents, using the MELTS software (Ghiorso and Sack 1995; Smith and Asimow 2005).

Introduction to Chapters 2 and 3: Water on the Moon

Analyses made in the 1970s of lunar samples returned from the Moon by the Apollo and Luna missions revealed that the isotopes of several elements were present in the same ratios in both lunar and terrestrial rocks (e.g., Clayton and Mayeda 1975), and that the Moon was highly depleted in volatile elements (e.g., Na, Pb, K) compared to the Earth (e.g., Taylor 1979). No water was initially detected in lunar rocks, leading to the widely held belief that the Moon was "bone dry" (Newsom and Taylor 1989; Taylor and Esat 1996). The striking geochemical similarities between lunar and terrestrial rocks, and the strong depletion of volatiles on the Moon lent credence to the popular "giant impact" theory of lunar formation, in which the Moon is proposed to form as the result of a highly energetic collision between the proto-Earth and a Mars-sized impactor (Hartmann and Davis 1975; Cameron and Ward 1976). Simulations of this giant impact (e.g., Canup and Asphaug 2001; Canup 2004; Pahlevan and Stevenson 2007) indicated widespread melting and efficient mixing of the material that accreted to form the Moon, seemingly forming a self-consistent story for the formation of the Moon that addressed the available geochemical (e.g., lunar isotopic composition, iron-depletion and volatile depletion) and geophysical (e.g., angular momentum of the Earth-Moon system, mass of the Moon) constraints.

Over the decades that followed the Apollo and Luna missions, the development of techniques for *in situ* analysis of volatile elements in geological materials took several leaps forward: Techniques were developed for the application of Fourier transform infrared spectroscopy (FTIR) to the analysis of dissolved water in silicate glasses (Stolper 1982; Newman et al. 1986) and for the analysis of very low concentrations of water in silicate minerals (Rossman 1996; Bell et al. 2003). Additionally, techniques were developed for the analysis of volatile elements in silicate glasses (Hauri et al. 2002) and minerals (Mosenfelder et al. 2011) by secondary ionization mass spectrometry (SIMS). These techniques improved the spatial resolution and detection limits of measurements of water in geological materials by several orders of magnitude.

These vast improvements in analytical techniques for the measurement of volatiles in silicate glasses and minerals inspired Saal and co-workers to revisit the analyses made in the 1970s of volatile elements in lunar rocks, so they decided to search for water in the pristine lunar glasses characterized by Delano (1986). These glass beads were thought to be the products of Hawaiian-style "fire fountain" eruptions on the Moon (Wasson et al. 1976). They were excellent candidates for the search for volatiles, because they were already known to contain dissolved sulfur (Delano et al. 1994) and they were also known to be coated in a layer of moderately volatile elements such as sulfur, zinc, potassium, copper, and chlorine (Butler Jr and Meyer Jr 1976; Wasson et al. 1976). The eruption of the lunar glass beads is widely thought to have been driven by a CO-rich carrier gas in response to graphite oxidation or exsolution of dissolved carbon during magma ascent (Fogel and Rutherford 1995; Nicholis and Rutherford 2009; Rutherford and Papale 2009; Wetzel et al. 2013; Wetzel et al. 2015). However, other authors have argued for a carrier gas rich in fluorine and chlorine (Elkins-Tanton et al. 2003), sulfide (Butler Jr and Meyer Jr 1976), or (more recently) a vapor rich in molecular hydrogen (Sharp et al. 2013).

Upon analysis of the lunar glass beads by SIMS and nanoSIMS, Saal et al. (2008) detected 10s of ppm of water and characterized concentration gradients of water, sulfur, fluorine, and chlorine across a single bead. The shapes of these gradients were consistent with their formation during syneruptive degassing. Modeling of all four volatile elements together allowed Saal et al. (2008) to constrain the initial concentrations of the volatiles in the melt prior to degassing. Their model of diffusive volatile loss and concomitant surface evaporation during the flight of the bead from its volcanic vent to its final resting place led Saal et al. (2008) to make the startling conclusion that the melt may have contained a pre-degassing water concentration of ~745 ppm. This inference was

confirmed when ~1400 ppm water was measured in olivine-hosted melt inclusions associated with the lunar volcanic glasses (Hauri et al. 2011), leading to the realization that at least some regions of the Moon's interior that melted to produce the lunar volcanic glasses had water contents comparable to the major magma-forming regions in the Earth's upper mantle (Saal et al. 2002). The presence of water in the Moon's interior has been further supported by detections of water in lunar apatites (Boyce et al. 2010; McCubbin et al. 2010; Greenwood et al. 2011; Tartèse et al. 2014), plagioclase from lunar highland anorthosites (Hui et al. 2013), lunar regolith (Liu et al. 2012), and by additional studies of the lunar volcanic glasses (Saal et al. 2013; Chen et al. 2015; Wetzel et al. 2015). The current state of this active field of research has been recently reviewed by Hauri et al. (2015), McCubbin et al. (2015) and Robinson and Taylor (2014).

The degassing model presented by Saal et al. (2008) predicts an initial water concentration for the lunar glasses that is broadly consistent with the concentrations measured in their associated olivine-hosted melt inclusions (Hauri et al. 2011). However, there is still much that we do not understand about the degassing histories of the lunar volcanic glasses. For example, the model of Saal et al. (2008) uses a diffusivity for water that is temperature dependent, but not concentration dependent (Zhang and Stolper 1991). Although there were at the time of publication of Saal et al. (2008) no studies of water diffusion in natural silicate melts at the low water concentrations relevant to these lunar volcanic glasses, many studies of water diffusion at higher concentrations indicate that the diffusivity of water in silicate melts is highly concentration dependent at water contents > 0.1 wt% (Zhang and Stolper 1991; Zhang et al. 1991; Persikov et al. 2010; Zhang and Ni 2010; Ni et al. 2012). If the concentration dependence of the diffusivity of water in silicate melts can be extrapolated to the low water concentrations relevant to lunar volcanic glass formation, it would suggest that the model of Saal et al. (2008) could have significantly overestimated the extent of water degassing from the lunar volcanic glasses. The role played by the lower oxygen fugacity on the Moon is also debated, with some authors arguing that H_2 may play a significant role in the transport of H-bearing species through the melt beads (Zhang 2011). In addition, the evaporation rate of water at the surface of the lunar glass bead is a fit parameter in the model of Saal et al. (2008) and there are not yet any experiments or physical models that constrain the kinetics of evaporation of water at the melt-vapor interface.

In Chapter 2 and Chapter 3 of this thesis, I address many of the issues described above by experimentally determining the solubility and diffusivity of water in lunar basalt and in an iron-

free basaltic analogue at the low water concentrations and low values of oxygen fugacity (fO_2) thought to be relevant to the eruption of lunar basalts (Sato 1976; Wadhwa 2008). Experiments have been conducted at 1 atm and 1350 °C over a range of fO_2 conditions from IW-3 to IW+6.7 (where "IW" indicates the position of the iron-wüstite oxygen buffer) and over a range of pH_2/pH_2O from nominally zero to 24. The water concentrations measured in our quenched experimental glasses vary from a few ppm to ~430 ppm, whereas existing experimental studies of water diffusion in basaltic melts extend from much higher water concentrations down to ~1000 ppm (Zhang and Stolper 1991; Persikov et al. 2010), and thus our experiments fill a significant gap in our knowledge of water diffusion in basic silicate melts at low water concentrations.

Introduction to Chapter 4: Chemical zonation in olivine-hosted melt inclusions

Olivine-hosted melt inclusions are small aliquots of melt (typically tens to a few hundred micrometers in diameter) that are trapped in growing olivine phenocrysts. Their olivine hosts provide the inclusions with a certain amount of protection from the many processes that operate to change magma compositions on their journey from crustal magma chambers to the surface (e.g., magma mixing, crustal assimilation, volatile exsolution, and crystal fractionation). This is reflected in the compositions of olivine-hosted melt inclusions, which tend to preserve more compositional variability, more primitive compositions, and higher concentrations of volatile elements than their carrier lavas (Kent 2008). For these reasons, olivine-hosted melt inclusions have long been used by petrologists to estimate the compositions of primitive mantle melts (e.g., Saal et al. 2002), to infer pre-eruptive magma volatile concentrations (e.g., Métrich and Wallace 2008) and to study mantle heterogeneity (e.g., Maclennan et al. 2003).

It is often implicitly assumed that glassy melt inclusions in phenocrysts are homogeneous and thus that analyses from near the center of an inclusion are representative of the inclusion composition. Likewise, inclusion homogeneity is usually assumed in models of melt inclusion formation and evolution (Qin et al. 1992; Danyushevsky et al. 2000; Cottrell et al. 2002; Danyushevsky et al. 2002a; Danyushevsky et al. 2002b; Gaetani and Watson 2002; Chen et al. 2013; Lloyd et al. 2013). *A priori*, this would seem to be a reasonable assumption, since even though crystallization of the host mineral on the walls of the inclusion and reequilibration of the melt inclusion with the host mineral are known to affect inclusion composition (Danyushevsky et al. 2000; Danyushevsky et al. 2002a; Danyushevsky et al. 2002b; Gaetani and Watson 2002), the time scales for diffusive homogenization of melt inclusions $\lesssim 10^2$ μm in diameter are expected to

be $\lesssim 10^2$ min at magmatic temperatures based on known diffusivities in silicate melts — orders of magnitude smaller than residence times of phenocrysts in magma chambers and than the time scales for significant diffusion of most elements into the host mineral (Qin et al. 1992; Cottrell et al. 2002; Danyushevsky et al. 2002b; Gaetani and Watson 2002; Morgan et al. 2004; Costa and Dungan 2005). However, there have been reports of concentration profiles away from the host-glass interface in glassy inclusions from a variety of magmatic settings (Anderson 1974; Danyushevsky et al. 2002b; Mercier 2009; Colin et al. 2012), indicating that there are processes acting on melt inclusions on time scales sufficient for measurable concentration profiles to have been generated, but insufficient for the profiles to have been erased by diffusion.

Chapter 4 of this thesis presents a detailed examination of concentration profiles in glassy, olivine-hosted melt inclusions in submarine lavas from the Siqueiros Fracture Zone and in subaerial and submarine lavas from the Galapagos Islands. We show that the presence of significant zonation in melt inclusions is the norm rather than the exception; that the cores of melt inclusions can be significantly influenced by simultaneous growth of the host mineral on inclusion walls and multicomponent diffusion in the melt inclusion; and that aspects of the resultant concentration profiles can be used to constrain the last stages of the thermal histories of their host magmas.

References

Anderson AT (1974) Evidence for a picritic, volatile-rich magma beneath Mt. Shasta, California. Journal of Petrology 15 (2):243

Bell DR, Rossman GR, Maldener J, Endisch D, Rauch F (2003) Hydroxide in olivine: A quantitative determination of the absolute amount and calibration of the IR spectrum. Journal of Geophysical Research: Solid Earth 108 (B2):n/a-n/a. doi:10.1029/2001jb000679

Boyce JW, Liu Y, Rossman GR, Guan Y, Eiler JM, Stolper EM, Taylor LA (2010) Lunar apatite with terrestrial volatile abundances. Nature 466 (7305):466-469

Butler Jr J, Meyer Jr C Sulfur prevails in coatings on glass droplets-Apollo 15 green and brown glasses and Apollo 17 orange and black/devitrified/glasses. In: Lunar and Planetary Science Conference Proceedings, 1976. pp 1561-1581

Cameron AGW, Ward WR (1976) The Origin of The Moon. Abstracts of the Lunar and Planetary Science Conference 7

Canup RM (2004) Dynamics of Lunar Formation. Annual Review of Astronomy and Astrophysics 42 (1):441-475. doi:doi:10.1146/annurev.astro.41.082201.113457

Canup RM, Asphaug E (2001) Origin of the Moon in a giant impact near the end of the Earth's formation. Nature 412 (6848):708-712

Chen Y, Provost A, Schiano P, Cluzel N (2013) Magma ascent rate and initial water concentration inferred from diffusive water loss from olivine-hosted melt inclusions. Contributions to Mineralogy and Petrology 165 (3):525-541. doi:10.1007/s00410-012-0821-x

Chen Y, Zhang Y, Liu Y, Guan Y, Eiler J, Stolper EM (2015) Water, fluorine, and sulfur concentrations in the lunar mantle. Earth and Planetary Science Letters 427:37-46. doi:http://dx.doi.org/10.1016/j.epsl.2015.06.046

Clayton R, Mayeda T Genetic relations between the moon and meteorites. In: Lunar and Planetary Science Conference Proceedings, 1975. pp 1761-1769

Colin A, Faure F, Burnard P (2012) Timescales of convection in magma chambers below the Mid-Atlantic ridge from melt inclusions investigations. Contributions to Mineralogy and Petrology 164 (4):677-691. doi:10.1007/s00410-012-0764-2

Costa F, Dungan M (2005) Short time scales of magmatic assimilation from diffusion modeling of multiple elements in olivine. Geology 33 (10):837-840. doi:10.1130/g21675.1

Cottrell E, Spiegelman M, Langmuir CH (2002) Consequences of diffusive reequilibration for the interpretation of melt inclusions. Geochem Geophys Geosyst 3. doi:10.1029/2001gc000205

Danyushevsky LV, Della-Pasqua FN, Sokolov S (2000) Re-equilibration of melt inclusions trapped by magnesian olivine phenocrysts from subduction-related magmas: petrological implications. Contributions to Mineralogy and Petrology 138 (1):68-83. doi:10.1007/pl00007664

Danyushevsky LV, McNeill AW, Sobolev AV (2002a) Experimental and petrological studies of melt inclusions in phenocrysts from mantle-derived magmas: an overview of techniques, advantages and complications. Chem Geol 183 (1–4):5-24. doi:10.1016/s0009-2541(01)00369-2

Danyushevsky LV, Sokolov S, Falloon TJ (2002b) Melt Inclusions in Olivine Phenocrysts: Using Diffusive Re-equilibration to Determine the Cooling History of a Crystal, with Implications for the Origin of Olivine-phyric Volcanic Rocks. Journal of Petrology 43 (9):1651-1671. doi:10.1093/petrology/43.9.1651

Delano J, Hanson B, Watson W Abundance and diffusivity of sulfur in lunar picritic magmas. In: Lunar and Planetary Science Conference, 1994. p 325

Delano JW (1986) Pristine Lunar Glasses: Criteria, Data, and Implications. J Geophys Res 91 (B4):D201-D213. doi:10.1029/JB091iB04p0D201

Elkins-Tanton LT, Chatterjee N, Grove TL (2003) Magmatic processes that produced lunar fire fountains. Geophysical Research Letters 30 (10):n/a-n/a. doi:10.1029/2003gl017082

Fogel RA, Rutherford MJ (1995) Magmatic volatiles in primitive lunar glasses: I. FTIR and EPMA analyses of Apollo 15 green and yellow glasses and revision of the volatile-assisted fire-fountain theory. Geochimica et Cosmochimica Acta 59 (1):201-215. doi:http://dx.doi.org/10.1016/0016-7037(94)00377-X

Gaetani GA, Watson EB (2002) Modeling the major-element evolution of olivine-hosted melt inclusions. Chem Geol 183 (1-4):25-41. doi:10.1016/s0009-2541(01)00370-9

Ghiorso MS, Sack RO (1995) Chemical mass transfer in magmatic processes IV. A revised and internally consistent thermodynamic model for the interpolation and extrapolation of liquid-solid equilibria in magmatic systems at elevated temperatures and pressures. Contributions to Mineralogy and Petrology 119 (2):197-212

Greenwood JP, Itoh S, Sakamoto N, Warren P, Taylor L, Yurimoto H (2011) Hydrogen isotope ratios in lunar rocks indicate delivery of cometary water to the Moon. Nature Geoscience 4 (2):79-82

Hartmann WK, Davis DR (1975) Satellite-sized planetesimals and lunar origin. Icarus 24 (4):504-515. doi:http://dx.doi.org/10.1016/0019-1035(75)90070-6

Hauri E, Wang J, Dixon JE, King PL, Mandeville C, Newman S (2002) SIMS analysis of volatiles in silicate glasses: 1. Calibration, matrix effects and comparisons with FTIR. Chemical Geology 183 (1–4):99-114. doi:http://dx.doi.org/10.1016/S0009-2541(01)00375-8

Hauri EH, Saal AE, Rutherford MJ, Van Orman JA (2015) Water in the Moon's interior: Truth and consequences. Earth and Planetary Science Letters 409:252-264. doi:http://dx.doi.org/10.1016/j.epsl.2014.10.053

Hauri EH, Weinreich T, Saal AE, Rutherford MC, Van Orman JA (2011) High Pre-Eruptive Water Contents Preserved in Lunar Melt Inclusions. Science 333 (6039):213-215. doi:10.1126/science.1204626

Hui H, Peslier AH, Zhang Y, Neal CR (2013) Water in lunar anorthosites and evidence for a wet early Moon. Nature Geosci 6 (3):177-180. doi:http://www.nature.com/ngeo/journal/v6/n3/abs/ngeo1735.html#supplementary-information

Kent AJR (2008) Melt Inclusions in Basaltic and Related Volcanic Rocks. Reviews in Mineralogy and Geochemistry 69 (1):273-331. doi:10.2138/rmg.2008.69.8

Liu Y, Guan Y, Zhang Y, Rossman GR, Eiler JM, Taylor LA (2012) Direct measurement of hydroxyl in the lunar regolith and the origin of lunar surface water. Nature Geosci 5 (11):779-782. doi:http://www.nature.com/ngeo/journal/v5/n11/abs/ngeo1601.html#supplementary-information

Lloyd A, Plank T, Ruprecht P, Hauri E, Rose W (2013) Volatile loss from melt inclusions in pyroclasts of differing sizes. Contributions to Mineralogy and Petrology 165 (1):129-153. doi:10.1007/s00410-012-0800-2

Maclennan J, McKenzie D, Grönvold K, Shimizu N, Eiler J, Kitchen N (2003) Melt mixing and crystallization under Theistareykir, northeast Iceland. Geochemistry, Geophysics, Geosystems 4 (11)

McCubbin FM, Steele A, Hauri EH, Nekvasil H, Yamashita S, Hemley RJ (2010) Nominally hydrous magmatism on the Moon. Proceedings of the National Academy of Sciences 107 (25):11223-11228

McCubbin FM, Vander Kaaden KE, Tartèse R, Klima RL, Liu Y, Mortimer J, Barnes JJ, Shearer CK, Treiman AH, Lawrence DJ, Elardo SM, Hurley DM, Boyce JW, Anand M (2015) Magmatic volatiles (H, C, N, F, S, Cl) in the lunar mantle, crust, and regolith: Abundances, distributions, processes, and reservoirs. American Mineralogist 100 (8-9):1668-1707. doi:10.2138/am-2015-4934CCBYNCND

Mercier M (2009) Abondance et signification de l'eau dans les magmas mafiques. Développement de la spectroscopie vibrationnelle (Raman et FTIR). Thesis, Université Paris Sud-Paris XI,

Métrich N, Wallace PJ (2008) Volatile abundances in basaltic magmas and their degassing paths tracked by melt inclusions. Reviews in Mineralogy and Geochemistry 69 (1):363-402

Morgan DJ, Blake S, Rogers NW, DeVivo B, Rolandi G, Macdonald R, Hawkesworth CJ (2004) Time scales of crystal residence and magma chamber volume from modelling of diffusion profiles in phenocrysts: Vesuvius 1944. Earth and Planetary Science Letters 222 (3–4):933-946. doi:http://dx.doi.org/10.1016/j.epsl.2004.03.030

Mosenfelder JL, Le Voyer M, Rossman GR, Guan Y, Bell DR, Asimow PD, Eiler JM (2011) Analysis of hydrogen in olivine by SIMS: Evaluation of standards and protocol. Am Miner 96 (11-12):1725-1741. doi:10.2138/am.2011.3810

Newman S, Stolper EM, Epstein S (1986) Measurement of water in rhyolitic glasses--calibration of an infrared spectroscopic technique. American Mineralogist 71 (11):1527-1541

Newsom HE, Taylor SR (1989) Geochemical implications of the formation of the Moon by a single giant impact. Nature 338 (6210):29-34

Ni H, Xu Z, Zhang Y (2012) Hydroxyl and Molecular H_2O Diffusivity in a Haploandesitic Melt. Geochimica et Cosmochimica Acta

Nicholis MG, Rutherford MJ (2009) Graphite oxidation in the Apollo 17 orange glass magma: Implications for the generation of a lunar volcanic gas phase. Geochimica et Cosmochimica Acta 73 (19):5905-5917. doi:http://dx.doi.org/10.1016/j.gca.2009.06.022

Pahlevan K, Stevenson DJ (2007) Equilibration in the aftermath of the lunar-forming giant impact. Earth and Planetary Science Letters 262 (3):438-449

Persikov ES, Newman S, Bukhtiyarov PG, Nekrasov AN, Stolper EM (2010) Experimental study of water diffusion in haplobasaltic and haploandesitic melts. Chemical Geology 276 (3–4):241-256. doi:10.1016/j.chemgeo.2010.06.010

Qin ZW, Lu FQ, Anderson AT (1992) Diffusive Reequilibration of Melt and Fluid Inclusions. Am Miner 77 (5-6):565-576

Robinson KL, Taylor GJ (2014) Heterogeneous distribution of water in the Moon. Nature Geosci 7 (6):401-408. doi:10.1038/ngeo2173

Rossman GR (1996) Studies of OH in nominally anhydrous minerals. Phys Chem Minerals 23 (4-5):299-304. doi:10.1007/bf00207777

Rutherford MJ, Papale P (2009) Origin of basalt fire-fountain eruptions on Earth versus the Moon. Geology 37 (3):219-222. doi:10.1130/g25402a.1

Saal AE, Hauri EH, Cascio ML, Van Orman JA, Rutherford MC, Cooper RF (2008) Volatile content of lunar volcanic glasses and the presence of water in the Moon's interior. Nature 454 (7201):192-195. doi:http://www.nature.com/nature/journal/v454/n7201/suppinfo/nature07047_S1.html

Saal AE, Hauri EH, Langmuir CH, Perfit MR (2002) Vapour undersaturation in primitive mid-ocean-ridge basalt and the volatile content of Earth's upper mantle. Nature 419 (6906):451-455. doi:http://www.nature.com/nature/journal/v419/n6906/suppinfo/nature01073_S1.html

Saal AE, Hauri EH, Van Orman JA, Rutherford MJ (2013) Hydrogen Isotopes in Lunar Volcanic Glasses and Melt Inclusions Reveal a Carbonaceous Chondrite Heritage. Science 340 (6138):1317-1320. doi:10.1126/science.1235142

Sato M Oxygen fugacity and other thermochemical parameters of Apollo 17 high-Ti basalts and their implications on the reduction mechanism. In: Lunar and Planetary Science Conference Proceedings, 1976. pp 1323-1344

Sharp ZD, McCubbin FM, Shearer CK (2013) A hydrogen-based oxidation mechanism relevant to planetary formation. Earth and Planetary Science Letters 380:88-97. doi:http://dx.doi.org/10.1016/j.epsl.2013.08.015

Smith PM, Asimow PD (2005) Adiabat_1ph: A new public front-end to the MELTS, pMELTS, and pHMELTS models. Geochem Geophys Geosyst 6 (2):Q02004

Stolper E (1982) Water in silicate glasses: An infrared spectroscopic study. Contributions to Mineralogy and Petrology 81 (1):1-17. doi:10.1007/bf00371154

Stolper EM, Baker MB, Newcombe ME, Schmidt ME, Treiman AH, Cousin A, Dyar MD, Fisk MR, Gellert R, King PL, Leshin L, Maurice S, McLennan SM, Minitti ME, Perrett G, Rowland S, Sautter V, Wiens RC, Team MS (2013) The Petrochemistry of Jake_M: A Martian Mugearite. Science 341 (6153). doi:10.1126/science.1239463

Tartèse R, Anand M, McCubbin FM, Elardo SM, Shearer CK, Franchi IA (2014) Apatites in lunar KREEP basalts: The missing link to understanding the H isotope systematics of the Moon. Geology 42 (4):363-366

Taylor R, Esat TM (1996) Geochemical constraints on the origin of the Moon. GEOPHYSICAL MONOGRAPH-AMERICAN GEOPHYSICAL UNION 95:33-46

Taylor S Lunar and terrestrial potassium and uranium abundances-Implications for the fission hypothesis. In: Lunar and Planetary Science Conference Proceedings, 1979. pp 2017-2030

Wadhwa M (2008) Redox Conditions on Small Bodies, the Moon and Mars. Reviews in Mineralogy and Geochemistry 68 (1):493-510. doi:10.2138/rmg.2008.68.17

Wasson JT, Boynton WV, Kallemeyn GW, Sundberg LL, Wai CM Volatile compounds released during lunar lava fountaining. In: Lunar and Planetary Science Conference Proceedings, 1976. pp 1583-1595

Wetzel DT, Hauri EH, Saal AE, Rutherford MJ (2015) Carbon content and degassing history of the lunar volcanic glasses. Nature Geosci advance online publication. doi:10.1038/ngeo2511

http://www.nature.com/ngeo/journal/vaop/ncurrent/abs/ngeo2511.html#supplementary-information

Wetzel DT, Rutherford MJ, Jacobsen SD, Hauri EH, Saal AE (2013) Degassing of reduced carbon from planetary basalts. Proceedings of the National Academy of Sciences 110 (20):8010-8013

Zhang Y Water" in Lunar Basalts: The Role of Molecular Hydrogen (H2), Especially in the Diffusion of the H Component. In: 42nd Lunar and Planetary Science Conference, held March 7--11, 2011 at The Woodlands, Texas. LPI Contribution, 2011. vol 1608.

Zhang Y, Ni H (2010) Diffusion of H, C, and O Components in Silicate Melts. Reviews in Mineralogy and Geochemistry 72 (1):171-225. doi:10.2138/rmg.2010.72.5

Zhang Y, Stolper EM (1991) Water diffusion in a basaltic melt. Nature 351 (6324):306-309

Zhang Y, Stolper EM, Wasserburg GJ (1991) Diffusion of water in rhyolitic glasses. Geochimica et Cosmochimica Acta 55 (2):441-456. doi:10.1016/0016-7037(91)90003-n

C h a p t e r 2

SOLUBILITY OF WATER IN LUNAR BASALT AT LOW pH_2O

M.E. Newcombe[a], A. Brett[b], J.R. Beckett[a], M.B. Baker[a], S. Newman[a], Y. Guan[a], and E.M. Stolper[a]

[a] Division of Geological and Planetary Sciences, California Institute of Technology, Pasadena, CA 91125, USA

[b] Imperial College London, South Kensington Campus, London SW7 2AZ, UK

1. Abstract

We report the solubility of water in Apollo 15 'Yellow Glass' and an iron-free basaltic analogue composition at 1 atm and 1350 °C. We equilibrated melts in a 1-atm furnace with flowing H_2/CO_2 gas mixtures that spanned ~8 orders of magnitude in fO_2 (from IW-3 to IW+5) and ~3 orders of magnitude in pH_2/pH_2O (from 0.03 to 24). Our quenched experimental glasses were analyzed by Fourier transform infrared spectroscopy (FTIR) and secondary ionization mass spectrometry (SIMS) and were found to contain up to ~420 ppm water. Our results demonstrate that, under the conditions of our experiments: (1) hydroxyl is the only H-bearing species detected by FTIR; (2) the solubility of water is proportional to the square root of pH_2O in the furnace atmosphere and is independent of fO_2 and pH_2/pH_2O; (3) the solubility of water is very similar in both melt compositions; (4) the concentration of H_2 in our iron-free experiments is <3 ppm, even at oxygen fugacities as low as IW-2.3 and pH_2/pH_2O as high as 24; and (5) SIMS analyses of water in iron-rich glasses equilibrated under variable fO_2 conditions can be strongly influenced by matrix effects, even when the concentrations of water in the glasses are low. Our results can be used to constrain the entrapment pressure of the lunar melt inclusions of Hauri et al. (2011).

2. Introduction

Recent detections of dissolved water in lunar volcanic glasses (Saal et al. 2008; Hauri et al. 2011; Saal et al. 2013; Chen et al. 2015; Wetzel et al. 2015), lunar apatites (Boyce et al. 2010; McCubbin et al. 2010; Greenwood et al. 2011; Tartèse et al. 2014), and plagioclase from lunar highland anorthosites (Hui et al. 2013) have led to a reevaluation of what has appeared for

decades to be one of the definitive results of study of lunar samples returned by the lunar sample return missions, i.e., that the sources of lunar magmas—and by inference the entire Moon—are much poorer in water than the Earth; indeed the Moon was described as "bone dry" (Newsom and Taylor 1989). In particular, direct measurements of water in incompletely degassed, primitive lunar glasses made in several laboratories have shown that water concentrations are similar to those observed in magmas from Earth's depleted upper mantle (Saal et al. 2008; Chen et al. 2015; Wetzel et al. 2015), and that the isotopic composition of this water is approximately chondritic (Saal et al. 2013; Barnes et al. 2014; Tartèse et al. 2014). Although there are still some that dispute these results (or their generality to the Moon as a whole; Sharp et al. 2010; Albarède et al. 2015), these observations have been interpreted in terms of a common origin for terrestrial and lunar water (Saal et al. 2013). The incorporation of water into the Moon in concentrations similar to those of the Earth are seemingly at odds with the widely held view of the origin of the Moon as the result of an impact between the early Earth and a Mars-sized impactor (e.g., Canup and Asphaug 2001; Pahlevan and Stevenson 2007), so the identification of unexpectedly wet lunar glasses (and other phases) has led to a resurgence of interest in the formation and evolution of the Moon in light of this fact (Nakajima and Stevenson 2014; Canup et al. 2015).

In addition to its importance for understanding the origin of the Moon, the unexpectedly high water concentrations that have been observed or inferred also have implications for our understanding of magma generation, migration, and eruption on the Moon. However, full exploration of these implications requires knowledge of phase equilibria (e.g., water solubility) and transport properties (e.g., the diffusivity of water) for molten lunar basalts under conditions relevant to the near surface of the Moon. Although extensively studied for terrestrial melt compositions and conditions (e.g., Stolper 1982a; Zhang and Stolper 1991; Dixon et al. 1995; Moore et al. 1998; Persikov et al. 2010), water solubility and diffusion have not been studied for melts approaching the high iron contents, low pH_2O, and low fO_2 conditions on the Moon. The goal of the work described here is to measure the solubility of water in a lunar volcanic glass composition and in a simplified basaltic system under the low pH_2O and low fO_2 conditions thought to be prevalent during lunar volcanic eruptions (Sato 1976; Wadhwa 2008). We conducted water solubility experiments by equilibrating melts with H_2O-bearing vapor at 1 atm over a range of fO_2 and pH_2/pH_2O and then measuring the concentrations of water in our experimental glasses by FTIR and SIMS. We compare our results to the few published studies of water solubility in basaltic melts at low pressures and to extrapolations to low pressures of existing models of water solubility in silicate melts. We then use our data to place constraints on

the concentration of molecular hydrogen dissolved in silicate melts equilibrated under highly reducing conditions (i.e., with oxygen fugacities more than two log units below the iron-wüstite buffer) and to constrain the depths of entrapment of the lunar melt inclusions described by Hauri et al. (2011).

3. Background

3.1. Speciation of water in silicate melts

A silicate melt in equilibrium with a water-bearing vapor dissolves water as both water molecules (H_2O_m) and hydroxyl groups (OH) according to the following chemical reactions (Stolper 1982a):

$$\mathrm{H_2O}^{vapor} \leftrightarrow \mathrm{H_2O_m}^{melt} \quad (1)$$

$$\mathrm{H_2O_m}^{melt} + \mathrm{O}^{0,melt} \leftrightarrow 2\mathrm{OH}^{melt} \quad (2)$$

In reaction (2), $\mathrm{O}^{0,melt}$ could be a bridging oxygen (i.e., an oxygen bridging two tetrahedrally coordinated, network-forming cations), a non-bridging oxygen in an aluminosilicate tetrahedron, or a "free" oxygen; and OH^{melt} represents a hydroxyl group bonded to an aluminosilicate polymer (Behrens and Nowak 1997; Kohn 2000). Reactions (1) and (2) can be combined to a reaction governed by the equilibrium constant K_{eq} (Stolper 1982a):

$$K_{eq} \propto \frac{[\mathrm{OH}^{melt}]^2}{f\mathrm{H_2O}^{vapor}[\mathrm{O}^{0,melt}]} \quad (3)$$

where square brackets indicate mole fractions on a single oxygen basis, and $f\mathrm{H_2O}^{vapor}$ is the fugacity of water in the vapor. Concentrations of molecular water and hydroxyl have been measured by Fourier transform infrared spectroscopy (FTIR) in glasses quenched from melts for several bulk compositions across a wide range of total water concentrations, where total water refers to the sum of the molecular water and hydroxyl species (Stolper 1982b; Silver and Stolper 1989; Silver et al. 1990; Dixon et al. 1995). These studies have shown that hydroxyl is the dominant dissolved species at low total water concentrations. At higher concentrations of a few weight percent water, the concentration of dissolved hydroxyl levels off and molecular water becomes the dominant species. The concentrations of hydroxyl and molecular water at different

total water concentrations are well described by equations (1)–(3), although the appropriate solution model for the mixing of OH, H_2O_m and O^0 in the melt is still not completely resolved (Figure 1; Silver and Stolper 1989; Silver et al. 1990; Dixon et al. 1995).

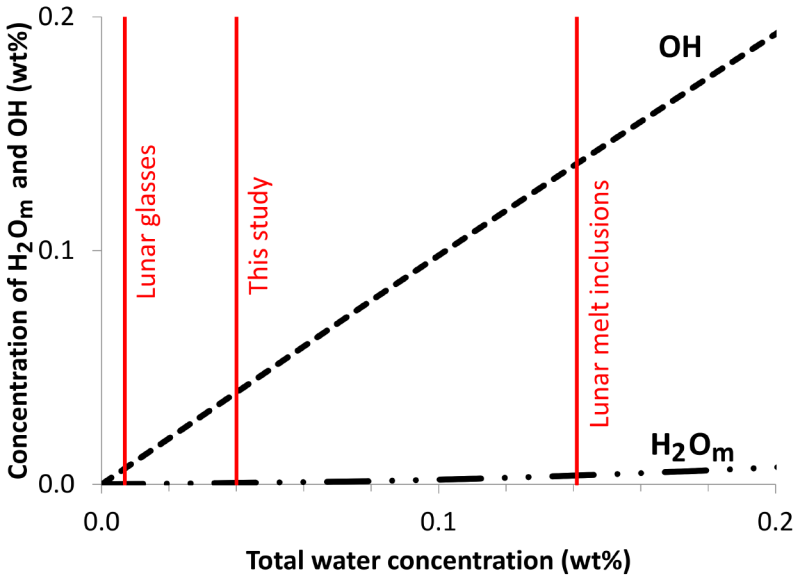

Figure 1 Concentrations of hydroxyl and molecular water in a melts with low total water concentrations. The dominant dissolved species is hydroxyl under these conditions. Curves were generated using VolatileCalc (Newman and Lowenstern 2002) which adopts the regular solution model of Silver and Stolper (1989). Red vertical lines indicate the maximum total water concentrations measured in lunar olivine-hosted melt inclusions (Hauri et al. 2011) and lunar glasses (Saal et al. 2008; Saal et al. 2013), and the maximum total water concentration considered in this study.

The solubility of water in silicate melts is known to be strongly dependent on pressure (e.g., McMillan 1994; Dixon et al. 1995). At low pressures where only small quantities of water are soluble, the reaction of molecular water with bridging oxygens in the melt to produce hydroxyl groups causes a negligible reduction of the large number of available bridging oxygens, so it can be assumed that the concentration of bridging oxygens in the melt ($[O^{0,melt}]$) is approximately constant. Therefore, under low pressure conditions, reaction (3) can be re-arranged as follows:

$$[OH^{melt}] \propto \sqrt{f H_2O^{vapor}} \quad (4)$$

and since at the low water contents of lunar magmas (<1,500 ppm), less than 50 ppm is expected to be dissolved as water molecules (i.e., ~3% of the dissolved water at 1500 ppm and ~0.4 % of

the dissolved water at 50 ppm), [OH^{melt}] is essentially identical to the total amount of dissolved water.

The relationship in equation (4) is analogous to Sieverts' law in metallurgy, which describes the dissolution of diatomic gases in metals (Sieverts 1929). The solubility of water in glasses at ambient pressure has long been of interest to researchers in the glass industry, and several studies have demonstrated that applicability of equation (4) to a range of synthetic silicate glass and melt compositions (McMillan 1994). One of the aims of this study is to test the applicability of equation (4) to conditions relevant to lunar basaltic melts.

3.2. Potential role of H_2 dissolution under reducing conditions

In addition to molecular water and hydroxyl, silicate melts can also dissolve H-bearing species in the form of H_2 molecules. Following a similar treatment to that described above for water, it can be shown that the solubility of H_2 in a silicate melt in equilibrium with an H-bearing vapor is expected to scale linearly with the fugacity of H_2 in the vapor:

$$H_2^{vapor} \leftrightarrow H_2^{melt} \quad (5)$$

$$K_{eq} \propto \frac{[H_2^{melt}]}{fH_2} \quad (6)$$

$$[H_2^{melt}] \propto fH_2 \quad (7)$$

Molecular hydrogen has not been directly detected in studies of natural terrestrial silicate melts or glasses and it is thought that concentrations of H_2 in mafic terrestrial melts are negligible at the low pressures, high temperatures, and relatively oxidizing conditions relevant to volcanic eruptions at the surface of the Earth (e.g., Zhang and Ni 2010). However, significant quantities of H_2 could be dissolved in terrestrial melts in the deep mantle (Hirschmann et al. 2012), and it is possible that H_2 dissolution could also be significant in the eruptive products of planetary bodies that are more reduced than the Earth, including the Moon (Zhang and Ni 2010; Zhang 2011).

Natural lunar basalts record oxygen fugacities between the iron-wüstite buffer (IW) and two log units below this buffer (Wadhwa 2008). Under these relatively reducing conditions, H_2 is stabilized relative to H_2O in low pressure, high temperature C-O-H vapors (note that at high pressures, methane is also stabilized; Zhang and Duan 2009). As described by Zhang (2011), the

molar H_2/H_2O ratio in a low pressure, high temperature vapor can be determined from thermodynamic data (e.g., Deines et al. 1974) for the following reaction:

$$H_2^{vapor} + 0.5O_2^{vapor} \leftrightarrow H_2O^{vapor} \quad (8)$$

The equilibrium constant for reaction (8) is:

$$K_{eq} = \frac{fH_2O}{fH_2 \cdot fO_2^{0.5}} \quad (9)$$

Therefore, we can rearrange equation (9) to find the dependence of the fH_2/fH_2O ratio on oxygen fugacity:

$$\frac{fH_2}{fH_2O} = \frac{1}{K_{eq} \cdot fO_2^{0.5}} \quad (10)$$

Zhang (2011) used the analysis above and an estimate of the solubility of H_2 in silicate melt (based on experimental results for silica glass, since data constraining H_2 solubility in basaltic melts were not available at the time) to propose that, at magmatic temperatures and an oxygen fugacity of IW-2, the concentration of H_2 dissolved in silicate melt could exceed the concentration of dissolved H_2O_m. However, extrapolation to low pressures of recent experimental data on the solubility of H_2 in basaltic and andesitic melts (Hirschmann et al. 2012) suggests that H_2 is unlikely to be a significant volatile species in low-pressure lunar melts.

Our experiments offer the opportunity to explore the importance of H_2 dissolution in lunar basalt for water solubility: i.e., we have equilibrated lunar basaltic melts over a range of fH_2/fH_2O ratios from 0.03 – 24 and the quenched melts from these experiments have been analyzed by FTIR and SIMS. FTIR can be used to quantify the concentrations of individual H-bearing species in silicate melts (Stolper 1982b; Newman et al. 1986), including H_2 if present in concentrations greater than ~900 ppm (Hirschmann et al. 2012), whereas SIMS measures bulk H contents. By comparing concentrations of H-bearing species measured by both techniques in experiments with varying fH_2/fH_2O, it is possible to set limits on the amount of dissolved H_2 and to determine whether it is a significant component of dissolved H-bearing species in melts at the low pressures relevant to the near-surface lunar environment.

3.3. Method for controlling the partial pressures of H_2, CO_2, H_2O, CO and O_2 in a 1-atm furnace atmosphere

Flowing mixtures of H_2 and CO_2 gases can be used to control the oxygen fugacity and the partial pressures of H_2, CO_2, H_2O and CO in the hotspot of a 1-atm furnace. At any given temperature, the initial H_2/CO_2 ratio of the gas mixture (R), fixes its equilibrium pH_2O, pO_2, pCO_2, and pH_2 (Figure 2; Deines et al. 1974). [Note that at 1 atm and magmatic temperatures the behavior of the gas mixture is so close to ideal that the fugacity of each species is essentially equal to its partial pressure, which is in turn equal to the mole fraction of that species in the vapor. The assumption of gas ideality will be applied for the remainder of this study, and fugacity and partial pressure will be used interchangeably.] With decreasing R, pH_2 decreases monotonically, pCO_2 increases monotonically, and pH_2O shows a maximum at R=1, i.e. at IW+0.3 (Fig. 2). Therefore, for any value of pH_2O (except at the maximum), there are 2 possible values of pH_2. We can exploit this feature of the system to determine the dependence (if any) of water solubility on pH_2 and pO_2.

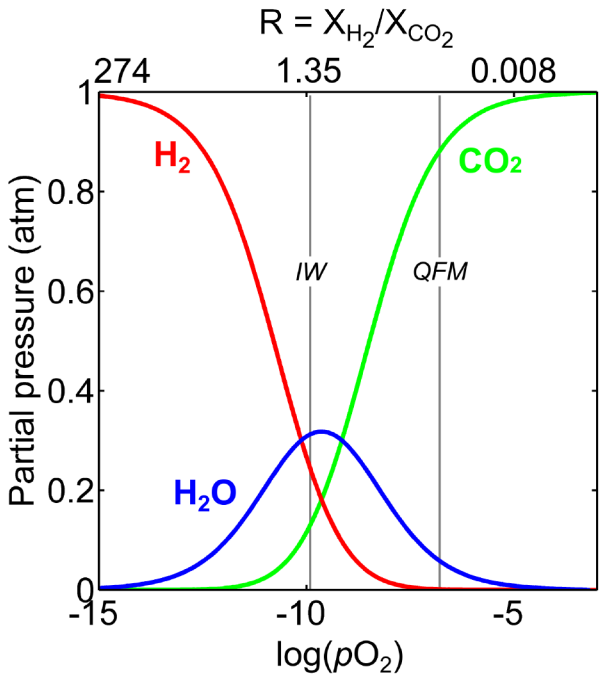

Figure 2 Partial pressures of H_2, CO_2 and H_2O in vapor as functions of $\log(pO_2)$ at 1350°C and P_{tot}=1 atm. Top axis: R is the ratio of mole fractions of H_2 and CO_2 in the introduced gas mixture. Gray vertical lines are buffers (IW = iron-wüstite; QFM = quartz-fayalite-magnetite).

4. Methods

We equilibrated a synthetic Apollo 15 'Yellow Glass' composition (thought to be produced by a Hawaiian-style "fire fountain" eruption; Delano 1986) and two mixtures of anorthite and diopside glasses with flowing H_2-CO_2 gas mixtures at 1350°C and 1 atm total pressure. pH_2/pH_2O was varied from 0.003 to 24, resulting in a variation of pO_2 was from ~10^{-13} to ~10^{-5} (IW-3 to IW+5). Concentrations of dissolved water were measured by FTIR and SIMS.

4.1. Starting materials

Synthetic Apollo 15 'Yellow Glass' (hereafter referred to as 'lunar glass'; LG) was made by combining reagent-grade powdered oxides. Oxide and carbonate powders were weighed on a balance with a precision of 0.1 mg after baking at appropriate temperatures prior to weighing in order to remove adsorbed water. The resultant powder plus ethanol was mixed in an alumina mortar for ~4 hours. The powder was decarbonated at 800 °C and then placed in a shallow alumina boat and reduced at 400 °C in a horizontal Lindberg furnace: A mixture of H_2 and CO_2 with an oxygen fugacity of IW+1 was flowed through a platinum mesh in order to catalyze the reaction between H_2 and CO_2 (Beckett and Mendybaev 1997) and this gas mixture was then allowed to flow over the powder. After ~1 hour, the furnace was switched off, and the alumina boat was slowly pulled towards the cool part of the furnace (whilst maintaining a seal to prevent oxidation of the powder). The efficacy of the powder reduction could be assessed by the change in color of the powder from red to gray (caused by the reduction of red Fe_2O_3 to FeO). Following this reduction step, the powder was pressed into pellets measuring ~1 cm in diameter, and chips of these pellets weighing ~20 – 70 mg were balanced on rhenium wire loops (99.97% rhenium wire with diameter of 0.25 mm) and used as starting material for the LG experiments.

Mixtures of anorthite and diopside glasses corresponding to compositions close to the 1-atm eutectic composition on the anorthite-diopside join ($An_{36}Di_{64}$) were prepared by weighing out anorthite and diopside glasses (provided by G.J. Fine of Corning Glass). These glasses were crushed and mixed together under ethanol in an alumina mortar for ~4 hours. The resultant glass powder was placed in a platinum crucible and melted in a 1-atm Deltech vertical furnace under air at 1398 °C for 16 hours. The anorthite-diopside (AD) melt was quenched to a glass by pulling the platinum crucible out of the top of the furnace and plunging it into a beaker of distilled water. The AD glass was removed from the platinum crucible and broken into small chips with the use of a percussion mortar. Potential contamination of the glass by small flakes of metal from the

percussion mortar was avoided by passing a magnet over the glass chips. Chips of glass weighing 20 – 90 mg were balanced on platinum loops and used as starting material for the AD experiments. The compositions of LG and AD glasses are reported in Table 1.

Oxide (wt%)	AD Batch 1	AD Batch 3	LG Batch 2
SiO_2	49.35(65)	49.94(32)	43.44(17)
TiO_2	0.022(24)	0.019(22)	3.41(4)
Al_2O_3	18.51(74)	16.58(28)	8.89(11)
FeO	0.034(28)	0.036(20)	22.13(18)
MgO	9.31(20)	10.46(7)	12.81(11)
CaO	23.60(10)	23.90(9)	8.65(5)
Na_2O	0.061(12)	0.084(21)	0.41(3)
K_2O	0.003(4)	0.010(7)	0.006(5)
Cr_2O_3	0.001(5)	0.010(16)	0.42(4)
MnO	0.014(19)	0.009(12)	0.28(3)
Total	100.91	101.05	100.44
Normative minerals (wt%)			
Anorthite	49.77	44.39	22.28
Diopside	47.76	52.14	16.96
Hypersthene			27.14
Albite			3.47
Orthoclase			0.06
Olivine	0.63	1.16	23.05
Chromite			0.62
Ilmenite	0.04	0.04	6.44
Nepheline	0.28	0.37	
Larnite	1.53	1.85	
Leucite		0.05	

Table 1. Composition and CIPW norms of starting materials. Values in parentheses indicate one standard deviation of replicate analyses (10 analyses of AD Batch 1, 10 analyses of AD Batch 3, and 12 analyses of Synthetic Apollo 'Yellow Glass' (LG) Batch 2) in terms of the least number of units cited [i.e., 49.35(65) = 49.35 ± 0.65]. The CIPW norm is calculated assuming that all Fe is Fe^{2+}.

4.2. Experimental methods

Chips of AD glass and LG pressed powder pellets weighing ~50 mg were balanced on wire loops. Once molten, the starting material formed beads of silicate melt with diameters of ~3 mm that clung to the wire loops by surface tension. It was important to avoid contamination of the starting materials by volatile material, so no binder was used to stabilize the glass or pressed

powder pellets on the loops. All AD glass chips were hung on platinum wire loops. Most of the LG experiments were hung on rhenium wire loops so as to reduce the loss of iron from the melt to the metal (via the reaction $FeO^{melt} \leftrightarrow Fe^{metal} + 0.5O_2$) over the course of the experiment (Borisov and Jones 1999). However, rhenium volatilizes at oxygen fugacities above ~QFM (Borisov and Jones 1999) at the temperatures of our experiments, so thin platinum wire loops (0.008 inch diameter) were used to hang the most oxidizing LG experiment. Two of the most reducing experiments (LG6 at IW-2.2 and LG7 at IW-3.0) were hung on molybdenum wire, because under such reducing conditions, molybdenum has been shown to be even more effective than rhenium for avoiding iron loss (Hess et al. 1975). As shown in Figure 3, the use of rhenium wire loops proved to be successful at minimizing iron loss from experiments with oxygen fugacities between IW-1 and QFM. Experiments LG40 and LG7 were reducing enough that they precipitated iron metal blebs and this left the residual melt significantly depleted in iron. As described above, the most oxidizing experiment (LG35) was hung from a thin platinum wire loop, and as anticipated, this experiment experienced very minimal iron loss into the platinum.

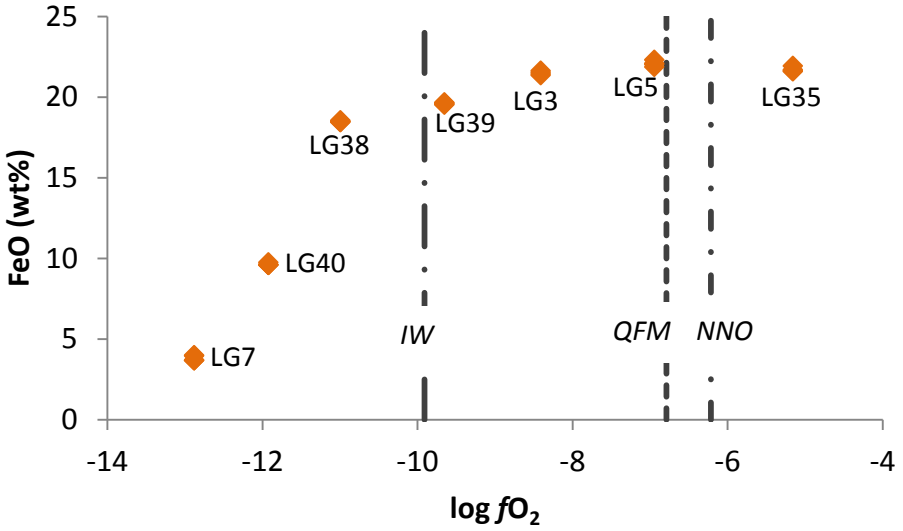

Figure 3 Post-run concentrations of FeO in LG experiments run under a range of oxygen fugacities. Vertical dashed lines are buffers (IW = iron-wüstite; QFM = quartz-fayalite-magnetite; NNO = nickel-nickel oxide).

All experiments were conducted at 1350 °C and the oxygen fugacity inside the furnace was controlled using flowing mixtures of H_2 and CO_2 gases as explained in section 2.3. Temperature measurements were made using a type-B thermocouple and the oxygen fugacity was measured using an yttria-stabilized zirconia oxygen sensor (SIRO2; Ceramic Oxide Fabricators, Eaglehawk, Australia). The accuracy of the sensor was checked at the IW buffer and was found to

be within 0.15 log units of the calibrations of Huebner (1971) and O'Neill and Pownceby (1993). In later runs (AD23, AD25, AD26, LG35, LG38, LG39, LG40), the flow rates of H_2 and CO_2 were set using Sierra SmartTrak M100 and Sierra MicroTrak M101 mass flow controllers. For these experiments, it was possible to compare the oxygen fugacity measured by the oxygen sensor with the oxygen fugacity calculated from the known flow rates, and these values agreed to within 0.1 log units. Note that the temperature and gas mixture were set up prior to each run, but for the most part, the experiments were conducted without the presence of a thermocouple and oxygen sensor in the furnace.

At the beginning of each experiment, the furnace was flushed with N_2 gas and the sample was placed above the hotspot at a temperature of a few hundred degrees centigrade. Once the furnace had been sealed, the N_2 gas was switched off and the H_2/CO_2 gas mixture for that experiment flushed the furnace for ~10 minutes. These steps prevented the volatilization of the rhenium wire used for the LG experiments by preventing contact between rhenium and air at high temperature. The sample was then lowered into the hotspot and allowed to equilibrate with the gas mixture for 3 – 72 hours before being drop-quenched in deionized water. Those experiments that stayed intact during the quench were cut through their centers on a Unipress Precision Wire Saw and one half was doubly polished to produce a wafer of glass with a thickness of a few hundred microns. For those experiments that broke on quenching, a few large fragments relatively free of cracks were doubly-polished. All experiments were then analyzed by Fourier transform infrared spectroscopy (FTIR).

4.3. Measuring the concentration of dissolved water by FTIR

Our experimental glasses were analyzed by transmission FTIR using a Nicolet Magna-IR 860 FTIR spectrometer equipped with a Nicolet Continuμm IR microscope, a CaF_2 beamsplitter, and a MCT/A detector cooled with liquid N_2. Spectra were collected using a ~25×80 μm aperture across a wavenumber range of 1300 – 7000 cm^{-1} with a resolution of 4 cm^{-1}, and 2048 scans were averaged for each analysis.

Because of the low concentrations of water in our samples and their small thicknesses we used the 3550 cm^{-1} absorption band (Figure 4) to determine total water contents of our samples. This band is due to fundamental vibrational modes in both hydroxyl and molecular water (Stolper 1982b; Newman et al. 1986; Dixon et al. 1995), i.e., it does not distinguish between these two

dissolved species and gives only a measurement of total water. The concentration of water was calculated using the Beer-Lambert law (Stolper 1982b):

$$[H_2O] = \frac{100 \times Abs_{3550} \times 18.015}{d \times \rho \times \varepsilon_{3550}} \quad (11)$$

In this expression, $[H_2O]$ is the concentration of water in wt% (i.e., the amount of water that would be measured if all of the molecular water and hydroxyl were removed as H_2O on heating), Abs_{3550} is the background-corrected peak height of the absorbance peak at ~3550 cm^{-1}; 18.015 is the molecular weight of H_2O in atomic mass units; d is the thickness of the glass wafer in cm; ρ is the density of the glass in g/l; and $\varepsilon_{3550}$is the molar absorptivity of water at 3550 cm^{-1} in $l \cdot mol^{-1} cm^{-1}$. We employed a linear background correction (a selection of background-corrected spectra are shown in Figure 4b), and densities of the AD and LG glasses were measured using a digital Berman balance by comparing the weights of fragments of each glass composition in air and toluene.

Estimation of ε_{3550}

A challenge for the study of water concentrations in glasses by FTIR is the determination of the molar absorption coefficient, ε, which is known to vary with glass composition (Dixon et al. 1995; Mandeville et al. 2002; Mercier et al. 2010). A common approach to this problem is to calibrate ε for each glass composition separately via the measurement of water concentrations by an independent technique such as Karl Fischer Titration. However, such measurements require the synthesis of significant quantities of high water-concentration glasses that were not synthesized as part of the current study. Several studies have shown that basaltic melts have values of ε_{3550} that cluster around 63 $l \cdot mol^{-1} cm^{-1}$ (Pandya et al. 1992; Dixon et al. 1995; Yamashita et al. 1997; Mercier et al. 2010), and this is the value adopted for the AD and LG glasses in this study.

An alternative approach for estimating molar absorption coefficients is to search for relationships between ε and glass compositional parameters (Pandya et al. 1992; Dixon et al. 1995). However, whereas the molar absorption coefficients for the 5200 cm^{-1} and 4500 cm^{-1} bands have been shown to vary predictably with glass compositional parameters such as the cation fractions of Si^{4+} and Al^{3+} (Dixon et al. 1995), the relationship between ε_{3550} and glass composition appears to be more complex and currently less predictable (Pandya et al. 1992; Mandeville et al. 2002; Mercier et al. 2010). A recent compilation of ε_{3550}values by Mercier et

al. (2010) suggests that ε_{3550}varies from ~90 l·mol^{-1}cm^{-1} in the most polymerized melts (those with NBO/T close to zero and cation fraction of Si^{4+} + Al^{3+} close to one) to ~40 l·mol^{-1}cm^{-1} in less polymerized melts (with NBO/T ~0.7 and cation fraction of Si^{4+} + Al^{3+} ~0.6). The AD melt composition studied here lies at the depolymerized end of this compositional range, with NBO/T = 0.80 (T = Si^{4+}+ Al^{3+}+ Fe^{3+}+P^{5+}; calculated at IW and 1350 °C using the Fe^{3+}/Fe^{2+} calibration of Kress and Carmichael (1991)) and cation fraction of Si^{4+} + Al^{3+} = 0.64, suggesting that ε_{3550} for the AD composition could be at the low end of the range observed for natural silicate melts (i.e., ~40 l·mol^{-1}cm^{-1}). The LG composition is highly depolymerized with NBO/T = 1.7 (T = Si^{4+}+ Al^{3+}+ Fe^{3+}+P^{5+}; calculated at IW and 1350 °C using the Fe^{3+}/Fe^{2+} calibration of Kress and Carmichael (1991)) and cation fraction of Si^{4+} + Al^{3+} = 0.51, and as such lies outside the range of natural melt compositions for which ε_{3550} has been calibrated.

The paucity of data for ε_{3550} of highly depolymerized melts makes it difficult to estimate ε_{3550} for the AD and LG compositions with confidence. However, we note that the primary focus of this study is on relative (rather than absolute) concentrations of water dissolved in melts equilibrated with a wide range of pH_2O, fO_2, and pH_2/pH_2O conditions, and our FTIR data are well-suited to this focus despite the uncertainty in ε_{3550}. Absolute concentrations are considered when we compare our results to previous studies of water solubility in basaltic melts in section 5.1; for this analysis, we consider values of ε_{3550} from 40 to 80 l·mol^{-1}cm^{-1}.

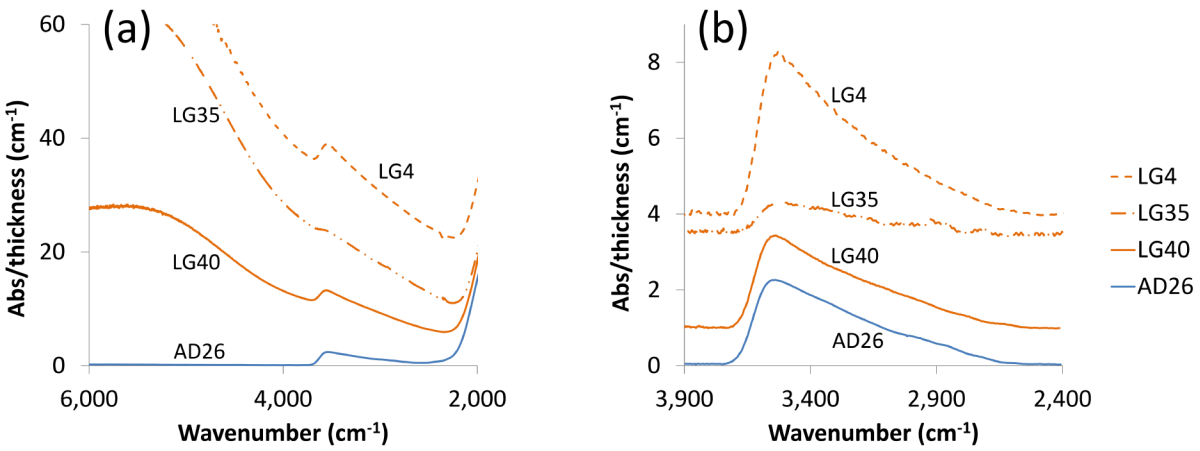

Figure 4 (a) Full spectra of LG and AD glasses from 2000 – 6000 cm-1. The 3550 cm^{-1} total water peak is clearly visible in all spectra. Note the lack of a molecular water peak at 5200 cm^{-1} and the lack of a hydrogen peak at ~4130 cm^{-1}(Hirschmann et al. 2012). In spectra of LG glasses, the 3550 cm^{-1} peak is superimposed on a broad region of high absorbance caused by the presence of large quantities of iron in this composition. The region of high absorbance at ~2000 cm^{-1} is attributed to absorbance by the silicate network. **(b)** Background-corrected spectra. The 3550 cm^{-1} peak was corrected using a linear background prior to measuring peak height. LG40 and AD26 were equilibrated in the furnace at the same time, under the same pH_2O and fO_2 conditions. LG35 contains the lowest measured water concentration of all the experiments (69 ppm); the 3550 cm^{-1} water peak is clearly resolved even at this low concentration. LG4 is one of the highest concentration experiments, with 370 ppm water.

4.4. Measuring the total concentration of H-bearing species by SIMS

In addition to measuring the concentration of water (as H_2O and/or OH) by FTIR, we also measured the total concentration of H-bearing species in the melt (dissolved as H_2O, OH, and potentially H_2) using the Cameca 7f-GEO SIMS at Caltech. Prior to analysis, chips of our experimental glasses were polished in dental resin. The polished glass chips were removed from the dental resin by soaking in acetone for a few hours before being ultrasonicated in three cycles each of toluene, acetone, and isopropanol. The chips were baked overnight in a vacuum oven at ~110 °C before being pressed into a 1-inch diameter aluminum mount filled with indium. Three days before the beginning of the analytical session, the mount was coated in a 50-nm layer of gold and was placed under vacuum in the sample exchange airlock. Samples were analyzed with a ~4-nA primary beam of cesium ions. The primary beam was rastered across a 15×15 μm^2 area during 120 s of presputtering, producing a crater with an approximate diameter of 20 µm, and area of the raster was reduced to 5×5 μm^2 during analysis. Use of a 100 µm field aperture ensured that only secondary ions from the central ~10 µm of the sputtered crater were collected. Counts of

^{16}OH, ^{18}O, ^{12}C, and ^{30}Si were measured by an electron multiplier. A mass resolving power of ~5000 was used to separate the ^{16}OH peak from ^{17}O.

5. Results

We conducted 10 experiments on AD (IW–2.3 to IW+4.8; pH_2/pH_2O from 0.003 to 8) and 14 experiments on LG (IW–3.0 to IW+4.8; pH_2/pH_2O from 0.003 to 24). Run conditions are listed in Table 1. Hydroxyl is the only dissolved H-bearing species detected in the quenched glasses, although we looked for molecular H_2O (by FTIR) and H_2 (by FTIR and SIMS). The concentrations of hydroxyl dissolved in both the LG and AD melts are proportional to $pH_2O^{½}$ (Figure 5) and range from ~70 to ~420 ppm (calculated as H_2O). Best fits to our data are

$$[H_2O]_{AD}\ (ppm) = (732 \pm 12)\sqrt{pH_2O\ (atm)} \quad (12)$$

$$[H_2O]_{LG}\ (ppm) = (687 \pm 12)\sqrt{pH_2O\ (atm)} \quad (13)$$

where $[H_2O]$ indicates the concentration of hydroxyl calculated as H_2O.

Concentrations of hydroxyl in the glasses depend only on pH_2O, and are independent of fO_2 and pH_2, i.e., when the pH_2O is the same for experiments on the oxidizing and reducing sides of the pH_2O vs. pO_2 curve, the dissolved water contents are the same (Figure 5). The constants of proportionality in equations (12) and (13) are similar, suggesting that water solubility is only weakly dependent on melt composition under these conditions. This inference is further supported by the symmetry of the water concentrations on either side of the pH_2O bell curve in Figure 5d, despite the extensive Fe-loss suffered by the most reducing experiments (Figure 3).

Experiment	*Loop*	*Batch (AD)*	*log(fO_2)*	*ΔIW*	*R*	*pH_2*	*pH_2O*	*pH_2/pH_2O*	*H_2O (ppm)*	*1σ*
AD1b	Pt	1	-8.79	1.12	0.48	0.06	0.27	0.22	402.14	5.09
AD2	Pt	1	-10.63	-0.72	2.36	0.45	0.25	1.79	383.33	4.46
AD3b	Pt	1	-9.55	0.36	0.93	0.16	0.32	0.52	388.96	6.30
AD5	Pt	1	-8.00	1.91	0.23	1.47E-02	0.17	0.09	317.41	5.09
AD6	Pt	1	-6.22	3.69	0.03	3.58E-04	0.03	0.01	146.47	1.56
AD7	Pt	1	-6.84	3.07	0.07	1.40E-03	0.06	0.02	198.98	3.73
AD9	Pt	1	-11.27	-1.35	4.33	0.64	0.17	3.71	268.44	8.67
AD10	Pt	1	-9.49	0.42	0.88	0.15	0.32	0.48	376.29	61.86
AD11	Pt	1	-12.23	-2.32	11.97	0.85	0.07	11.31	192.83	8.44
AD12	Pt	1	-9.85	0.06	1.19	0.23	0.32	0.73	403.70	5.74
AD13	Pt	1	-8.68	1.23	0.44	0.05	0.26	0.19	397.25	3.93
AD23	Pt	3	-5.15	4.76	9.9E-03	3.2E-05	9.8E-03	3.3E-03	89.85	10.62
AD25	Pt	3	-9.65	0.26	1.01	0.18	0.32	0.58	424.85	5.11
AD26	Pt	3	-11.92	-2.01	8.56	0.79	0.10	7.91	228.54	2.35
LG1	Re		-11.12	-1.20	3.73	0.60	0.19	3.12	269.35	7.38
LG2	Re		-10.50	-0.58	2.08	0.41	0.27	1.53	337.43	8.76
LG3	Re		-8.41	1.50	0.34	0.03	0.22	0.14	313.64	12.95
LG4	Re		-8.83	1.08	0.50	0.06	0.27	0.22	370.45	11.77
LG5	Re		-6.94	2.97	0.07	1.7E-03	0.07	0.03	184.04	52.79
LG6	Mo		-12.16	-2.25	11.03	0.84	0.08	10.38	185.89	4.90
LG7	Mo		-12.88	-2.97	24.46	0.92	0.04	23.79	142.73	3.47
LG35	Pt		-5.15	4.76	9.9E-03	3.2E-05	9.8E-03	3.3E-03	68.87	3.12
LG38	Re		-10.99	-1.08	3.31	0.56	0.21	2.71	322.75	8.29
LG39	Re		-9.65	0.26	1.01	0.18	0.32	0.58	414.01	11.69
LG40	Re		-11.92	-2.01	8.56	0.79	0.10	7.91	225.28	5.70

Table 1. Run conditions and results. All experiments were conducted at 1350 °C and 1 atm. ΔIW is the difference between the oxygen fugacity of the experiment and the oxygen fugacity of the iron-wüstite buffer (calculated in log units). *R* is the ratio of mole fractions of H_2 and CO_2 in the introduced gas mixture (see Figure 2). pH_2 and pH_2O are the partial pressures of hydrogen and water respectively, as calculated from the measured fO_2 of the gas mixture (Deines et al. 1974). Water concentrations were measured by FTIR, and 1σ errors of these measurements were estimated using a Monte Carlo approach, accounting for measurement errors in sample thickness, glass density, and peak height of the 3550 cm^{-1} peak on the FTIR spectra.

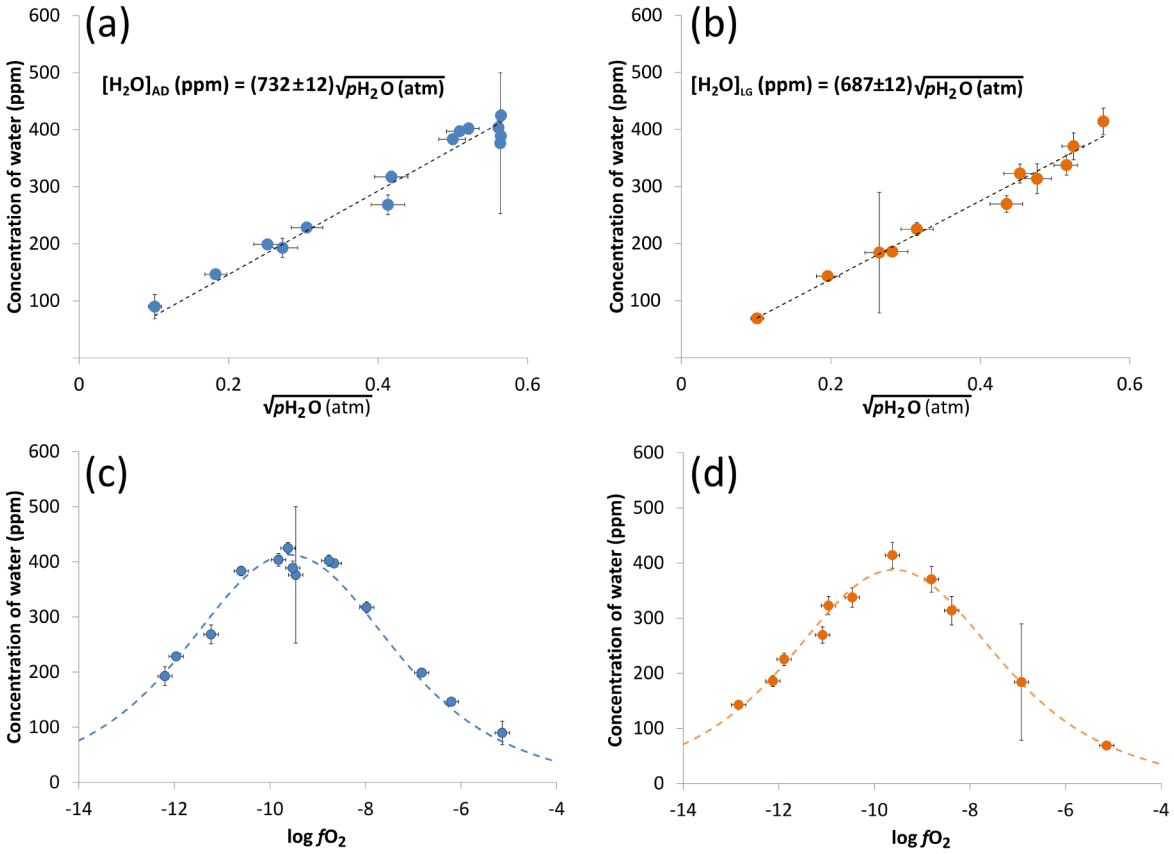

Figure 5 (a) Demonstration of linear relationship between concentration of water in AD experimental glasses (measured by FTIR) and the square root of the partial pressure of water in the furnace atmosphere (calculated from the known H_2/CO_2 ratio flowing through the furnace; Deines et al. (1974)). Dashed line is a least-squares linear regression forced through the origin; the equation of this line is given. Vertical error bars are 2σ and take into account measurement errors in peak height, density, and glass thickness. Horizontal error bars assume fO_2 measurement precision of 0.15 log units. **(b)** Demonstration of linear relationship between concentration of water in LG experimental glasses and square root of the partial pressure of water in the furnace atmosphere. Symbols and error bars as in (a). **(c)** Concentration of water in AD experimental glasses (measured by FTIR) vs. $\log(fO_2)$ (measured with an oxygen sensor). Concentration data define a symmetric bell-shaped curve suggesting that the solubility of water in AD melts is independent of pH_2/pH_2O, which decreases monotonically from low to high $\log(fO_2)$. Dashed curve is a translation of the best-fit line from (a) into $\log(fO_2)$ space, using the relationships of Deines et al. (1974). Symbols and error bars as in (a). **(d)** Same as (c) for LG composition.

SIMS was used to measure counts of $^{16}OH/^{18}O$ in experiments run under high and low pH_2/pH_2O conditions. Unlike FTIR, SIMS is thought to be insensitive to hydrogen speciation (Hirschmann et al. 2012), so SIMS measurements likely reflect the total concentration of H-bearing species in the experimental glasses. The expectation based on theory developed in sections 2.1 and 2.2 is that, if H_2 dissolution in the melts is significant under high pH_2/pH_2O conditions, then SIMS measurements may show elevated counts of $^{16}OH/^{18}O$ in reduced experiments as compared to oxidized experiments with similar pH_2O but lower pH_2/pH_2O.

Results from the AD experiments (Figure 6a) demonstrate that counts of $^{16}OH/^{18}O$ measured by SIMS are directly proportional to the concentration of water measured by FTIR and there is no apparent difference between the oxidized and reduced experiments. For the AD composition, we estimate that H_2 dissolution would be visibly apparent in our SIMS data if H_2 accounted for 10% or more of the total dissolved H in the most reduced experiments. This corresponds to a detection limit for H_2 of ~3 ppm and therefore suggests that the highest concentration of H_2 in our AD experiments is <3 ppm.

SIMS measurements of our LG experiments reveal a more complex relationship between counts of $^{16}OH/^{18}O$ measured by SIMS and measurements of water concentration by FTIR: Experiments conducted on the reducing side of the pH_2O bell-shaped curve have lower counts of $^{16}OH/^{18}O$ at a given FTIR-measured water concentration than those conducted on the oxidizing side of the pH_2O bell curve (Figure 6b). This is the opposite of what we might expect if the difference between the oxidized and reduced experiments was due to H_2 dissolution, and instead it likely indicates that counts of $^{16}OH/^{18}O$ are being influenced by changes in the matrix composition. The LG composition contains ~22 wt% FeO (Table 1). Over the large fO_2 range of our experiments, the iron in the LG composition changes from being dominantly metallic iron in coexisting metallic blebs in the most reducing experiments (such that the total amount of FeO dissolved in the melt in these experiments is ~5 times lower than in the experiments at ~IW), to dominantly ferrous iron dissolved in the melt at ~IW, to dominantly ferric iron dissolved in the melt in the most oxidizing experiments (Figure 3). Changes in the oxidation state of iron are known to affect the physical properties of silicate melts (e.g., Lange and Carmichael 1990; Mysen and Richet 2005), so it is perhaps unsurprising that such a dramatic change in a major component of the LG composition could produce a matrix effect in the SIMS analyses. Our SIMS analyses of the LG composition suggest that, contrary to the findings of Hauri et al. (2002) for terrestrial volcanic glasses, matrix effects could influence SIMS analyses of water in Fe-rich glass compositions, even at very low water concentrations.

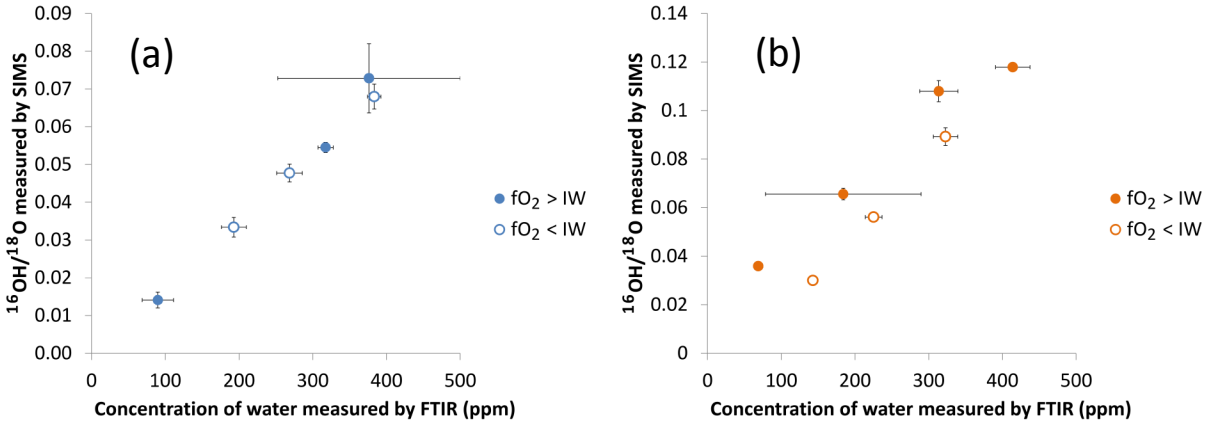

Figure 6 (a) Counts of $^{16}OH/^{18}O$ measured by SIMS vs. concentration of water measured by FTIR in AD experimental glasses. Filled symbols are experiments run under oxidizing conditions (fO_2 above the IW buffer) and open symbols are experiments run under reducing conditions (fO_2 below IW). For AD glasses, SIMS and FTIR data vary linearly, even for the most reducing experiments, suggesting that all of the hydrogen in the melt is dissolved as hydroxyl and the dissolution of H_2 cannot be detected. Vertical and horizontal error bars represent 2σ of replicate measurements. **(b)** Same as (a) for LG composition. For this composition, the oxidizing and reducing experiments are each roughly linear but define different lines, neither of which passes through the origin. Instead, the oxidized experiments produce higher counts of $^{16}OH/^{18}O$ at a given FTIR-measured water concentration. This is the opposite of what would be expected if H_2 dissolution were contributing to the counts of $^{16}OH/^{18}O$, so instead this likely indicates the influence of melt structure and composition on the production and transport of secondary ions in the SIMS (i.e., the difference between the reduced and oxidized experiments may be a matrix effect related to the differences in iron oxidation state and iron concentration in the melt in response to several orders of magnitude variability in fO_2). Symbols and error bars as in (a)

6. Discussion

6.1. Comparison to previous work on the solubility of water in basaltic melts

Due to the strong influence of dissolved water in silicate melts on the physical properties of magma (e.g., density, viscosity, diffusivities of other components) and on volcanic eruptive style, there is a large body of existing work dedicated to understanding the dissolution of water in natural silicate melt compositions (see reviews by McMillan (1994) and Moore (2008)). In this section, we compare our water solubility data to the small subset of existing experimental data that considers the solubility of water in natural, basic silicate melts at relatively low total pressures and/or low partial pressures of water (Baker and Grove 1985; Dixon et al. 1995). We also compare our data to extrapolations to low pressures of water solubility models by Newman and Lowenstern (2002), Moore et al. (1998), and Papale et al. (2006).

Figure 7a shows a comparison between our data and the experimental data of Baker and Grove (1985) and Dixon et al. (1995). Baker and Grove (1985) measured the solubility of water in basaltic andesite at 1200 °C and a total pressure of 1 atm. They equilibrated their experimental charges with mixtures of H_2/CO_2 and H_2/H_2O gases. The excellent agreement between our LG and AD solubility experiments (which were conducted at 1350 °C and 1 atm total pressure) and the experiments of Baker and Grove (1985) are consistent with water solubility in silicate melts being strongly dependent on pressure but only weakly dependent on temperature and melt composition.

Our data is also in good agreement with the water solubility data of Dixon et al. (1995), which was measured on a mid-ocean ridge basalt (MORB) composition at a temperatures of ~1200 °C and pressures of 176 – 980 bar. Extrapolations of our results to the conditions of the Dixon et al, experiments using equations (12) and (13) provide good matches to the concentrations of hydroxyl measured by Dixon et al. (1995) but project to lower concentrations than the total water content of these experiments (i.e., the sum of dissolved molecular water and hydroxyl). This is as expected: based on equation (3), a quadratic relationship is expected between the amount of water dissolved as hydroxyl and pH_2O, whereas based on equation (1), a linear (and proportional) relationship is expected between the amount of water dissolved as molecules of water and pH_2O. At low total water contents such those in our vapor-saturated melts, essentially all the dissolved water is present as hydroxyl groups, so the total water content has a quadratic relationship with pH_2O. In the experiments of Dixon et al. (1995), however, pH_2O is high enough that molecular water dissolution is significant, and the proportionality between total water concentration and the square root of pH_2O no longer holds. However, even under these conditions, equation (3) still describes the relationship between the amount of water dissolved as hydroxyl groups and pH_2O, so provided that the solubility of water as hydroxyl groups is not strongly dependent on melt composition, this is consistent with the observation in Figure 7a that the hydroxyl concentrations of the Dixon et al. experiments plot on the extension of the line defined by the results of our experiments which only contain hydroxyls.

Panels b, c, and d of Figure 7 show comparisons between our experimental data and extrapolations to low pressures of three different water solubility models. The first model considered, in Figure 7b, is the VolatileCalc model of Newman and Lowenstern (2002). The solid and dashed curves in Figure 7b are concentrations of total water, hydroxyl, and molecular water predicted by VolatileCalc for a basaltic melt composition with 43 wt% SiO_2 (chosen to match the LG composition) at 1350 °C in equilibrium with water vapor. The agreement between this model

and our data is excellent, both in terms of the absolute concentrations of hydrous species predicted and also in terms of the linear relationship predicted between water concentration and the square root of pH_2O under these low pressure conditions.

In Figure 7c, we compare our data to the model of Moore et al. (1998). This empirical model incorporates a parameterization of the dependence of water solubility on the mole fractions of Al_2O_3, FeO^T, and Na_2O in the silicate melt solvent, and therefore predicts slightly different water solubilities for the AD and LG compositions considered in this study. However, the Moore et al. model curves are lower than our data at a given pH_2O by ~40%. This could be explained by ε_{3550} values of 40 l/mol·cm rather than the 63 l/mol·cm we used; however, if the extinction coefficients were this low, our data would be far off the model results of Newman and Lowenstern (2002) shown in Figure 7b. Additionally, the Moore et al. model predicts a slight upward curvature of the solubility vs. the square root of pH_2O over the pH_2O range we investigated, which is inconsistent with our results.

In Figure 7d, our data are compared to the model of Papale et al. (2006). This model aims to capture the effects of melt composition on the shape and position of the volatile saturation surface via a fully non-ideal, multicomponent, thermodynamic treatment of H_2O-CO_2 solubility in silicate melts. This model fails to capture the linear relationship between water concentration and the square root of pH_2O at the low pressures that is a robust feature of our results, of the results of Dixon et al. (1995), and of considerable data from the glass literature (McMillan 1994). This likely reflects at least in part the fact that the Papale et al. model does not incorporate any information about the speciation of volatiles in the melt. However, the Papale et al. model predicts water concentrations in LG that are a factor of ~4 lower than measured values, and concentrations in AD that are a factor of ~20 lower than measured values, which would not be consistent with any reasonable extinction coefficients for the compositions we have studied.

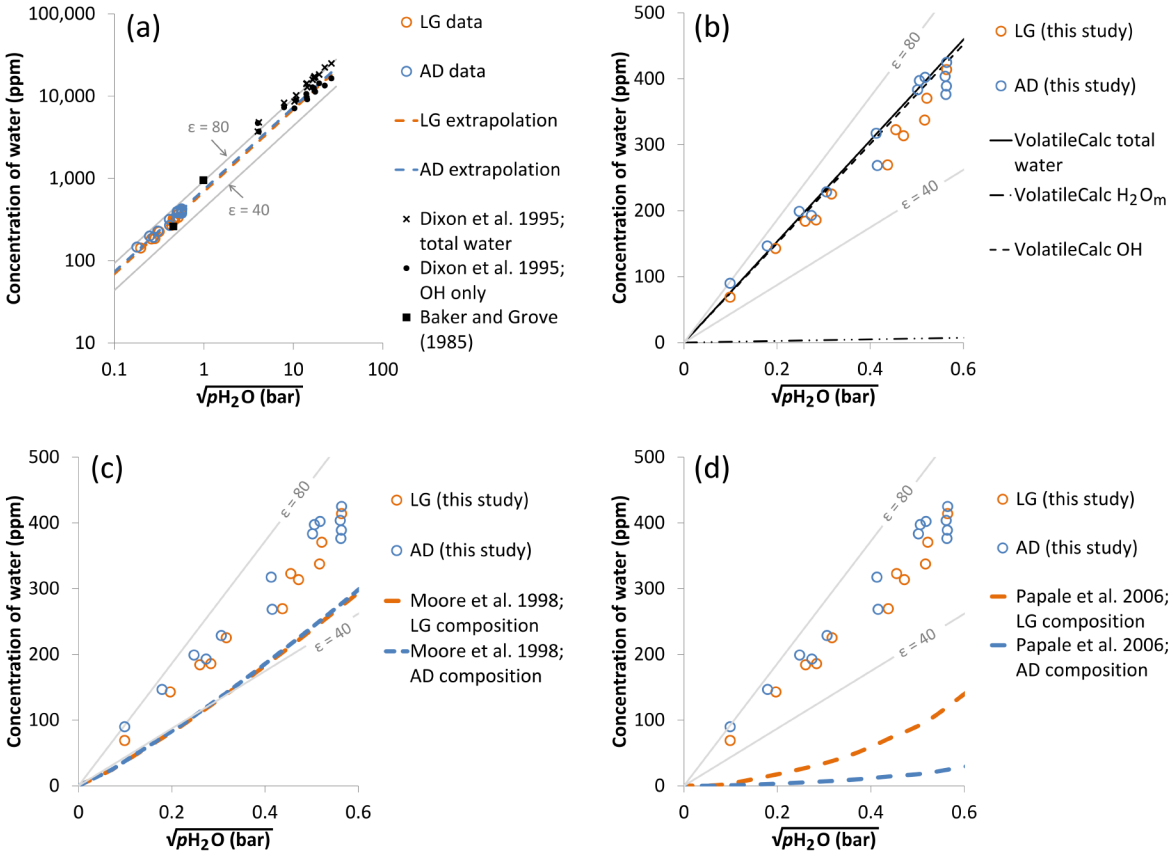

Figure 7 (a) Comparison between data collected during this study (open blue and orange circles) and data from previous studies of water solubility in basic silicate melts at relatively low pressures (black symbols). Data are plotted on a log-log scale to ease comparison of datasets that span several orders of magnitude in concentration. Dashed lines are extrapolations of least-squares linear regressions of our data to higher pressures. Gray lines labeled "ε = 40" and "ε = 80" show the projected positions of linear regressions of our data, assuming values of ε_{3550} between 40 and 80 l/mol·cm (see discussion in section 3.3). Baker and Grove (1985) data are measurements of the solubility of water in basaltic andesite melt equilibrated with H_2-H_2O and H_2/CO_2 gas mixtures at 1 atm and ~1200 °C. Data from Dixon et al. (1995) are for a MORB melt composition equilibrated at pressures of 180 – 720 bar and ~1200 °C. See main text for discussion. **(b)** Comparison between data collected during this study (open blue and orange circles) and the VolatileCalc model of Newman and Lowenstern (2002) for a basaltic melt at 1350 °C containing 43 wt% SiO_2 (black solid and dashed lines). Gray lines are as in (a). **(c)** Comparison between data collected during this study (blue and orange circles) and the composition-dependent water solubility model of Moore et al. (1998) (dashed colored curves). Gray lines as in (a) **(d)** Comparison between data collected during this study (blue and orange circles) and the composition-dependent mixed-volatile solubility model of Papale et al. (2006) (dashed colored curves). Model curves generated using the online calculator at http://ctserver.ofm-research.org/Papale/Papale.php. Gray lines as in (a).

6.2. Calculation of pH_2O in equilibrium with lunar glasses and melt inclusions

The water solubility relationship for lunar basalt, equation (13), can be used to determine the pH_2O of vapor in equilibrium with lunar glasses and melt inclusions (Saal et al. 2008; Hauri et

al. 2011; Saal et al. 2013; Wetzel et al. 2015) at 1350 °C. For example, a lunar basaltic melt containing ~1200 ppm water (as observed in melt inclusions by Hauri et al. (2011), after correction for post-entrapment crystallization) would be in equilibrium with vapor having pH_2O ~3 bar. Assuming an oxygen fugacity of IW-1 for lunar magmas (Sato 1976; Wadhwa 2008), we can use the gas phase reaction $H_2 + 0.5O_2 \leftrightarrow H_2O$ and data of Deines et al. (1974) to estimate pH_2~8 bar for this vapor. We can thus place a lower limit of ~11 bar on the entrapment pressure of lunar melt inclusions, which corresponds to a minimum depth of ~270 m below the lunar surface. A melt containing ~15 ppm CO_2 (e.g., Wetzel et al. (2015)) in addition to ~1200 ppm H_2O would imply pCO_2~30 atm and pCO~228 bar (using the solubility data of Dixon et al. (1995), the gas phase reaction $CO + 0.5O_2 \leftrightarrow CO_2$ and the equilibrium constant for this reaction given by Deines et al. (1974)), resulting in a total pressure of ~268 bar, corresponding to a depth in the lunar crust of ~6.6 km). The entrapment pressure would be higher still if the entrapped melt was not vapor-saturated, or if other gaseous species (e.g., S-bearing species) had significant partial pressures.

Wetzel et al. (2015) obtain similar results using a different approach to calculating the entrapment pressure of lunar melt inclusions: They use the carbon solubility model of Wetzel et al. (2013) and the water solubility determined by Newcombe et al. (2012) (i.e., an earlier version of equation (13); the addition of more experiments since the publication of Newcombe et al. (2012) has changed the proportionality constant in equation (13) by <1%) to modify the terrestrial MORB C-O-H solubility model of Dixon and Stolper (1995). Using this approach, and their measured concentrations of H_2O and CO_2 in the lunar glasses and melt inclusions, they determine final melt-gas equilibration pressures for their lunar olivine-hosted melt inclusions of up to 16.5 MPa (163 atm; corresponding to depths within the lunar crust of up to 4 km). When a correction is made for partitioning of C and H_2O into vapor bubbles in the melt inclusions, the corrected melt compositions record vapor saturation pressures of up to 276 MPa (2724 atm), which roughly correspond to depths of 61 km (i.e., below the base of the lunar crust at ~35 km; Wieczorek et al. (2013)).

6.3. Implications for the role of H_2 in lunar magmas

As described in section 2.2, Zhang (2011) used thermodynamic arguments and measurements of H_2 solubility in silica glass to make the tentative prediction that $[H_2]/[H_2O]$ (where square brackets indicate molar concentration) could be as high as ~1 in silicate melts under highly reducing conditions (IW-2). This would imply that there could be ~10 – 20 ppm by

weight H_2 dissolved in our most reducing experiments (e.g., AD11, AD26, LG6, LG7 and LG40, which contain ~100 – 200 ppm H_2O and were equilibrated at fO_2 < IW-2). However, extrapolation to 1 atm of the H_2 solubility experiments of Hirschmann et al. (2012) suggest that only ~0.4 ppm by weight H_2 would be soluble in LG and AD melts in equilibrium with 1 bar of pure H_2.

Note that the lack of an infrared detection of H_2 in the quenched glasses from our experiments cannot help to resolve the difference between predictions based on the Zhang (2011) and Hirschmann et al. (2012) results. This is because the results of Hirschmann et al. (2012) suggest that the detection limit for measurements of dissolved H_2 in silicate glasses (via measurement of the height of the peak at ~4130 cm^{-1}) is ~900 ppm, much higher concentrations of H_2 than we expect to find in our 1-atm experiments based on available data and models. However, our SIMS data for the AD composition places a stronger constraint on the concentration of H_2 dissolved in our most reducing experiments. As shown in Figure 6a, the total concentration of all H-bearing species in our AD experiments is proportional to the concentration of water measured by FTIR and we do not observe elevated counts of $^{16}OH/^{18}O$ in our most reducing experiments, as might be expected if a significant proportion of H was dissolved as molecular hydrogen. We estimate that this places an upper bound of ~3 ppm for the concentration of H_2 dissolved in our most reducing AD experiments. This upper bound is consistent with the results of Hirschmann et al. (2012) and is ~1 order of magnitude lower than predicted by the calculations of Zhang (2011). Nevertheless, even at this level our results still leave room for H_2 dissolution and transport to play a role in the degassing of lunar volcanic melts.

7. Conclusions

The solubility of water in lunar basaltic melt in equilibrium with a C-O-H vapor at 1350 °C and 1 atm is proportional to the square root of pH_2O in the vapor phase, and is independent of fO_2 and pH_2/pH_2O. Hydroxyl is the only H-bearing species detected in our experiments by FTIR and SIMS. SIMS measurements of our iron-free experimental glasses constrain the molar ratio of dissolved H_2/OH to be <0.1, in agreement with extrapolation to 1 atm of measurements of H_2 solubility in basalt by Hirschmann et al. (2012). We find evidence for matrix effects in SIMS measurements of water in iron-rich glasses equilibrated over a range of fO_2 conditions.

Our results constrain the pH_2O of vapor in equilibrium with lunar glasses and melt inclusions. We find that the most water-rich melt inclusion of Hauri et al. (2011) would be in

equilibrium with a vapor with pH_2O ~3 atm and pH_2~8 atm. Consideration of the dissolved concentration of carbon in lunar melt inclusions characterized by Wetzel et al. (2015) allows us to estimate a lower bound for entrapment pressure of these melt inclusions of ~268 atm, which corresponds to a depth within the lunar crust of ~6.5 km.

8. Acknowledgements

Newcombe gratefully acknowledges financial support from a NASA Earth and Space Sciences Fellowship (PLANET14R-0040).

9. References

Albarède F, Albalat E, Lee C-TA (2015) An intrinsic volatility scale relevant to the Earth and Moon and the status of water in the Moon. Meteoritics & Planetary Science 50 (4):568-577. doi:10.1111/maps.12331

Baker MB, Grove TL (1985) Kinetic controls on pyroxene nucleation and metastable liquid lines of descent in a basaltic andesite. American Mineralogist 70 (3-4):279-287

Barnes JJ, Tartèse R, Anand M, McCubbin FM, Franchi IA, Starkey NA, Russell SS (2014) The origin of water in the primitive Moon as revealed by the lunar highlands samples. Earth and Planetary Science Letters 390:244-252. doi:http://dx.doi.org/10.1016/j.epsl.2014.01.015

Beckett JR, Mendybaev RA (1997) The measurement of oxygen fugacities in flowing gas mixtures at temperatures below 1200°C. Geochimica et Cosmochimica Acta 61 (20):4331-4336. doi:http://dx.doi.org/10.1016/S0016-7037(97)00186-5

Behrens H, Nowak M (1997) The mechanisms of water diffusion in polymerized silicate melts. Contributions to Mineralogy and Petrology 126 (4):377-385. doi:10.1007/s004100050257

Borisov A, Jones JH (1999) An evaluation of Re, as an alternative to Pt, for the 1 bar loop technique: An experimental study at 140O C. American Mineralogist 84:1528-1534

Boyce JW, Liu Y, Rossman GR, Guan Y, Eiler JM, Stolper EM, Taylor LA (2010) Lunar apatite with terrestrial volatile abundances. Nature 466 (7305):466-469

Canup RM, Asphaug E (2001) Origin of the Moon in a giant impact near the end of the Earth's formation. Nature 412 (6848):708-712

Canup RM, Visscher C, Salmon J, Fegley Jr B (2015) Lunar volatile depletion due to incomplete accretion within an impact-generated disk. Nature Geosci advance online publication. doi:10.1038/ngeo2574

http://www.nature.com/ngeo/journal/vaop/ncurrent/abs/ngeo2574.html#supplementary-information

Chen Y, Zhang Y, Liu Y, Guan Y, Eiler J, Stolper EM (2015) Water, fluorine, and sulfur concentrations in the lunar mantle. Earth and Planetary Science Letters 427:37-46. doi:http://dx.doi.org/10.1016/j.epsl.2015.06.046

Deines P, Nafziger RH, Ulmer GC, Woermann E (1974) Temperature - Oxygen Fugacity Tables for Selected Gas Mixtures in the System C-H-O at One Atmosphere Total Pressure. Bulletin of the Earth and Mineral Sciences Experiment Station (88)

Delano JW (1986) Pristine Lunar Glasses: Criteria, Data, and Implications. J Geophys Res 91 (B4):D201-D213. doi:10.1029/JB091iB04p0D201

Dixon JE, Stolper EM (1995) An Experimental Study of Water and Carbon Dioxide Solubilities in Mid-Ocean Ridge Basaltic Liquids. Part II: Applications to Degassing. Journal of Petrology 36 (6):1633-1646

Dixon JE, Stolper EM, Holloway JR (1995) An Experimental Study of Water and Carbon Dioxide Solubilities in Mid-Ocean Ridge Basaltic Liquids. Part I: Calibration and Solubility Models. Journal of Petrology 36 (6):1607-1631

Greenwood JP, Itoh S, Sakamoto N, Warren P, Taylor L, Yurimoto H (2011) Hydrogen isotope ratios in lunar rocks indicate delivery of cometary water to the Moon. Nature Geoscience 4 (2):79-82

Hauri E, Wang J, Dixon JE, King PL, Mandeville C, Newman S (2002) SIMS analysis of volatiles in silicate glasses: 1. Calibration, matrix effects and comparisons with FTIR. Chemical Geology 183 (1–4):99-114. doi:http://dx.doi.org/10.1016/S0009-2541(01)00375-8

Hauri EH, Weinreich T, Saal AE, Rutherford MC, Van Orman JA (2011) High Pre-Eruptive Water Contents Preserved in Lunar Melt Inclusions. Science 333 (6039):213-215. doi:10.1126/science.1204626

Hess P, Rutherford M, Guillemette R, Ryerson F, Tuchfeld H Residual products of fractional crystallization of lunar magmas-an experimental study. In: Lunar and Planetary Science Conference Proceedings, 1975. pp 895-909

Hirschmann MM, Withers AC, Ardia P, Foley NT (2012) Solubility of molecular hydrogen in silicate melts and consequences for volatile evolution of terrestrial planets. Earth and Planetary Science Letters 345–348:38-48. doi:http://dx.doi.org/10.1016/j.epsl.2012.06.031

Huebner JS (1971) Buffering Techniques for Hydrostatic Systems at Elevated Pressures. In: Ulmer G (ed) Research Techniques for High Pressure and High Temperature. Springer Berlin Heidelberg, pp 123-177. doi:10.1007/978-3-642-88097-1_5

Hui H, Peslier AH, Zhang Y, Neal CR (2013) Water in lunar anorthosites and evidence for a wet early Moon. Nature Geosci 6 (3):177-180. doi:http://www.nature.com/ngeo/journal/v6/n3/abs/ngeo1735.html#supplementary-information

Kohn SC (2000) The dissolution mechanisms of water in silicate melts; a synthesis of recent data. Mineralogical Magazine 64 (3):389-408

Kress V, Carmichael IE (1991) The compressibility of silicate liquids containing Fe2O3 and the effect of composition, temperature, oxygen fugacity and pressure on their redox states. Contributions to Mineralogy and Petrology 108 (1-2):82-92. doi:10.1007/bf00307328

Lange RL, Carmichael ISE (1990) Thermodynamic properties of silicate liquids with emphasis on density, thermal expansion and compressibility. Reviews in Mineralogy and Geochemistry 24 (1):25-64

Mandeville CW, Webster JD, Rutherford MJ, Taylor BE, Timbal A, Faure K (2002) Determination of molar absorptivities for infrared absorption bands of H2O in andesitic glasses. American Mineralogist, vol 87. doi:10.2138/am-2002-0702

McCubbin FM, Steele A, Hauri EH, Nekvasil H, Yamashita S, Hemley RJ (2010) Nominally hydrous magmatism on the Moon. Proceedings of the National Academy of Sciences 107 (25):11223-11228

McMillan PF (1994) Water solubility and speciation models. Reviews in Mineralogy and Geochemistry 30 (1):132-156

Mercier M, Muro AD, Métrich N, Giordano D, Belhadj O, Mandeville CW (2010) Spectroscopic analysis (FTIR, Raman) of water in mafic and intermediate glasses and glass inclusions. Geochimica et Cosmochimica Acta 74 (19):5641-5656. doi:http://dx.doi.org/10.1016/j.gca.2010.06.020

Moore G (2008) Interpreting H2O and CO2 contents in melt inclusions: constraints from solubility experiments and modeling. Reviews in Mineralogy and Geochemistry 69 (1):333-362

Moore G, Vennemann T, Carmichael I (1998) An empirical model for the solubility of H2O in magmas to 3 kilobars. American Mineralogist 83 (1):36-42

Mysen B, Richet P (2005) Silicate glasses and melts: properties and structure, vol 10. Elsevier,

Nakajima M, Stevenson D Hydrodynamic Escape does not Prevent the``Wet"Moon Formation. In: Lunar and Planetary Science Conference, 2014. p 2770

Newcombe M, Brett A, Beckett J, Baker M, Newman S, Stolper E Solubility and Diffusivity of H-Bearing Species in Lunar Basaltic Melts. In: Lunar and Planetary Institute Science Conference Abstracts, 2012. p 2777

Newman S, Lowenstern JB (2002) VolatileCalc: a silicate melt–H2O–CO2 solution model written in Visual Basic for excel. Computers & Geosciences 28 (5):597-604. doi:http://dx.doi.org/10.1016/S0098-3004(01)00081-4

Newman S, Stolper EM, Epstein S (1986) Measurement of water in rhyolitic glasses--calibration of an infrared spectroscopic technique. American Mineralogist 71 (11):1527-1541

Newsom HE, Taylor SR (1989) Geochemical implications of the formation of the Moon by a single giant impact. Nature 338 (6210):29-34

O'Neill HC, Pownceby M (1993) Thermodynamic data from redox reactions at high temperatures. I. An experimental and theoretical assessment of the electrochemical method using stabilized zirconia electrolytes, with revised values for the Fe-"FeO", Co-CoO, Ni-NiO and Cu-Cu2O oxygen buffers, and new data for the W-WO2 buffer. Contributions to Mineralogy and Petrology 114 (3):296-314. doi:10.1007/bf01046533

Pahlevan K, Stevenson DJ (2007) Equilibration in the aftermath of the lunar-forming giant impact. Earth and Planetary Science Letters 262 (3):438-449

Pandya N, Muenow DW, Sharma SK (1992) The effect of bulk composition on the speciation of water in submarine volcanic glasses. Geochimica et Cosmochimica Acta 56 (5):1875-1883. doi:http://dx.doi.org/10.1016/0016-7037(92)90317-C

Papale P, Moretti R, Barbato D (2006) The compositional dependence of the saturation surface of H2O + CO2 fluids in silicate melts. Chemical Geology 229 (1–3):78-95. doi:http://dx.doi.org/10.1016/j.chemgeo.2006.01.013

Persikov ES, Newman S, Bukhtiyarov PG, Nekrasov AN, Stolper EM (2010) Experimental study of water diffusion in haplobasaltic and haploandesitic melts. Chemical Geology 276 (3–4):241-256. doi:10.1016/j.chemgeo.2010.06.010

Saal AE, Hauri EH, Cascio ML, Van Orman JA, Rutherford MC, Cooper RF (2008) Volatile content of lunar volcanic glasses and the presence of water in the Moon's interior. Nature 454 (7201):192-195. doi:http://www.nature.com/nature/journal/v454/n7201/suppinfo/nature07047_S1.html

Saal AE, Hauri EH, Van Orman JA, Rutherford MJ (2013) Hydrogen Isotopes in Lunar Volcanic Glasses and Melt Inclusions Reveal a Carbonaceous Chondrite Heritage. Science 340 (6138):1317-1320. doi:10.1126/science.1235142

Sato M Oxygen fugacity and other thermochemical parameters of Apollo 17 high-Ti basalts and their implications on the reduction mechanism. In: Lunar and Planetary Science Conference Proceedings, 1976. pp 1323-1344

Sharp ZD, Shearer CK, McKeegan KD, Barnes JD, Wang YQ (2010) The Chlorine Isotope Composition of the Moon and Implications for an Anhydrous Mantle. Science 329 (5995):1050-1053. doi:10.1126/science.1192606

Sieverts A (1929) Absorption of gases by metals. Z Metallkund 21:37

Silver L, Ihinger P, Stolper E (1990) The influence of bulk composition on the speciation of water in silicate glasses. Contributions to Mineralogy and Petrology 104 (2):142-162. doi:10.1007/bf00306439

Silver L, Stolper E (1989) Water in albitic glasses. Journal of Petrology 30 (3):667-709
Stolper E (1982a) The speciation of water in silicate melts. Geochimica et Cosmochimica Acta 46 (12):2609-2620
Stolper E (1982b) Water in silicate glasses: An infrared spectroscopic study. Contributions to Mineralogy and Petrology 81 (1):1-17. doi:10.1007/bf00371154
Tartèse R, Anand M, McCubbin FM, Elardo SM, Shearer CK, Franchi IA (2014) Apatites in lunar KREEP basalts: The missing link to understanding the H isotope systematics of the Moon. Geology 42 (4):363-366
Wadhwa M (2008) Redox Conditions on Small Bodies, the Moon and Mars. Reviews in Mineralogy and Geochemistry 68 (1):493-510. doi:10.2138/rmg.2008.68.17
Wetzel DT, Hauri EH, Saal AE, Rutherford MJ (2015) Carbon content and degassing history of the lunar volcanic glasses. Nature Geosci advance online publication. doi:10.1038/ngeo2511
http://www.nature.com/ngeo/journal/vaop/ncurrent/abs/ngeo2511.html#supplementary-information
Wetzel DT, Rutherford MJ, Jacobsen SD, Hauri EH, Saal AE (2013) Degassing of reduced carbon from planetary basalts. Proceedings of the National Academy of Sciences 110 (20):8010-8013
Wieczorek MA, Neumann GA, Nimmo F, Kiefer WS, Taylor GJ, Melosh HJ, Phillips RJ, Solomon SC, Andrews-Hanna JC, Asmar SW, Konopliv AS, Lemoine FG, Smith DE, Watkins MM, Williams JG, Zuber MT (2013) The Crust of the Moon as Seen by GRAIL. Science 339 (6120):671-675. doi:10.1126/science.1231530
Yamashita S, Kitamura T, Kusakabe M (1997) Infrared spectroscopy of hydrous glasses of arc magma compositions. GEOCHEMICAL JOURNAL-JAPAN- 31:169-174
Zhang C, Duan Z (2009) A model for C–O–H fluid in the Earth's mantle. Geochimica et Cosmochimica Acta 73 (7):2089-2102. doi:http://dx.doi.org/10.1016/j.gca.2009.01.021
Zhang Y Water" in Lunar Basalts: The Role of Molecular Hydrogen (H2), Especially in the Diffusion of the H Component. In: 42nd Lunar and Planetary Science Conference, held March 7--11, 2011 at The Woodlands, Texas. LPI Contribution, 2011. vol 1608.
Zhang Y, Ni H (2010) Diffusion of H, C, and O Components in Silicate Melts. Reviews in Mineralogy and Geochemistry 72 (1):171-225. doi:10.2138/rmg.2010.72.5
Zhang Y, Stolper EM (1991) Water diffusion in a basaltic melt. Nature 351 (6324):306-309

C h a p t e r 3

EFFECTS OF pH_2O, pH_2 AND fO_2 ON THE DIFFUSION OF H-BEARING SPECIES IN LUNAR BASALT AND AN IRON-FREE BASALTIC ANALOGUE AT 1 ATM

M.E. Newcombe, J.R. Beckett, M.B. Baker, S. Newman, Y. Guan, J.M. Eiler, and E.M. Stolper

Division of Geological and Planetary Sciences, California Institute of Technology, Pasadena, CA 91125, USA

1. Abstract

Water diffusion experiments in an iron-free basaltic analogue melt (AD) and in Apollo 15 "yellow glass" (LG) were conducted at 1 atm and 1350 °C over a range of fO_2 conditions from IW-2.2 to IW+6.7 and over a range of pH_2/pH_2O from (nominally) zero to ~10. The water concentrations measured in our quenched experimental glasses by SIMS and FTIR vary from a few ppm to ~430 ppm. Water concentration gradients in each of our AD and LG experiments are well described by models in which the diffusivity of water (D^*_{water}) is assumed to be constant. In AD melts containing ~20 – 420 ppm water, D^*_{water} is found to be independent of water concentration. The relationships between D^*_{water} and concentration for our AD and LG experiments are well described by a modified speciation model (Ni et al. 2012) in which both molecular water and hydroxyl are allowed to diffuse. The success of this modified speciation model for describing our results suggests that we have resolved the diffusivity of hydroxyl in basaltic melt for the first time. Best-fit values of D^*_{water} are found to be higher in LG melt than AD melt, which is suggestive of a positive correlation between D_{OH} and melt depolymerization (as hypothesized by Ni et al. (2012)).

Best-fit values of D^*_{water} for our LG experiments vary within a factor of ~2 over a range of pH_2/pH_2O from 0.007 to 9.7, a range of fO_2 from IW-2.2 to IW+4.9, and a water concentration range from ~80 ppm to ~280 ppm. The relative insensitivity of our best-fit values of D^*_{water} to variations in pH_2 suggests that H_2 diffusion was not significant during degassing of the lunar glasses of Saal et al. (2008). D^*_{water} during dehydration and hydration in H_2/CO_2 gas mixtures are approximately the same in both LG and AD melts, which supports an equilibrium boundary condition for these experiments. However, dehydration experiments into CO_2 and CO/CO_2 gas

mixtures leave some scope for the importance of kinetics during dehydration into H-free environments. The value of D^{*}_{water} chosen by Saal et al. (2008) for modeling the diffusive degassing of the lunar volcanic glasses is within a factor of three of our measured value in LG melt at 1350 °C.

2. Introduction

From the earliest Apollo missions until the last few years, the Moon was thought to be "bone dry" (e.g., Newsom and Taylor 1989). This widely held belief was based on measurements made in the 1970s of samples returned from the Moon by the Apollo and Luna missions. The apparent lack of water on the Moon became regarded as an inevitable consequence of the popular "giant impact" theory of lunar formation, which proposes that the Moon formed when a Mars-sized body collided with the early Earth (Hartmann and Davis 1975; Cameron and Ward 1976). However, the recent detection of up to ~70 ppm water in lunar glass spherules (Saal et al. 2008; Saal et al. 2013; Wetzel et al. 2015) thought to form during Hawaiian-style fire-fountain eruptions (Delano 1986) challenged this viewpoint. Moreover, a model of syneruptive diffusive volatile loss by Saal et al. (2008) (Figure 1) predicted that the lunar glass spherules had lost ~98% of their original water, suggesting that the source magma for the fire-fountain eruptions that produced the lunar volcanic glasses contained ~745 ppm water. This extraordinary claim was confirmed when ~1400 ppm water was measured in olivine-hosted melt inclusions associated with the lunar volcanic glasses (Hauri et al. 2011), leading to the realization that at least some regions of the Moon's interior that melted to produce the lunar volcanic glasses had water contents comparable to the major magma-forming regions in the Earth's upper mantle (Saal et al. 2002).

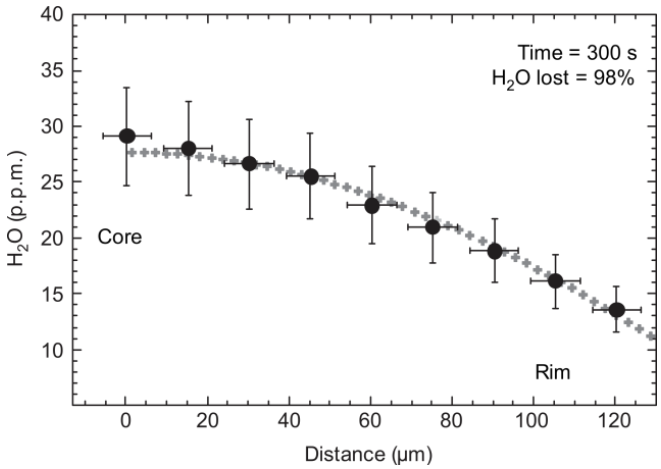

Figure 1 Concentration profile of H_2O measured from core to rim of a single bead of very low Ti green glass, taken directly from Saal et al. (2008). Circles are the original SIMS data with 2σ error bars; grey crosses track a model of water diffusion with concomitant loss due to surface evaporation. This model uses an expression for water diffusivity determined for a terrestrial basaltic melt with 0.2 wt% water (Zhang and Stolper 1991).

Although the lunar volcanic glasses and their associated olivine-hosted melt inclusions appear to give a self-consistent story, there is still much that we do not understand about the degassing history of the pyroclastic bead illustrated in Figure 1. For example, the model shown in Figure 1 uses a diffusivity for water that is temperature dependent, but not concentration dependent (Zhang and Stolper 1991). Although there were at the time of publication of Saal et al. (2008) no studies of water diffusion in natural silicate melts at the low water concentrations relevant to these lunar volcanic glasses, many studies of water diffusion at higher concentrations indicate that the diffusivity of water in silicate melts is highly concentration dependent at water contents > 0.1 wt% (Zhang and Stolper 1991; Zhang et al. 1991b; Persikov et al. 2010; Zhang and Ni 2010; Ni et al. 2012). If the observed (and well-defined) dependence of the diffusivity of water in silicate melts can be extrapolated to the low water concentrations relevant to lunar volcanic glass formation, it would suggest that the model of Saal et al. (2008) could have significantly overestimated the extent of water degassing from the lunar volcanic glasses. The role played by the lower oxygen fugacity on the Moon is also debated, with some authors arguing that H_2 (which occurs in high quantities in a low pressure vapor phase under reducing conditions—see Figure 2 of Chapter 2) may play a significant role in the transport of H-bearing species through the melt beads (Zhang 2011). In addition, the rate of evaporation of water at the surface of the bead in Figure 1 is a fit parameter in the model of Saal et al. (2008) and there are not yet any experiments or physical models that constrain the kinetics of evaporation of water at the melt-vapor interface.

The goal of this study is to address many of the issues described above by experimentally determining the diffusivity of water in lunar basalt and in an iron-free basaltic analogue at the low water concentrations and low values of oxygen fugacity (fO_2) thought to be relevant to the eruption of lunar basalts (Sato 1976; Wadhwa 2008). We have conducted water diffusion experiments at 1 atm and 1350 °C over a range of fO_2 conditions from IW-2.2 to IW+6.7 (where "IW" indicates the position of the iron-wüstite oxygen buffer) and over a range of pH_2/pH_2O from nominally zero to ~10. The water concentrations measured in our quenched experimental glasses vary from a few ppm to ~430 ppm, whereas existing experimental studies of water diffusion in basaltic melts extend from much higher water concentrations down to ~1000 ppm (Zhang and Stolper 1991; Persikov et al. 2010), and thus our experiments fill a significant gap in our knowledge of water diffusion in basic silicate melts at low water concentrations (Figure 2).

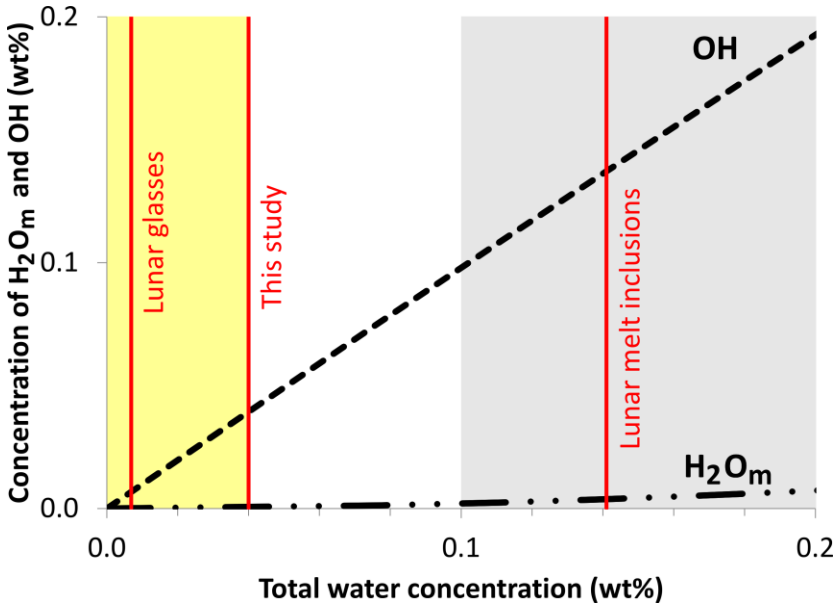

Figure 2 Water concentration range of the diffusion experiments conducted during this study (yellow shaded region) and the lowest water concentrations of previous experimental studies of water diffusion in basaltic melts (gray shaded region; Zhang and Stolper 1991; Persikov et al. 2012). The dominant dissolved species is hydroxyl under the conditions of our experiments. Hydroxyl (OH) and molecular water (H_2O_m) curves were generated using VolatileCalc (Newman and Lowenstern 2002) which adopts the regular solution model of Silver and Stolper (1989). Red vertical lines indicate the maximum total water concentrations measured in lunar olivine-hosted melt inclusions (Hauri et al. 2011) and lunar glasses (Saal et al. 2008; Saal et al. 2013), and the maximum total water concentration considered in this study.

3. Background

3.1. Diffusion of water in silicate melts

The diffusion of water in silicate melts and glasses has been widely studied due to its importance for driving volcanic eruptions (Zhang et al. 2007), controlling the rate of bubble growth and volatile degassing in magmas (Sparks 1978; Bottinga and Javoy 1990; Proussevitch et al. 1993; Blower et al. 2001), and due to its impact on the physical properties of commercially produced silicate glasses (e.g., Doremus 1973). Of the existing studies of water diffusion in silicate melts, most experiments have focused on rhyolitic compositions (Shaw 1974; Delaney and Karsten 1981; Karsten et al. 1982; Zhang et al. 1991b; Nowak and Behrens 1997; Zhang and Behrens 2000; Okumura and Nakashima 2004; Behrens et al. 2007; Ni and Zhang 2008; Behrens and Zhang 2009; Wang et al. 2009; Persikov et al. 2014), with relatively few studies of water diffusion in dacitic (Behrens et al. 2004; Liu et al. 2004; Okumura and Nakashima 2006; Ni et al. 2009a; Persikov et al. 2014), andesitic (Behrens et al. 2004; Okumura and Nakashima 2006; Ni et al. 2009b; Persikov et al. 2010; Ni et al. 2012), and basaltic compositions (Zhang and Stolper 1991; Okumura and Nakashima 2006; Persikov et al. 2010). Most of the experimental studies listed above characterized water concentration gradients in silicate glasses and melts, which they then used to determine the diffusivity of water from the following diffusion equation (Zhang et al. 1991b, a):

$$\frac{\partial[\text{water}]}{\partial t} = \frac{\partial}{\partial x}\left(D^{*}_{\text{water}} \frac{\partial[\text{water}]}{\partial x}\right) \quad (1)$$

In equation (1), [water] is the mole fraction of water in the melt, t is time, x is distance, and D^{*}_{water} is the diffusivity of water.

The majority of studies of water diffusion in natural silicate melts have found that the diffusivity of water (D^{*}_{water}) is dependent on water concentration. Much of the experimental data supports a proportional relationship between water diffusivity and water concentration (Behrens et al. 2004; Okumura and Nakashima 2004; Okumura and Nakashima 2006), while other experimental studies have found evidence for an exponential relationship between water diffusivity and water concentration (Delaney and Karsten 1981; Karsten et al. 1982; Persikov et al. 2010; Persikov et al. 2014). Other workers have argued for a proportional relationship between water diffusivity and water concentration at low water concentrations, and an exponential relationship at higher water concentrations (Nowak and Behrens 1997; Liu et al. 2004). Although

the proposed proportional and exponential models describe the experimental data measured at moderate water concentrations (i.e., ~1 – 3 wt% water) almost equally well (e.g., Persikov et al. 2010), these two models diverge considerably at very high and very low water concentrations: At very low water concentrations, the proportional model predicts that the diffusivity of water should tend towards zero, whereas the exponential model predicts that the diffusivity of water should tend towards a constant value. The water concentrations of the experiments conducted in this study extend down to a few tens of ppm water, so one of the major aims of this study is to distinguish between extrapolations to low water concentrations of the proportional and exponential models for the relationship between water diffusivity and water concentration.

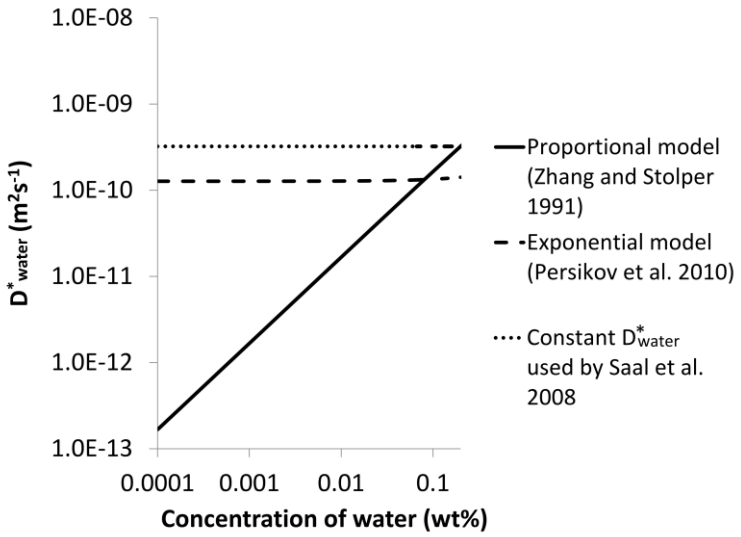

Figure 3 Extrapolations of existing models of the dependence of water diffusivity on water concentration diverge at the low water concentrations considered in this study. The proportional model (in which D^*_{water} is assumed to be proportional to water concentration) tends towards zero as the concentration of water tends towards zero, whereas the exponential model (in which D^*_{water} is assumed to be an exponential function of water concentration) tends towards a constant value as the concentration of water tends towards zero. The model of Saal et al. (2008) used a temperature-dependent but concentration-independent value of D^*_{water} based on the results of Zhang and Stolper (1991) measured at 0.2 wt% water. The proportional model and the constant D^*_{water} model on this figure were calculated at 1350 °C, whereas the exponential model of Persikov et al. (2010) is fit to experiments at 1300 °C.

The dependence of water diffusivity on water concentration can be rationalized in the context of the speciation model for the dissolution of water in silicate melts (Stolper 1982a; Stolper 1982b). As described in Chapter 2 of this thesis, the speciation model proposes that water

dissolves in silicate melts as both water molecules (H_2O_m) and hydroxyl groups (OH) according to the following chemical reaction (Stolper 1982a):

$$H_2O_m + O^0 \leftrightarrow 2OH \quad (2)$$

In reaction (2), O^0 is anhydrous oxygen and charges on each species (e.g., OH^-) are neglected. Reaction (2) is governed by the equilibrium constant K_{eq} (Stolper 1982a):

$$K_{eq} \propto \frac{[OH]^2}{[H_2O_m][O^0]} \quad (3)$$

In equation (3), square brackets indicate mole fractions on a single oxygen basis (Stolper 1982a), such that $[H_2O_m] + [O^0] + [OH] = 1$. Stolper (1982a) developed a model in which he assumed ideal mixing in the melt between anhydrous oxygens, molecular water, and hydroxyl. The development of Fourier transform infrared spectroscopy (FTIR) for measuring the concentrations of hydroxyl and molecular water in silicate melts (Stolper 1982b; Newman et al. 1986) confirmed the predictions of the speciation model that melts with low total water concentrations (less than ~0.2 wt%) are dominated by hydroxyl dissolution (e.g., Figure 2), whereas melts with water concentrations greater than ~4 wt% are dominated by molecular water dissolution.

In addition to successfully describing the solubility behavior of water in silicate melts, the speciation model of Stolper (1982a) also has implications for the diffusion behavior of water in melts, since molecular water and hydroxyl diffuse through melts at different rates. A mechanistic model for the diffusion of water in silicate melts was outlined by Wasserburg (1988) and Chekhmir et al. (1988), who derived the following expression for the diffusion of water in silicate melts:

$$\frac{\partial[\text{water}]}{\partial t} = \frac{\partial}{\partial x}\left(D_{H_2O_m}\frac{\partial[H_2O_m]}{\partial x} + D_{OH}\frac{\partial[OH]/2}{\partial x}\right) \quad (4)$$

In equation (4), [water] is the mole fraction of total water (i.e., the sum of the mole fractions of molecular water and hydroxyl), t is time, x is distance, $D_{H_2O_m}$ is the diffusivity of molecular water, and D_{OH} is the diffusivity of hydroxyl. This treatment was developed by Zhang et al. (1991b), who used FTIR to measure concentration gradients of molecular water and hydroxyl in rhyolite glasses and showed that the concentrations of these species could be almost perfectly reproduced by a model that assumes that molecular water is the diffusing species and hydroxyl is immobile (i.e., $D_{OH} = 0$), and that molecular water and hydroxyl maintain equilibrium at all

points along the concentration gradient (according to equations (2) and (3)). The relationship between $D_{\mathrm{H_2O_m}}$, D_{OH}, and D^*_{water} (as defined in equation (1)) is as follows (Chekhmir et al. 1988; Zhang et al. 1991a):

$$D^*_{\mathrm{water}} = D_{\mathrm{H_2O_m}} \frac{d[\mathrm{H_2O_m}]}{d[\mathrm{water}]} + D_{\mathrm{OH}} \frac{d[\mathrm{OH}]}{d[\mathrm{water}]} \quad (5)$$

Equation (5) is only valid when there are unique relationships between [H_2O_m] and [water], and [OH] and [water] (e.g., when the species are in equilibrium). If it is assumed that $D_{\mathrm{OH}} = 0$ (Zhang et al. 1991b) then equation (5) can be simplified to:

$$D^*_{\mathrm{water}} = D_{\mathrm{H_2O_m}} \frac{d[\mathrm{H_2O_m}]}{d[\mathrm{water}]} \quad (6)$$

and it can be shown that the application of the speciation model to the diffusion of water in silicate melts produces a relationship between D^*_{water} and water concentration that is approximately proportional (e.g., Zhang and Stolper 1991; Persikov et al. 2010).

The speciation-based model of Zhang et al. (1991b) has been highly successful for reproducing empirical data for water diffusion in rhyolitic melts and glasses (Zhang et al. 1991b; Zhang and Behrens 2000; Behrens et al. 2007; Ni and Zhang 2008; Wang et al. 2009), dacitic melts (Behrens et al. 2004; Ni et al. 2009a), andesitic melts (Persikov et al. 2010) and basaltic melts (Zhang and Stolper 1991; Persikov et al. 2010). However, some studies have reported deviations from this model. For example, Behrens et al. (2004) and Okumura and Nakashima (2006) find that D^*_{water} is only weakly dependent on water concentration in andesitic melt. Also, of particular relevance to this study, Ni et al. (2012) performed diffusion couple experiments on haploandesitic melts where one half of the diffusion couples contained a very low concentration of water (~0.01 wt%) and they found a significant misfit between their data and the traditional speciation model (with $D_{\mathrm{OH}} = 0$) at the low concentration ends of their water concentration profiles. Their low water concentration data implied a higher D^*_{water} than that predicted by the speciation model (in which D^*_{water} tends to zero as the concentration of water tends to zero). In order to fit their low water concentration data, Ni et al. (2012) developed a 'modified speciation model' in which they relaxed the assumption that $D_{\mathrm{OH}} = 0$; this modified speciation model provided a good fit to their data across the entire water concentration range of their experiments.

Ni et al. (2012) also make the tentative suggestion that the diffusion of hydroxyl may play a more significant role in mafic melts than felsic melts (based on an observed increase in K_{eq}

for reaction (2) reported by Ni et al. (2009b) from rhyolitic to dacitic to andesitic melts, which suggests a higher proportion of OH compared to H_2O_m at a given total water concentration in mafic melts). The lunar basalt considered in this study is a highly mafic composition with ~22 wt% FeO and ~13 wt% MgO, suggesting that, if the tentative hypothesis of Ni et al. (2012) is correct, our study of water diffusion in a highly mafic melt at low total water concentrations may well be influenced by the diffusion of hydroxyl.

3.2. Diffusion of molecular hydrogen in silicate melts

The results of existing studies of the diffusion of H-bearing species (i.e., H_2O, OH, H_2, CH_4, etc.) in terrestrial silicate melts are broadly consistent with H_2O_m being the dominant diffusing species (Zhang et al. 1991b) and are broadly inconsistent with a significant role for molecular hydrogen diffusion (Zhang and Ni 2010). The lack of evidence for H_2 diffusion in terrestrial melts is likely due to the low solubility of H_2 in silicate melts at low pressures (Hirschmann et al. 2012) and due to the oxidizing nature of most terrestrial melts such that H_2 is rapidly oxidized to H_2O (Zhang and Ni 2010). However, Zhang and Ni (2010) and Zhang (2011) have suggested that H_2 diffusion may play a role in the transport of H-bearing species through lunar melts due to the reducing nature of these melts (Sato 1976; Wadhwa 2008). Zhang (2011) hypothesizes (based on measurements of H_2 solubility in silica melt and H_2O_m solubility in rhyolite) that "in highly reducing melt (such as IW-2), dissolved H_2 concentration exceeds dissolved H_2O_m concentration" and that "at high temperatures as lunar magma is cooling down, H_2 rather than H_2O_m is likely the dominant diffusing species in the melt." It should be noted that these hypotheses are described by Zhang (2011) as tentative, due to the lack of available experimental data on H_2 diffusivity and solubility in relevant melt compositions. Additional evidence for a significant role of molecular hydrogen diffusion in natural silicate melts has been observed in low-pressure (up to 2 kbar) and low-temperature (up to 1000 °C) experiments in obsidian glasses and melts (Gaillard et al. 2002; Gaillard et al. 2003a; Gaillard et al. 2003b).

The experiments conducted during this study may shed some light on the debate as to whether or not H_2 diffusion is significant during the degassing of lunar magmas. Our experiments were conducted over a large range of fO_2 conditions from IW-2.2 to IW+6.7 and over a range of pH_2/pH_2O from (nominally) zero to ~10. If H_2 diffusion is significant under reducing conditions, then we might expect to observe a higher diffusivity of 'total H' (i.e., H_2 + H_2O_m + OH) in our low fO_2, high pH_2 experiments compared to our high fO_2, low pH_2 experiments, where (following

the approach of Zhang and Ni (2010) and assuming local chemical equilibrium) the diffusivity of 'total H' is defined as:

$$D_{\text{total H}} = 2D_{\text{H}_2}\frac{\partial[\text{H}_2]}{\partial[\text{total H}]} + 2D_{\text{H}_2\text{O}_\text{m}}\frac{\partial[\text{H}_2\text{O}_\text{m}]}{\partial[\text{total H}]} + D_{\text{OH}}\frac{\partial[\text{OH}]}{\partial[\text{total H}]} \quad (7)$$

In equation (7), $D_{\text{total H}}$ is the diffusivity of total H, D_{H_2} is the diffusivity of molecular hydrogen, and square brackets indicate mole fractions.

4. Methods

We conducted hydration and dehydration experiments on a synthetic Apollo 15 'Yellow Glass' composition (Delano 1986) and a mixture of anorthite and diopside glasses close in composition to the 1-atm anorthite-diopside eutectic ($An_{36}Di_{64}$). All experiments were conducted in a Deltech 1-atm vertical furnace. The partial pressures of water, carbon dioxide, carbon monoxide, hydrogen, and oxygen were fixed in the furnace atmosphere by flowing known ratios of H_2/CO_2 or CO/CO_2 gases through the furnace (further details of this process are given in section 2.3 of Chapter 2). Experiments were analyzed by secondary ionization mass spectrometry (SIMS) and Fourier transform infrared spectroscopy (FTIR).

4.1. Starting materials

Synthetic Apollo 15 'Yellow Glass' (hereafter referred to as 'lunar glass'; LG) was made by combining reagent-grade oxides using methods described in Chapter 2 of this thesis. The composition of the LG starting material is given in Table 1 of Chapter 2. The anorthite-diopside composition (hereafter referred to as AD) was made by combining anorthite and diopside glasses, as described in section 3.1 of Chapter 2. The composition of the AD starting material is given in Table 1 of Chapter 2.

4.2. Experimental methods

Experiments were conducted at 1 atm and 1350 °C, over a range of oxygen fugacities from IW-2 to IW+7. Temperature measurements were made using a type-B thermocouple and the oxygen fugacity was measured using an yttria-stabilized zirconia oxygen sensor (SIRO2; Ceramic Oxide Fabricators, Eaglehawk, Australia). For LG experiments, chips of pressed powder pellets weighing ~25 – 70 mg were balanced on rhenium wire loops. Rhenium wire was used during experiments in which the oxygen fugacity was considerably below the quartz-fayalite-magnetite

(QFM) buffer in order to minimize iron loss (Borisov and Jones 1999). Experiments LG42 and LG43 were run under conditions that were oxidizing enough to cause rhenium volatilization, so these experiments were hung on thin platinum loops. For AD experiments, chips of AD glass were loaded into 3.6 mm ID platinum crucibles.

The results of our solubility experiments (Chapter 2) have demonstrated that LG and AD melts equilibrated in H_2-CO_2 gas mixtures at 1 atm and 1350 °C will dissolve up to ~420 ppm water. The amount of water dissolved in the melt is dependent only on pH_2O, and can be controlled by varying the H_2/CO_2 ratio flowing into the furnace. We can use these results to create melts with homogeneous, well-constrained water concentrations. By exposing these homogeneous melts to atmospheres with either lower or higher pH_2O for short durations (on the order of a few minutes) we can generate concentration gradients of water in the melts, and the lengths and shapes of these concentration gradients (along with knowledge of the initial conditions and boundary conditions from the results of our solubility experiments) can be used to determine the diffusivity of water in AD and LG melts. As outlined below, three different types of experiments were performed as part of this study:

1. Hydration experiments

Water concentration gradients were generated in a three-stage process: (1) melt was fused at 1350 °C for ~24 – 70 hours using a CO-CO_2 gas mixture to fix the fO_2. Charges equilibrated in this way contain ~10 – 20 ppm water (as measured by FTIR and SIMS). (2) With the sample still hanging in the furnace, the gas mixture was switched to a H_2-CO_2 mixture at the same fO_2, which fixed pH_2O and pH_2 (see Chapter 2). (3) After exposure to the H_2-CO_2 gas for up to10 minutes (which generated a ~10^3 µm diffusion profile), the sample was quenched in deionized water. Several of these experiments shattered shortly after quenching or during sample preparation, so AD2b was annealed in air for ~20 minutes at 500 °C immediately after quenching. The annealing process did not solve the problem of the experimental glass shattering during sample preparation, though AD2b broke into larger pieces than other experiments in this series, implying that perhaps the annealing process was partially successful. AD hydration experiments at very low fO_2 (IW-1.5 and IW-2.2) were attempted, however, under highly reducing conditions we found that the melt crawled out of the platinum capsules.

2. Dehydration experiment (AD melt)

During the first stage of dehydration experiment AD38, melt was fused at 1350 °C for ~18 hours using an H_2-CO_2 gas mixture to fix the fO_2 and pH_2O. This produced a homogeneous melt with a water concentration of ~420 ppm. Next, the experimental charge was exposed to a CO/CO_2 gas mixture at the same fO_2 but with a pH_2O of close to zero. After exposure to CO/CO_2 for 7 minutes, the sample was drop-quenched in deionized water.

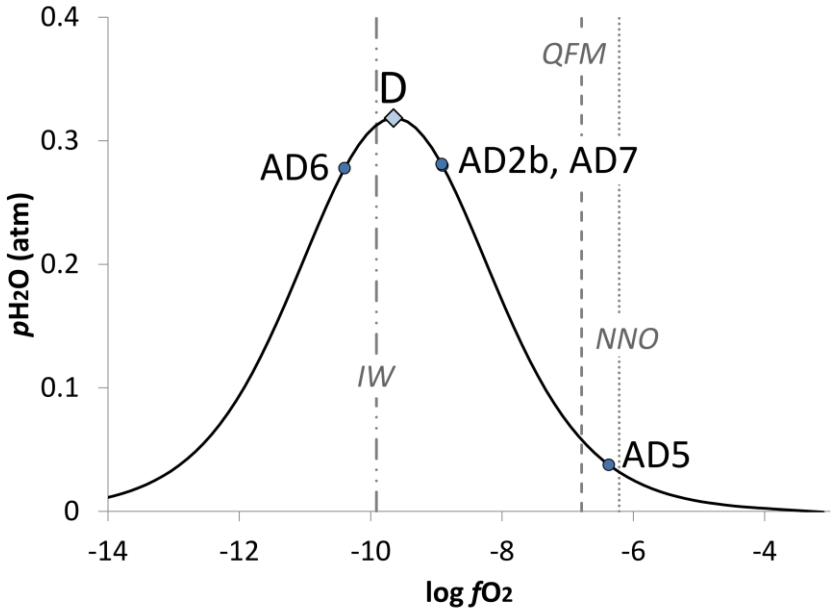

Figure 4 pH_2O and fO_2 conditions of hydration experiments (AD2b, AD5, AD6 and AD7; blue filled circles) and of the initial condition for dehydration experiment AD38 (blue filled diamond marked 'D'). Black curve indicates expected pH_2O produced by H_2/CO_2 gas mixtures over a range of fO_2. Gray dashed lines indicate the positions of the main oxygen buffers (IW = iron-wüstite; QFM = quartz-fayalite-magnetite; NNO = nickel-nickel oxide).

3. Small gradient, simultaneous hydration and dehydration experiments in H_2-CO_2, quenched in air

This series of experiments was conducted at 1 atm and 1350 °C under flowing H_2/CO_2 gas mixtures. First, one experimental charge was equilibrated for ~24 hours with a "high" pH_2O gas mixture and another experimental charge was equilibrated for ~24 hours with a "low" pH_2O gas mixture. The results of our solubility experiments (Chapter 2) were used to select pH_2O conditions for these two experimental charges that would produce melts that differed in their water concentrations by ~60 ppm (Figure 5). Charges were quenched in air by pulling the sample holder out of the top of the furnace. Following this pre-equilibration step, both charges were hung from the same sample holder and put back into the furnace at the same time (except for experiments AD36 and AD37 which were conducted separately), under an H_2/CO_2 gas mixture with an "intermediate" pH_2O (designed to produce a boundary condition that was ~30 ppm lower than the high water charge and ~30 ppm higher than the low water charge). Exposure of the two experimental charges to this intermediate pH_2O gas mixture caused the high water charge to dehydrate and the low water charge to hydrate. After exposure to this intermediate pH_2O gas mixture for 5 – 10 minutes, both charges were quenched in air at the same time by pulling the sample holder out of the top of the furnace. This quenching technique was successful in producing experimental glasses that did not crack during sample preparation. Our lowest concentration experiment pair spanned water concentrations from 10 – 80 ppm and our highest concentration experiments spanned water concentrations from ~330 – 430 ppm. pH_2/pH_2O also varied significantly across our experiments, from 0.003 to 10.

This series of experiments was designed to isolate the dependence, if any, of D^*_{water} on water concentration by conducting experiments over narrow concentration ranges (e.g., Persikov et al. 2012). These pairs of experiments will also be useful for looking for differences between the diffusive behavior of water during hydration versus dehydration. One of the major advantages to running our hydration and dehydration experiments in pairs is that we can be sure that each pair of experiments experienced exactly the same temperature history and boundary condition.

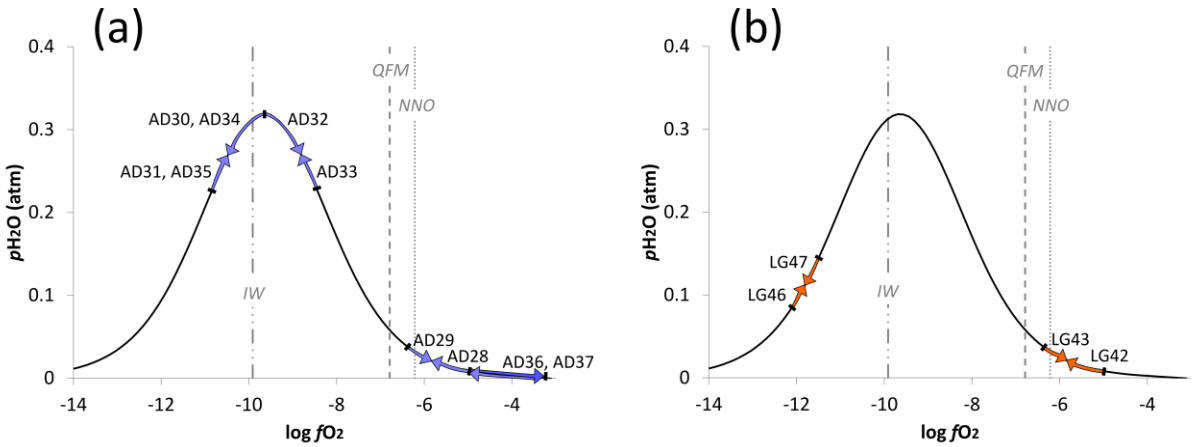

Figure 5 Summary of pH_2O and fO_2 conditions of small gradient hydration and dehydration experiments. (a) Conditions of AD experiments. Black curve indicates expected pH_2O produced by H_2/CO_2 gas mixtures over a range of fO_2. Blue arrows show the ranges of pH_2O conditions experienced by each individual experiment; the bases of the arrows indicate the initial conditions of the experiments and the heads of the arrows point towards the boundary conditions of the experiments. Gray dashed lines indicate the positions of the main oxygen buffers (IW = iron-wüstite; QFM = quartz-fayalite-magnetite; NNO = nickel-nickel oxide). (b) Conditions of LG experiments. Symbols and curves as in (a).

4.3. Analytical techniques

Water concentration gradients across our experimental glasses were characterized by SIMS and FTIR. Prior to analysis, most experiments were cut in half using a Unipress Precision Wire Saw and polished to 0.25 µm. Typically, one half of the experiment was double-polished and analyzed by FTIR, and the other half of the experiment was analyzed by SIMS. However, some experiments were analyzed by SIMS only, and some experiments were analyzed first by FTIR and then the same portion of the experiment was re-mounted in indium for analysis by SIMS.

4.3.1. Analysis of water concentration profiles by FTIR

FTIR analyses were performed on double-polished samples using a Nicolet Magna-IR 860 FTIR spectrometer equipped with a Nicolet Continuµm IR microscope, a CaF_2 beamsplitter, and a MCT/A detector cooled with liquid N_2. Spectra were collected using a ~25×80 µm aperture across a wavenumber range of 1300 – 7000 cm^{-1} with a resolution of 4 cm^{-1}, and up to 2048 scans were averaged for each analysis. Measurements were made along linear traverses using an automatic stage, which was programmed to move the sample ~80 µm between each analysis. Water concentrations were determined from the height of the 3550cm^{-1} peak using the Beer-

Lambert law (Stolper 1982b), with a molar absorption coefficient of 63 $l \cdot mol^{-1} cm^{-1}$ (Dixon et al. 1995) for both the AD and the LG compositions.

Attempts to characterize our early experiments by FTIR were met with some challenges: Experiments that were drop-quenched into water tended to break up badly during sample preparation. As a result, large areas of each experiment were riddled with cracks and scattered infrared light, such that they could not be analyzed by FTIR. Another problem we encountered was that we were forced to analyze relatively thick glass wafers (~500 – 1500 μm) in order to prevent the water-quenched experimental charges from breaking into fragments. These problems were resolved for the small-gradient experiments, which were quenched in air at room temperature. This marginally slower quench rate (samples glowed red for ~5 seconds immediately after removal from the furnace) produced crack-free glasses that could be polished to thicknesses of ~200 μm for FTIR analysis.

4.3.2. Analysis of water concentration profiles by SIMS

We measured the total concentration of H-bearing species in the melt (dissolved as H_2O, OH, and potentially H_2) using the Cameca 7f-GEO SIMS at Caltech. Prior to analysis, our experimental glasses were polished in dental resin. The polished samples were removed from the dental resin by soaking in acetone for a few hours, before being ultrasonicated in three cycles each of toluene, acetone, and isopropanol. Samples were baked overnight in a vacuum oven at ~110 °C before being pressed into a 1-inch diameter aluminum mount filled with indium. Three days before the beginning of the analytical session, the mount was coated in a 50-nm layer of gold and was placed under vacuum in the sample exchange airlock. Line profiles across the samples were analyzed with a ~4-nA primary beam of cesium ions. Analyses were spaced ~50 – 80 μm apart. The primary beam was rastered across a 15×15 μm^2 area during 120 s of presputtering, producing a crater with an approximate diameter of 20 μm, and area of the raster was reduced to 5×5 μm^2 during analysis. Use of a 100 μm field aperture ensured that only secondary ions from the central ~10 μm of the sputtered crater were collected. Counts of ^{16}OH, ^{18}O, ^{12}C, and ^{30}Si were measured by an electron multiplier. A mass resolving power of ~5000 was used to separate the ^{16}OH peak from ^{17}O. SIMS data were calibrated using the calibration curves shown in Figure 6 of Chapter 2. The calibration of our AD experiments was straightforward, because counts of $^{16}OH/^{18}O$ were found to be linearly correlated to water concentration as measured by FTIR. However, the relationship between $^{16}OH/^{18}O$ and water concentration measured by FTIR for our LG experiments was more complex because the LG experiments had a

range of iron concentrations and this introduced matrix effects. For this reason, SIMS measurements of our LG experiments were calibrated individually: LG42 and LG43 were calibrated against solubility experiment LG35 (see Chapter 2); LG46a and LG46b were calibrated against solubility experiment LG40 (see Chapter 2); and water concentrations in LG47a and LG47b were measured independently by FTIR.

5. Results

5.1. Results of AD hydration experiments

Four hydration experiments were conducted on AD melt, spanning a range of fO_2 from IW-0.5 to IW+3.5 and a range of pH_2/pH_2O from 0.01 to 1.4 (Table 1). Water concentrations in these experiments range from ~15 ppm to ~350 ppm. All hydration experiments on AD melt are well described by error functions, suggesting that D^*_{water} is not concentration dependent under these conditions (Figure 6). Best fit values of D^*_{water} for all four hydration experiments are within a factor of three of each other, and there is no clear relationship between D^*_{water} and pH_2/pH_2O or fO_2 (Table 1). The fitting procedure for these experiments is described in the caption to Table 1.

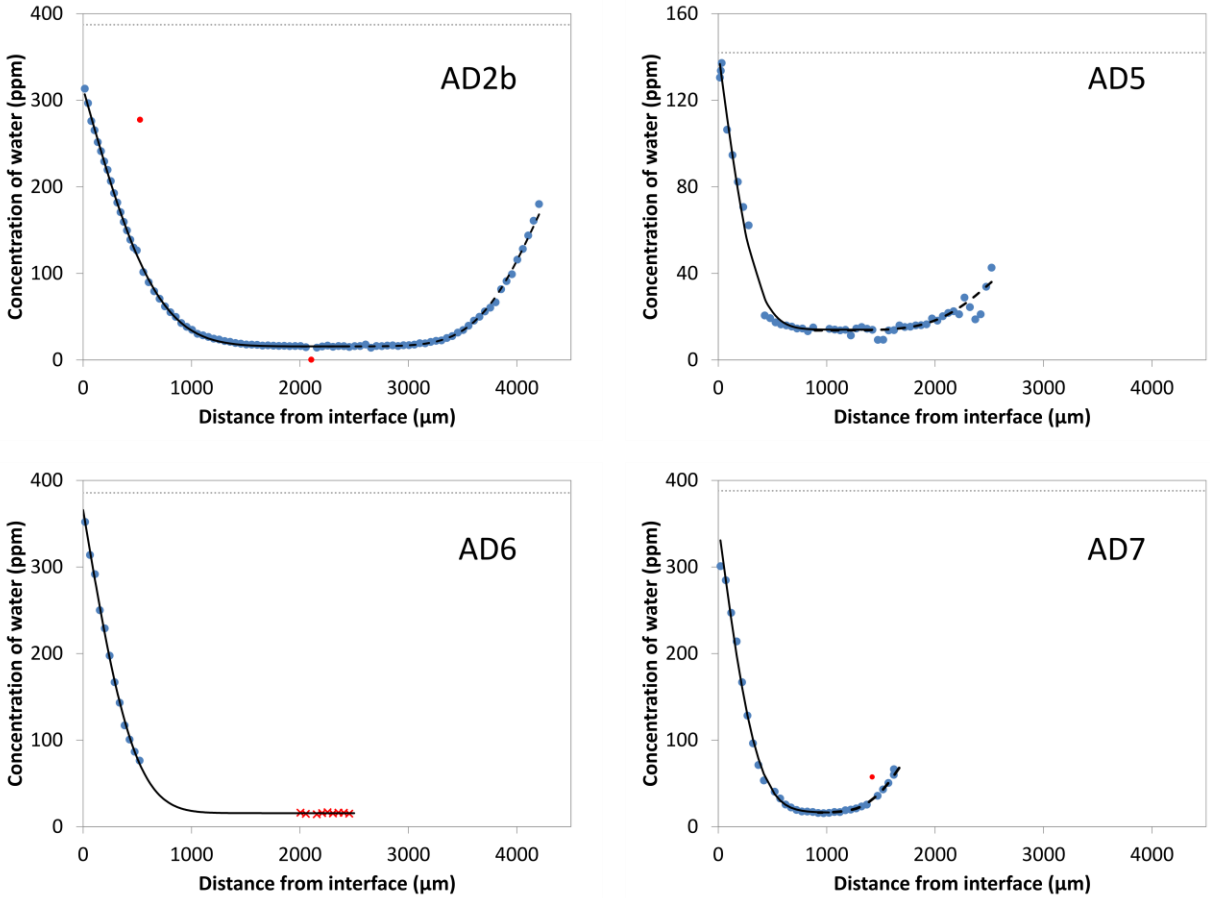

Figure 6 Characterization by SIMS of water concentration gradients in AD hydration experiments. AD2b was allowed to hydrate for 10 minutes, whereas AD5, AD6 and AD7 were allowed to hydrate for 5 minutes. Consequently, the water concentration gradients in AD2b extend over greater distances than those in AD5, AD6 and AD7. Concentrations of water were observed at the melt-vapor interface and also against the sides and bases of the platinum capsules, suggesting that water may be able to diffuse rapidly through the platinum. The interiors of the samples contain ~15 ppm water. Concentration gradients are well described by error functions (solid black and dashed black curves are fits to the concentration gradients at the melt-vapor interfaces and at the bases of the capsules respectively), suggesting that D^*_{water}may be assumed to be constant in this concentration range. SIMS data are plotted as blue and red filled circles: blue data points were included in the fitting procedure, whereas the red points in AD2b and AD7 were excluded. Boundary conditions predicted by the results of our solubility experiments (Chapter 2) are indicated by gray dashed lines. Experiment AD5 broke during sample preparation and the first ~500 µm of the water concentration gradient were measured on a chip of glass that may have become tilted during polishing in the indium mount. This introduces some uncertainty in the distances of all AD5 concentration measurements from the melt-vapor interface, and may explain the mismatch between the first ~500 µm of this profile with the rest of the profile. Experiment AD6 broke during sample preparation leaving only a small chip from the top surface of the sample for analysis. In order to fit data from AD6, 10 data points from the interior of AD2b were added to the AD6 data (red crosses on AD6 plot), making the assumption that the interior of this sample had approximately the same water concentration as the other experiments in this series (i.e., ~15 ppm).

Experiment	*Duration (minutes)*	*pH_2/pH_2O*	*D^*_{water} (m^2s^{-1})*	*D^*_{water} upper bound (m^2s^{-1})*	*D^*_{water} lower bound (m^2s^{-1})*
AD2b	10	0.24	2.39E-10	2.43E-10	2.34E-10
AD5	5	0.01	1.21E-10	1.39E-10	1.08E-10
AD6	5	1.36	2.29E-10	2.33E-10	2.25E-10
AD7	5	0.25	1.31E-10	1.37E-10	1.27E-10
AD2b base	10	0.24	1.76E-10	1.79E-10	1.64E-10
AD2b side	10	0.24	2.09E-10	2.33E-10	1.92E-10
AD5 base	5	0.01	2.94E-10	5.07E-10	1.65E-10
AD7 base	5	0.25	9.73E-11	1.08E-10	8.76E-11

Table 1 Compilation of results of AD hydration experiments. Water concentration gradients were fit assuming D^*_{water} to be constant and applying equation 3.13 of Crank (1979) for diffusion in a semi-infinite medium with a uniform initial concentration, C_0, whose surface is maintained at a constant concentration, C_1. C_0 was obtained by averaging ~10 points in the interior of each experiment. C_1 and D^*_{water} were treated as free parameters. The MATLAB function *fminbnd* was used to find values of C_1 and D^*_{water} for which the sum of the absolute values of the residuals between the model and the data was minimized. Upper and lower bounds on D^*_{water} were calculated using a Monte Carlo technique: For each experiment, 1000 new concentration profiles were generated by adding noise to the original data (drawn from a normal distribution with 1σ calculated as the standard deviation of ~10 data points in the uniform interior of the experiment). D^*_{water} was fit to each of these 1000 concentration profiles. The upper and lower bounds on $D^*_{\mathrm{water}}$are the 99th and 1st percentile values of $D^*_{\mathrm{water}}$for these 1000 profiles.

5.2. Results of AD dehydration experiment

Experiment AD38 was hydrated for 18 hours in an H_2/CO_2 gas mixture at IW+0.3 containing a pH_2O of 0.3 bar before being dehydrated for seven minutes under a CO/CO_2 gas mixture at IW+0.3. This produced a melt with an interior water concentration of ~400 ppm and a water concentration close to the melt-vapor interface of ~40 ppm. Unlike the hydration experiments described above, the concentration gradient produced at the melt-vapor interface this experiment is not well described by an error function. However, the concentration gradient produced up against the base of the platinum capsule containing AD38 is well described by an error function (Figure 7).

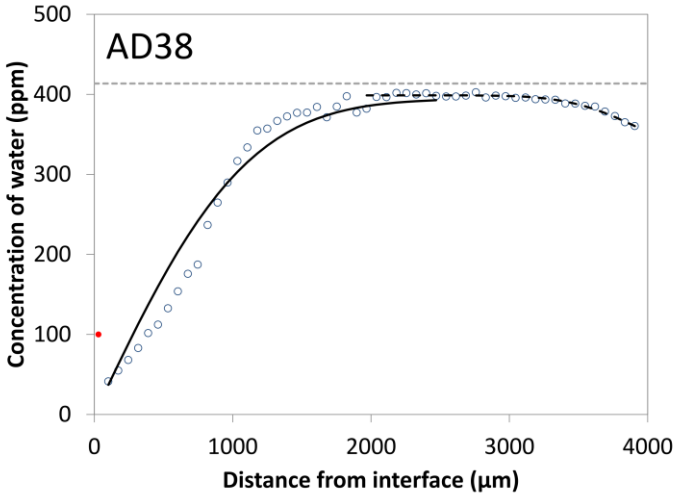

Figure 7 Concentration of water measured in dehydration experiment AD38 by SIMS (open blue circles and red circle). The red data point was excluded from the fitting procedure. The concentration gradient produced at the melt-vapor interface has a sinusoidal shape and is not well described by an error function (black curve). The concentration gradient against the base of the platinum capsule is well described by an error function (black dashed curve). The initial condition expected for this experiment based on the results of our solubility experiments (Chapter 2) is indicated by a gray dashed line.

We can think of three possible reasons to explain the sinusoidal shape of the water concentration gradient in AD38:

1. The sinusoidal shape could be indicative of concentration-dependent diffusion.

2. Advection of the melt in the platinum capsule caused by a large change in the shape of the melt meniscus during the experiment could be distorting the diffusive water concentration gradient.

3. Water may be kinetically inhibited from leaving the melt at the melt-vapor interface when exposed to a CO/CO_2 environment.

A sinusoidal water concentration profile is one of the hallmarks of concentration-dependent water diffusion (e.g., Persikov et al. 2010). However, we think it is unlikely that the shape of the water concentration gradient in AD38 is a result of concentration-dependent diffusion, because we did not observe concentration-dependent diffusion in the hydration experiments described above (which covered a similar water concentration range) and we did not observe concentration-dependent diffusion in the small-gradient simultaneous hydration and dehydration experiments described in the next section. Additionally, the concentration gradient at

the base of AD38 is well described by a constant D^*_{water} of 2.03E-10 m^2s^{-1}, which is very similar to the values obtained by fitting our hydration experiments (Table 1).

Advection of the melt during dehydration of AD38 seems to us to be a possible cause of the sinusoidal shape of the water concentration gradient in this experiment. We have observed that experiments run under CO/CO_2 gas mixtures have much shallower menisci than those run in H_2/CO_2 (Figure 8). We estimate (using a simple trigonometric calculation) that the change in meniscus shape expected for AD38 could result in advection of melt over a distance on the order of 1000 µm. Depending on the time scale of this melt advection (i.e., if it occurred almost instantaneously compared to the minute time scale of the experiment it would not affect the resultant water diffusion profile), this process could significantly distort the water concentration gradient produced in the melt by diffusion, and could conceivably cause the sinusoidal shape of the gradient observed in AD38. However, it is interesting to note that our AD hydration experiments appear to be unaffected by this process (i.e., they are all well described by error functions) despite the fact that the menisci of these experiments likely steepened when the gas mixture was changed from CO/CO_2 to H_2/CO_2.

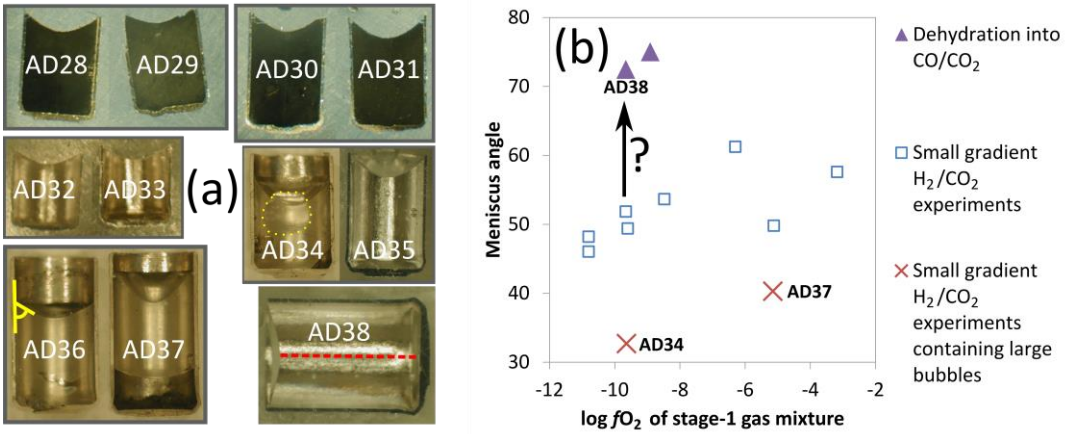

Figure 8 (a) Photographs of dehydration experiment AD38 and small-gradient hydration and dehydration experiments AD28 through AD37. Each experiment has been cut in half down the long axis of its platinum capsule. Experiments AD28 through AD31 have been polished, pressed into indium, and coated in 50 nm of gold. The remaining experiments are pictured at earlier stages of sample preparation. Each capsule has an ID of 3.6 mm. AD34 contains a bubble (outlined in yellow) and AD37 has a large air cavity at the base of the capsule. The presence of bubbles appears to have steepened the meniscus in these experiments compared to the other experiments. Note that AD38 has a particularly shallow meniscus. The yellow angle indicated on AD36 was measured to characterize the shape of the meniscus in each experiment (the "meniscus angle" in (b)). The red dashed line on AD38 shows a representative water concentration profile measured by SIMS, extending from the center of the top surface of the melt to the base of the platinum capsule. **(b)** Relationship between meniscus angle and log fO_2 of the furnace atmosphere (the fO_2 of the initial equilibration stage is plotted, though a similar relationship is seen if the fO_2 of the final gas mixture is

used, since the difference between these quantities is small). Small gradient experiments hint at a gradual flattening of the meniscus (i.e., an increase in the meniscus angle) as the fO_2 of the gas mixture is increased. The menisci of experiments containing large air bubbles are considerably steeper than experiments without large bubbles. Menisci of experiments dehydrated into CO/CO_2 are flatter than experiments conducted in H_2/CO_2. This suggests that significant advection of melt may have occurred in AD38 in response to flattening of the meniscus (indicated by the black arrow).

We also consider the possibility that the sinusoidal shape of AD38 was caused by kinetic inhibition of water loss from the melt-vapor interface of this experiment. As discussed in the following section, no such kinetic effects are observed in our paired dehydration and hydration experiments in H_2/CO_2 environments. Therefore, if water was indeed kinetically inhibited from leaving the surface of AD38, then this suggests that the kinetic effect may be particular to diffusive loss of water into a CO/CO_2 atmosphere. AD37 (discussed in the following section) also has a sinusoidal water concentration gradient, and this experiment was dehydrated into an atmosphere of pure CO_2, adding further weight to the inference that water loss could be kinetically inhibited during diffusion into an atmosphere lacking H-bearing species. The relatively high concentration of water (~40 ppm) observed at the melt-vapor interface of AD38 is also suggestive of a kinetic effect. The results of our hydration experiments demonstrate that a melt equilibrated with a CO/CO_2 environment for multiple days contains ~15 ppm water, so the 40 ppm water observed at the melt-vapor interface of AD38 is higher than would be expected for equilibrium partitioning between the vapor and melt.

5.3. Results of small gradient hydration and dehydration experiments in H_2/CO_2

Four pairs of small gradient hydration and dehydration experiments were conducted on AD melt, spanning a range of fO_2 from IW-0.6 to IW+4.8 and a range of pH_2/pH_2O from nominally zero to 1.5 (Table 2). Water concentrations in these experiments range from ~15 ppm to ~430 ppm (Figure 9). Of these four pairs of experiments, three were conducted simultaneously (i.e., both experiments in the pair were hung in the furnace at the same time, thereby guaranteeing that they experienced identical temperature histories and boundary conditions). AD36 and AD37 were conducted separately. The initial condition for experiment AD31 was compromised (the lid of the furnace was loose for the final ~10 minutes of the pre-equilibration stage of this experiment), so the results of AD31 are not considered reliable, and this experiment is omitted from Figure 12. Experiments AD34 and AD37 were found to contain large vapor bubbles (Figure 8), and it is thought that this may have affected the shape of the water concentration gradients in these experiments (especially in AD37, which is also observed to have a very steep meniscus; see Figure 8).

Excluding experiments AD31 and AD37 (for reasons described above) all of the remaining experiments in this series are well described by error functions, suggesting that D^*_{water} is not concentration dependent under these conditions (Figure 10). Best fit values of D^*_{water} are approximately constant across the entire experimental range (Figure 12) and there is no clear relationship between D^*_{water} and $p\mathrm{H_2}/p\mathrm{H_2O}$ (Table 2). Moreover, hydration and dehydration pairs (AD28 and AD29; AD32 and AD33; and AD34 and AD35) appear to be symmetric and appear to have identical concentrations at the melt-vapor interface. This can be seen most clearly in Figure 11, in which we demonstrate the quality of fits to these paired experiments making the assumptions that D^*_{water} and the boundary condition for both experiments are the same. The symmetry of our hydration and dehydration experiments, the similarity between concentrations of water at the melt-vapor interface for paired experiments in this series, and the close correspondence between measured concentrations of water at the melt-vapor interface to the concentrations expected based on the results of our solubility experiments (Figure 10) suggests that our implicit assumption of equilibrium at the melt-vapor interface for these experiments is correct (i.e., kinetic factors are not significant under the conditions of our paired experiments). However, as described in Section 4.2, kinetic factors may come into play during dehydration in environments devoid of H-bearing species (e.g., AD37 and AD38).

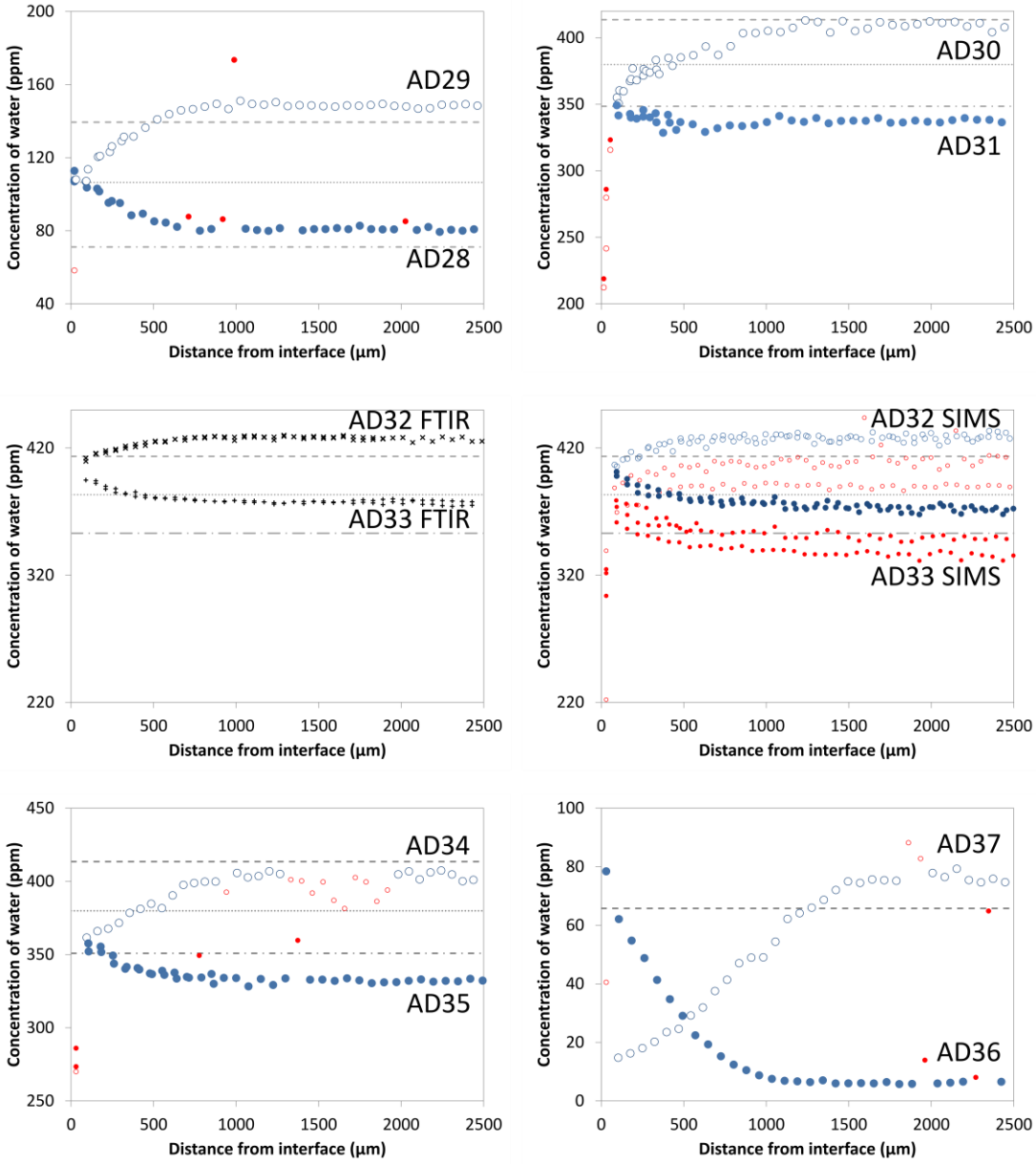

Figure 9 Water concentration gradients measured across small gradient AD experiments by SIMS (all experiments) and FTIR (AD32 and AD33 only). Dehydration experiments are plotted as open circles; hydration experiments are plotted as filled circles. Data plotted as blue circles was used for diffusion fitting; data points that were removed prior to fitting are plotted in red. SIMS data for AD32 and AD33 are noisy, and re-measurements of these samples on different days gave non-reproducible results, so these samples were also characterized by FTIR (FTIR data plotted as black crosses). SIMS data for AD32 and AD33 was then shifted in concentration to match the water concentration in the interior of these samples according to the FTIR data (shifted concentration data plotted as blue circles). For all experiments, the expected initial concentration and boundary concentration (based on the results of the solubility experiments described in Chapter 2) are indicated by gray dashed and dotted lines. Most of the measured interior and boundary water concentrations are within ~10% of their expected values, excluding some of the lowest concentration experiments (e.g., the edge of AD36 has a measured concentration 31% higher than expected, however, this corresponds to and absolute difference of only 18 ppm).

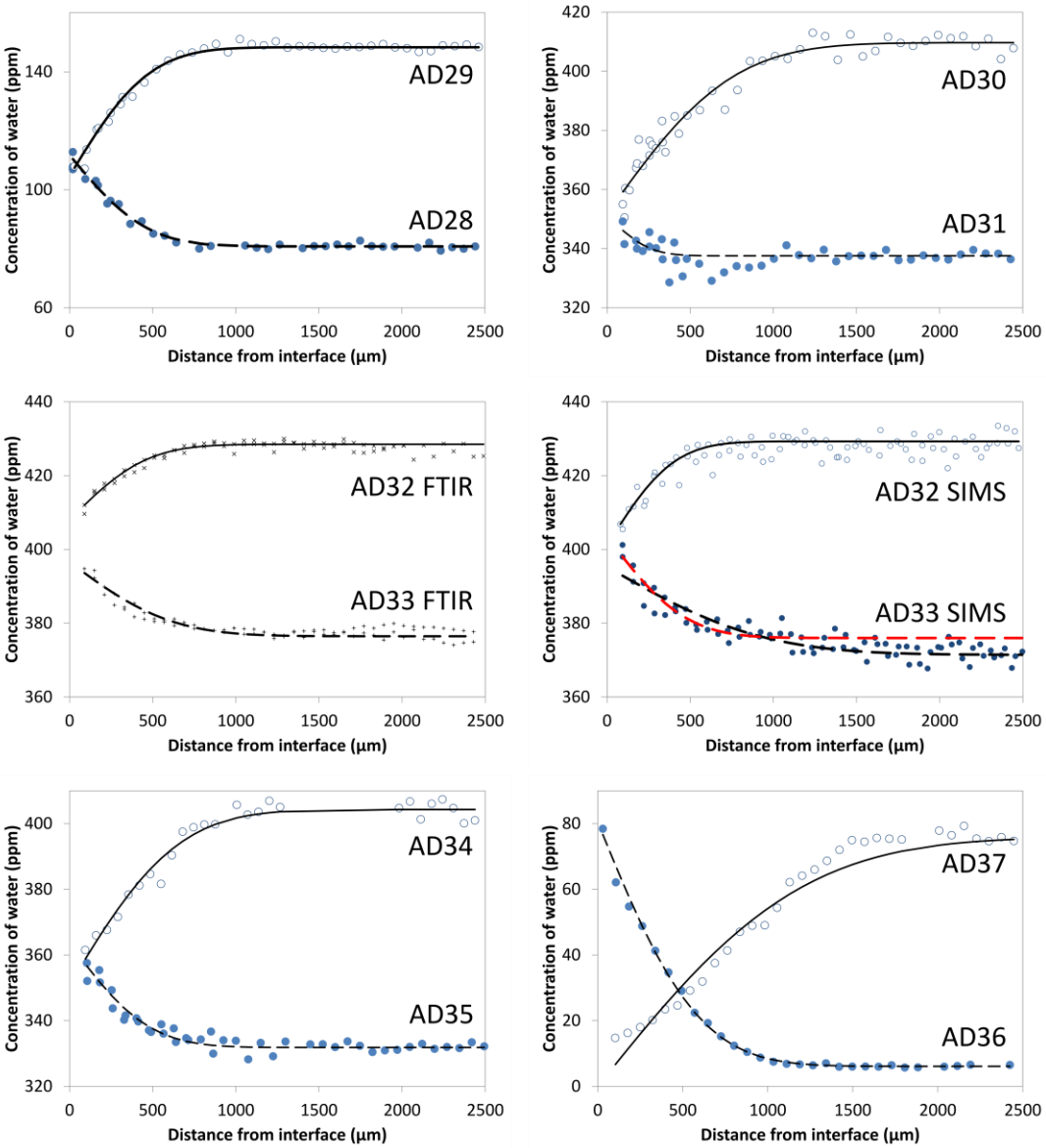

Figure 10 Results of fitting water concentration gradients in AD small gradient hydration and dehydration experiments, assuming D^*_{water} to be constant. The initial concentration was fixed to be the average of ~10 points from the interior of each sample, and the boundary condition was a free parameter. SIMS data are plotted as blue filled circles; FTIR data are plotted as black crosses; best fits to the data are plotted as solid and dashed black curves. Experiment AD31 is thought to have had a non-uniform initial condition (the lid of the furnace was loose for the last ~10 minutes of the pre-equilibration stage), and the difference in water concentration between the edge and the interior of this sample is smaller than intended (<10 ppm) so the results from this experiment are considered unreliable. The SIMS data for AD33 shows a continual decrease in water up to >2500 µm away from the melt-vapor interface, whereas the FTIR data for this experiment shows that the water concentration in this sample becomes uniform just beyond 1000 µm from the melt-vapor interface. This discrepancy may indicate that the SIMS analyses were drifting over time (perhaps due to slight tilting of the sample, or due to a decrease in beam current over the course of the run). We expect FTIR to be more stable than SIMS, so it is likely that the best fit to the AD33 SIMS data has a D^*_{water} that is too high. We have fit the AD33 SIMS data a second way, using the FTIR interior concentration as an initial condition, and the best fit following this method is shown as a red dashed curve. Note that all experiments are well described by error functions except for AD37.

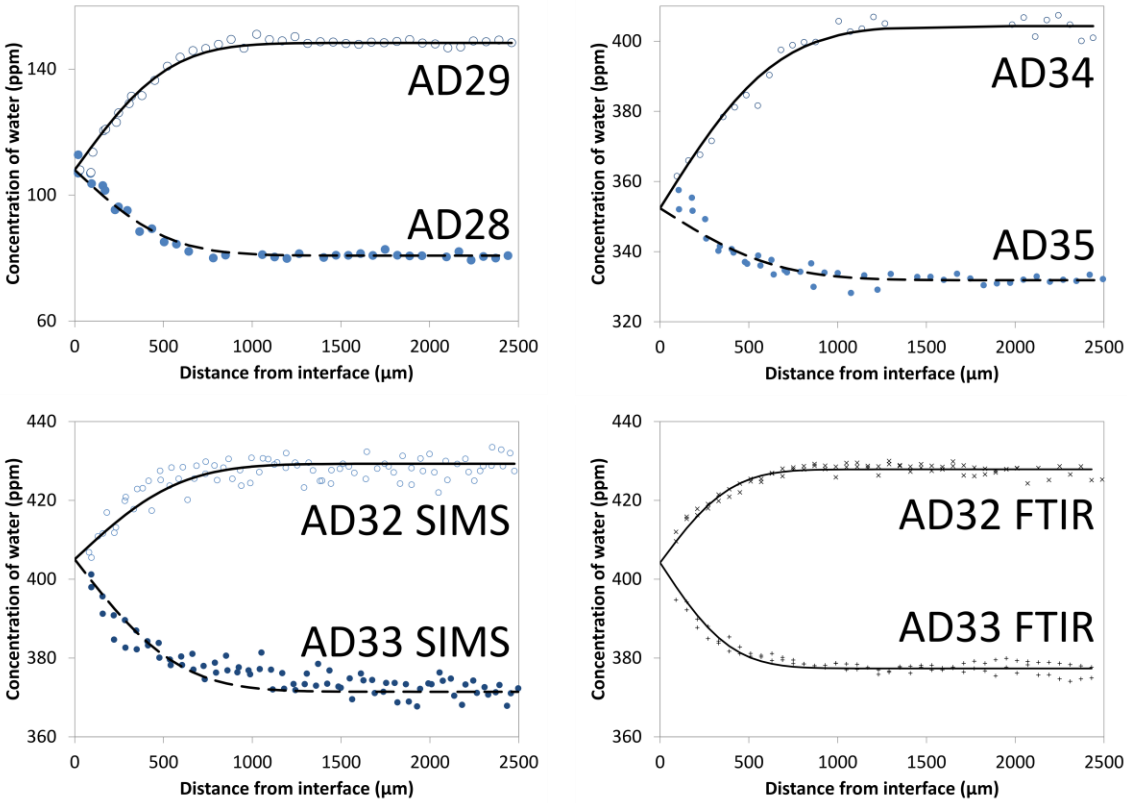

Figure 11 Results of fitting pairs of hydration and dehydration experiments together. Pairs of experiments were fit simultaneously, assuming that both experiments in the pair had the same D^*_{water} and the same concentration of water at the melt-vapor interface. SIMS data are plotted as blue circles, FTIR data are plotted as black crosses, and best fits to each experiment are plotted as solid or dashed black curves.

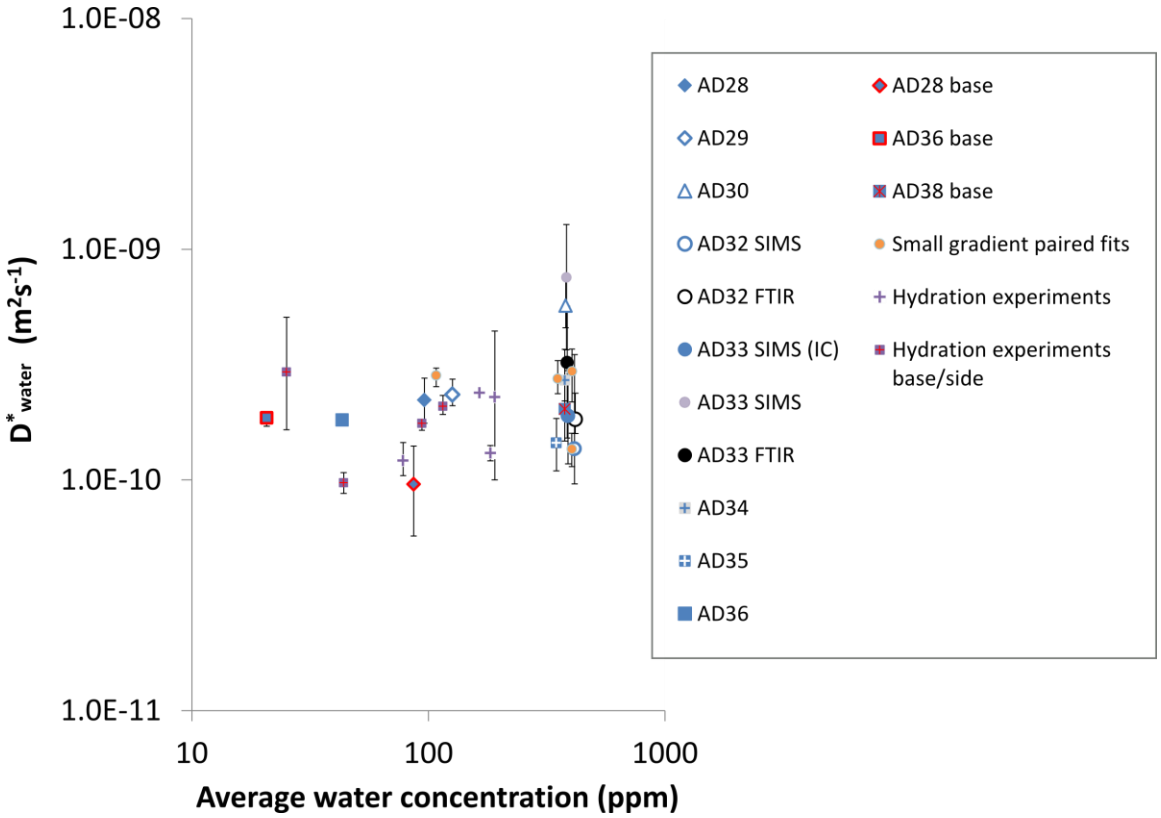

Figure 12 Summary of best fit values of D^*_{water} obtained by fitting our AD hydration and small gradient experiments. D^*_{water} is approximately constant across the whole experimental range. 'Average water concentration' is the average of the water concentration at the edge and in the interior of each sample, except for the paired fits to the small gradient experiments, for which the concentration at the melt-vapor interface is plotted. Note that the results of fitting our simultaneous hydration and dehydration experiments as pairs (orange circles) lie within the scatter of the results of fitting these experiments separately. Fits to water concentration gradients at the melt-vapor interfaces of AD37 and AD38 are excluded from this figure because they have sinusoidal shapes that are not well described by error functions. AD31 is also excluded because it had a compromised initial condition.

Experiment	*Duration (s)*	*pH_2/pH_2O*	*D^*_{water} (m^2s^{-1})*	*D^*_{water} upper bound (m^2s^{-1})*	*D^*_{water} lower bound (m^2s^{-1})*
AD28	300	0.007	2.22E-10	2.76E-10	1.76E-10
AD29	300	0.007	2.35E-10	2.74E-10	2.10E-10
AD30	304	1.506	5.70E-10	7.55E-10	4.57E-10
AD31	*304*	*1.506*	*6.29E-11*	*1.10E-10*	*1.45E-11*
AD32 SIMS	357	0.222	1.37E-10	3.50E-10	9.61E-11
AD32 FTIR	357	0.222	1.83E-10	2.38E-10	1.59E-10
AD33 SIMS	357	0.222	7.56E-10	1.28E-09	3.67E-10
AD33 FTIR	357	0.222	3.23E-10	5.66E-10	1.52E-10
AD33 SIMS with initial concentration of 376 ppm	357	0.222	1.90E-10	2.98E-10	1.17E-10
AD34	478	1.506	2.71E-10	3.68E-10	2.20E-10
AD35	478	1.506	1.45E-10	1.85E-10	1.10E-10
AD36	595	0.003	1.82E-10	1.93E-10	1.78E-10
AD37	*590*	*0.000*	*7.45E-10*	*7.87E-10*	*6.40E-10*
AD38	*420*	*0.000*	*8.89E-10*	*1.00E-09*	*8.13E-10*
Fits to concentration profiles against the base of the Pt capsule					
AD28 base	300	0.007	9.59E-11	1.40E-10	5.72E-11
AD36 base	595	0.003	1.86E-10	1.97E-10	1.71E-10
AD38 base	420	0.000	2.03E-10	3.11E-10	1.48E-10
Fits to paired experiments					
AD28 + AD29	300	0.007	2.84E-10	3.05E-10	2.54E-10
AD32 + AD33 FTIR	300	0.222	1.36E-10	1.59E-10	1.14E-10
AD32 + AD33 SIMS	300	0.222	2.96E-10	3.70E-10	2.18E-10
AD34 + AD35	478	1.506	2.75E-10	3.29E-10	2.37E-10

Table 2 Compilation of results of fitting AD small gradient hydration and dehydration experiments, and AD38. The results of AD31, AD37 and AD38 are excluded from Figure 12: AD31 is excluded because the initial condition of this experiment was compromised; AD37 and AD38 are excluded because concentration gradients across these experiments are not well described by error functions (see Figures 7 and 10). The fitting procedure is the same as for the AD hydration experiments and is described in the caption to Table 1. This procedure was modified slightly for the fits to the paired experiments: For these experiments, D^*_{water} and the water concentration at the melt-vapor interface were constrained to be the same for both experiments in the pair, and the best fit was calculated by minimizing the misfit between the data and the model for both experiments simultaneously.

5.4. Results of LG small gradient simultaneous hydration and dehydration experiments in H_2/CO_2

Two pairs of small gradient hydration and dehydration experiments were conducted on LG melt, spanning a range of fO_2 from IW-2.2 to IW+4.9 and a range of pH_2/pH_2O from 0.007 to 9.7 (Table 3). Water concentrations in these experiments range from ~80 ppm to ~280 ppm. For each of these pairs of experiments (LG42 and LG43; LG46b and LG47b) both experiments in the pair were hung in the furnace at the same time, thereby guaranteeing that they experienced identical temperature histories and boundary conditions.

Unlike our AD experiments, which were conducted in open platinum capsules, our LG experiments were hung from rhenium wire loops and melted to form approximately spherical droplets with diameters of ~2 – 3 mm. As shown in Figure 13, the water concentration gradients in our LG experiments extend across their entire diameters, so we cannot assume that the concentrations measured in the centers of these experiments correspond to the initial concentrations of the experiments. The estimation of the initial concentrations of these experiments is the largest source of uncertainty in the best-fit values of D^*_{water} obtained for our LG experiments. LG42 was pre-equilibrated at the same time as AD28 and LG43 was pre-equilibrated at the same time as AD29, so we can use the water concentrations in the interiors of AD28 and AD29 to estimate the initial concentrations of LG42 and LG43 (making a small correction for the difference in water solubility observed between the two melt compositions in Chapter 2). For experiments LG46 and LG47, we intentionally ran 'initial condition' experiments: LG46b was pre-equilibrated in the furnace at the same time as LG46a, and LG47b was pre-equilibrated at the same time as LG47a. LG46a and LG47a were then characterized by FTIR (LG47a only) and SIMS (both experiments). These constraints of the initial concentrations of our LG experiments are plotted in Figure 13 as red dashed lines.

A noteworthy feature of our LG data in Figure 13 is that both hydration experiments (LG42 and LG46b) have narrow maxima in water concentration at their edges (i.e., the concentration of water in these experiments measured from edge to center begins at a low value, increases rapidly over a distance of ~200 μm, reaches a maximum, and then decreases gradually towards the center of the spherical sample). A narrow (~200 μm) zone of water depletion is also observed at the edges of the dehydration experiments. Characterization of initial condition experiments LG46a and LG47a (which were intended to be homogeneous, but instead show a decrease in water concentration in their outer ~300 μm) demonstrates that the complex features at

the edges of our LG experiments were likely generated during water loss on quench (Figure 14). For this reason, data points at the edges of our LG experiments have been excluded from our fitting procedure (excluded data points are plotted in red in Figure 13).

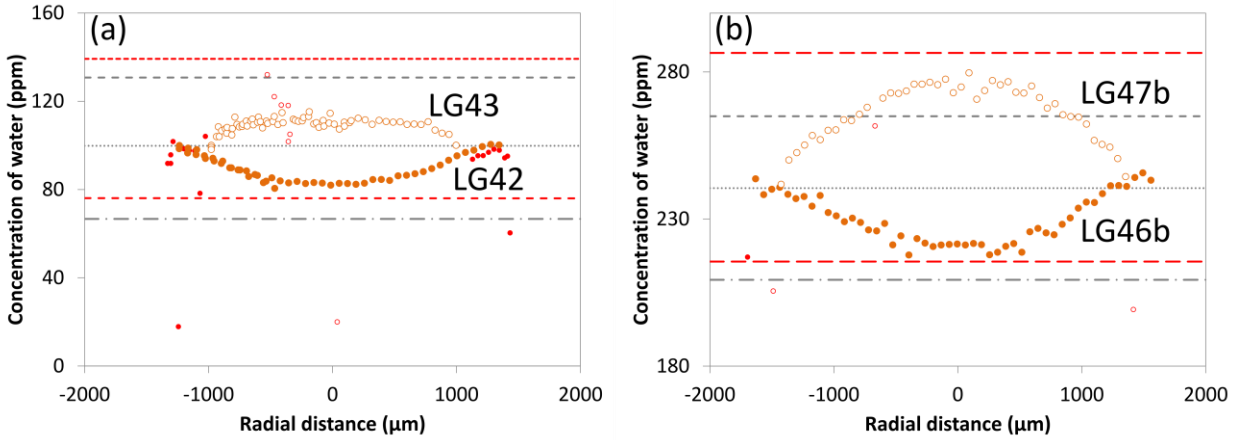

Figure 13 Water concentration gradients measured across small gradient LG experiments by SIMS. Dehydration experiments are plotted as open circles; hydration experiments are plotted as filled circles. Data plotted as orange circles was used for diffusion fitting; data points that were removed prior to fitting are plotted as smaller red circles. Note that the water concentrations of all of the LG experiments are observed to decrease strongly in a narrow (~200 µm) zone at their edges; this effect is thought to be produced during quench (see Figure 14) and the data points in this zone were removed prior to fitting. The expected initial concentration and boundary concentration (based on the results of the solubility experiments described in Chapter 2) are indicated by gray dashed and dotted lines. The initial conditions used for fitting are plotted as red dashed lines. For LG42 and LG43, these initial concentrations were estimated from the concentrations in the interiors of AD28 and AD29 respectively (AD28 and LG42 were pre-equilibrated in the furnace at the same time, as were AD29 and LG43, so these pairs of experiments were exposed to exactly the same pH_2O. We make a small correction to the AD experiment interior concentrations to account for the difference in water solubility of the two melt compositions). LG46b and LG47b were paired with initial condition runs LG46a and LG47a respectively (i.e., two samples were hung in the furnace at the same time during the pre-equilibration stage of these experiments), so the initial concentrations of LG46b and LG47b could be directly measured (LG46a was characterized by SIMS and LG47a was characterized by SIMS and FTIR).

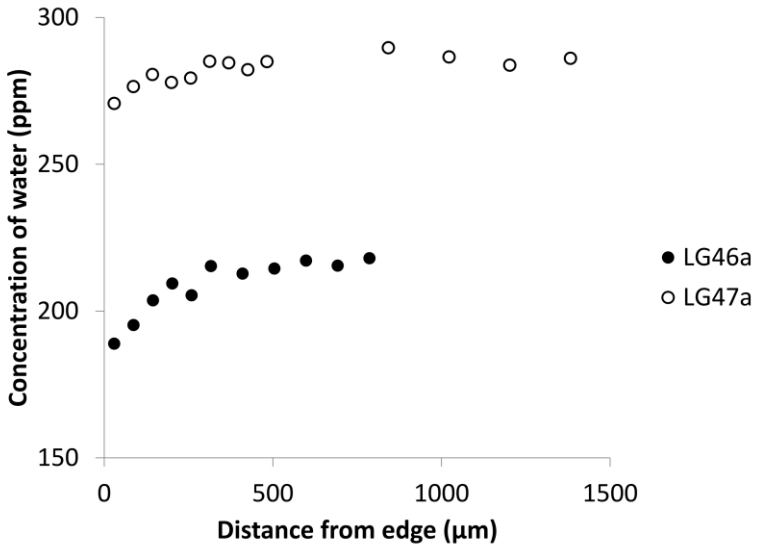

Figure 14 Concentrations of water measured by SIMS in 'initial condition' experiments LG46a and LG47a. These experiments were equilibrated in H_2/CO_2 for ~24 hours before being quenched in air by pulling the sample holder out of the top of the furnace. The outer ~300 µm of LG46a and LG47a show a slight decrease in water concentration which was likely produced during the air quench. This suggests that experiments LG42, LG43, LG46b and LG47b may also have suffered some water loss at their edges during quenching, and this might explain the small maxima in water concentration at the edges of LG42 and LG46b.

Our LG small gradient hydration and dehydration experiments are all well described by equation 6.18 of Crank (1979) for diffusion in a sphere with a uniform initial concentration (C_0), a constant boundary concentration (C_1), and constant D^*_{water} (Figure 15). We used a Monte Carlo approach to estimate the uncertainty in D^*_{water}, and this is described in the caption to Table 3.

As shown in Figure 16 and Table 3, best-fit values of D^*_{water} obtained for our LG experiments are all within error of each other and vary within a factor of 2.2 across our entire experimental range.

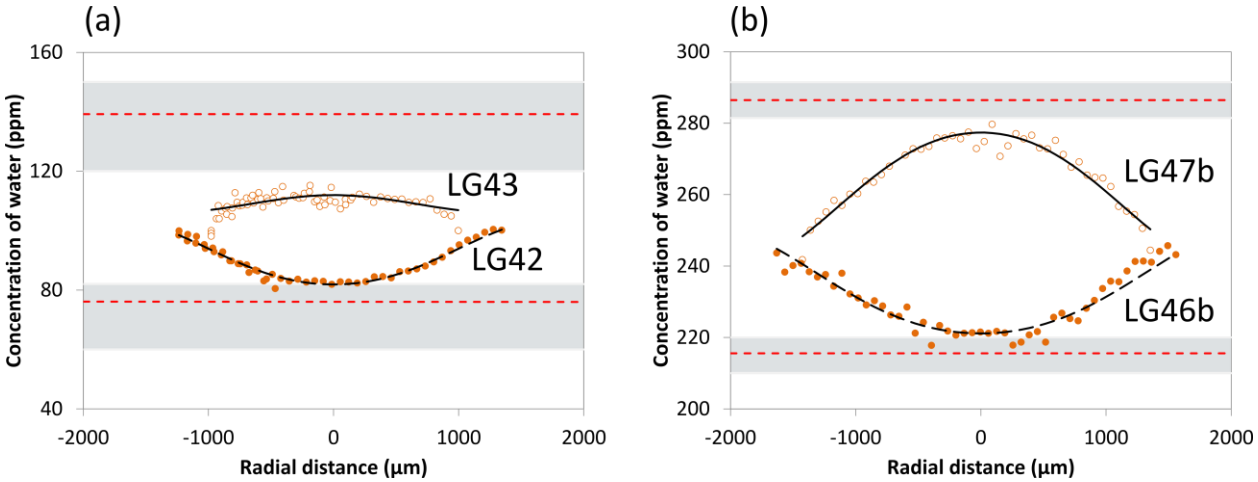

Figure 15 Results of fitting water concentration gradients in LG small gradient hydration and dehydration experiments, assuming D^*_{water} to be constant. The red dashed lines indicate constraints on the initial concentration of each experiment (see caption to Figure 13 for an explanation of these values). Error bounds were placed on D^*_{water} by using a Monte Carlo approach (see caption to Table 3) and by varying the initial concentration within the gray shaded regions (see results in Table 3). The boundary condition was a free parameter in our model. SIMS data are plotted as orange circles; best fits to the data are plotted as solid and dashed black curves.

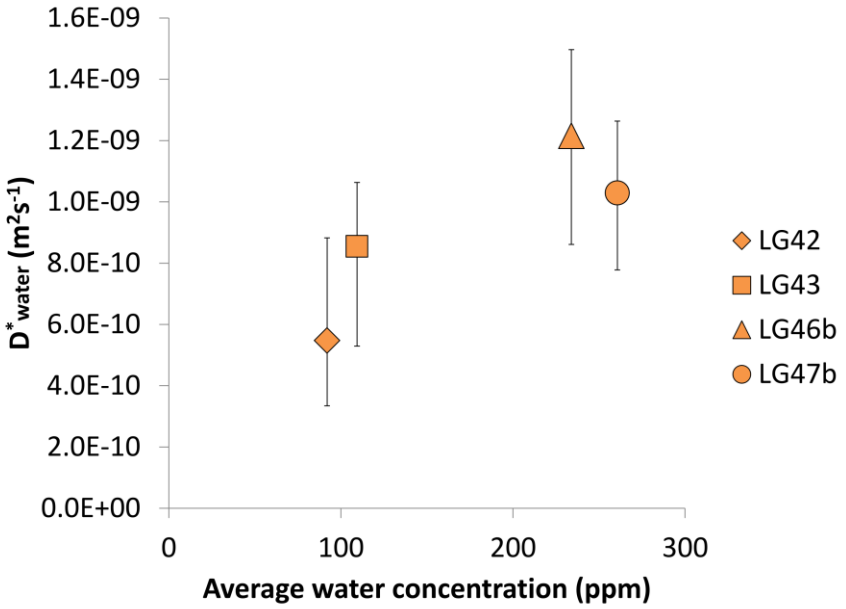

Figure 16 Best fit values of D^*_{water} obtained by fitting our LG small gradient hydration and dehydration experiments. Error bars were calculated using a Monte Carlo technique (described in the caption to Table 3). 'Average water concentration' is the average of the measured water concentration at the edge and in the interior of each sample. All values of D^*_{water} are within error of each other and best fit values vary within a factor of ~2.

Experiment	*ΔIW stage 1*	*ΔIW stage 2*	*pH_2/pH_2O stage 1*	*pH_2/pH_2O stage 2*	*D^*_{water} (m^2s^{-1})*	*D^*_{water} upper bound (m^2s^{-1})*	*D^*_{water} lower bound (m^2s^{-1})*
LG42	4.91	4.07	0.003	0.007	5.47E-10	8.82E-10	3.34E-10
LG43	3.58	4.07	0.013	0.007	8.55E-10	1.06E-09	5.29E-10
LG46b	-2.19	-1.89	9.66	6.86	1.22E-09	1.50E-09	8.61E-10
LG47b	-1.59	-1.89	4.86	6.86	1.03E-09	1.26E-09	7.78E-10

Table 3 Compilation of results of LG small gradient experiments. Water concentration gradients were fit assuming D^*_{water} to be constant and applying equation 6.18 of Crank (1979) for diffusion in a sphere with a uniform initial concentration, C_0, whose surface is maintained at a constant concentration, C_1. C_0 was estimated (for LG42 and LG43) or directly measured (LG46b and LG47b) following techniques described in the caption to Figure 13. C_1 and D^*_{water} were treated as free parameters. The MATLAB function *fminbnd* was used to find values of C_1 and D^*_{water} for which the sum of the absolute values of the residuals between the model and the data was minimized. Upper and lower bounds on D^*_{water} were calculated using a Monte Carlo technique: for each experiment, 1000 new concentration profiles were generated by adding noise to the original data (drawn from a normal distribution with 1σ calculated as the standard deviation of ~6 data points in the uniform interior of the experiment). 1000 different values of C_0 were assigned to the new concentration profiles by a random draw from the gray shaded regions indicated in Figure 15. D^*_{water} and C_1 were fit to each of these 1000 concentration profiles by minimizing the sum of the absolute value of the residuals between the model and the data. The upper and lower bounds on D^*_{water} are the 99th and 1st percentile values of D^*_{water} for these 1000 profiles.

6. Discussion

6.1. Comparison of our results with previous studies of water diffusion in silicate melts

As described in Section 2.1, the majority of previous studies of water diffusion in silicate melts have found that the diffusivity of water is dependent on the concentration of water. Some authors have proposed a proportional relationship between water diffusivity and concentration, while other authors have proposed an exponential relationship. As shown in Figure 3, these models differ significantly in their extrapolations to low water concentrations: the proportional model (which at low water concentrations closely matches the mechanistic speciation model of Zhang et al. (1991b) in which molecular water is assumed to be the only diffusing hydrous species) predicts that the diffusivity of water should tend towards zero as the water concentration tends towards zero, whereas the exponential model predicts that the diffusivity of water should tend towards a constant value at low water concentrations. One of the major aims of this study was to measure directly the diffusivity of water at low water concentrations to remove the large uncertainties associated with extrapolating from data at higher concentrations.

The results of our experiments on AD melt allow us to make the following observations:

1. Water concentration gradients in our experiments are well described by error functions (Figure 6, Figure 10 and Figure 11).

2. Pairs of small-gradient hydration and dehydration experiments can be fit with the same D^*_{water}, and there is no systematic difference observed between best fit values of D^*_{water} for hydration and dehydration experiments, suggesting that D^*_{water} is the same during hydration and dehydration (Figure 11 and Figure 12).

3. Best-fit values of D^*_{water} are approximately constant across the water concentration range of our experiments (~15 – 430 ppm; Figure 12).

Our observations of water diffusion in AD melt demonstrate that D^*_{water} is constant and independent of water concentration under the conditions of our experiments, in good agreement with the predictions of the exponential model of Persikov et al. (2010). At the low end of the concentration range considered in this study, the results of our experiments suggest that D^*_{water} in AD melt is almost two orders of magnitude higher than predicted by the proportional model of Zhang and Stolper (1991) (Figure 17).

Although our experiments are not in agreement with the speciation model for the diffusion of water in which $D_{\mathrm{OH}} = 0$, our best-fit values of D^*_{water} in AD melt are well described by a modified speciation model in which hydroxyl is allowed to diffuse (Ni et al. 2012) (Figure 17). Our observations that D^*_{water} is constant in AD melts containing ~15 – 430 ppm and that hydration and dehydration are symmetric in this concentration range suggest that our experiments may have isolated the diffusion of the hydroxyl component in AD melt. Our LG experiments are also consistent with a modified speciation model in which hydroxyl diffusion dominates at very low water concentrations (Figure 17b).

Other authors have also found experimental evidence for the mobility of hydroxyl in silicate melts: Tomozawa (1985) observe that the diffusion of water in silica glass at low temperatures (192 °C) and low water contents (<0.4 wt%) is well described by a complementary error function, which they argue is consistent with the diffusion of hydroxyl. Behrens (2006) report that D^*_{water} is independent of water concentration in float melt and soda lime silicate melt containing 0.02 to 0.25 wt% water, suggesting that they may have isolated D_{OH} in these sodic

melt compositions. Most recently, Ni et al. (2012) found that the low water concentration regions of their water diffusion experiments in haploandesite were well described by a speciation model in which hydroxyl was allowed to diffuse. However, they were unable to isolate D_{OH} from their experiments and instead they constrained the ratio $D_{\mathrm{OH}}/D_{\mathrm{H_2O_m}}$(which they report to be 0.1 – 0.2 at 1619 – 1842 K as the total water concentration tends towards zero).

Our results support the tentative hypothesis of Ni et al. (2012) that the diffusivity of hydroxyl is significant in highly depolymerized melts at low water concentrations. Furthermore, our experiments hint at a dependence of D_{OH} on melt polymerization (as characterized by NBO/T; Mysen and Richet (2005)): We observe that D^*_{water} in the highly depolymerized LG melt composition (NBO/T = 1.7) is a factor of ~3 higher than D^*_{water} in AD melt (NBO/T = 0.80).

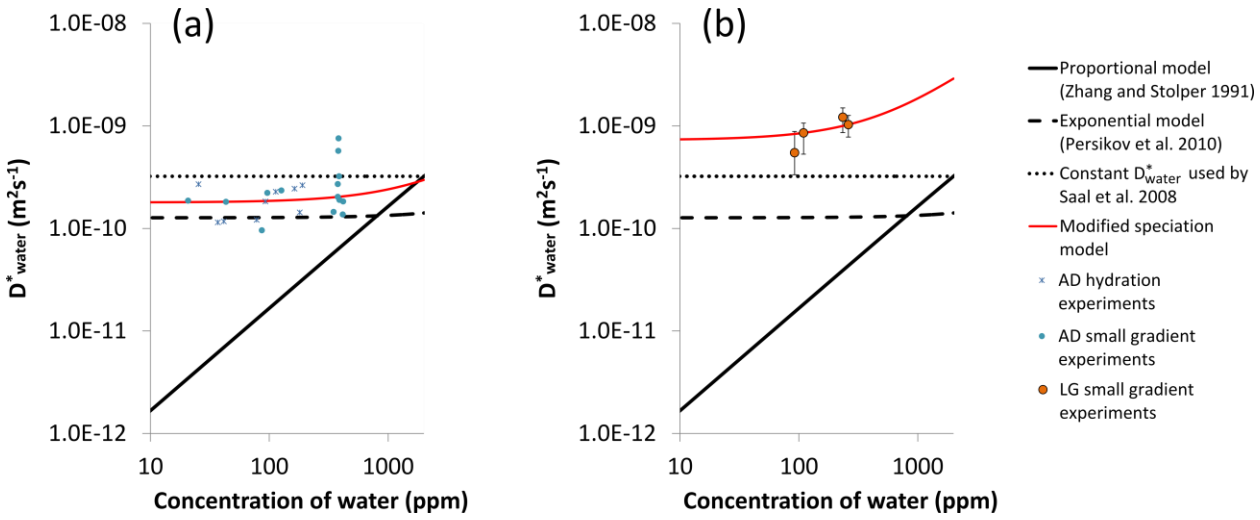

Figure 17 Comparison of our results with extrapolations from higher water concentrations of existing models for water diffusion in basaltic melts (black dashed and solid curves). The value of D^*_{water} (calculated at 1350 °C) used in the lunar glass degassing model of Saal et al. (2008) is shown for reference, and is in good agreement with the results of this study. (a) Results of AD experiments (blue symbols) are well described by the modified speciation model of Ni et al. (2012) in which $D_{\mathrm{OH}} = 1.8 \times 10^{-10}\mathrm{m^2s^{-1}}$ and $D_{\mathrm{H_2O_m}} = 22 \times 10^{-10}\mathrm{m^2s^{-1}}$ (red curve). (b) Results of LG experiments (orange symbols) are well described by the modified speciation model of Ni et al. (2012) in which $D_{\mathrm{OH}} = 7.3 \times 10^{-10}\mathrm{m^2s^{-1}}$ and $D_{\mathrm{H_2O_m}} = 370 \times 10^{-10}\mathrm{m^2s^{-1}}$ (red curve). Note that there is a direct trade-off between $D_{\mathrm{H_2O_m}}$and the equilibrium constant (K_{eq}) for the reaction $H_2O + O = 2OH$: high values of K_{eq} result in higher best-fit values of $D_{\mathrm{H_2O_m}}$ and vice versa. K_{eq} is not known for the melt compositions considered here, but a value of 0.5 has been used in all calculations, following the reasoning of Zhang and Stolper (1991).

6.2. Role of H_2 diffusion in silicate melts at 1 atm under reducing conditions

The reducing conditions thought to be prevalent on the Moon (Sato 1976; Wadhwa 2008) have led some authors to propose that H_2 diffusion could play a significant role in the degassing of the lunar spherules (Zhang and Ni 2010; Zhang 2011). Zhang (2011) estimates that the concentration of H_2 dissolved in a silicate melt could exceed the concentration of molecular water at an oxygen fugacity of IW-2. Although small quantities of dissolved H_2 are difficult to detect directly by SIMS or FTIR, our experiments are well placed to test the hypothesis of Zhang (2011) because they span a range of fO_2 conditions from IW-2.2 to IW+6.7 and a range of pH_2/pH_2O from (nominally) zero to ~10; if H_2 diffusion is significant under reducing conditions, then we might expect to observe a higher diffusivity of 'total H' (i.e., $H_2 + H_2O_m + OH$) in our low fO_2, high pH_2 experiments compared to our high fO_2, low pH_2 experiments.

As shown in Figure 12, we find that D^*_{water} is approximately constant in AD melt over two orders of magnitude in pH_2/pH_2O, so our results do not support a significant role for the diffusion of H_2 in AD melt at high temperatures and low pressures, even under reducing conditions (our most reducing AD experiment was conducted at IW-0.6). Best-fit values of D^*_{water} for our LG experiments are slightly higher under high pH_2/pH_2O conditions (Table 3), however, all values of D^*_{water} for this composition are within error of each other, and the apparent increase in D^*_{water} may also be explained by molecular water diffusion (Figure 17). Zhang and Ni (2010) have shown that the ratio of the contribution of molecular H_2 diffusion to the contribution of H_2O_m diffusion (assuming local chemical equilibrium in the melt between all H-bearing species) should scale linearly with the concentration of H_2 in the melt, which in turn should scale linearly with pH_2. Our LG experiments span three orders of magnitude in pH_2/pH_2O and five orders of magnitude in pH_2, yet the best-fit values of D^*_{water} for these experiments are all within a factor of ~2, so our results do not support a significant role for simple H_2 diffusion, even under conditions as reducing as IW-2.2.

One possibility remains for the involvement of H_2 diffusion in our LG experiments: The higher D^*_{water} observed in LG melts relative to AD melts could reflect a contribution to the transport of H-bearing species by hydrogen-iron redox exchange in the iron-rich LG composition. This complex process, observed by Gaillard et al. (2003b) in obsidian melts and glasses, involves the diffusion of H_2 into the silicate structure followed by reaction of this H_2 with Fe^{3+} to form Fe^{2+} and hydroxyl. Gaillard et al. (2003b) observe (in order of decreasing advancement through the melt or glass) a redox front, a hydroxyl front, and an H_2 front. Interestingly, at low water

concentrations (~0.1 wt% OH) and fH_2 of 0.5 bar, Gaillard et al. (2003b) observe concentration gradients of hydroxyl in their experiments that have maxima near the sample edges, which are similar in shape to those observed in our LG experiments (although, in the case of our experiments these features can be easily explained by water loss during quenching; see Figures 13 and 14). In order to determine whether hydrogen-iron redox exchange is a viable mechanism in our LG experiments, it would be interesting to look for gradients in the oxidation state of iron across our experiments (perhaps by XANES; Cottrell and Kelley (2011)). It would also be useful to conduct further experiments at different temperatures, which would allow us to establish the activation energy of the diffusion of H-bearing species in our LG experiments; this would enable us to distinguish between a process dominated by hydroxyl diffusion versus a process dominated by the diffusion and reaction of molecular hydrogen, because hydroxyl diffusion is known to have a much higher activation energy than molecular hydrogen diffusion (Gaillard et al. 2003b). It should be reiterated, however, that our LG experiments span five orders of magnitude in pH_2, yet our best-fit values of D^*_{water} vary within a factor of two, so it seems unlikely that a mechanism whose rate likely depends on the solubility of H_2 in the melt could be at play.

6.3. Boundary condition during hydration and dehydration

Saal et al. (2008) developed a model for the degassing of the lunar volcanic spherules that assumes diffusive volatile loss from a sphere with concomitant surface evaporation as a boundary condition. The rate of surface evaporation was treated as a free parameter in this model, since experimental constraints on the boundary condition were not available at that time. A key observation reported by Saal et al. (2008) is that the concentration gradient of water in the lunar glass bead that they characterized projects to a water concentration of ~10 ppm at the edge of the glass bead. This non-zero concentration implies either kinetic inhibition of water evaporation into an atmosphere devoid of H-bearing species, or it suggests degassing of water into a vapor cloud with a low but non-zero pH_2O (pH_2O = 0.0002 bar; calculated using our solubility results presented in Chapter 2).

The symmetry of our paired hydration and dehydration experiments in AD and LG melts and the fact that the edge concentrations of both experiments in our hydration and dehydration pairs are the same (Figure 11 and Figure 13) suggests an equilibrium boundary condition for our experiments in H_2/CO_2 gas mixtures. However, our AD dehydration experiments into nominally H-free atmospheres leave scope for possible kinetic inhibition of water loss from the melt-vapor interface: AD37 and AD38 were dehydrated into CO_2 and CO/CO_2 gases respectively, and the

concentrations of water at the melt-vapor interface of these experiments were ~15 ppm for AD37 and ~40 ppm for AD38 (we note that the interiors of our AD hydration experiments—which were equilibrated with CO/CO_2 gas mixtures—contain ~15 ppm water, suggesting that this value might be indicative of impurities in our CO and/or CO_2 gases). Additionally, the resultant water concentration gradients across these experiments were not well described by a constant D^*_{water}, although the complexity of the shapes of the water concentration gradients in these experiments may be due to melt advection (as discussed in Section 4.2). The complexities observed in our dehydration experiments into nominally H-free gas mixtures suggest that further dehydration experiments into gases such as argon, nitrogen, or different CO/CO_2 mixtures could be an interesting avenue for future research.

6.4. Implications for degassing of lunar spherules

The primary motivation for this study was to provide a direct measurement of the diffusivity of water in lunar basalt under conditions thought to be relevant to the Moon (i.e., at low water contents and under reducing conditions). It was initially thought that the assumption made by the lunar volcanic glass degassing model of Saal et al. (2008) that D^*_{water} is not dependent on the concentration of water at low water concentrations might lead to an overestimation of the initial water concentration in the lunar glasses. However, our results (Figure 17) show that this assumption was correct. Moreover, the value of D^*_{water} chosen by Saal et al. (2008) to model the degassing of the lunar volcanic glasses is within a factor of three of our measured values in Apollo 15 yellow glass at 1350 °C. The substitution in the Saal et al. (2008) degassing model of our measured value of D^*_{water} in LG melt will increase the predicted starting concentration of water in the lunar volcanic glasses. Collaboration with Alberto Saal is currently underway to estimate the initial water concentrations of the lunar volcanic glasses using our new value of D^*_{water} in LG melt.

7. Conclusions

1. We have conducted water diffusion experiments in an iron-free basaltic analogue melt (AD) and in Apollo 15 "yellow glass" (LG) at 1 atm and 1350 °C over a range of fO_2 conditions from IW-2.2 to IW+6.7 and over a range of pH_2/pH_2O from (nominally) zero to ~10. The water concentrations measured in our quenched experimental glasses vary from a few ppm to ~430 ppm.

2. We find that the concentration gradients in our experiments are well described by models in which D^*_{water} is constant.
3. In AD melts containing ~20 – 420 ppm water, D^*_{water} is found to be independent of water concentration. The relationship between D^*_{water} and concentration for our AD experiments is well described by a modified speciation model in which hydroxyl is allowed to diffuse, suggesting that we have resolved the diffusivity of hydroxyl in a basaltic melt for the first time.
4. Best-fit values of D^*_{water} for our LG experiments vary within a factor of ~2 over a range of $p\mathrm{H_2}/p\mathrm{H_2O}$ from 0.007 to 9.7, a range of $f\mathrm{O_2}$ from IW-2.2 to IW+4.9, and a water concentration range from ~80 ppm to ~280 ppm. The relative insensitivity of our best-fit values of D^*_{water} to variations in $p\mathrm{H_2}$ suggests that $\mathrm{H_2}$ diffusion was not significant during degassing of the lunar glasses of Saal et al. (2008).
5. Our best-fit values of D^*_{water} in AD and LG melts hint at a positive correlation between D_{OH} and melt depolymerization.
6. D^*_{water} during dehydration and hydration in $\mathrm{H_2}/\mathrm{CO_2}$ gas mixtures are approximately the same in LG and AD melts, which supports an equilibrium boundary condition for these experiments. However, dehydration experiments into $\mathrm{CO_2}$ and $\mathrm{CO}/\mathrm{CO_2}$ gas mixtures leave some scope for the importance of kinetics during dehydration into H-free environments.
7. The value of D^*_{water} chosen by Saal et al. (2008) for modeling the diffusive degassing of the lunar volcanic glasses is within a factor of three of our measured value in LG melt at 1350 °C. Further work is currently underway to establish the implications of our results for estimates of the initial water concentration in these lunar volcanic deposits.

8. Acknowledgements

Newcombe gratefully acknowledges financial support from a NASA Earth and Space Sciences Fellowship (PLANET14R-0040).

9. References

Behrens H Water diffusion in silicate glasses and melts. In: Advances in Science and Technology, 2006. Trans Tech Publ, pp 79-88

Behrens H, Zhang Y (2009) H2O diffusion in peralkaline to peraluminous rhyolitic melts. Contributions to Mineralogy and Petrology 157 (6):765-780. doi:10.1007/s00410-008-0363-4

Behrens H, Zhang Y, Leschik M, Wiedenbeck M, Heide G, Frischat GH (2007) Molecular H2O as carrier for oxygen diffusion in hydrous silicate melts. Earth and Planetary Science Letters 254 (1–2):69-76. doi:http://dx.doi.org/10.1016/j.epsl.2006.11.021

Behrens H, Zhang Y, Xu Z (2004) H2O diffusion in dacitic and andesitic melts. Geochimica et Cosmochimica Acta 68 (24):5139-5150. doi:http://dx.doi.org/10.1016/j.gca.2004.07.008

Blower JD, Mader HM, Wilson SDR (2001) Coupling of viscous and diffusive controls on bubble growth during explosive volcanic eruptions. Earth and Planetary Science Letters 193 (1–2):47-56. doi:http://dx.doi.org/10.1016/S0012-821X(01)00488-5

Borisov A, Jones JH (1999) An evaluation of Re, as an alternative to Pt, for the 1 bar loop technique: An experimental study at 140O C. American Mineralogist 84:1528-1534

Bottinga Y, Javoy M (1990) MORB degassing: Bubble growth and ascent. Chemical Geology 81 (4):255-270. doi:http://dx.doi.org/10.1016/0009-2541(90)90050-H

Cameron AGW, Ward WR (1976) The Origin of The Moon. Abstracts of the Lunar and Planetary Science Conference 7

Chekhmir A, Epel'baum M, Simakin A (1988) Water transport in magmas. Geochem Int 26:125-127

Cottrell E, Kelley KA (2011) The oxidation state of Fe in MORB glasses and the oxygen fugacity of the upper mantle. Earth and Planetary Science Letters 305 (3):270-282

Crank J (1979) The mathematics of diffusion. Oxford university press,

Delaney JR, Karsten JL (1981) Ion microprobe studies of water in silicate melts. Concentration-dependent water diffusion in obsidian. Earth and Planetary Science Letters 52 (1):191-202. doi:http://dx.doi.org/10.1016/0012-821X(81)90220-X

Delano JW (1986) Pristine Lunar Glasses: Criteria, Data, and Implications. J Geophys Res 91 (B4):D201-D213. doi:10.1029/JB091iB04p0D201

Dixon JE, Stolper EM, Holloway JR (1995) An Experimental Study of Water and Carbon Dioxide Solubilities in Mid-Ocean Ridge Basaltic Liquids. Part I: Calibration and Solubility Models. Journal of Petrology 36 (6):1607-1631

Doremus RH (1973) Glass science. Wiley,

Gaillard F, Pichavant M, Mackwell S, Champallier R, Scaillet B, McCammon C (2003a) Chemical transfer during redox exchanges between H2 and Fe-bearing silicate melts. American Mineralogist, vol 88. doi:10.2138/am-2003-2-308

Gaillard F, Scaillet B, Pichavant M (2002) Kinetics of iron oxidation-reduction in hydrous silicic melts. American Mineralogist, vol 87. doi:10.2138/am-2002-0704

Gaillard F, Schmidt B, Mackwell S, McCammon C (2003b) Rate of hydrogen–iron redox exchange in silicate melts and glasses. Geochimica et Cosmochimica Acta 67 (13):2427-2441. doi:http://dx.doi.org/10.1016/S0016-7037(02)01407-2

Hartmann WK, Davis DR (1975) Satellite-sized planetesimals and lunar origin. Icarus 24 (4):504-515. doi:http://dx.doi.org/10.1016/0019-1035(75)90070-6

Hauri EH, Weinreich T, Saal AE, Rutherford MC, Van Orman JA (2011) High Pre-Eruptive Water Contents Preserved in Lunar Melt Inclusions. Science 333 (6039):213-215. doi:10.1126/science.1204626

Hirschmann MM, Withers AC, Ardia P, Foley NT (2012) Solubility of molecular hydrogen in silicate melts and consequences for volatile evolution of terrestrial planets. Earth and Planetary Science Letters 345–348:38-48. doi:http://dx.doi.org/10.1016/j.epsl.2012.06.031

Karsten JL, Holloway JR, Delaney JR (1982) Ion microprobe studies of water in silicate melts: Temperature-dependent water diffusion in obsidian. Earth and Planetary Science Letters 59 (2):420-428. doi:http://dx.doi.org/10.1016/0012-821X(82)90143-1

Liu Y, Zhang Y, Behrens H (2004) H2O diffusion in dacitic melts. Chemical Geology 209 (3–4):327-340. doi:http://dx.doi.org/10.1016/j.chemgeo.2004.06.019

Mysen B, Richet P (2005) Silicate glasses and melts: properties and structure, vol 10. Elsevier,

Newman S, Lowenstern JB (2002) VolatileCalc: a silicate melt–H2O–CO2 solution model written in Visual Basic for excel. Computers & Geosciences 28 (5):597-604. doi:http://dx.doi.org/10.1016/S0098-3004(01)00081-4

Newman S, Stolper EM, Epstein S (1986) Measurement of water in rhyolitic glasses--calibration of an infrared spectroscopic technique. American Mineralogist 71 (11):1527-1541

Newsom HE, Taylor SR (1989) Geochemical implications of the formation of the Moon by a single giant impact. Nature 338 (6210):29-34

Ni H, Behrens H, Zhang Y (2009a) Water diffusion in dacitic melt. Geochimica et Cosmochimica Acta 73 (12):3642-3655. doi:http://dx.doi.org/10.1016/j.gca.2009.03.029

Ni H, Liu Y, Wang L, Zhang Y (2009b) Water speciation and diffusion in haploandesitic melts at 743–873 K and 100 MPa. Geochimica et Cosmochimica Acta 73 (12):3630-3641. doi:http://dx.doi.org/10.1016/j.gca.2009.03.024

Ni H, Xu Z, Zhang Y (2012) Hydroxyl and Molecular H_2O Diffusivity in a Haploandesitic Melt. Geochimica et Cosmochimica Acta

Ni H, Zhang Y (2008) H2O diffusion models in rhyolitic melt with new high pressure data. Chemical Geology 250 (1–4):68-78. doi:http://dx.doi.org/10.1016/j.chemgeo.2008.02.011

Nowak M, Behrens H (1997) An experimental investigation on diffusion of water in haplogranitic melts. Contributions to Mineralogy and Petrology 126 (4):365-376. doi:10.1007/s004100050256

Okumura S, Nakashima S (2004) Water diffusivity in rhyolitic glasses as determined by in situ IR spectroscopy. Phys Chem Minerals 31 (3):183-189. doi:10.1007/s00269-004-0383-1

Okumura S, Nakashima S (2006) Water diffusion in basaltic to dacitic glasses. Chemical Geology 227 (1–2):70-82. doi:http://dx.doi.org/10.1016/j.chemgeo.2005.09.009

Persikov E, Bukhtiyarov P, Newman S (2012) Experimental study of the effect of concentration of dissolved water on diffusion of H2O in haplodacite melts at high pressures. Vestn Otd nauk Zemle 4

Persikov ES, Bukhtiyarov PG, Nekrasov AN, Bondarenko GV (2014) Concentration dependence of water diffusion in obsidian and dacitic melts at high-pressures. Geochem Int 52 (5):365-371. doi:10.1134/s0016702914050085

Persikov ES, Newman S, Bukhtiyarov PG, Nekrasov AN, Stolper EM (2010) Experimental study of water diffusion in haplobasaltic and haploandesitic melts. Chemical Geology 276 (3–4):241-256. doi:10.1016/j.chemgeo.2010.06.010

Proussevitch AA, Sahagian DL, Kutolin VA (1993) Stability of foams in silicate melts. Journal of Volcanology and Geothermal Research 59 (1):161-178. doi:http://dx.doi.org/10.1016/0377-0273(93)90084-5

Saal AE, Hauri EH, Cascio ML, Van Orman JA, Rutherford MC, Cooper RF (2008) Volatile content of lunar volcanic glasses and the presence of water in the Moon's interior. Nature 454 (7201):192-195. doi:http://www.nature.com/nature/journal/v454/n7201/suppinfo/nature07047_S1.html

Saal AE, Hauri EH, Langmuir CH, Perfit MR (2002) Vapour undersaturation in primitive mid-ocean-ridge basalt and the volatile content of Earth's upper mantle. Nature 419 (6906):451-455. doi:http://www.nature.com/nature/journal/v419/n6906/suppinfo/nature01073_S1.html

Saal AE, Hauri EH, Van Orman JA, Rutherford MJ (2013) Hydrogen Isotopes in Lunar Volcanic Glasses and Melt Inclusions Reveal a Carbonaceous Chondrite Heritage. Science 340 (6138):1317-1320. doi:10.1126/science.1235142

Sato M Oxygen fugacity and other thermochemical parameters of Apollo 17 high-Ti basalts and their implications on the reduction mechanism. In: Lunar and Planetary Science Conference Proceedings, 1976. pp 1323-1344

Shaw HR (1974) Diffusion of H2O in granitic liquids: Part I. Experimental data; Part II. Mass transfer in magma chambers. In: Geochemical transport and kinetics, vol 634. Carnegie Inst. Washington Publ, pp 139-170

Silver L, Stolper E (1989) Water in albitic glasses. Journal of Petrology 30 (3):667-709

Sparks RSJ (1978) The dynamics of bubble formation and growth in magmas: A review and analysis. Journal of Volcanology and Geothermal Research 3 (1):1-37. doi:http://dx.doi.org/10.1016/0377-0273(78)90002-1

Stolper E (1982a) The speciation of water in silicate melts. Geochimica et Cosmochimica Acta 46 (12):2609-2620

Stolper E (1982b) Water in silicate glasses: An infrared spectroscopic study. Contributions to Mineralogy and Petrology 81 (1):1-17. doi:10.1007/bf00371154

Tomozawa M (1985) Concentration Dependence of the Diffusion Coefficient of Water in SiO2 Glass. Journal of the American Ceramic Society 68 (9):C-251-C-252. doi:10.1111/j.1151-2916.1985.tb15804.x

Wadhwa M (2008) Redox Conditions on Small Bodies, the Moon and Mars. Reviews in Mineralogy and Geochemistry 68 (1):493-510. doi:10.2138/rmg.2008.68.17

Wang H, Xu Z, Behrens H, Zhang Y (2009) Water diffusion in Mount Changbai peralkaline rhyolitic melt. Contributions to Mineralogy and Petrology 158 (4):471-484. doi:10.1007/s00410-009-0392-7

Wasserburg GJ (1988) Diffusion of Water in Silicate Melts. The Journal of Geology 96 (3):363-367

Wetzel DT, Hauri EH, Saal AE, Rutherford MJ (2015) Carbon content and degassing history of the lunar volcanic glasses. Nature Geosci advance online publication. doi:10.1038/ngeo2511

http://www.nature.com/ngeo/journal/vaop/ncurrent/abs/ngeo2511.html#supplementary-information

Zhang Y Water" in Lunar Basalts: The Role of Molecular Hydrogen (H2), Especially in the Diffusion of the H Component. In: 42nd Lunar and Planetary Science Conference, held March 7--11, 2011 at The Woodlands, Texas. LPI Contribution, 2011. vol 1608.

Zhang Y, Behrens H (2000) H2O diffusion in rhyolitic melts and glasses. Chemical Geology 169 (1–2):243-262. doi:http://dx.doi.org/10.1016/S0009-2541(99)00231-4

Zhang Y, Ni H (2010) Diffusion of H, C, and O Components in Silicate Melts. Reviews in Mineralogy and Geochemistry 72 (1):171-225. doi:10.2138/rmg.2010.72.5

Zhang Y, Stolper EM (1991) Water diffusion in a basaltic melt. Nature 351 (6324):306-309

Zhang Y, Stolper EM, Wasserburg GJ (1991a) Diffusion of a multi-species component and its role in oxygen and water transport in silicates. Earth and Planetary Science Letters 103 (1–4):228-240. doi:http://dx.doi.org/10.1016/0012-821X(91)90163-C

Zhang Y, Stolper EM, Wasserburg GJ (1991b) Diffusion of water in rhyolitic glasses. Geochimica et Cosmochimica Acta 55 (2):441-456. doi:10.1016/0016-7037(91)90003-n

Zhang Y, Xu Z, Zhu M, Wang H (2007) Silicate melt properties and volcanic eruptions. Reviews of Geophysics 45 (4):n/a-n/a. doi:10.1029/2006rg000216

C h a p t e r 4

CHEMICAL ZONATION IN OLIVINE-HOSTED MELT INCLUSIONS

M.E. Newcombe[a,], A. Fabbrizio[a, b], Youxue Zhang[c], C. Ma[a], M. Le Voyer[a, d], Y. Guan[a], J. Eiler[a], A. Saal[e], E.M. Stolper[a]

[a] Division of Geological and Planetary Sciences, California Institute of Technology, Pasadena, CA 91125, USA

[b] Laboratoire Magmas et Volcans, CNRS UMR 6524, Université Blaise-Pascal, OPGC-IRD, 5 Rue Kessler, 63038 Clermont-Ferrand Cedex, France

[c] Department of Earth and Environmental Sciences, University of Michigan, Ann Arbor, MI 48109, USA

[d] Department of Terrestrial Magnetism, Carnegie Institution of Washington, Washington, DC 20015, USA

[e] Department of Geological Sciences, Brown University, Providence, RI 02912, USA

*Adapted from Newcombe, M. E., et al. "Chemical zonation in olivine-hosted melt inclusions."*Contributions to Mineralogy and Petrology* 168.1 (2014): 1-26. *doi:10.1007/s00410-014-1030-6*

1. Abstract

Significant zonation in major, minor, trace, and volatile elements has been documented in naturally glassy olivine-hosted melt inclusions from the Siqueiros Fracture Zone and the Galapagos Islands. Components with a higher concentration in the host olivine than in the melt (MgO, FeO, Cr_2O_3, and MnO) are depleted at the edges of the zoned melt inclusions relative to their centers, whereas except for CaO, H_2O, and F, components with a lower concentration in the host olivine than in the melt (Al_2O_3, SiO_2, Na_2O, K_2O, TiO_2, S, and Cl) are enriched near the melt inclusion edges. This zonation is due to formation of an olivine-depleted boundary layer in the adjacent melt in response to cooling and crystallization of olivine on the walls of the melt inclusions concurrent with diffusive propagation of the boundary layer toward the inclusion center.

Concentration profiles of some components in the melt inclusions exhibit multicomponent diffusion effects such as uphill diffusion (CaO, FeO) or slowing of the diffusion of typically rapidly diffusing components (Na_2O, K_2O) by coupling to slow diffusing components such as SiO_2 and Al_2O_3. Concentrations of H_2O and F decrease towards the edges of some of the Siqueiros melt inclusions, suggesting either that these components have been lost from the inclusions into the host olivine late in their cooling histories and/or that these components are exhibiting multicomponent diffusion effects.

A model has been developed of the time-dependent evolution of MgO concentration profiles in melt inclusions due to simultaneous depletion of MgO at the inclusion walls due to olivine growth and diffusion of MgO in the melt inclusions in response to this depletion. Observed concentration profiles were fit to this model to constrain their thermal histories. Cooling rates determined by a single-stage linear cooling model are 150–13,000 °C hr^{-1} from the liquidus down to ~1000 °C, consistent with previously determined cooling rates for basaltic glasses; compositional trends with melt inclusion size observed in the Siqueiros melt inclusions are described well by this simple single-stage linear cooling model. Despite the overall success of the modeling of MgO concentrations profiles using a single-stage cooling history, MgO concentration profiles in some melt inclusions are better fit by a two-stage cooling history with a slower-cooling first stage followed by a faster-cooling second stage; the inferred total duration of cooling from the liquidus down to ~1000 °C is 40 s to just over one hour.

Based on our observations and models, compositions of zoned melt inclusions (even if measured at the centers of the inclusions) will typically have been diffusively fractionated relative to the initially trapped melt; for such inclusions, the initial composition cannot be simply reconstructed based on olivine-addition calculations, so caution should be exercised in application of such reconstructions to correct for post-entrapment crystallization of olivine on inclusion walls. Off-center analyses of a melt inclusion can also give results significantly fractionated relative to simple olivine crystallization.

All melt inclusions from the Siqueiros and Galapagos sample suites exhibit zoning profiles, and this feature may be nearly universal in glassy, olivine-hosted inclusions. If so, zoning profiles in melt inclusions could be widely useful to constrain late-stage syneruptive processes and as natural diffusion experiments.

Keywords: Melt inclusions, chemical zonation, diffusion, geospeedometry

2. Introduction

It is often implicitly assumed that glassy melt inclusions in phenocrysts are homogeneous and thus that analyses from near the center of an inclusion are representative of the inclusion composition. Likewise, inclusion homogeneity is usually assumed in models of melt inclusion formation and evolution (Qin et al. 1992; Danyushevsky et al. 2000; Cottrell et al. 2002; Danyushevsky et al. 2002a; Danyushevsky et al. 2002b; Gaetani and Watson 2002; Lloyd et al. 2012; Chen et al. 2013). *A priori*, this would seem to be a reasonable assumption, since even though crystallization of the host mineral on the walls of the inclusion and reequilibration of the melt inclusion with the host mineral are known to affect inclusion composition (Danyushevsky et al. 2000; Danyushevsky et al. 2002a; Danyushevsky et al. 2002b; Gaetani and Watson 2002), the time scales for diffusive homogenization of melt inclusions $\lesssim 10^2$ μm in diameter are expected to be $\lesssim 10^2$ min at magmatic temperatures based on known diffusivities in silicate melts — orders of magnitude smaller than residence times of phenocrysts in magma chambers and than the time scales for significant diffusion of most elements into the host mineral (Qin et al. 1992; Cottrell et al. 2002; Danyushevsky et al. 2002b; Gaetani and Watson 2002; Morgan et al. 2004; Costa and Dungan 2005). However, there have been reports of concentration profiles away from the host-glass interface in glassy inclusions from a variety of magmatic settings (Anderson 1974; Danyushevsky et al. 2002b; Mercier 2009; Colin et al. 2012), indicating that there are processes

acting on melt inclusions on time scales sufficient for measurable concentration profiles to have been generated, but insufficient for the profiles to have been erased by diffusion.

In this chapter, we examine in detail concentration profiles in glassy, olivine-hosted melt inclusions in submarine lavas from the Siqueiros Fracture Zone and in subaerial and submarine lavas from the Galapagos Islands. We demonstrate that significant zonation in melt inclusions is the norm rather than the exception; that the cores of melt inclusions can be significantly influenced by simultaneous growth of the host mineral on inclusion walls and multicomponent diffusion in the melt inclusion; and that aspects of the resultant concentration profiles can be used to constrain the last stages of the thermal histories of their host magmas.

3. Samples

Thirty-five glassy, olivine-hosted melt inclusions were characterized for this study: 26 from the Siqueiros Fracture Zone and nine from the Galapagos Islands. All inclusions were naturally glassy (i.e., no homogenization procedures were applied). Sample names and locations are given in Table S1 of Appendix I, and backscattered electron images of the inclusions are shown in Figure 1 and in Online Resource 2. The inclusions from the Siqueiros Fracture Zone were collected in May-June 1991 by dredging (sample names containing D20 in Table S1 of Appendix I) and by the submersible ‘Alvin’ (sample names containing 2384). The samples from this study are from the glassy rinds of pillow basalts that were collected from depths of >3000 m (Perfit et al. 1996; Saal et al. 2002). The locations of the samples and their petrography and compositions are described in detail by Perfit et al. (1996). A subset of the Siqueiros inclusions were analyzed previously by Saal et al. (2002); these inclusions are listed in Table S1 (Appendix I). The remaining Siqueiros inclusions were prepared from new olivine separates. Two of the melt inclusions we studied from the Galapagos Islands are from Fernandina Island, and seven are from Santiago Island. The Fernandina inclusions were sampled from a submarine flank of the island at a depth of ~2900 m during dredge AHA25 of the AHA-Nemo2 cruise in 2000 (Geist et al. 2006), and the Santiago inclusions were sampled from a glassy subaerial hornito (Koleszar et al. 2009). All nine Galapagos inclusions have been analyzed previously by Koleszar et al. (2009).

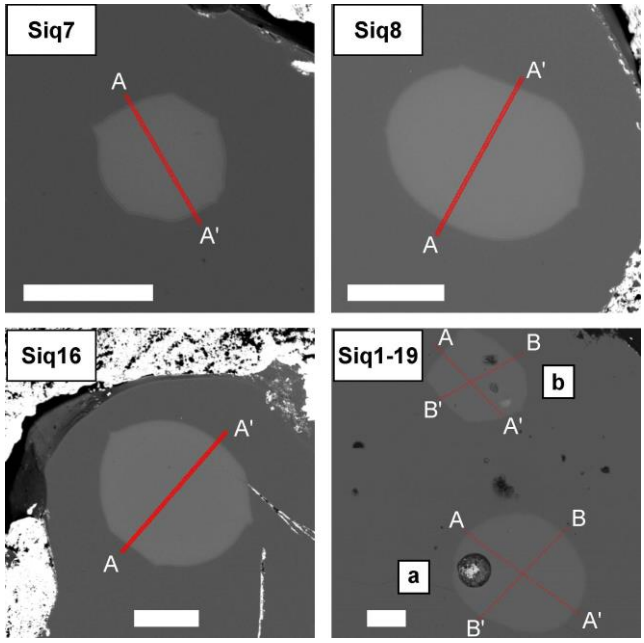

Figure 1 Backscattered electron images of a subset of the Siqueiros melt inclusions used in this study. Further images are provided in Online Resource 2. White bars are 100 μm in length. Electron microprobe analyses are marked in red. The nanoSIMS profile measured across Siq8 closely followed the marked path of the electron microprobe traverse.

The Siqueiros Fracture Zone is on the northern East Pacific Rise (EPR); its lavas span a broad range of basaltic compositions and include some of the most primitive samples known from the EPR (Perfit et al. 1996). The olivines we studied are from lavas ranging in composition from magnesian basalts to picrites that are thought to have been affected by variable amounts of olivine accumulation (Perfit et al. 1996). These lavas are more depleted in incompatible trace elements than normal mid-ocean ridge basalt (N-MORB) observed elsewhere on the EPR (Perfit et al. 1996). The Siqueiros melt inclusions have relatively primitive compositions with MgO contents up to 9.5 wt. % (and up to 12.8 wt. % after correction for post-entrapment olivine crystallization (Saal et al. 2002; Danyushevsky et al. 2003)). Following correction for post-entrapment olivine crystallization, most of the Siqueiros inclusions are thought to represent nearly primary mantle melts (Saal et al. 2002). However, the compositions of some Siqueiros inclusions are relatively enriched in Al_2O_3, CaO, and Sr, and relatively depleted in Na_2O, TiO_2, and incompatible elements; these are thought to have been affected by variable amounts of assimilation of gabbroic material (Danyushevsky et al. 2003; Danyushevsky et al. 2004). The Siqueiros inclusions are

contained in Fo_{89-91} olivine phenocrysts (Saal et al. 2002), similar to mantle olivine and hence consistent with crystallization from nearly primary mantle melts.

The olivines we studied from Fernandina are from the 'normal series' of submarine tholeiitic basaltic lavas described by Geist et al. (2006). These magmas are thought to have fractionated in a magma chamber at a depth of ~2 km before being injected laterally, entraining variable amounts of olivine, clinopyroxene, and plagioclase from a crystal mush zone less than one year before eruption. The Fernandina melt inclusions have higher Mg#s than associated matrix glasses, and the matrix glass compositions can be largely accounted for by fractionation of plagioclase, olivine, and minor clinopyroxene from the melt inclusion compositions (Geist et al. 2006; Koleszar et al. 2009). The melt inclusions are contained in $Fo_{81–87}$ olivine phenocrysts (Koleszar et al. 2009). There is a positive correlation between the forsterite content of the host olivines and the variability of incompatible trace element concentration ratios in the trapped melts (as represented by the La/Yb ratio); e.g. more primitive olivines with $Fo_{86–87}$ contain inclusions with La/Yb ratios ranging from 0.91–7.0 (chondritic La/Yb is 1.5 (McDonough and Sun 1995)), whereas more evolved olivines with $Fo_{<82}$ contain melts with La/Yb ratios ranging only from 5.3–6.1 (approximately the same as the average concentration of Fernandina lavas (Koleszar et al. 2009)). This trend is suggestive of concurrent crystallization and mixing of incompatible trace-element-enriched and -depleted melts (e.g., Maclennan et al. 2003). Of the two Fernandina melt inclusions we studied, one has a low La/Yb ratio of 0.91 and is hosted in a Fo_{87} olivine (Gal-AHA2-24) and one has a relatively high La/Yb ratio of 5.5 and is hosted in a Fo_{83} olivine (Gal-AHA2-27) (Koleszar et al. 2009).

The host lavas of the Santiago melt inclusions are typical of N-MORB (White et al. 1993; Koleszar et al. 2009). The melt inclusions have variable major element compositions at similar Mg# that cannot be easily reproduced by fractional crystallization of any combination of olivine, clinopyroxene, and/or plagioclase (Koleszar et al. 2009). Saal et al. (2007) proposed that this variability can be explained by assimilation of plagioclase during interaction of the melt with lithospheric gabbros. The melt inclusions are mostly contained in $Fo_{86–87}$ olivine phenocrysts; there are two exceptions with lower forsterite contents of Fo_{82} and Fo_{85} (Koleszar et al. 2009). Unlike the Fernandina inclusions, the Santiago inclusions are relatively uniform in their incompatible trace element concentrations, and their incompatible trace element concentrations are similar to their associated matrix glasses.

4. Analytical techniques

Inclusion-bearing olivines previously studied in Saal et al. (2002) (21 inclusions; indicated in Table S1) were mounted in epoxy. The remaining inclusion-bearing olivines (five from the Siqueiros Fracture Zone, two from Fernandina, Galapagos, and nine from Santiago, Galapagos) were polished (using alumina lapping films and 0.25 μm diamond paste) and pressed into indium (e.g., Hauri et al. 2002; Koleszar et al. 2009). Care was taken to expose the maximum possible surface area of the melt inclusions during polishing.

Concentration profiles of major, minor, and trace elements were measured across the glass inclusions in WDS mode using the JEOL JXA-8200 electron microprobe at Caltech. For most of the inclusions, concentrations of SiO_2, TiO_2, Al_2O_3, Cr_2O_3, FeO, MnO, MgO, CaO, NiO, Na_2O, K_2O, and P_2O_5 were measured in the glass with an accelerating voltage of 15 kV, a beam current of 10 nA, and counting times of 20 s on-peak and 10 s on high and low backgrounds. In the early phases of the study, the beam diameter was set to 5 μm, and automated line profiles were constructed across the melt inclusions with analyses spaced at 10 μm intervals (we will refer to this distance as the 'step size'). In order to improve spatial resolution, later line profiles were measured with a focused beam (with a nominal diameter of ~150 nm) and a step size of 1–2 μm. The following standards were used for the electron microprobe analyses: Shankland forsterite (Mg); VG2 basalt glass (SiO_2); synthetic TiO_2 (TiO_2); synthetic anorthite (Al_2O_3, CaO); synthetic Cr_2O_3 (Cr_2O_3); synthetic fayalite (FeO); synthetic tephroite (MnO); Amelia albite (Na_2O); synthetic Ni olivine (NiO); Durango apatite (P_2O_5); and Asbestos microcline (K_2O). Data were reduced using a modified ZAF procedure (CITIZAF; Armstrong (1988)). Secondary standards (BHVO-2g, BIR-1g, and/or VG2 basaltic glasses) were analyzed 5–10 times at the beginning and end of each traverse, under the same analytical conditions used to analyze the melt inclusions. Although no corrections have been applied to our concentration data based on analyses of secondary standards, the percentage deviation from the accepted values for these standards (calculated as 100*[1– [mean measured value/accepted value]]) is within 1.0% for SiO_2, 1.6% for TiO_2, 2.5% for Al_2O_3, 1.3% for FeO, 5.8% for MgO, 2.4% for CaO, and 4.7% for Na_2O. Our analyses of the secondary standards are given in Online Resource 2. 105 replicate analyses of BHVO during an analytical session in May 2010 gave relative standard deviations (100*standard deviation/mean) of 0.6% for SiO_2, 0.06% for TiO_2, 1.0% for Al_2O_3, 0.9% for FeO, 1.4% for MgO, 0.9% for CaO, and 2.7% for Na_2O.

In order to improve analytical precision for minor and trace elements (TiO_2, K_2O, Cr_2O_3, MnO, P_2O_5, NiO, Na_2O, and S), concentration profiles in some inclusions were re-measured using longer counting times (400 s on-peak and 400 s on background for MnO; 360 s on-peak and 360 s on background for Cr_2O_3; 280 s on-peak and 280 s on background for TiO_2; 120 s on-peak and 120 s on background for K_2O, P_2O_5, S, and NiO; and 60 s on-peak and 60 s on background for Na_2O), a higher beam current (30 nA), and a 5 μm beam diameter. The detection limits at 99% confidence for this setup were 0.007 wt. % for MnO, 0.011 wt. % for Cr_2O_3, 0.004 wt. % for TiO_2, 0.006 wt. % for K_2O, 0.011 wt. % for P_2O_5, 0.015 wt. % for NiO, 0.004 wt. % for S, and 0.016 wt. % for Na_2O. The concentrations of NiO and Cr_2O_3 in the glasses were below the detection limit under these analytical conditions. For all of the other oxides, the percent errors on the measurements calculated from counting statistics were <10 % in the glasses. These re-measurements of the minor elements were made along approximately the same profiles as the major element analyses.

H_2O, Cl, F, and S profiles were measured across five Siqueiros melt inclusions mounted in indium with the Cameca NanoSIMS 50L at Caltech, using methods similar to those outlined by Hauri et al. (2002). A primary beam of $^{133}Cs^+$ ions with a beam current of ~3.5 pA (on-sample) and a beam diameter of ~100–200 nm was used to sputter secondary ions from the sample surface over a 2×2 μm rastered area, with charge compensation provided by an electron flood gun. Pre-sputtering for 158 s before each analysis removed the gold coating from the sample surface within the analysis crater and reduced contamination by surface-adsorbed volatiles. Electronic gating was used such that only secondary ions from the central 30% of the rastered area were detected. This technique reduces contamination from volatiles adsorbed on the sample surface. Negatively charged ions of $^{16}O^1H^-$, $^{35}Cl^-$, $^{19}F^-$, $^{32}S^-$, $^{24}Mg^{16}O^-$, and $^{18}O^-$ were detected simultaneously using six electron multipliers. The mass resolution power for $^{16}O^1H$ was sufficient to distinguish $^{16}O^1H$ from ^{17}O. $^{18}O^-$ was used as a denominator of all reported ion intensity ratios, and the intensity of the $^{24}Mg^{16}O^-$ ion beam was used to distinguish between analyses of olivine vs. analyses of glass. San Carlos olivine containining 0.3 ± 0.1 ppm H_2O (GRR997; Mosenfelder et al. (2011)) was analyzed to determine the analytical blank, and a selection of homogeneous basaltic and andesitic glasses were used as standards. Four replicate analyses of GRR997 were used to assess the detection limits at 99% confidence for H_2O, Cl, F, and S, following equation (7) of Long and Winefordner (1983). The detection limits were 74 ppm for H_2O, 1.8 ppm for F, 0.9 ppm for S, and 0.4 ppm for Cl. Further details regarding the calibration of our SIMS data are provided in Appendix II.

5. Results

Chemical zonation was observed in all of the studied melt inclusions. Concentration profiles of major elements across inclusion Siq16 are shown in Figure 2. The concentration profiles are approximately symmetric about the center of the melt inclusion. Oxides that have higher concentrations in the olivine than the melt (e.g., FeO and MgO) are depleted at the edges of the inclusion, whereas oxides that have lower concentrations in the olivine than the melt (e.g., SiO_2, Al_2O_3, CaO, and Na_2O) are generally enriched at the edges. The minor and trace elements in the inclusions are also zoned (analyses of Siq1-19b are shown in Figure 3). TiO_2 and K_2O, which are incompatible in olivine, are enriched at the edges of the inclusions, while MnO, which is compatible in olivine, is depleted at the edges of the inclusions. Although the concentrations of P_2O_5 and Cr_2O_3 are close to or below the detection limit of the electron microprobe given our analytical procedures, some inclusions appear to show the expected enhancement of P_2O_5 and depletion of Cr_2O_3 toward their edges (e.g., Siq1-19b; see Figure 3 and Online Resource 2). As shown in Figure 4, nanoSIMS measurements of H_2O, S, F, and Cl across the Siq8 inclusion revealed zonation in these elements. Given that they are incompatible in olivine, we would have expected the concentration of all of these volatile components to increase from the center to the edge of the inclusion. However, although the expected behavior is observed for S and Cl, the concentrations of H_2O and F *decrease* towards the edges of this melt inclusion. Similar trends were observed across the other melt inclusions analyzed with the nanoSIMS (see Appendix II). Also of note is the similarity between the shapes of the concentrations profiles of H_2O and F (see Figure 4 and Appendix II).

The width of the concentration profile varies from element to element in a given melt inclusion. For example, the widths of the concentration profiles of SiO_2, Al_2O_3, and Na_2O are all similar in Siq16 (~30 μm; Figure 2), whereas the concentration profile of MgO propagates much further into the inclusion (~80 μm; Figure 2). The shapes of the concentration profiles from the edges of the melt inclusions to the centers can also be variable: although most elements show a monotonic increase or decrease in concentration from edge to center, Ca and Fe sometimes increase, reach a maximum and then decrease from edge to center; this is the case for inclusion Siq16 (Figure 2). A similar trend may also be apparent in profiles of H_2O and F across inclusion Siq16 (see Appendix II). In melt inclusions Siq7, Siq8, and Siq16, the shapes of the H_2O and F concentration profiles mimic the shapes of the Fe concentration profiles.

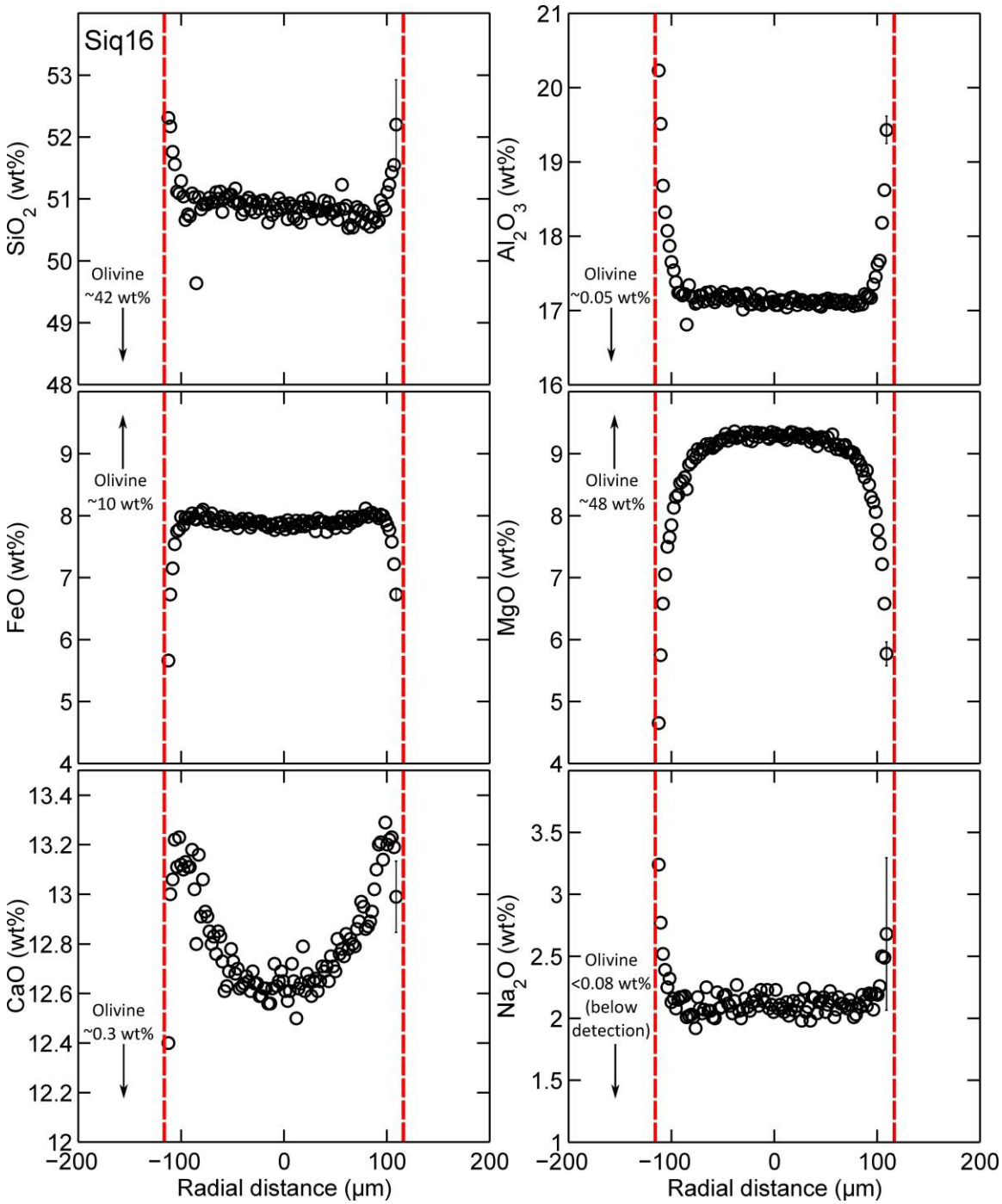

Figure 2 Major element concentration profiles in melt inclusion Siq16 measured by electron microprobe. Only analyses of the melt are shown; a typical olivine analysis is labeled on the left of each panel. The distance between analyses is ~2 μm and the beam was focused to a nominal diameter of 150 nm. The edges of the melt inclusion are indicated by vertical red dashed lines. The ±2σ error bars on the rightmost data point in each panel are ±2 standard deviations of replicate analyses of basaltic glass standard VG2 during the analytical session. Analyses of secondary standards are provided in Online Resource 2.

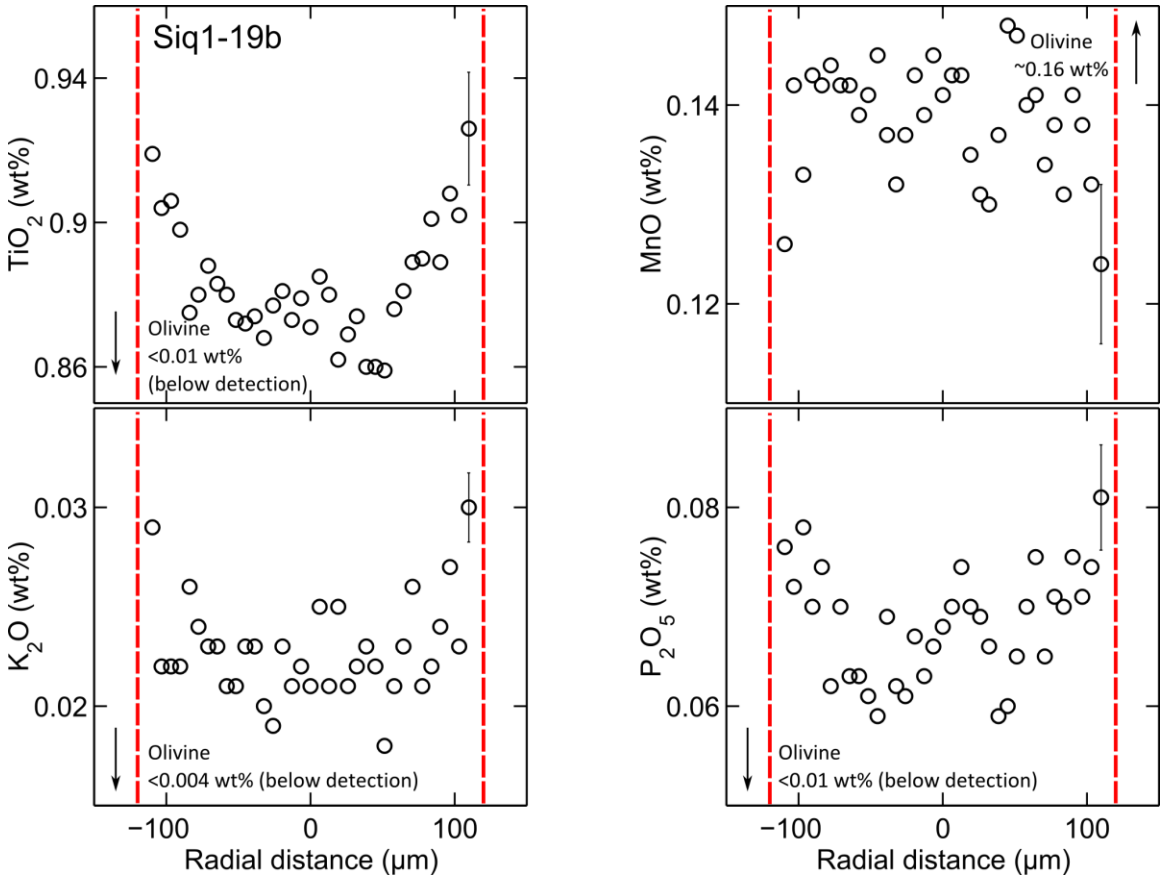

Figure 3 Minor and trace element concentration profiles in melt inclusion Siq1-19b, measured by electron microprobe. Only analyses of the melt are shown; a typical olivine analysis is labeled at the edge of each panel. The distance between analyses is ~10 μm and the beam diameter was set to 5 μm. Symbols and error bars as in Figure 2.

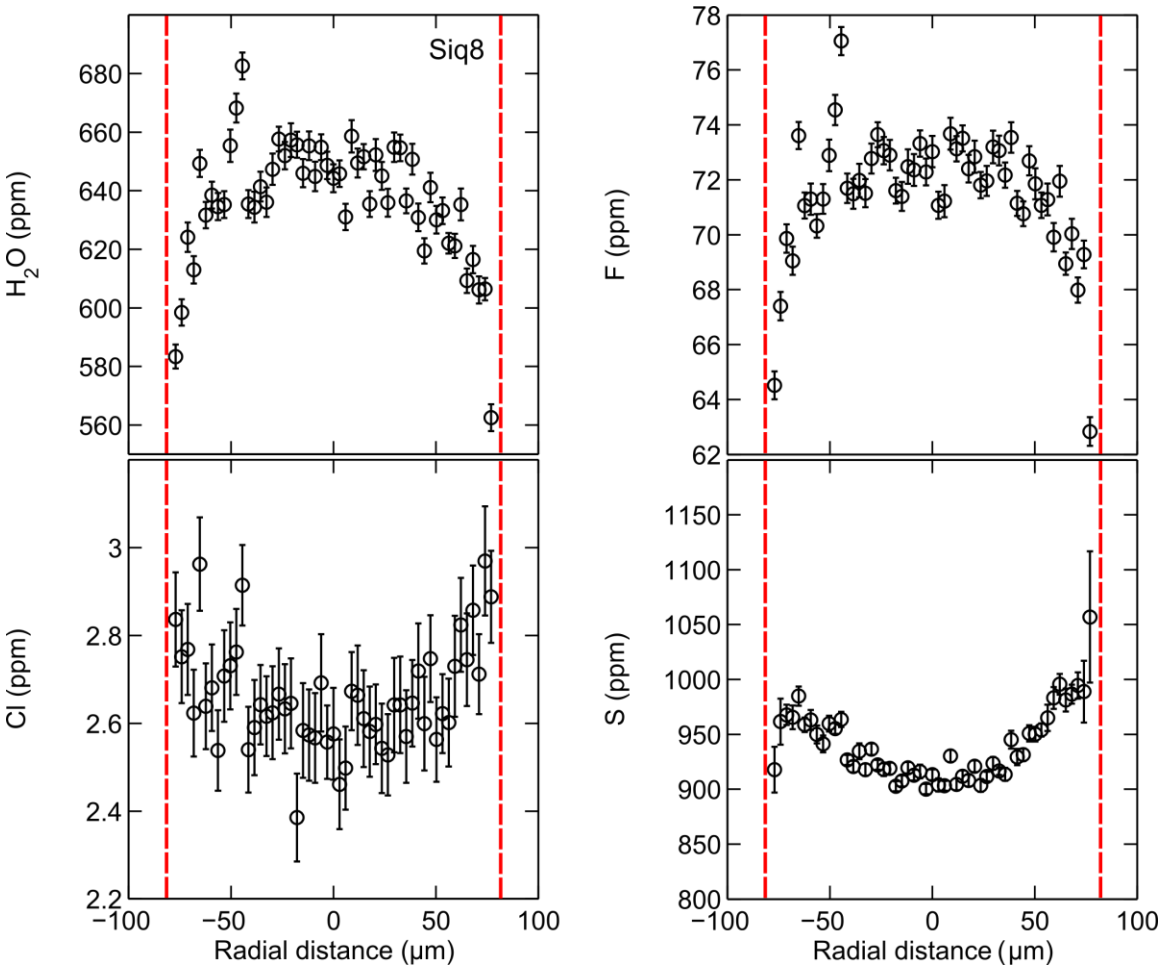

Figure 4 Concentration profiles of H_2O, S, Cl, and F in melt inclusion Siq8, measured by nanoSIMS. Only analyses of the melt are shown. Analyses of H_2O, S, Cl, and F in the host olivine are below the detection limits of 74 ppm for H_2O, 0.9 ppm for S, 0.4 ppm for Cl, and 1.8 ppm for F. The distance between analyses is ~3 μm. The edges of the melt inclusions are indicated by dashed red lines. Error bars are $\pm 2\sigma$ (σ = standard error of the mean of 100 cycles of analyses).

There is a relationship between the glass composition measured in the center of an inclusion and the radius of the inclusion. As shown in Figure 5, the smallest inclusions in the Siqueiros suite are enriched in elements that are incompatible in olivine and depleted in elements that are compatible in olivine. As inclusion radius increases, the degree of incompatible element enrichment and compatible element depletion decreases until the composition reaches a roughly constant value. The radius at which this concentration 'plateau' is reached is different for each element: For SiO_2 and FeO, the center concentration is approximately constant for melt inclusions larger than ~30 μm; for Al_2O_3, the concentration plateau is reached at radii larger than ~60 μm; for MgO, the concentration plateau is reached at radii larger than ~100 μm; and for CaO, the

variability of center concentration with radius extends to inclusions with even larger radii. No discernible trend is observed for central Na_2O concentration with inclusion size. The variability observed in central concentrations of Na_2O in the Siqueiros inclusions could be due to interaction of these melts with plagioclase prior to their entrapment (e.g., Danyushevsky et al. 2003; Danyushevsky et al. 2004; Saal et al. 2007).

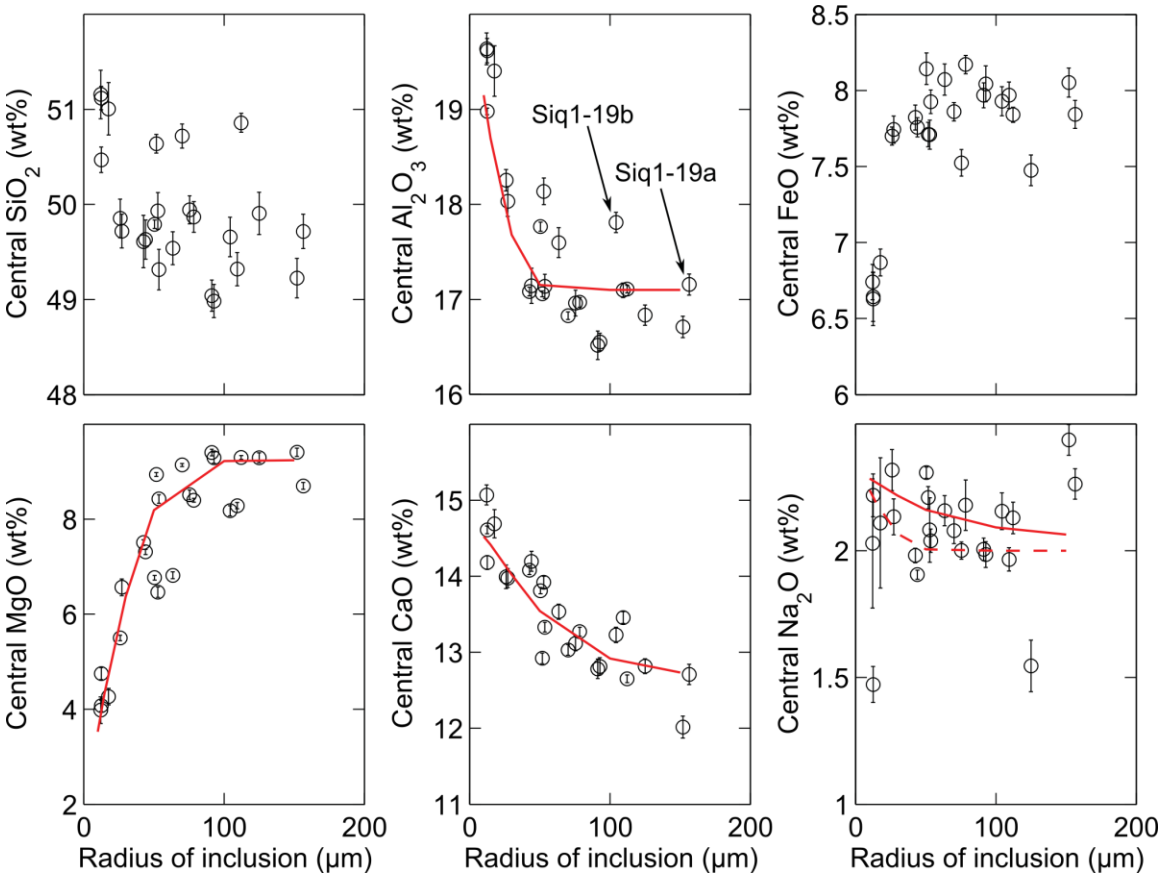

Figure 5 Major element composition measured in the center of each melt inclusion plotted against inclusion radius. Each point represents the mean of 3–25 analyses (with the number of analyses used dependent on the size of the melt inclusion and the point spacing) taken from the central portion of each melt inclusion. Error bars indicate ±1 standard deviation of these analyses. Solid and dashed red curves are the results of a simulation of a representative linear cooling history (2220 °C/hr over 10 minutes) for six melt inclusions with an assumed initial composition close to the composition of the largest melt inclusions in the Siqueiros suite (see caption to Figure 13) and with radii ranging from 10 to 150 μm (see section 6.4 and Figure 12). Melt inclusions Siq1-19a and Siq1-19b are labeled in the plot of Al_2O_3 to emphasize that Siq1-19b has a concentration of Al_2O_3 that is elevated relative to other melt inclusions of a similar size in the Siqueiros suite (see discussion in section 6.3.8).

Concentration gradients within melt inclusions have been observed previously. For example, a study of olivine-hosted melt inclusions from Mt. Shasta by Anderson et al. (1974)

noted that ‘concentration gradients are common in glass inclusions within about 10 microns of the olivine host’. Danyushevsky et al. (2002b) also observed depressed concentrations of FeO and MgO in a zone that extends up to 5–6 μm from the walls of both naturally and experimentally quenched olivine-hosted melt inclusions from a variety of magmatic and tectonic settings (MORB from the Siqueiros transform fault, arc tholeiite from Hunter Ridge, komatiite from Belingwe, and high-Ca boninite from the Tonga arc). The zonation observed in this study is more extensive, and demonstrably reaches the center of many of the Siqueiros inclusions (e.g., the CaO concentration profile in Figure 2). Colin et al. (2012) observed concentration gradients of MgO, SiO_2, Al_2O_3, and FeO within olivine-hosted melt inclusions from a Mid-Atlantic ridge pillow basalt (sample RD87DR10). Their concentration gradients of Al_2O_3 are 20–30 μm wide, consistent with the Siqueiros and Galapagos melt inclusions described in this study; they also measured concentration gradients of Al_2O_3 in matrix glass extending outward from the rims of some of the olivine phenocrysts, and these concentration profiles are similar to those measured inward from the edges of the inclusions. Additionally, Mercier (2009) observed zonation of MgO, Al_2O_3, and CaO in olivine-hosted melt inclusions in scoria from La Sommata (Vulcano Island). The concentration gradients observed in the La Sommata sample suite are shorter than those described in this study (e.g., ~20 μm for MgO and ~10 μm for Al_2O_3), and SiO_2 and Na_2O do not show zonation. However, the shapes of the concentration profiles of Al_2O_3, CaO, and MgO are generally consistent with those reported here for the Siqueiros and Galapagos melt inclusions.

6. Discussion

6.1. Formation of the zonation – general considerations

As an olivine-hosted melt inclusion cools, it will typically crystallize olivine on its walls (e.g., Anderson 1974; Danyushevsky et al. 2002b), and an olivine-depleted boundary layer will form in the melt near the olivine-melt interface. This boundary layer is depleted in elements that are compatible in olivine (such as Mg, Fe, Mn, and Cr) and enriched in elements that are incompatible (such as Si, Al, Ca, Na, Ti, K, and P). There is, however, a competition between the development of the boundary layer due to olivine growth and its relaxation due to diffusion between the boundary layer and the interior of the melt inclusion. In the case of partitioning of a trace element between olivine and melt, if the olivine growth were into a melt of infinite extent and the olivine growth rate, the diffusion coefficient of the element in the melt, and the partition coefficient of the element between the olivine and melt were all constant, a steady-state concentration profile of the element would develop in the melt (Tiller et al. 1953; Smith et al.

1955; Albarede and Bottinga 1972; Zhang 2008). In melt inclusions, however, the volume of the inclusion is finite rather than infinite, and if the olivine on the inclusion wall is growing in response to a decrease in temperature, neither the partition coefficients nor the diffusion coefficients of any elements are constant, so the resulting profiles will be time dependent and more complex. Additional complications in natural systems with substantial major-element variability along the concentration profile are that diffusion coefficients may vary along the profile and that there may be interactions between the diffusivities of the various elements leading to cross terms in the diffusion matrix that can even lead to uphill diffusion. Such "multicomponent diffusion" features have been described in many experimental studies (Watson 1982; Watson and Jurewicz 1984; Zhang et al. 1989; Kress and Ghiorso 1995; Mungall et al. 1998; Lundstrom 2000; Richter et al. 2003; Chen and Zhang 2008) and in a small number of studies of natural samples of quartz xenocrysts dissolving in basaltic and andesitic melts (Maury and Bizouard 1974; Sato 1975).

We have developed a model of olivine growth and the evolution of MgO and perfectly incompatible elements across a melt inclusion in response to a given cooling history using the effective binary diffusion treatment. The model is described in detail in section 6.3, but the results of two simple simulations are described here to provide a framework for thinking about what to expect for a melt inclusion undergoing olivine crystallization on its wall. Figure 6 shows the evolution of the concentration of a compatible oxide (MgO) and an incompatible oxide (Al_2O_3) in an olivine-hosted melt inclusion that is suddenly cooled by 100 °C and then held at a constant temperature. At the start of the process, the melt is homogeneous, with a scaled concentration (i.e., concentration at any time *t* / initial concentration) of 1.0 (Figure 6a and Figure 6b; in black). When the temperature is suddenly decreased from 1300 °C to 1200 °C (Figure 6c), it is assumed that MgO concentration in the interface melt reaches instantaneous interface equilibrium, leading to a pulse of rapid olivine growth (Figure 6d). This results in a narrow boundary layer in the melt adjacent to the newly grown olivine, with the concentration of MgO lowest at the interface and increasing up to its initial concentration far from the olivine-melt interface (Figure 6a; in blue), and the concentration of Al_2O_3 highest at the interface and decreasing down to its initial concentration far from the olivine-melt interface (Figure 6b; in blue). When the temperature is then held constant at 1200 °C, the profiles of MgO and Al_2O_3 relax progressively due to diffusion in the melt (Figures 6a and 6b; red, cyan and green curves). As stated in the previous paragraph, the widths and shapes of the resultant MgO and Al_2O_3 concentration profiles depend on the partition coefficients of MgO and Al_2O_3 between the melt and the olivine, the growth rate of the

olivine, and the diffusivities of MgO and Al_2O_3 in the melt. After approximately 20 minutes for MgO and one hour for Al_2O_3 at 1200 °C, the concentration profiles disappear, and the melt again becomes homogeneous, depleted in MgO and enriched in Al_2O_3 relative to the starting composition of the melt inclusion (assuming back reaction with the olivine can be neglected; see the detailed description of the model in section 6.3).

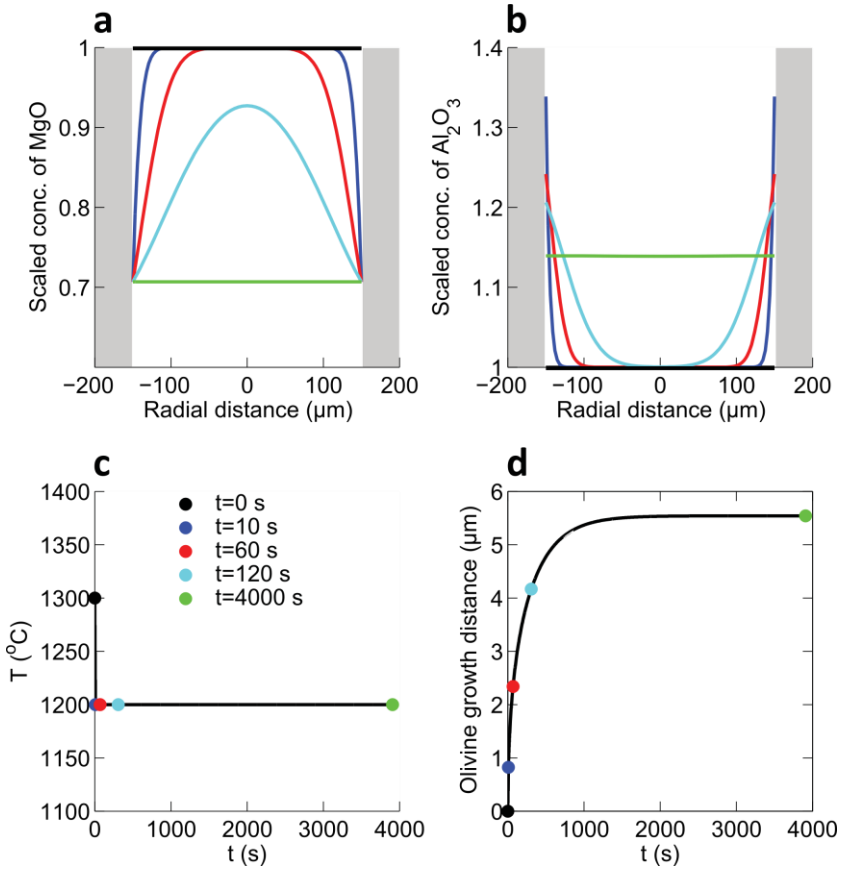

Figure 6 (a) Forward model of MgO concentration in a melt inclusion with a radius of 150 μm in response to sudden cooling followed by a period of diffusive relaxation at a constant temperature. Scaled MgO = concentration of MgO / initial concentration of MgO. Thick black line, initial condition; blue line, concentration profile after 10 s; red line, concentration profile after 1 minute; cyan line, concentration profile after 2 minutes; green line, concentration profile after just over 1 hour. Grey shaded regions are olivine. Note that the edges of the melt inclusion are assumed to be fixed in the model, whereas in reality, the edges of the melt inclusion would be expected to move inwards by up to a few microns as a result of the crystallization of a thin rim of olivine on the inclusion walls. This assumption is discussed further in section 6.3.2. **(b)** Forward model of Al_2O_3 concentration in response to the same thermal history as (a). Scaled Al_2O_3 = concentration of Al_2O_3 / initial concentration of Al_2O_3. Colors and line styles as in (a). **(c)** Thermal history used to generate (a) and (b). Colored points highlight the times of the snapshots plotted in (a) and (b). The system begins in equilibrium at 1300 °C. The temperature is decreased by 100 °C over 10 seconds and is then held at 1200 °C for just over 1 hour. **(d)** Width of olivine growth during cooling and re-equilibration of melt inclusion. Colored points as in (c). Note that the amount of olivine crystallized during this simulation is large compared to the natural samples (which tend to crystallize an olivine rim with a width of ~1% of their radii – see section 6.3.2).

Although the process modeled in Figure 6 is illustrative, in nature it is unlikely that cooling and olivine growth can be separated in time from diffusive relaxation in the melt in the manner described in the previous paragraph. Instead, cooling, crystallization, and diffusion are concurrent and continuous. In Figure 7, we illustrate the effect of a simple linear cooling history on the distribution of MgO and Al_2O_3 in a melt inclusion. Again, the initial condition is a homogeneous melt inclusion with scaled concentrations of MgO and Al_2O_3 of 1.0. As the melt cools and crystallizes, a boundary layer depleted in MgO and enriched in Al_2O_3 builds up and is maintained at the moving olivine-melt interface. As crystallization continues with decreasing temperature, the depletion of MgO and the enrichment of Al_2O_3 become stronger at the olivine-melt interface, and the boundary layer is maintained even as it propagates by diffusion toward the center of the inclusion. Eventually, as the system cools sufficiently, olivine crystallization and diffusion of MgO and Al_2O_3 slow down to the point that the concentration profiles in the boundary layer are quenched and preserved in the glassy melt inclusion. The important point here is that if melt inclusions cool at a rate slow enough to allow continuous olivine crystallization on their walls before quenching but fast enough such that the diffusive boundary layers are not completely erased, then diffusively moderated concentration profiles in the boundary layers can be preserved in glassy inclusions as the kinetics of crystal growth and diffusion in the melt slow sufficiently on cooling; this differs from the example described in the previous paragraph where given sufficient time, the concentration gradients due to a pulse of olivine growth can always be erased by diffusion.

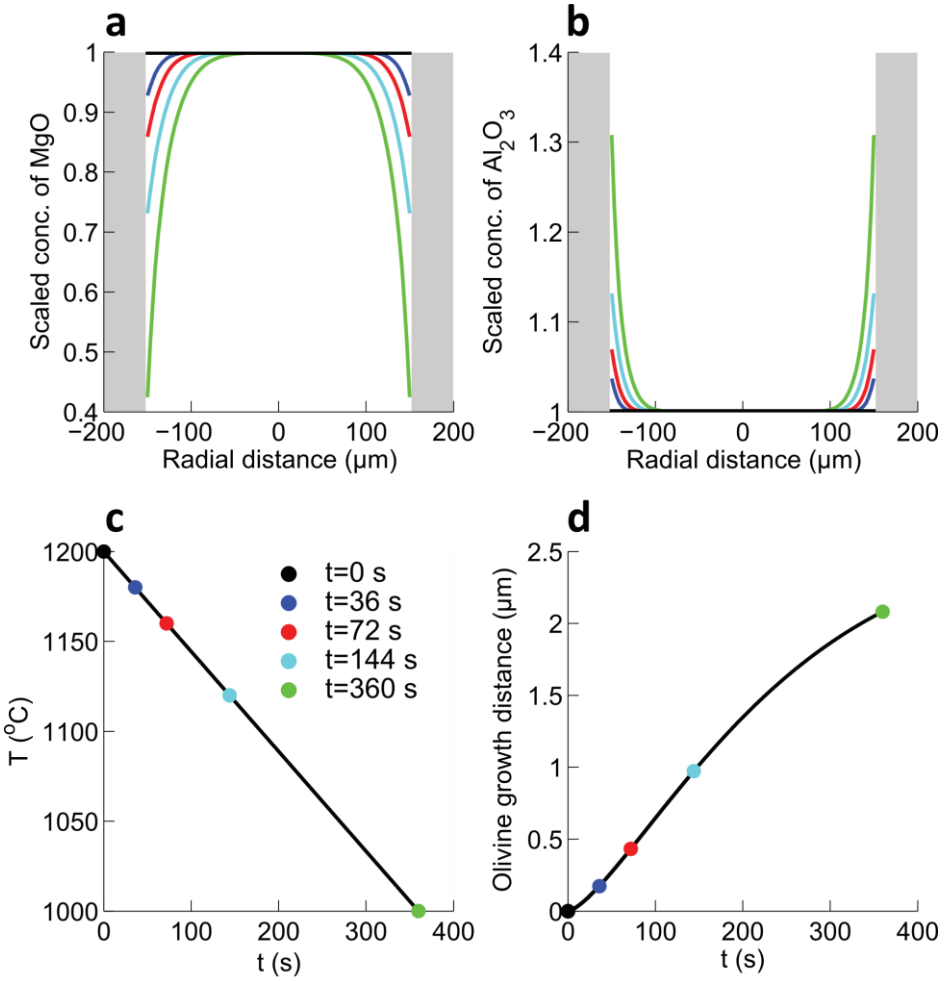

Figure 7 (a) Forward model of MgO concentration in a melt inclusion with a radius of 150 μm in response to cooling from 1200 to 1000 °C at a constant rate of 2000 °C/hr. The black solid line shows the homogeneous initial condition; the blue line shows the model concentration profile after 36 seconds; the red line shows the model concentration profile after 72 seconds; the cyan line shows the model concentration profile after 144 seconds; and the green line shows the model concentration profile after 360 seconds. Grey shaded regions are olivine. Scaled MgO = concentration of MgO / initial concentration of MgO. Note that the melt at the edges of the inclusion is assumed to be in equilibrium with the host olivine at all times, so the concentration of MgO decreases with time at the edges of the inclusion as the system cools, reflecting the temperature dependence of the partitioning of MgO between melt and olivine (Chen and Zhang 2008). **(b)** Forward model of Al_2O_3 concentration in response to the same thermal history as (a). Scaled Al_2O_3 = concentration of Al_2O_3 / initial concentration of Al_2O_3. Colors and line styles as in (a). **(c)** Thermal history used to generate (a) and (b). Colored points highlight the times of the snapshots plotted in (a) and (b). The system begins in equilibrium at 1200 °C and cools at a constant rate of 2000 °C/hr for 6 minutes. **(d)** Width of olivine growth during cooling and re-equilibration of melt inclusion. Colored points as in (c).

These simple examples emphasize the critical result of our study: In the final stages of their magmatic histories, the walls of all melt inclusions we have studied underwent olivine

growth at rates sufficient to generate concentration profiles extending ca. 10-100 μm into the adjacent melt (this length differs from inclusion to inclusion and from element to element); although these profiles were modified by diffusion in the melt, they have been preserved in the quenched glassy inclusions. In the remainder of this discussion, we describe the implications of chemical zonation in melt inclusions for the understanding of chemical diffusion in silicate melts (section 6.2), and we illustrate how this zonation can be used to constrain the final stages of the thermal histories of olivine-hosted melt inclusions (section 6.3). Finally, we discuss the implications of the chemical zonation for the interpretation of melt inclusion compositions (sections 6.4 and 6.5).

6.2. Multicomponent diffusion effects

As briefly described in section 5, some of the concentration profiles in the Siqueiros and Galapagos melt inclusions exhibit apparently 'anomalous' diffusion behavior, suggestive of multicomponent diffusion effects. For example, in inclusion Siq16, profiles of FeO and CaO from inclusion edge to center increase, reach a maximum, and then decrease, indicating that these oxides are diffusing up their own concentration gradients (Figures 2 and 8c). This phenomenon is called "uphill diffusion" (e.g., Lasaga 1979; Liang 2010). It is often observed during olivine dissolution experiments (Zhang et al. 1989; Chen and Zhang 2008) and reflects diffusive coupling between components in the melt (i.e., the flux of a component responds to concentration gradients in other components in addition to its own concentration gradient). Uphill diffusion of FeO and/or CaO is observed in all of the melt inclusions for which we collected high spatial resolution major element profiles. In most of these inclusions, the FeO and CaO profiles look similar to those in Siq16 (Figures 2 and 8c). However, in Siq7, which is a relatively small inclusion (Figure 8d), although uphill diffusion of FeO is not apparent, the uphill diffusion in CaO has reached the center of the inclusion, thereby entirely inverting the shape of the concentration profile expected for an element that is incompatible in olivine (i.e., from concave-up, which would be expected for an incompatible oxide like CaO, to concave-down).

Another seemingly anomalous feature of the concentration profiles in the Siqueiros and Galapagos inclusions is the similarity in the shapes of the SiO_2, Al_2O_3, and Na_2O profiles (Figures 8a and 8b; K_2O profiles, although noisier, also demonstrate this behavior – additional K_2O data are provided in Online Resource 2) despite significant differences among the experimentally determined diffusion coefficients of these oxides in basaltic melts: for example, determinations of the diffusivities of SiO_2 (Lesher et al. 1996; self diffusion), Al_2O_3 (Kress and Ghiorso 1995;

effective binary diffusion coefficient derived from multicomponent diffusion experiments), and Na_2O (Jambon 1982; Zhang et al. 2010; tracer diffusion) indicate that SiO_2 and Al_2O_3 have diffusion coefficients that are approximately two orders of magnitude smaller than the tracer diffusivity of Na_2O in basaltic melts. The similarity of the profiles of SiO_2, Al_2O_3, and Na_2O (Fig. 8a,b) thus suggests that the diffusion of Na_2O is strongly coupled to SiO_2 and/or Al_2O_3, and in particular it suggests that the propagation of the Na_2O concentration into the inclusions is tied to (and therefore limited by) the slower propagation of the SiO_2 and/or Al_2O_3 profiles (Watson 1982; Zhang et al. 1989; Zhang 1993).

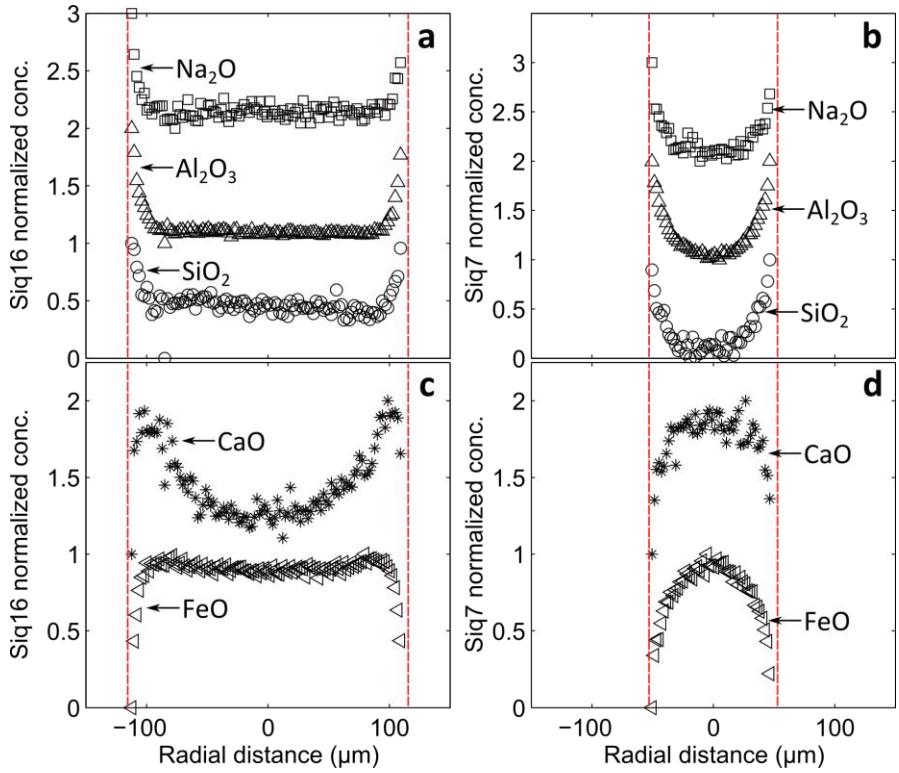

Figure 8 In panels (a)–(d), the concentrations of each oxide have been scaled to lie between 0 and 1, and then offset by one unit for easy comparison. The edges of the melt inclusions are marked as vertical red dashed lines. **(a)** Comparison of shapes of concentration profiles of Na_2O, Al_2O_3, and SiO_2 across inclusion Siq16. Note the similarity between all three concentration profiles, despite significant differences in the experimentally determined diffusion coefficients for these oxides (see section 6.2). **(b)** Comparison of shapes of concentration profiles of Na_2O, Al_2O_3 and SiO_2 across inclusion Siq7. As in (a), these concentration profiles are similar. **(c)** Scaled concentration profiles of FeO and CaO in inclusion Siq16. From edge to center, these oxides increase, reach a maximum, and then decrease again. This suggests uphill diffusion (see section 6.2). **(d)** Scaled concentration profiles of FeO and CaO in inclusion Siq7. Note that CaO, despite being incompatible during olivine crystallization, decreases towards the inclusion edge. This suggests uphill diffusion; however, in this small melt inclusion (radius = 51μm), the diffusion of CaO away from the silica-rich melt adjacent to the crystallizing olivine reached the center of the inclusion, thereby inverting the expected shape of the CaO profile.

Although to our knowledge, uphill diffusion of FeO and CaO has not been observed in natural samples, it has been observed in experiments on olivine dissolution in basaltic melts (Zhang et al. 1989; Chen and Zhang 2008). In these studies, FeO and CaO are seen to diffuse towards less polymerized (i.e., lower SiO_2) melts and may be modeled by the modified effective binary diffusion model (Zhang 1993). These observations agree with the behavior of FeO and CaO observed in the Siqueiros and Galapagos melt inclusions, where FeO and CaO are inferred to have diffused away from the Al_2O_3- and SiO_2-enriched melt at the edges of the inclusions.

The coupling of Na_2O to SiO_2 and/or Al_2O_3 suggested by the similarity of the Na_2O concentration profiles to the profiles of SiO_2 and Al_2O_3 could arise in several ways. One possibility is that it reflects the motion of structural units in the melt (e.g., the "stuffed tridymite" structure proposed by Taylor and Brown (1979)) which would force Na_2O to move in concert with Al_2O_3 and SiO_2. Another is that Na_2O is strongly partitioned into silica-rich melt, as observed in the two-liquid partitioning experiments of Ryerson and Hess (1978) and Watson (1982), such that the observed Na_2O profiles represent a "quasi-equilibrium" state, where rapidly diffusing Na_2O has distributed itself to equalize its chemical potential across the melt inclusions, and its concentration profile only evolves as the more slowly changing SiO_2 and Al_2O_3 profiles propagate into the interior of the melt inclusion (Watson 1982; Zhang 1993). Anomalous diffusion behavior of Na_2O in melts with compositional gradients has been seen many times both in experiments (Ryerson and Hess 1978; Watson 1982; Watson and Jurewicz 1984; Zhang et al. 1989; Baker 1990; Mungall et al. 1998; Lundstrom 2000; Richter et al. 2003) and in natural samples (Maury and Bizouard 1974; Sato 1975), and it has been semi-quantitatively modeled (Zhang 1993).

Although it is beyond the scope of the current study, it may be possible to use the concentration profiles in the Siqueiros and Galapagos inclusions as "natural diffusion experiments" that could help constrain the diffusivity matrix for MORB. Knowledge of the diffusivity matrix for MORB would enable the calculation of timescales for igneous processes such as magma mixing, the transport of basaltic melts through the mantle, melt degassing, crystal growth and dissolution, and the assimilation and eruption of xenoliths. Unfortunately, determination of the diffusivity matrix for MORB melts is proving to be a difficult problem due to the large number of components in natural silicate melts (Trial and Spera 1994; Kress and Ghiorso 1995; Liang 2010). Therefore, in the modeling we do in the next section, although it is imperfect, we adopt the simpler effective binary diffusion approach (Cooper 1968; Zhang 2010); i.e., we will assume that there is no diffusive coupling between oxides in the melt. This is likely

to be a good approximation for MgO, which does not exhibit anomalous diffusion behavior and is thought to be the principal equilibrium-determining component during olivine growth and dissolution (Zhang et al. 1989; Chen and Zhang 2008). However, the effective binary diffusion approach cannot describe the behavior of those elements such as FeO, CaO, and Na_2O that are observably influenced by multicomponent diffusion.

6.3. Using zonation in melt inclusions to derive thermal histories

In this section, we describe the forward model we have used to simulate the development of MgO concentration profiles across olivine-hosted melt inclusions as they cool and to determine cooling histories that best fit the MgO concentration profiles of individual melt inclusions. We focused on MgO concentration profiles because the temperature-dependent fractionation of MgO between olivine and melt is well understood (e.g., Roeder and Emslie 1970; Sugawara 2000; Putirka 2008; Matzen et al. 2011) and because MgO diffusion during olivine dissolution and growth has been shown to be approximated well as an effective binary diffusion problem (Zhang et al. 1989; Chen and Zhang 2008).

6.3.1. Description of the forward model

Our model of concurrent olivine growth and MgO diffusion describes the evolution of melt composition across a spherical basaltic melt inclusion of a given radius in response to an arbitrary cooling history. The evolution of the concentration gradient of a component in melt adjacent to a growing olivine crystal depends on the partitioning of that component between olivine and melt, on the diffusivity of the component in the olivine (which we neglect), and on the diffusivity of the component in the melt. Although there are many parameterizations of the olivine-melt partition coefficient for MgO (e.g., Roeder and Emslie 1970; Sugawara 2000; Putirka 2008; Matzen et al. 2011) and of the chemical diffusion coefficient of MgO in basaltic melts (e.g., LaTourrette et al. 1996; Lundstrom 2003; Chen and Zhang 2008, 2009), we have adopted the simple temperature-dependent formulations of Chen and Zhang (2008):

$$C_{MgO} = \exp\left(7.82 - \frac{8040}{T}\right) \quad (1)$$

$$D_{MgO} = \exp\left(-7.895 - \frac{26257}{T}\right) \quad (2)$$

In equations (1) and (2), T is the temperature in kelvins; C_{MgO} is the concentration of MgO in wt. % in melt coexisting with San Carlos olivine; and D_{MgO} is the diffusivity of MgO in m^2s^{-1} in the melt.

Diffusion of MgO in the model melt inclusion is described by the radial component of the diffusion equation in spherical polar coordinates:

$$\frac{\partial C_{MgO}}{\partial t} = D_{MgO}\left(\frac{\partial^2 C_{MgO}}{\partial r^2} + \frac{2}{r}\frac{\partial C_{MgO}}{\partial r}\right) \quad (3)$$

The boundary condition at $r = 0$ is $\partial C_{MgO}/\partial r|_{r=0} = 0$. The boundary condition at $r = a$ (where a is the radius of the melt inclusion) is assumed to be instantaneous equilibrium: i.e., $C_{MgO}|_{r=a} = C_{MgO}|_T$.

In equation (3), t is time in seconds, r is radial distance from the center of the melt inclusion in meters, and boundary motion is ignored in the numerical solution. Given a monotonically decreasing relationship between temperature and time and equation (2) to describe D_{MgO}, equation (3) can be solved using equation (1) as a boundary condition at the olivine-melt interface to find the concentration profile of MgO in the melt inclusion through time. The initial condition in the melt is a constant concentration of MgO (i.e., the melt is assumed to be homogeneous at the start of the cooling history). Initial concentrations of MgO were chosen based on the highest MgO concentration measured among all melt inclusions collected at the same location or during the same dredge. For example, inclusions Siq7 and Siq8 were both collected during the same dredge (A25-D20-1), so we assumed that, prior to eruption, these melt inclusions began their cooling histories with the same MgO concentration, implying a common temperature of equilibration with their host olivines. In the case of inclusions Siq7 and Siq8, an initial concentration of 8.4 wt. % MgO was used, which was calculated by finding the mean of the central six MgO analyses in Siq8. The decision to calculate the initial concentration of MgO in this way (as opposed to other possible choices, such as the MgO concentration in equilibrium with the far-field olivine host or the MgO concentration of the pillow-rim glass for the Siqueiros inclusions) is discussed further in Appendix I.

We initially assumed a one-stage linear cooling history defined by three parameters: The starting temperature (T_{high}), the constant cooling rate (q), and the final temperature (T_{low}). T_{high} and T_{low} were determined from measured concentrations of MgO in the melt inclusions by using

equation (1); T_{high} was calculated using the initial concentration of MgO in the inclusion (chosen as described in the previous paragraph), and T_{low} (which was typically ~1000 °C) was calculated using the lowest measured MgO in the inclusion. Both T_{high} and T_{low} are thus based on measured glass compositions, but the cooling rate is a free parameter that can be varied to produce the best fit to the MgO concentration profile. Further description of the model is provided in Appendix I.

6.3.2. Assumptions of the forward model

Equations (1) and (2) are empirical fits to the results of olivine dissolution experiments that used San Carlos olivine ($Fo_{90.6}$) as a starting material (Chen and Zhang 2008). By adopting equation (1), we assume implicitly that the melt at the edge of the model melt inclusion is always in equilibrium with $Fo_{90.6}$ olivine. In reality, the composition of the olivine decreases from ~Fo_{90} far (i.e., $\gtrsim$ 20 μm) from the Siqueiros melt inclusions to ~Fo_{88} at the olivine-melt interface (as measured by electron microprobe – see Online Resource 2), and the composition of the olivine adjacent to the Galapagos inclusions can be as low as Fo_{82}, and if higher resolution analytical techniques were available, it is possible that an even stronger decrease in the forsterite content of the olivine could be observed right at the olivine-melt interface. This assumption in the modeling that the temperature reflects MgO partitioning between the melt and San Carlos olivine is thus an imperfect approximation and results in an underestimation of the temperature of equilibration of the olivine and melt at the outer edges of the melt inclusions (~50 °C for the Siqueiros inclusions and up to ~70 °C for the Galapagos inclusions). This underestimation of the temperature corresponding to a given MgO concentration in the liquid translates to an underestimation of the best fit cooling rates by approximately a factor of two (see discussion in Appendix I).

The width of the olivine growth rim implied by the forward models that best fit the observed MgO concentration profiles (see section 6.3.8 and Appendix I for details of this calculation) ranges from ~0.1 to ~2 μm and is typically ~1 % of the radius of the Siqueiros and Galapagos melt inclusions. In each time step, the boundary motion is of the order 0.001 μm, and because accounting for these small increments of boundary motion would significantly increase the complexity of the programing, we assume that the movement of the boundary of the melt inclusion can be neglected during the diffusion calculation. We recalculated the MgO profiles considering olivine growth (using the olivine growth rate derived by the previous calculation as the new boundary condition – see section 6.3.8 and Appendix I). The two calculations of the MgO profiles based on these different boundary conditions were in good agreement (Figure S1 of

Appendix I), consistent with our assertion that the movement of the boundary of the melt inclusion is not a significant source of error in our model.

Chen and Zhang (2008) derived equation (2) using the effective binary diffusion approximation (i.e., it is assumed that the diffusion of MgO in the melt is independent of concentration gradients in other components). The validity of this approximation during olivine dissolution and growth is discussed in Chen and Zhang (2008) and Zhang et al. (1989).

6.3.3. The inverse model: using the measured MgO to solve for cooling rate

We used the forward model described above to calculate the distribution of MgO in a quenched olivine-hosted melt inclusion based on an assumed cooling history. In this section, we describe how we used this model to find the cooling rate that best fits the measured concentration profile of MgO across an inclusion.

As explained earlier, the single-stage linear cooling histories used in the forward model are defined by three parameters: a starting temperature (T_{high}), a final temperature (T_{low}), and a cooling rate (q). Since T_{high} and T_{low} can be calculated from equation (1), the only free parameter is the cooling rate (q), which can be varied to find the best fit to the MgO data. Given an arbitrary starting value for the cooling rate, we can fit the MgO data by minimizing the mean squared error of our forward model (calculated as the sum of the squares of the residuals divided by the number of measurements of MgO across a given melt inclusion – we refer to this quantity as the "misfit"). We used the MATLAB function "*fminsearch*", which employs a Nelder-Mead simplex algorithm (Lagarias et al. 1998) to perform this stage of the calculation.

The error on the cooling rate found by the inverse model was estimated using the parametric bootstrap method (Efron and Tibshirani 1985). This method involves assuming a statistical distribution for the MgO analyses, and then drawing from this distribution to create synthetic data sets. In this case, we assume that each MgO measurement is normally distributed with a mean corresponding to the measured value and a standard deviation of 0.1 wt. % (estimated from our replicate analyses of BHVO-2g, BIR-1g, and VG2 basaltic glasses; see Online Resource 2). Best-fit cooling rates were then determined for 100 of these synthetic data sets, and the reported uncertainty on the cooling rate for each inclusion is the standard deviation of these best fits to the synthetic data sets.

6.3.4. Results: Single-stage linear cooling histories

Best fits to the MgO data using the single-stage linear cooling model are plotted as red curves in Figure 9 for a subset of the melt inclusions in which we collected high resolution (~2 μm point spacing) MgO data. Best-fit cooling rates were determined for all of the melt inclusions with >5 points, and all the cooling histories, including those not shown in Figures 9–10, are tabulated in Appendix I. In general, the single-stage linear cooling model produces a good fit to the MgO data. However, in some melt inclusions (e.g., Siq16 and Gal-AHA2-24; Figure 9) there are subtle changes in curvature across the profiles that are not well matched by the single-stage linear cooling model. These melt inclusions tend to have steeper MgO gradients at their edges and shallower gradients across their centers relative to the results of single-stage linear cooling histories. Since the edges of an inclusion are more sensitive to the final stages of cooling than their centers (because the boundary layer produced in the final stages of olivine growth can only propagate a short distance into the inclusion), the differences in MgO gradient from edge to center relative to the single-stage model are suggestive of a two-stage cooling history, with a slower-cooling first stage and a faster-cooling second stage. Such models are explored in detail in section 6.3.5.

The cooling rates determined by the single-stage linear cooling model range from 150–13,000 °C hr^{-1} (see circles on Figure 10 and Appendix I) and are consistent with glass cooling rates determined by calorimetric geospeedometry. For example, Nichols et al. (2009) measured cooling rates of 720–170,000 °C hr^{-1} for the rims of pillow basalts from the HSDP2 drill core, and Wilding et al. (2000) reported cooling rates of 11–1440 °C hr^{-1} for hyaloclastites from the EPR.

Another geospeedometer based on the kinetics of the reaction $H_2O + O \leftrightarrow 2OH$ in rhyolitic glasses (Zhang et al. 1997; Zhang et al. 2000) has been used to determine cooling rates of rhyolitic samples of different sizes, using air, water, and liquid nitrogen as quench media (Xu and Zhang 2002). Xu and Zhang (2002) found that, for samples of the same size, quench rates in water were higher than quench rates in air or liquid nitrogen. However, the quench rates in air were inversely correlated with sample size, and the smallest samples had quench rates in air that overlapped with the range of quench rates observed in the water-quenched samples. Xu and Zhang (2002) used their technique to measure the cooling rates of natural pyroclasts quenched in air from the most recent eruption of Mono Craters, California, USA, for which they found a range of cooling rates from 10 to 200,000 °C hr^{-1}(although only one sample had a cooling rate <6000 °C hr^{-1}). The cooling rates determined in this study are consistent with the results of Xu and

Zhang (2002). We analyzed seven melt inclusions from a subaerial hornito on Santiago Island, Galapagos, and these inclusions have cooling rates that are at the high end of the range determined for our sample suite (Figure 10). These high cooling rates may reflect the small pyroclast size expected for the products of this style of volcanic eruption.

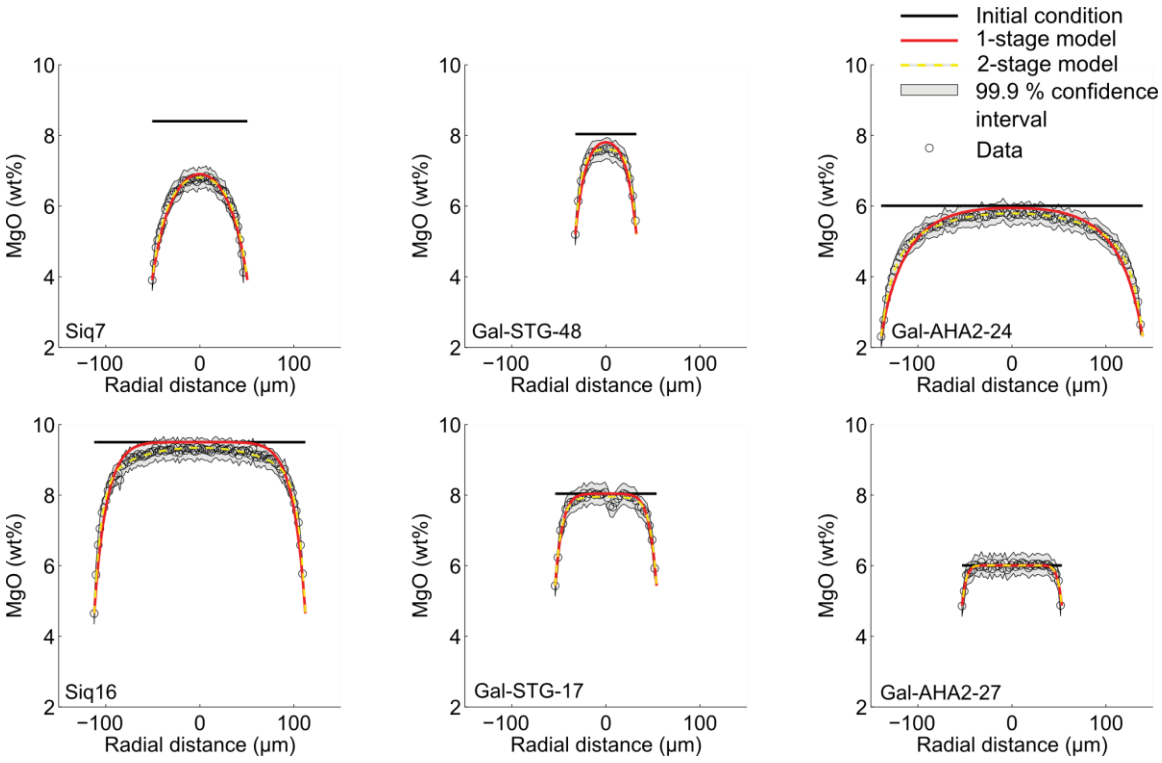

Figure 9 Fits to MgO data for a subset of melt inclusions measured with 2 μm point spacing (two inclusions from each of Siqueiros, Santiago, and Fernandina). Assumed initial conditions are shown as horizontal black lines; best fits to the single-stage linear cooling model are shown as red curves; best fits to the two-stage linear cooling model are shown as yellow dashed curves; the 99.9% confidence intervals on the measured MgO data are shown as grey envelopes; and the measured MgO concentrations are shown as black circles.

6.3.5. Inverting the MgO concentration profiles for two-stage linear cooling histories

As described in section 6.3.4, subtle but persistent differences between the curvatures of measured MgO profiles and the best-fit profiles based on single-stage linear cooling histories in some of the melt inclusions shown in Figure 9 suggest that a two-stage linear cooling history might improve the fit to the data: i.e., an initial stage of slow cooling could allow the propagation of a shallower MgO gradient into the center of a melt inclusion, and a final stage of rapid cooling could produce a steeper MgO gradient at its edges. In this section, we describe the results of

modeling such two-stage linear cooling histories and fitting the observed MgO profiles based on such cooling histories.

Two-stage linear cooling histories can be defined by five parameters: A starting temperature (T_{high}), an intermediate temperature (T_{mid}), a final temperature (T_{low}), and two cooling rates (q_1 and q_2). The intermediate temperature is defined as the temperature at which the cooling rate decreases from q_1 to q_2 (see Figure 11a). As for the single-stage model, T_{high} and T_{low} are fixed from measured MgO concentrations in the centers and at the edges of inclusions using equation (1). This leaves three free parameters that can be varied to minimize the misfit between the model and the measured MgO concentration profiles. The Nelder-Mead simplex algorithm was used to find the values of q_1, q_2, and T_{mid} that give the best fit to the data. The parametric bootstrap method was again used to determine the range of values of each parameter that give a good fit to the data given the precision of the MgO analyses: i.e., 100 synthetic data sets were generated by adding normally distributed noise to the original MgO data (assuming a standard deviation of 0.1 wt% for each MgO analysis), then each of these synthetic data sets was fit by minimizing the misfit between the forward model and the data. This process provides a 'best fit' set of model parameters for each of the 100 synthetic (i.e., "noisy") MgO profiles. There are trade-offs between the three free parameters, so rather than reporting a standard deviation the ranges of each parameter value separately, we have calculated a 95% confidence ellipsoid (using the MATLAB function "*error_ellipse*") for the set of 100 best-fit values of q_1, q_2, and T_{mid} found by the parametric bootstrap method. The best-fit values of q_1 and q_2 are not normally distributed, and tend to be skewed towards higher cooling rates, particularly for small melt inclusions with fewer data points (typical of the melt inclusions from Santiago); this is because, beyond a certain point, increasing the cooling rate to higher values has little effect on the resultant distribution of MgO within the melt inclusions. However, taking the logarithm of the best fit values of q_1 and q_2 results in a closer approximation to a normal distribution, and in most cases prevents the 95% confidence ellipsoids around the best fit values from extending to non-physical values (i.e., to negative cooling rates). This is the approach taken for the calculation of the q_1-q_2 error ellipses in Figure 10. Error ellipses calculated by assuming a normal distribution rather than a lognormal distribution are included in Appendix I for reference.

As indicated in Table S1 (Appendix I), some melt inclusions in the Siqueiros and Galapagos suites have concentration measurements spaced 2 μm apart, whereas others were measured with 10 μm point spacing. Concentration profiles with 2 μm point spacing give much better constraints on the cooling history (i.e., their q_1-q_2 error ellipses are significantly smaller)

than those spaced at 10 µm. For this reason, we have chosen to show figures for only those inclusions measured with 2 µm point spacing in Figure 10. However, two-stage cooling histories were determined for all of the inclusions with >5 points, and all the cooling histories, including those for inclusions not shown in Figure 10, are listed in Table S2 of Appendix I. We have tested the sensitivity of our inversion technique to the density of MgO concentration measurements, the size of the inclusion, and error in the starting temperature using a model melt inclusion with a known two-stage cooling history (this data was generated using the forward model). These results are presented in Appendix I.

6.3.6. Results of the two-stage linear cooling model

Best fits to the MgO data determined by the two-stage linear cooling model are plotted as yellow dashed curves in Figure 9. The two-stage linear cooling model successfully captures the shallow MgO concentration gradient in the centers of some of the melt inclusions (this is especially clear in melt inclusions Siq16 and Gal-AHA2-24, Figure 9) and the steep MgO gradient at their edges that the single-stage cooling histories do not always capture. The success of the two-stage model at reproducing these features results in a significant reduction in misfit for some of the inclusions in comparison with the single-stage linear cooling model (see Appendix I). As shown in Figure 10, the calculated q_1-q_2 error ellipses do not all overlap, indicating that there are statistically significant differences among the cooling histories of melt inclusions within the Siqueiros, Fernandina, and Santiago sample suites, and that it is possible to distinguish these differences using our inversion technique. Values of q_2 determined for the subaerial melt inclusions (Figure 10 c, d) extend to higher cooling rates than those determined for the submarine melt inclusions (Figure 10 a, b, d), in agreement with the results of the single-stage cooling model (see section 6.3.4).

The best fit values of q_1 plotted in Figure 10 range from 64 to 1100 °C hr^{-1}, and the best fit values of q_2 range from 320 to 22,000 °C hr^{-1}. These ranges are consistent with cooling rates determined for glasses by calorimetric geospeedometry and water speciation geospeedometry. However, the ranges of cooling rates determined in this study tend to be at the low end of the ranges of cooling rates found by other methods. This may be because calorimetric geospeedometry and water speciation geospeedometry are designed to measure near-instantaneous cooling rates as a melt quenches to a glass (calorimetric geospeedometry measures the cooling rate as a melt passes through the glass transition, and water speciation geospeedometry measures the cooling rate as the melt passes through the temperature at which

the water speciation reaction in the melt can no longer maintain equilibrium), whereas the method described here determines the cooling rate over the last minutes to hours before quenching: The total length of the cooling histories recorded by the Siqueiros and Galapagos melt inclusions ranges from ~40 seconds (submarine inclusion Gal-AHA2-27) to just over one hour (submarine inclusion Gal-AHA2-24), with most melt inclusions having cooling histories ~5 minutes in length. The cooling rates determined in this study are also consistent with simple conductive cooling (in a semi-infinite half space with a constant boundary condition – see Appendix I) at distances of a few centimeters from the air-lava or water-lava interface.

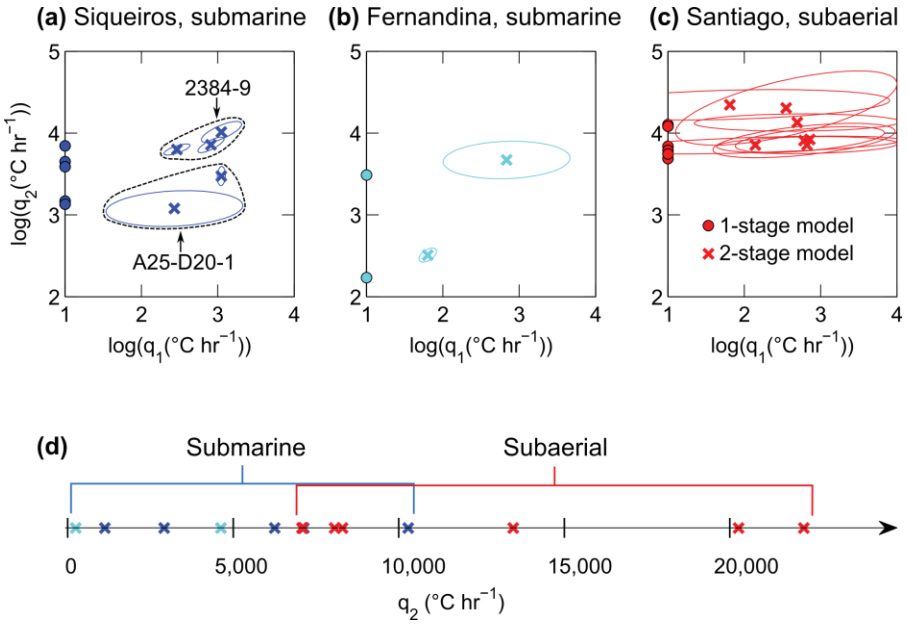

Figure 10 $\log_{10}(q_1)$-$\log_{10}(q_2)$ 95% confidence error ellipses for all of the melt inclusions that were measured with 2 μm point spacing. For each melt inclusion, 100 best fits were determined for 100 different MgO concentration profiles (created by adding normally distributed noise to the original data – see section 6.3.5). The median values of $\log_{10}(q_1)$ and $\log_{10}(q_2)$ determined via this method are marked by crosses. The colored circles plotted along $\log_{10}(q_1)=1$ are the results of the single-stage linear cooling model. The best-fit cooling rate determined by the single-stage linear cooling model (colored circles) tends to be similar to but systematically low relative to the best-fit values for $\log_{10}(q_2)$ (colored crosses), and the relative order of best-fit cooling rates is successfully predicted by the single-stage model. The 95% confidence error ellipses do not all overlap, suggesting that the melt inclusions underwent distinguishable thermal histories and that this inversion method is capable of resolving these differences. **(a)** Submarine Siqueiros melt inclusions. All samples in this panel are from one of two locations (see Table S1 in Appendix I): Siq7 and Siq8 are from dredge A25-D20-1; Siq13, Siq15 and Siq16 were collected during an Alvin submersible dive, and the thermal histories of melt inclusions from these different locations group together. **(b)** Submarine Fernandina melt inclusions. Symbols as in (a). **(c)** Subaerially quenched Santiago melt inclusions. These inclusions are generally small (radii ~25–55 μm) and tend to be well-described by single-stage cooling histories (e.g., Gal-STG-17 on Fig. 9), so their $\log_{10}(q_1)$-$\log_{10}(q_2)$ error ellipses for the 2-stage cooling model are relatively poorly constrained. **(d)** Values of q_2 for Siqueiros, Fernandina, and Santiago melt inclusions. Cooling rates determined for the subaerially quenched melt inclusions extend from the high end of cooling rates found for the submarine inclusions to much higher values.

The two-stage linear cooling histories determined by the model described above are not unique; other functional forms for the cooling history are also able to fit the data. However, for some of the melt inclusions in this sample suite, the MgO data are best fit by a two-stage cooling history with an initial slow stage of cooling followed by rapid cooling, so it is natural to ask what the petrological significance of these two stages might be. One possibility is that the first (i.e., slow) cooling stage corresponds to the journey of the host olivine crystals through the magmatic conduit and/or the interior of a lava flow, and that the second (i.e., fast) cooling stage represents the quenching of the melt upon eruption (i.e, against seawater in the case of the Siqueiros pillow rim phenocrysts and the phenocrysts from the Fernandina submarine eruption; or against air in the case of the subaerial Santiago phenocrysts).

In summary, the measured MgO concentration profiles in the melt inclusions suggest more complex thermal histories than single-stage cooling. This information cannot be readily quantified by calorimetric geospeedometry (e.g., Wilding et al. 2000; Nichols et al. 2009), and although the geospeedometer based on the reaction kinetics of $H_2O + O \leftrightarrow 2OH$ can provide hints about a more complicated thermal history (e.g., Zhang et al. 1995), it has not yet been used to infer quantitatively such thermal histories. In the following two subsections we further test the two-stage linear cooling model implied by MgO concentrations in melt inclusions.

6.3.7. Testing the two-stage linear cooling model – 1. Multiple inclusions in a single olivine

Several olivines contain more than one inclusion, and in a few cases, the radii of the two inclusions differ by a factor of >1.5. Such pairs of melt inclusions provide opportunities to test the robustness of our modeling and the derived cooling histories, since both melt inclusions in a pair must have experienced identical thermal histories, and thus we should be able to find a single thermal history that is capable of describing the MgO profiles of both melt inclusions.

The MgO concentrations measured by electron microprobe across melt inclusions Siq1-19a and Siq1-19b are plotted in Figure 11b. The two inclusions have radii of ~110 μm and 175 μm, respectively, and the central concentration of MgO in the small inclusion is lower than that in the large inclusion. Assuming that both inclusions trapped the same parental melt composition, this suggests that the depletion of MgO during cooling and crystallization of olivine had time to affect the center of the smaller inclusion, but affected the center of the large inclusion to a lesser extent (or not at all). We fit MgO profiles in both melt inclusions simultaneously to the two-stage linear cooling model, requiring the thermal history parameters and the starting concentration of

MgO to be the same for both inclusions. As demonstrated in Figure 11b, a two-stage linear cooling history (Figure 11a) results in an excellent match to the MgO concentration profiles in both melt inclusions.

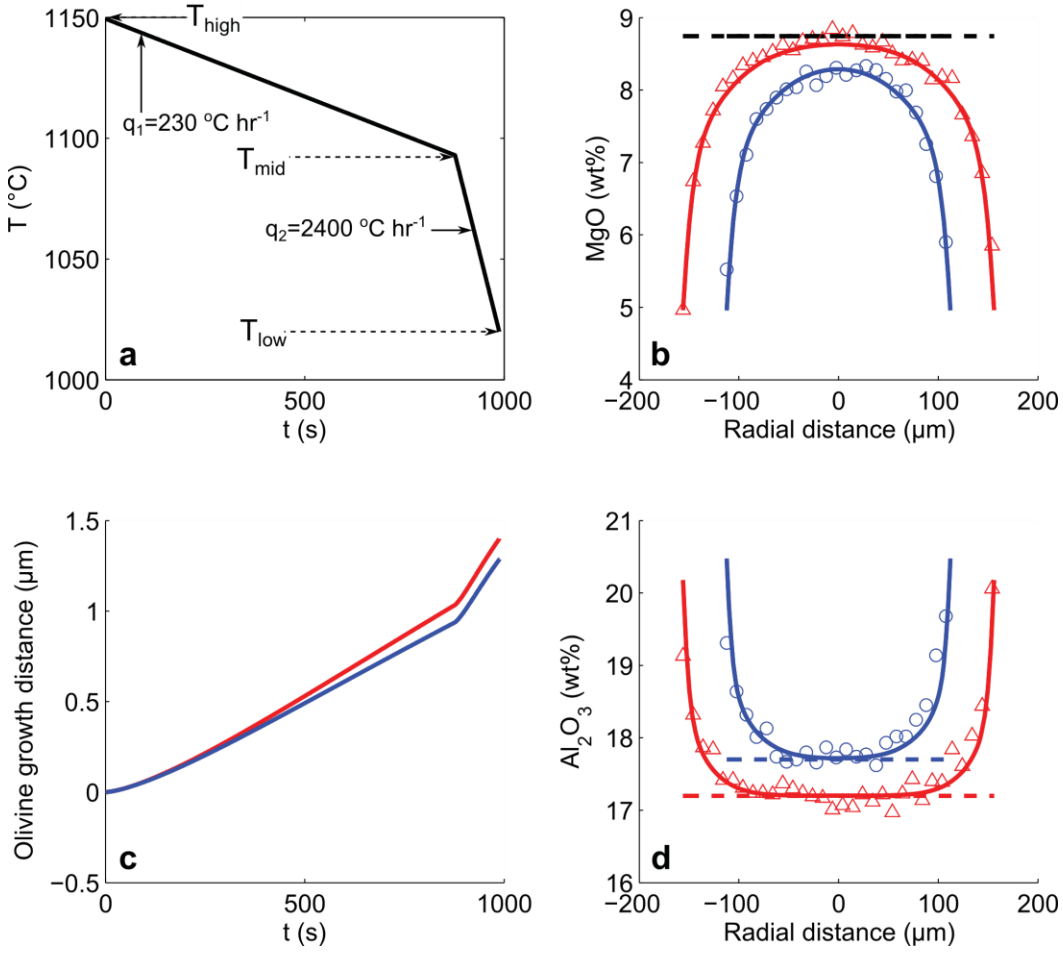

Figure 11 (a) Best-fit two-stage linear cooling history for melt inclusions Siq1-19a and Siq1-19b (hosted in the same olivine crystal; see Figure 1). **(b)** Results of fitting MgO in melt inclusions Siq1-19a (triangles) and Siq1-19b (circles) using the two-stage linear cooling model. MgO concentration profiles in both inclusions were fit simultaneously to find the best-fit thermal history shown in (a). The initial concentration of MgO was assumed to be the same for both inclusions (dashed black line). **(c)** Olivine growth distance in inclusions Siq1-19a (red) and Siq1-19b (blue) in response to the thermal history in (a). **(d)** Forward model of Al_2O_3 diffusion in Siq1-19a (red) and Siq1-19b (blue) using the best-fit thermal history determined by fitting the MgO concentration profiles in these inclusions. The only free parameter in this model is the starting concentration of Al_2O_3 (red dashed line for Siq1-19a and blue dashed line for Siq1-19b).

6.3.8. Testing the two-stage linear cooling model – 2. Modeling zonation of Al_2O_3

As discussed in section 6.2, the concentration profiles of many of the major elements display features attributable to complex multicomponent diffusion effects. As such, the simple effective-binary-diffusion treatment used to model MgO diffusion cannot be applied to these elements. However, Al_2O_3 appears to be behaving simply; profiles of Al_2O_3 do not show uphill diffusion, and the width of the zonation in Al_2O_3 is compatible with measured values of effective binary diffusion coefficient for Al_2O_3 (e.g., Kress and Ghiorso 1995). Another simplifying factor in modeling Al_2O_3 diffusion in this system is that Al_2O_3 is highly incompatible in olivine, so the simplifying assumption can be made that Al_2O_3 is entirely excluded from the olivine crystallized on the walls of the melt inclusions during cooling.

We have designed a forward model of concurrent olivine crystallization and Al_2O_3 diffusion, using the two-stage linear thermal histories derived by fitting the MgO profiles as described in section 6.3.1 and section 6.3.5. First, the amount of olivine crystallized on the walls of the melt inclusion is calculated at each time step using mass balance arguments: The amount of MgO extracted from the melt at each time step is converted into a corresponding volume of olivine of a constant composition (containing 48 wt % MgO, chosen to match the compositions of the Siqueiros olivines). The volume of olivine crystallized is then divided by the surface area of the (assumed spherical) melt inclusion to estimate the distance propagated by the olivine crystallization front in the time step.

Once the olivine growth history was determined as described in the previous paragraph, we can calculate the effect that the crystallization front of olivine would have on the distribution of Al_2O_3 within the melt inclusion. The boundary condition at the edge of the melt inclusion then becomes the following expression of mass balance across the olivine-melt interface:

$$D\left.\frac{\partial C}{\partial r}\right|_{r=a} = V\left(C_{r=a} - C_{olivine}\right) \tag{4}$$

In this expression, D is the effective-binary-diffusion coefficient for Al_2O_3, V is the olivine growth rate, $C_{r=a}$ is the concentration of Al_2O_3 in the interface melt and $C_{olivine}$ is the concentration of Al_2O_3 in the olivine. Since we assume perfect incompatibility of Al_2O_3 in olivine, equation (4) simplifies to:

$$D\frac{\partial C}{\partial r}\bigg|_{r=a} = VC_{r=a} \quad (5)$$

We have used the temperature-dependent effective-binary-diffusion coefficient for Al_2O_3 given by Kress and Ghiorso (1995) to solve the spherical diffusion equation (equation (3)) subject to equation (5). We have used the cooling history derived from our fit to the MgO profiles across inclusions Siq1-19a and Siq1-19b to run a forward model of Al_2O_3 evolution within these melt inclusions. The results of this forward model compare well with the measured concentrations of Al_2O_3 across the melt inclusions (see Figure 11d). Note that we require the small inclusion to have a higher initial concentration of Al_2O_3 (by ~3% relative) than the large inclusion in order to obtain a good match between the model and the Al_2O_3 concentration in the inclusion center. This variability in starting concentrations is greater than the scatter of our electron microprobe analyses of Al_2O_3 based on replicate analyses of secondary standards (e.g., replicate analyses of basaltic glass VG2 vary within 0.5 relative percent for Al_2O_3 – see Online Resource 2) and could indicate that the melt inclusions trapped melts with different initial concentrations of Al_2O_3. The compositional trends seen in Figure 5 would appear to support this, since inclusion Siq1-19b has an anomalously high central concentration of Al_2O_3 for its size. Inclusion Siq1-19b also has a higher Sr/Sr* than Siq1-19a (based on unpublished data from Alberto Saal), and thus appears to have a signature of melt-plagioclase interaction (Danyushevsky et al. 2003), consistent with the elevated Al_2O_3 of this inclusion. The observed variability in starting concentrations of Al_2O_3 is also consistent with the variability of matrix glass compositions sampled from the A-B fault of the Siquerios Fracture Zone (2–3 relative percent for Al_2O_3; Perfit et al. (1996)). However, it could also indicate a small mismatch between the temperature dependent diffusivity of MgO from Chen and Zhang (2008), which was used to constrain the cooling history, and the temperature-dependent diffusivity of Al_2O_3 determined by Kress and Ghiorso (1995); i.e., in order for this model to work perfectly, these two diffusivities must be both precise and accurate to a degree that would be unusual for the determination of diffusion coefficients in magmatic systems. Another possibility is that the smaller melt inclusion is cut slightly off-center, thus sampling more of the diffusive boundary layer, which would elevate its measured Al_2O_3 concentration (see discussion in section S2.6 of Appendix I).

It should be emphasized that the Al_2O_3 forward model described above has no free parameters other than the small adjustment made to the initial concentration of Al_2O_3 in the smaller inclusion. In this context, we regard the success of the model in reproducing the Al_2O_3 profiles in this pair of inclusions as significant.

6.4. Relationship between inclusion size and composition in the center of the inclusion

As described in section 4 and illustrated in Figure 5, there is a relationship between the glass composition measured in the center of an inclusion and the radius of the inclusion. The simple explanation of this relationship is that the composition at the center of the inclusion preserves the initial melt composition until the leading edge of the propagating boundary layer reaches the center. Thus, all other things being equal, there is a critical radius for each oxide below which the measured composition at the inclusion center will be influenced by olivine fractionation and diffusion in the melt and above which the initial melt composition will be preserved; moreover, we expect that this critical radius will be larger for components with higher diffusion coefficients because the leading edge of the boundary layer propagates farther for such elements. In this section we explore this effect quantitatively for the Siqueiros melt inclusions using the model described above.

We have run a simulation of a representative single-stage linear cooling history (2200 °C/hr over 10 minutes) for five model melt inclusions with an assumed initial composition close to the composition of the largest melt inclusions in the Siqueiros suite (the composition is listed in the caption to Figure 13) and with radii ranging from 10 to 150 μm (Figure 12). Al_2O_3, CaO, and Na_2O were assumed to be perfectly incompatible in olivine, and temperature dependent effective binary diffusion coefficients of Al_2O_3 and CaO were taken from Kress and Ghiorso (1995). The results of this simulation are plotted as red curves on Figure 5. The shapes of the model curves correspond to the qualitative expectations described in the previous paragraph. A good match between the model and the data is achieved for MgO, Al_2O_3, and CaO using this simple approach, despite the fact that CaO is affected by uphill diffusion, which has been neglected in this model. For Na_2O, two different approaches were attempted: First, an effective binary diffusion coefficient of Na_2O from Kress and Ghiorso (1995) was used. This method gave a good match to the trend of central Na_2O versus inclusion size (solid red line on Figure 5), but was unable to reproduce the magnitude of the observed enrichment of Na_2O at the edges of the melt inclusions (e.g., Figure 2). Based on the observation that the Na_2O profiles have similar shapes to the profiles of Al_2O_3 (section 6.2) we ran the simulation a second time for Na_2O, this time using the diffusion coefficient of Al_2O_3 (Kress and Ghiorso 1995) in place of the diffusion coefficient of Na_2O. This second approach gave a good match to the trend of central concentration with inclusion size (dashed red line on Figure 5) and also reproduced the observed enrichment of Na_2O at the edges of the melt inclusions (not shown).

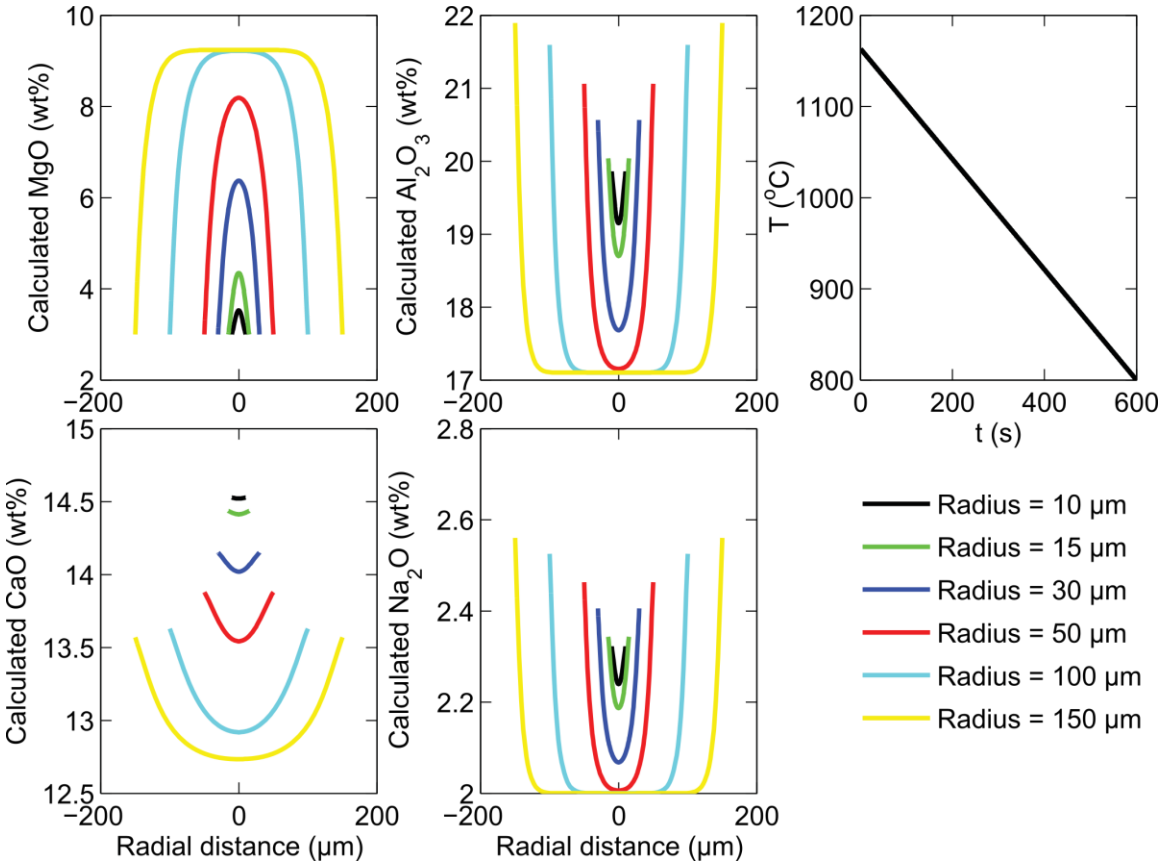

Figure 12 Forward model simulation to illustrate the response of melt inclusions of different sizes to the same single-stage thermal history (2200 °C/hr from 1160 to 800 °C over 10 minutes). Results of this simulation are also plotted as red curves in Figure 5. A cooling rate of 2200 °C/hr was chosen for this simulation because it provides a good match to the data in Figure 5, and because it is within the range of cooling rates determined by the single-stage linear cooling model for the Siqueiros melt inclusions (Figure 10a and Appendix I). See section 6.4 for discussion.

Trends of melt inclusion composition with size have been reported by Anderson (1974), who noted that olivine-hosted melt inclusions with diameters <~25 μm had compositions that differed from the compositions of larger inclusions. It was proposed by Roedder (1984) that small inclusions could trap volumetrically more of the compositional boundary layer around the host crystal during melt inclusion formation than large inclusions, which might explain the anomalous compositions of the small inclusions observed by Anderson (1974). However, the success of our post-entrapment boundary layer diffusion model in describing compositional trends of MgO, Al_2O_3, CaO, and Na_2O suggests that the variability of melt inclusion compositions with size can be explained without requiring small and large melt inclusions to trap significantly different melt compositions. This result agrees with the experimental study of Faure and Schiano (2005), who

found that inclusions in polyhedral olivines (like the Siqueiros and Galapagos olivines considered in this study) trap melts that lie on the liquid line of descent of their parental magmas.

An important implication of our observations is that the central composition of a melt inclusion may be diffusively fractionated from an olivine control line linking the initial trapped melt composition to the measured composition. For example, it can be seen from Figure 5 that Siqueiros melt inclusions with radii of ~50 μm have been significantly depleted in MgO and enriched in CaO by propagation of the diffusive boundary layer into their centers. However, the enrichment of Al_2O_3 and Na_2O at the edges of these inclusions has not yet had a significant impact on their central compositions. This means that the central composition of zoned melt inclusions in which the boundary layer has propagated to the inclusion center cannot be accurately corrected for post-entrapment olivine crystallization by simply moving the melt composition along an olivine control line until it reaches Fe/Mg equilibrium with the host crystal. The importance of this effect depends on the magnitude of the divergence of the central compositions of melt inclusions from olivine control lines as a result of diffusive fractionation. This issue is explored in Figure 13, where we plot the central compositions of Siqueiros melt inclusions (from this study and from Danyushevsky et al. (2003)) alongside a diffusive fractionation trend calculated by the model described above (in red) and an olivine control line calculated using MELTS (in blue; Ghiorso and Sack (1995); Smith and Asimow (2005)). For Na_2O, the scatter in the data prevents discrimination between the two processes. However, the diffusive fractionation model successfully captures the curvature in the Al_2O_3 and CaO data from this study. The shape of the FeO* vs. MgO trend significantly diverges from the olivine control line, however, we cannot model quantitatively the effects of diffusive fractionation on the MgO-FeO* trend. This is due to complications introduced by the effects of multicomponent diffusion on FeO* (Zhang et al. 1989; Chen and Zhang 2008), a poorly constrained boundary condition for FeO*, and the unknown distribution of Fe^{2+} and Fe^{3+} within the inclusions. Nevertheless, the fact that FeO* appears to diffuse more slowly than MgO (Figure 2 and Figure 5) would result in an initial decrease in MgO at the inclusion center without a corresponding decrease in FeO* followed by a falloff in both oxides until, for sufficiently small inclusions, the composition at the center of the inclusions eventually closely approximates the highly fractionated end of the simple olivine control line (i.e., when the inclusion has nearly homogenized with respect to these elements), and this is the overall shape of the MgO-FeO* trend observed in the actual inclusions. Another implication of chemical zonation in melt inclusions (even those for which the boundary layer has not propagated to their center) is that slightly off-center analyses of a melt inclusion

(either due to uncertainty in beam position or due to the polished section through the inclusion being slightly off center) can also give results that are diffusively fractionated relative to simple olivine crystallization, leading to potential inaccuracies in reconstructing unfractionated melt inclusion compositions by addition of olivine. Experimental homogenization of melt inclusions could correct for this effect (e.g., Danyushevsky et al. 2002a). Alternatively, the compositions of well-characterized, chemically zoned melt inclusions could be numerically integrated and averaged in order to correct for diffusive fractionation of their compositions.

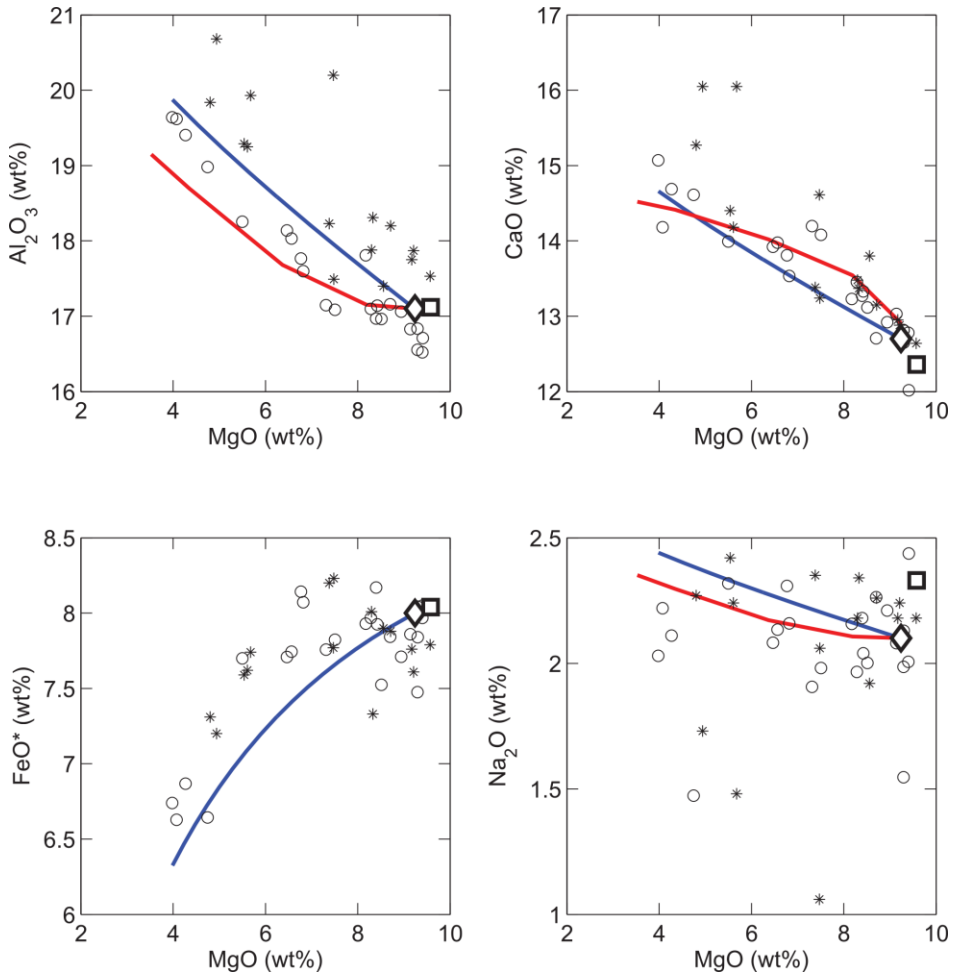

Figure 13 Comparison of central compositions of Siqueiros melt inclusions with a diffusive fractionation trend (for the same cooling history described in the caption to Figure 12) and an olivine control line calculated using MELTS. Circles are data from this study; stars are data from Danyushevsky et al. (2003); the large diamond is the starting composition for both the diffusive fractionation calculation and the MELTS calculation (all in wt. %: SiO_2=49.6, Al_2O_3 = 17.1, FeO* = 8.0, MgO = 9.24, CaO = 12.7, Na_2O = 2.1, TiO_2 = 0.9, MnO = 0.14, K_2O = 0.03, P_2O_5 = 0.07, Cr_2O_3 = 0.06, H_2O = 0.06); the large square is the composition of pillow rim glass from sample ALV-2384-3 (Perfit et al. 1996); red curves are the results of the diffusive fractionation calculation; blue curves are olivine control lines, calculated using MELTS. See section 5.4 for discussion.

6.5. Zonation of volatile elements

As described in section 5, zonation of H_2O (likely dissolved as hydroxyl based on spectroscopic measurements of glasses; Stolper (1982)), S, Cl, and F was observed in several of the Siqueiros melt inclusions (e.g., Figure 4). Given the incompatibility of these species in olivine, we were expecting that their concentrations would increase at the edges of the inclusions as observed for other incompatible elements (e.g., Al). However, although Cl and S show the expected behavior, concentrations of H_2O and F *decrease* towards the edges of the inclusions. We consider here two hypotheses to explain the decrease in H_2O and F toward the inclusion edge: (1) H_2O and F could be diffusing 'uphill' (i.e., against their own concentration gradients) due to coupling with other components in the melt as we have observed for Ca and Fe; see section 6.2). (2) The gradients in H_2O and F within the melt inclusions could reflect loss of these components into and/or through the olivine host.

The similarity between the shapes of concentration profiles of H_2O and F in the Siqueiros inclusions (Figure 4 and Appendix II), despite the ~1 order of magnitude difference between their experimentally determined diffusion coefficients (Zhang and Stolper 1991; Alletti et al. 2007), and the apparent uphill diffusion of H_2O and F observed in inclusion Siq16 (see Appendix II) suggest that multicomponent diffusion effects could be operating on these volatile species. In the three melt inclusions for which high quality volatile concentration data were obtained, concentration profiles of H_2O and F also have similar shapes to profiles of Fe, so it is possible that the distributions of H_2O and F are coupled to Fe. Although it is conceivable that the ionization of $^{16}O^{1}H$ and ^{19}F during the nanoSIMS measurements could have been affected by matrix effects (given the strong change in major element composition from the centers to the edges of the melt inclusions), the results of Hauri et al. (2002) suggest that calibration curves for H_2O and F are the same (up to 1.5 wt. % H_2O and up to ~600 ppm F) for basaltic, andesitic, and rhyolitic glass standards, so it seems unlikely that matrix effects are the cause of the similarity between the H_2O and F concentration profiles. It also seems unlikely that H_2O and F, as trace species in the Siqueiros melt inclusions, could affect each other's ionization efficiency.

The second possibility that we considered is that H_2O and F decrease toward the olivine host because they are being lost to the olivine during the final stages of cooling. Several studies have demonstrated that water can be lost from melt inclusions on timescales of hours to days (Hauri 2002; Massare et al. 2002; Portnyagin et al. 2008; Gaetani et al. 2012; Lloyd et al. 2012; Chen et al. 2013). Koleszar et al. (2009) found in their study of melt inclusions from the

Galapagos Islands (some of which were analyzed for this study) that the inclusions were open systems for both H_2O and F based on the observation that their H_2O and F concentrations were 'remarkably constant and comparable to those of the matrix glasses'. Another line of evidence to suggest that H_2O and F can be lost from olivine-hosted melt inclusions on eruptive time scales is the observation by Le Voyer et al. (2014) of concentration profiles of H_2O and F in olivine adjacent to melt inclusions, with higher concentrations of these components close to the olivine-melt interface and lower concentrations further from the inclusions, suggestive of loss of H_2O and F from the melt inclusions into and/or through the surrounding olivine. Although the Siqueiros melt inclusions are known to have very similar H_2O and F concentrations to their matrix glasses (Saal et al. 2002), suggesting that there might not be a large enough difference in the chemical potential of these species between the melt inclusions and the external melt to drive their diffusion out of the melt inclusions, it is possible that the H_2O and F concentrations of the melt inclusions increased in response to olivine crystallization on their walls in the final stages of eruption and cooling, thereby providing the driving force for H_2O and F loss from the melt inclusions into the surrounding olivine.

One way to distinguish between the two hypotheses outlined above would be to look for trends of H_2O and F concentrations with inclusion radius: If the enrichment of H_2O and F in the centers of the melt inclusions was a result of uphill diffusion, one might expect to see a negative correlation between the radii of the melt inclusions and the concentration of H_2O and F measured in their centers, since boundary layer enrichment of H_2O and F during olivine crystallization would more easily reach the centers of small inclusions than large inclusions. If, on the other hand, the shapes of the H_2O and F profiles were due to loss from the melt inclusions to the olivine, one would expect to see a positive correlation between the radii of the melt inclusions and the concentration of H_2O and F measured in their centers since smaller inclusions would lose more of their H_2O and F than larger ones. Although not enough H_2O and F data have been collected over the course of this study to discern a trend for the Siqueiros inclusions, Chen et al. (2013) observed a clear positive correlation between water concentration and inclusion radius in a suite of melt inclusions from La Sommata. This trend was interpreted to be a result of diffusive water loss from the melt inclusions, which would support our second hypothesis for the origin of the observed concentration gradients in H_2O and F. However, the two hypotheses described above are not mutually exclusive, and it is possible that the distribution of H_2O and F in the melt inclusions is being controlled by both uphill diffusion and synchronous loss of these components from the melt inclusions to the olivine.

7. Conclusions

We have observed zonation of major, minor, trace, and volatile elements in olivine-hosted melt inclusions from the Siqueiros Fracture Zone and the Galapagos Islands. Components that have a higher concentration in the host olivine than in the melt (MgO, FeO, Cr_2O_3, and MnO) are depleted at the edges of the zoned melt inclusions relative to their centers, whereas, except for CaO, H_2O, and F, components that have a lower concentration in the host olivine than in the melt (Al_2O_3, SiO_2, Na_2O, K_2O, TiO_2, S, and Cl) are enriched near the melt inclusion edges. This zonation forms in response to cooling and crystallization of olivine on the walls of the melt inclusions resulting in the formation of an olivine-depleted boundary layer in the adjacent melt. Competition between diffusive relaxation of this boundary layer into the centers of the melt inclusions and replenishment of the boundary layer by continued olivine crystallization produces concentration profiles in the melt inclusions. The widths and shapes of these concentration profiles vary from element to element, and depend on the diffusion coefficient of the element in the melt, its partition coefficient between melt and olivine, and the growth rate of the olivine.

Concentration profiles of some components in the melt inclusions exhibit multicomponent diffusion effects such as uphill diffusion (CaO, FeO) or slowing of the diffusion of typically rapidly diffusing components (Na_2O, K_2O) by coupling to slow diffusing components such as SiO_2 and Al_2O_3.

Concentrations of H_2O and F decrease towards the edges of some of the Siqueiros melt inclusions despite the incompatibility of these components in olivine. The similarity in the shapes and length scales of concentration profiles of H_2O and F suggests that this could be a multicomponent diffusion effect. However, it could also reflect rapid loss of H_2O and F into and/or through the olivine host, as expected based on previous work indicating that olivine-hosted melt inclusions do not always preserve their original H_2O and F concentrations.

A quantitative model of the time-dependence of concentration profiles in melt inclusions due to olivine crystallization and diffusion in the melt has been developed. This model was used along with simple cooling histories to fit observed MgO concentration profiles in olivine-hosted melt inclusions from the Siqueiros Fracture Zone and the Galapagos Islands. Best-fit cooling rates based on assuming single-stage linear cooling histories range from 150–13,000 °C hr^{-1}, consistent with previous constraints on the cooling rates of basaltic glasses. Cooling rates determined for seven subaerially quenched melt inclusions extend to higher values than those determined for

submarine melt inclusions. The amount of olivine overgrowth into the melt inclusions based on this modeling ranges from ~0.1 to ~2 μm.

MgO concentration profiles in some melt inclusions are better fit by a two-stage cooling history, with an initial stage of slow cooling (with cooling rates ranging from 64 to 1100 °C hr^{-1}) and a second stage of more rapid cooling (with cooling rates ranging from 320 to 22,000 °C hr^{-1}). The total time scales of cooling determined by the two-stage linear cooling model range from ~40 seconds to just over one hour.

The model has been successfully tested by fitting MgO and Al_2O_3 concentration profiles in pairs of melt inclusions of different size trapped in a single olivine grain that must have experienced identical cooling histories.

Awareness and characterization of zonation in melt inclusions is important for the correct interpretation of melt inclusion compositions. Even in some of the largest inclusions analyzed in this study, the propagation inward by diffusion of concentration profiles generated by olivine crystallization during the last 10^1–10^2 minutes of an eruption is able to influence the centers of the melt inclusions. An implication of this diffusive chemical zonation is that analyses of zoned melt inclusions, even if made near the centers of the inclusions, can be diffusively fractionated from the liquid line of differentiation of their parental melts. Experimental homogenization of melt inclusions could correct for this effect. Alternatively, the compositions of well-characterized, chemically zoned melt inclusions could be numerically integrated and averaged in order to correct for diffusive fractionation of their compositions. The model developed here is able to reproduce observed trends of melt composition in the centers of melt inclusions vs. inclusion size for MgO, Al_2O_3, CaO, and Na_2O.

Every melt inclusion analyzed during the course of this study is strongly chemically zoned. Additionally, we found reports of chemical zonation in picritic melt inclusions from Mt Shasta (Anderson 1974), in high-Ca boninitic inclusions from the Tonga arc (Danyushevsky et al. 2002b), in inclusions from the Sommata cinder cone on Vulcano Island in the Aeolian arc (Mercier 2009), and in inclusions of Mid-Atlantic ridge pillow basalt (Colin et al. 2012). Chemical zonation has also recently been observed in melt inclusions from Hawaii and the 1974 eruption of Volcán de Fuego (personal communication from Terry Plank, David Ferguson, and Alexander Lloyd). The observation of chemical zonation in melt inclusions from ridge, hotspot, and arc magmas suggests that this is a widespread phenomenon that could be useful for

constraining thermal histories of melt inclusions from a variety of magmatic/tectonic settings and that could also provide insights as a natural diffusion experiment.

8. Acknowledgements

We would like to thank Nicole Métrich and Leonid Danyushevsky for their thoughtful reviews, and Jon Blundy for editorial handling of the manuscript. We are grateful to Mike Baker for many encouraging and insightful discussions, and for editing the manuscript. We are also grateful for useful discussions with Paul Asimow, John Maclennan, and Madeleine Humphries. This work was funded by U.S. National Science Foundation Grants EAR-0739091 (AF), EAR-1019440 (YZ), and OCE-0962195 (AS).

9. References

Albarede F, Bottinga Y (1972) Kinetic disequilibrium in trace element partitioning between phenocrysts and host lava. Geochimica et Cosmochimica Acta 36 (2):141-156. doi:10.1016/0016-7037(72)90003-8

Alletti M, Baker DR, Freda C (2007) Halogen diffusion in a basaltic melt. Geochimica et Cosmochimica Acta 71 (14):3570-3580

Anderson AT (1974) Evidence for a picritic, volatile-rich magma beneath Mt. Shasta, California. Journal of Petrology 15 (2):243

Armstrong JT (1988) Quantitative analysis of silicate and oxide minerals: Comparison of Monte Carlo, ZAF and $\phi(\rho z)$ procedures. In: Newbury DE (ed) Microbeam analysis—1988 San Francisco Press, San Francisco:239-246

Baker D (1990) Chemical interdiffusion of dacite and rhyolite: anhydrous measurements at 1 atm and 10 kbar, application of transition state theory, and diffusion in zoned magma chambers. Contributions to Mineralogy and Petrology 104 (4):407-423. doi:10.1007/bf01575619

Chen Y, Provost A, Schiano P, Cluzel N (2013) Magma ascent rate and initial water concentration inferred from diffusive water loss from olivine-hosted melt inclusions. Contributions to Mineralogy and Petrology 165 (3):525-541. doi:10.1007/s00410-012-0821-x

Chen Y, Zhang Y (2008) Olivine dissolution in basaltic melt. Geochimica et Cosmochimica Acta 72 (19):4756-4777. doi:10.1016/j.gca.2008.07.014

Chen Y, Zhang Y (2009) Clinopyroxene dissolution in basaltic melt. Geochimica et Cosmochimica Acta 73 (19):5730-5747

Colin A, Faure F, Burnard P (2012) Timescales of convection in magma chambers below the Mid-Atlantic ridge from melt inclusions investigations. Contributions to Mineralogy and Petrology 164 (4):677-691. doi:10.1007/s00410-012-0764-2

Cooper AR (1968) The use and limitations of the concept of an effective binary diffusion coefficient for multi-component diffusion. Mass Transport in Oxides 296:79-84

Costa F, Dungan M (2005) Short time scales of magmatic assimilation from diffusion modeling of multiple elements in olivine. Geology 33 (10):837-840. doi:10.1130/g21675.1

Cottrell E, Spiegelman M, Langmuir CH (2002) Consequences of diffusive reequilibration for the interpretation of melt inclusions. Geochem Geophys Geosyst 3. doi:10.1029/2001gc000205

Danyushevsky LV, Della-Pasqua FN, Sokolov S (2000) Re-equilibration of melt inclusions trapped by magnesian olivine phenocrysts from subduction-related magmas: petrological implications. Contributions to Mineralogy and Petrology 138 (1):68-83. doi:10.1007/pl00007664

Danyushevsky LV, Leslie RAJ, Crawford AJ, Durance P (2004) Melt inclusions in primitive olivine phenocrysts: the role of localized reaction processes in the origin of anomalous compositions. Journal of Petrology 45 (12):2531-2553

Danyushevsky LV, McNeill AW, Sobolev AV (2002a) Experimental and petrological studies of melt inclusions in phenocrysts from mantle-derived magmas: an overview of techniques, advantages and complications. Chem Geol 183 (1–4):5-24. doi:10.1016/s0009-2541(01)00369-2

Danyushevsky LV, Perfit MR, Eggins SM, Falloon TJ (2003) Crustal origin for coupled'ultra-depleted'and'plagioclase'signatures in MORB olivine-hosted melt inclusions: evidence from the Siqueiros Transform Fault, East Pacific Rise. Contributions to Mineralogy and Petrology 144 (5):619-637

Danyushevsky LV, Sokolov S, Falloon TJ (2002b) Melt Inclusions in Olivine Phenocrysts: Using Diffusive Re-equilibration to Determine the Cooling History of a Crystal, with Implications for the Origin of Olivine-phyric Volcanic Rocks. Journal of Petrology 43 (9):1651-1671. doi:10.1093/petrology/43.9.1651

Efron B, Tibshirani R (1985) The bootstrap method for assessing statistical accuracy. DTIC Document,

Faure F, Schiano P (2005) Experimental investigation of equilibration conditions during forsterite growth and melt inclusion formation. Earth and Planetary Science Letters 236 (3–4):882-898. doi:10.1016/j.epsl.2005.04.050

Gaetani GA, O'Leary JA, Shimizu N, Bucholz CE, Newville M (2012) Rapid reequilibration of H_2O and oxygen fugacity in olivine-hosted melt inclusions. Geology 40 (10):915-918

Gaetani GA, Watson EB (2002) Modeling the major-element evolution of olivine-hosted melt inclusions. Chem Geol 183 (1-4):25-41. doi:10.1016/s0009-2541(01)00370-9

Geist DJ, Fornari DJ, Kurz MD, Harpp KS, Adam Soule S, Perfit MR, Koleszar AM (2006) Submarine Fernandina: Magmatism at the leading edge of the Galápagos hot spot. Geochemistry, Geophysics, Geosystems 7 (12):n/a-n/a. doi:10.1029/2006gc001290

Ghiorso MS, Sack RO (1995) Chemical mass transfer in magmatic processes IV. A revised and internally consistent thermodynamic model for the interpolation and extrapolation of liquid-solid equilibria in magmatic systems at elevated temperatures and pressures. Contributions to Mineralogy and Petrology 119 (2):197-212

Hauri E (2002) SIMS analysis of volatiles in silicate glasses, 2: isotopes and abundances in Hawaiian melt inclusions. Chem Geol 183 (1–4):115-141. doi:http://dx.doi.org/10.1016/S0009-2541(01)00374-6

Hauri E, Wang J, Dixon JE, King PL, Mandeville C, Newman S (2002) SIMS analysis of volatiles in silicate glasses: 1. Calibration, matrix effects and comparisons with FTIR. Chemical Geology 183 (1–4):99-114. doi:http://dx.doi.org/10.1016/S0009-2541(01)00375-8

Jambon A (1982) Tracer diffusion in granitic melts: experimental results for Na, K, Rb, Cs, Ca, Sr, Ba, Ce, Eu to 1300 C and a model of calculation. Journal of Geophysical Research: Solid Earth (1978–2012) 87 (B13):10797-10810

Koleszar AM, Saal AE, Hauri EH, Nagle AN, Liang Y, Kurz MD (2009) The volatile contents of the Galapagos plume; evidence for H_2O and F open system behavior in melt inclusions. Earth and Planetary Science Letters 287 (3–4):442-452. doi:10.1016/j.epsl.2009.08.029

Kress VC, Ghiorso MS (1995) Multicomponent diffusion in basaltic melts. Geochimica et Cosmochimica Acta 59 (2):313-324. doi:10.1016/0016-7037(94)00286-u

Lagarias J, Reeds J, Wright M, Wright P (1998) Convergence Properties of the Nelder--Mead Simplex Method in Low Dimensions. SIAM Journal on Optimization 9 (1):112-147. doi:doi:10.1137/S1052623496303470

Lasaga AC (1979) Multicomponent exchange and diffusion in silicates. Geochimica et Cosmochimica Acta 43 (4):455-469. doi:http://dx.doi.org/10.1016/0016-7037(79)90158-3

LaTourrette T, Wasserburg GJ, Fahey AJ (1996) Self diffusion of Mg, Ca, Ba, Nd, Yb, Ti, Zr, and U in haplobasaltic melt. Geochimica et Cosmochimica Acta 60 (8):1329-1340. doi:10.1016/0016-7037(96)00015-4

Le Voyer M, Asimow PD, Mosenfelder JL, Guan Y, Wallace PJ, Schiano P, Stolper EM, Eiler JM (2014) Zonation of H2O and F Concentrations around Melt Inclusions in Olivines. Journal of Petrology. doi:10.1093/petrology/egu003

Lesher C, Hervig R, Tinker D (1996) Self diffusion of network formers (silicon and oxygen) in naturally occurring basaltic liquid. Geochimica et Cosmochimica Acta 60 (3):405-413

Liang Y (2010) Multicomponent diffusion in molten silicates: theory, experiments, and geological applications. Reviews in Mineralogy and Geochemistry 72 (1):409-446

Lloyd AS, Plank T, Ruprecht P, Hauri EH, Rose W (2012) Volatile loss from melt inclusions in pyroclasts of differing sizes. Contributions to Mineralogy and Petrology:1-25

Long GL, Winefordner JD (1983) Limit of Detection A Closer Look at the IUPAC Definition. Analytical Chemistry 55 (7):712A-724A. doi:10.1021/ac00258a724

Lundstrom C (2003) An experimental investigation of the diffusive infiltration of alkalis into partially molten peridotite: implications for mantle melting processes. Geochemistry, Geophysics, Geosystems 4 (9)

Lundstrom CC (2000) Rapid diffusive infiltration of sodium into partially molten peridotite. Nature 403 (6769):527-530

Maclennan J, McKenzie D, Grönvold K, Shimizu N, Eiler J, Kitchen N (2003) Melt mixing and crystallization under Theistareykir, northeast Iceland. Geochemistry, Geophysics, Geosystems 4 (11)

Massare D, Métrich N, Clocchiatti R (2002) High-temperature experiments on silicate melt inclusions in olivine at 1 atm: inference on temperatures of homogenization and H_2O concentrations. Chem Geol 183 (1):87-98

Matzen AK, Baker MB, Beckett JR, Stolper EM (2011) Fe–Mg partitioning between olivine and high-magnesian melts and the nature of Hawaiian parental liquids. Journal of Petrology 52 (7-8):1243-1263

Maury RC, Bizouard H (1974) Melting of acid xenoliths into a basanite: An approach to the possible mechanisms of crustal contamination. Contributions to Mineralogy and Petrology 48 (4):275-286. doi:10.1007/bf00951335

McDonough WF, Sun Ss (1995) The composition of the Earth. Chem Geol 120 (3–4):223-253. doi:http://dx.doi.org/10.1016/0009-2541(94)00140-4

Mercier M (2009) Abondance et signification de l'eau dans les magmas mafiques. Développement de la spectroscopie vibrationnelle (Raman et FTIR). Thesis, Université Paris Sud-Paris XI,

Morgan DJ, Blake S, Rogers NW, DeVivo B, Rolandi G, Macdonald R, Hawkesworth CJ (2004) Time scales of crystal residence and magma chamber volume from modelling of diffusion profiles in phenocrysts: Vesuvius 1944. Earth and Planetary Science Letters 222 (3–4):933-946. doi:http://dx.doi.org/10.1016/j.epsl.2004.03.030

Mosenfelder JL, Le Voyer M, Rossman GR, Guan Y, Bell DR, Asimow PD, Eiler JM (2011) Analysis of hydrogen in olivine by SIMS: Evaluation of standards and protocol. Am Miner 96 (11-12):1725-1741. doi:10.2138/am.2011.3810

Mungall JE, Romano C, Dingwell DB (1998) Multicomponent diffusion in the molten system K 2 O-Na 2 O-Al 2 O 3 -SiO 2 -H 2 O. Am Miner 83 (7-8):685-699

Nichols ARL, Potuzak M, Dingwell DB (2009) Cooling rates of basaltic hyaloclastites and pillow lava glasses from the HSDP2 drill core. Geochimica et Cosmochimica Acta 73 (4):1052-1066. doi:10.1016/j.gca.2008.11.023

Perfit MR, Fornari DJ, Ridley WI, Kirk PD, Casey J, Kastens KA, Reynolds JR, Edwards M, Desonie D, Shuster R, Paradis S (1996) Recent volcanism in the Siqueiros transform fault: picritic basalts and implications for MORB magma genesis. Earth and Planetary Science Letters 141 (1–4):91-108. doi:10.1016/0012-821x(96)00052-0

Portnyagin M, Almeev R, Matveev S, Holtz F (2008) Experimental evidence for rapid water exchange between melt inclusions in olivine and host magma. Earth and Planetary Science Letters 272 (3):541-552

Putirka KD (2008) Thermometers and barometers for volcanic systems. Reviews in Mineralogy and Geochemistry 69 (1):61-120

Qin ZW, Lu FQ, Anderson AT (1992) Diffusive Reequilibration of Melt and Fluid Inclusions. Am Miner 77 (5-6):565-576

Richter FM, Davis AM, DePaolo DJ, Watson EB (2003) Isotope fractionation by chemical diffusion between molten basalt and rhyolite. Geochimica et Cosmochimica Acta 67 (20):3905-3923. doi:http://dx.doi.org/10.1016/S0016-7037(03)00174-1

Roedder E (1984) Fluid Inclusions, vol 12. Reviews in Mineralogy. Mineralogical Society of America,

Roeder P, Emslie R (1970) Olivine-liquid equilibrium. Contributions to Mineralogy and Petrology 29 (4):275-289

Ryerson FJ, Hess PC (1978) Implications of liquid-liquid distribution coefficients to mineral-liquid partitioning. Geochimica et Cosmochimica Acta 42 (6):921-932. doi:http://dx.doi.org/10.1016/0016-7037(78)90103-5

Saal AE, Hauri EH, Langmuir CH, Perfit MR (2002) Vapour undersaturation in primitive mid-ocean-ridge basalt and the volatile content of Earth's upper mantle. Nature 419 (6906):451-455. doi:http://www.nature.com/nature/journal/v419/n6906/suppinfo/nature01073_S1.html

Saal AE, Kurz MD, Hart SR, Blusztajn JS, Blichert-Toft J, Liang Y, Geist DJ (2007) The role of lithospheric gabbros on the composition of Galapagos lavas. Earth and Planetary Science Letters 257 (3–4):391-406. doi:http://dx.doi.org/10.1016/j.epsl.2007.02.040

Sato H (1975) Diffusion coronas around quartz xenocrysts in andesite and basalt from Tertiary volcanic region in northeastern Shikoku, Japan. Contributions to Mineralogy and Petrology 50 (1):49-64. doi:10.1007/bf00385221

Smith PM, Asimow PD (2005) Adiabat_1ph: A new public front-end to the MELTS, pMELTS, and pHMELTS models. Geochem Geophys Geosyst 6 (2):Q02004

Smith V, Tiller W, Rutter J (1955) A mathematical analysis of solute redistribution during solidification. Canadian Journal of Physics 33 (12):723-745

Stolper E (1982) Water in silicate glasses: An infrared spectroscopic study. Contributions to Mineralogy and Petrology 81 (1):1-17. doi:10.1007/bf00371154

Sugawara T (2000) Empirical relationships between temperature, pressure, and MgO content in olivine and pyroxene saturated liquid. Journal of Geophysical Research 105 (B4):8457-8472

Taylor M, Brown GE (1979) Structure of mineral glasses—I. The feldspar glasses $NaAlSi_3O_8$, $KAlSi_3O_8$, $CaAl_2Si_2O_8$. Geochimica et Cosmochimica Acta 43 (1):61-75

Tiller WA, Jackson KA, Rutter JW, Chalmers B (1953) The redistribution of solute atoms during the solidification of metals. Acta Metallurgica 1 (4):428-437. doi:http://dx.doi.org/10.1016/0001-6160(53)90126-6

Trial AF, Spera FJ (1994) Measuring the multicomponent diffusion matrix: Experimental design and data analysis for silicate melts. Geochimica et Cosmochimica Acta 58 (18):3769-3783. doi:10.1016/0016-7037(94)90362-x

Watson EB (1982) Basalt contamination by continental crust: Some experiments and models. Contributions to Mineralogy and Petrology 80 (1):73-87. doi:10.1007/bf00376736

Watson EB, Jurewicz SR (1984) Behavior of alkalies during diffusive interaction of granitic xenoliths with basaltic magma. The Journal of Geology:121-131

White WM, McBirney AR, Duncan RA (1993) Petrology and geochemistry of the Galápagos Islands: portrait of a pathological mantle plume.

Wilding M, Dingwell D, Batiza R, Wilson L (2000) Cooling rates of hyaloclastites: applications of relaxation geospeedometry to undersea volcanic deposits. Bulletin of Volcanology 61 (8):527-536. doi:10.1007/s004450050003

Xu Z, Zhang Y (2002) Quench rates in air, water, and liquid nitrogen, and inference of temperature in volcanic eruption columns. Earth and Planetary Science Letters 200 (3):315-330

Zhang Y (1993) A modified effective binary diffusion model. Journal of Geophysical Research: Solid Earth (1978–2012) 98 (B7):11901-11920

Zhang Y (2008) Geochemical kinetics. Princeton University Press, Princeton, N.J.

Zhang Y (2010) Diffusion in minerals and melts: theoretical background. Reviews in Mineralogy and Geochemistry 72 (1):5-59

Zhang Y, Jenkins J, Xu Z (1997) Kinetics of the reaction $H_2O+O\rightarrow 2OH$ in rhyolitic glasses upon cooling: Geospeedometry and comparison with glass transition. Geochimica et Cosmochimica Acta 61 (11):2167-2173

Zhang Y, Ni H, Chen Y (2010) Diffusion data in silicate melts. Reviews in Mineralogy and Geochemistry 72 (1):311-408

Zhang Y, Stolper EM (1991) Water diffusion in a basaltic melt. Nature 351 (6324):306-309

Zhang Y, Stolper EM, Ihinger P (1995) Kinetics of the reaction $H_2O+O=2OH$ in rhyolitic and albitic glasses: Preliminary results. Am Miner 80:593-612

Zhang Y, Walker D, Lesher CE (1989) Diffusive crystal dissolution. Contributions to Mineralogy and Petrology 102 (4):492-513. doi:10.1007/bf00371090

Zhang Y, Xu Z, Behrens H (2000) Hydrous species geospeedometer in rhyolite: improved calibration and application. Geochimica et Cosmochimica Acta 64 (19):3347-3355

Zhang Y, Xu Z, Zhu M, Wang H (2007) Silicate melt properties and volcanic eruptions. Reviews of Geophysics 45 (4):n/a-n/a. doi:10.1029/2006rg000216

APPENDICES AND ELECTRONIC SUPPLEMENTARY MATERIALS

Appendix I contains further description of the model, an error analysis, model inversion tests, a comparison of the single-stage and two-stage cooling models, conductive cooling calculations, a table of sample names/locations, a table summarizing the results of fitting MgO concentration profiles in Siqueiros and Galapagos melt inclusions to both single-stage and two-stage linear thermal histories, and 17 additional figures. Appendix I is referred to as 'Online Resource 1' in the online version of this paper.

Appendix II contains further discussion of our nanoSIMS data, including a table of compositions of glass standards, two sets of calibration curves, and concentration profiles of H_2O, S, Cl, and F in melt inclusions Siq16 and Siq7. Appendix II is referred to as 'Online Resource 3' in the online version of this paper.

Online Resource 2: File *ESM2.xls* contains supplementary electron microprobe data and backscattered electron images of all of the melt inclusions used in this study. This file is available online at *doi:10.1007/s00410-014-1030-6*

The MATLAB code used to constrain thermal histories of chemically zoned melt inclusions is available from the first author on request.

Chapter 5

FUTURE WORK

The results described in Chapters 2, 3, and 4 of this thesis have highlighted several interesting avenues for future exploration, and some of these are described below.

Calibration of the 3550 cm^{-1} FTIR peak for measuring absolute concentrations of water in lunar basalt

As described in Chapter 2, a challenge for the study of water concentrations in glasses by FTIR is the determination of the molar absorption coefficient, ε. A common approach to this problem is to calibrate ε for every glass composition of interest via the measurement of water concentrations by an independent technique such as Karl Fischer Titration. The molar absorptivity of the 3550 cm^{-1} FTIR peak has not been calibrated for the Apollo 15 "yellow glass" or the iron-free basaltic analogue composition considered in this thesis. Calibration of the molar absorption coefficient of the 3550 cm^{-1} FTIR peak for these compositions would be a significant experimental undertaking that would require a series of piston cylinder experiments (to synthesize glasses with relatively high water concentrations for independent measurement by Karl Fisher Titration or manometry), however, this would be a valuable contribution that would improve the accuracy of water concentration measurements in natural and experimental lunar glasses (e.g., current SIMS measurements of water concentration in lunar glasses (Saal et al. 2008; Hauri et al. 2011; Wetzel et al. 2015) are standardized using a series of terrestrial silicate glasses and may be subject to matrix effects).

Some authors have looked for relationships between glass compositional parameters and ε (Dixon et al. 1995; Mandeville et al. 2002; Mercier et al. 2010), however, while such relationships are well defined for the 5200 cm^{-1} and 4500 cm^{-1} water peaks, the relationship between ε_{3550} and glass composition appears to be more complex and currently less predictable. This may in part be due to the scatter in experimentally determined values of ε_{3550}. Other authors have developed a theoretical framework for the prediction of ε (Paterson 1982; Libowitzky and Rossman 1997). However, such treatments have had limited success in predicting ε_{3550} for the wide variety of geologically significant silicate melt compositions. Much further work is required in this area: (a) to improve the accuracy and precision of experimental determinations of ε; and (b) to understand the effects of melt composition and structure on ε_{3550}.

Further exploration of water diffusion in silicate melts at low water concentrations

The experiments presented in Chapter 3 of this thesis have demonstrated that the diffusivity of water (D^*_{water}) is constant in lunar basalt containing 10s to 100s of ppm water, and that D^*_{water} is independent of $p\mathrm{H_2}/p\mathrm{H_2O}$ under the conditions of our experiments. From these observations, we infer that hydroxyl is the diffusing species and that $D^*_{\mathrm{water}} = D_{\mathrm{OH}}$ under the conditions of our experiments. It would be interesting to extend our experiments to higher water concentrations, where the speciation model predicts that the diffusion of molecular water would begin to dominate (Zhang and Stolper 1991; Zhang et al. 1991). If the modified speciation model of (Ni et al. 2012) is correct, then such experiments would define a curved relationship between D^*_{water} and water concentration for lunar basalt from which the value of $D_{\mathrm{H_2O_m}}$ could be determined (assuming a value for the equilibrium constant, K_{eq}, which has not been experimentally determined for basaltic melts).

All of the experiments presented in Chapter 3 were conducted at 1350 °C. If we conducted further experiments at different temperatures then we could obtain the activation energy for D^*_{water} in lunar basalt, which would be useful for modeling the degassing of lunar basaltic pyroclasts (Saal et al. 2008). Knowledge of the activation energies for water diffusion in our LG and AD melt compositions may also help us to understand the mechanism(s) of water diffusion in each melt and perhaps their relationship to the melt composition (Behrens and Nowak 1997).

Diffusion of carbon in lunar basalt

The recent detection by SIMS of dissolved carbon in natural lunar basaltic glasses (Wetzel et al. 2015) suggests that it may be possible to use a similar experimental setup to that used in Chapter 3 of this thesis to generate concentration gradients of carbon in lunar basalt under conditions relevant to lunar volcanic eruptions, and to use such gradients to determine the diffusivity of carbon in lunar basaltic melts. This could be an important contribution for understanding the role of carbon in driving lunar fire fountain eruptions (Fogel and Rutherford 1995; Nicholis and Rutherford 2009; Rutherford and Papale 2009).

Application and calibration of the melt inclusion geospeedometer presented in Chapter 4

Chapter 4 presents a method for determining syneruptive cooling histories of olivine-hosted melt inclusions. In its current form, the method is calibrated using the results of the olivine dissolution experiments of (Chen and Zhang 2008). Limited applications of the method to natural

samples from the Siqueiros Fracture Zone and the Galapagos Islands show that the method has the potential to define multi-stage thermal histories and to distinguish between subaqueously and subaerially quenched samples (see Chapter 4). However, the accuracy of the technique is hard to assess.

Incoming graduate student Lee Saper is currently working on a new calibration of the melt inclusion geospeedometer by conducting controlled cooling rate experiments on olivine-hosted melt inclusions at 1 atm and then characterizing the resultant MgO gradients in the inclusions. It is hoped that Lee's results will vastly improve the accuracy of the technique and will help us to interpret the MgO concentration gradients observed in natural olivine-hosted melt inclusions.

In order to apply the melt inclusion geospeedometer to arc magmas, we need to explore the effects of syneruptive water loss from melt inclusions on the crystallization of olivine and generation of MgO gradients in the inclusions. Water loss and cooling are both drivers of olivine crystallization on the walls of melt inclusions, so it is likely that the correct application of the melt inclusion geospeedometer to hydrous magmas will need to account for syneruptive water loss (Gaetani et al. 2012; Bucholz et al. 2013; Lloyd et al. 2013; Le Voyer et al. 2014).

In the past few years, several short-timescale ascent chronometers have been developed (Demouchy et al. 2006; Wade et al. 2008; Chen et al. 2013; Le Voyer et al. 2014). These relatively new methods allow the estimation of magma ascent rates in the last few minutes to hours of a volcanic eruption. An interesting avenue of future research will be to apply these methods alongside the melt inclusion geospeedometer described in Chapter 4 of this thesis to assess syneruptive conditions in volcanic conduits.

Are melt inclusions isotopically zoned?

In Chapter 4, we document chemical zonation of major, minor, trace and volatile elements in olivine-hosted melt inclusions. However, we have not yet looked for zonation of isotopes inside melt inclusions. It is possible that melt inclusions could be zoned in important chemical tracers such as D/H. They may also be zoned in isotopes of magnesium and/or iron, which could provide constraints on the growth histories of their host olivine crystals (Teng et al. 2011).

References

Behrens H, Nowak M (1997) The mechanisms of water diffusion in polymerized silicate melts. Contributions to Mineralogy and Petrology 126 (4):377-385. doi:10.1007/s004100050257

Bucholz CE, Gaetani GA, Behn MD, Shimizu N (2013) Post-entrapment modification of volatiles and oxygen fugacity in olivine-hosted melt inclusions. Earth and Planetary Science Letters 374 (0):145-155. doi:http://dx.doi.org/10.1016/j.epsl.2013.05.033

Chen Y, Provost A, Schiano P, Cluzel N (2013) Magma ascent rate and initial water concentration inferred from diffusive water loss from olivine-hosted melt inclusions. Contributions to Mineralogy and Petrology 165 (3):525-541. doi:10.1007/s00410-012-0821-x

Chen Y, Zhang Y (2008) Olivine dissolution in basaltic melt. Geochimica et Cosmochimica Acta 72 (19):4756-4777. doi:10.1016/j.gca.2008.07.014

Demouchy S, Jacobsen SD, Gaillard F, Stern CR (2006) Rapid magma ascent recorded by water diffusion profiles in mantle olivine. Geology 34 (6):429-432. doi:10.1130/g22386.1

Dixon JE, Stolper EM, Holloway JR (1995) An Experimental Study of Water and Carbon Dioxide Solubilities in Mid-Ocean Ridge Basaltic Liquids. Part I: Calibration and Solubility Models. Journal of Petrology 36 (6):1607-1631

Fogel RA, Rutherford MJ (1995) Magmatic volatiles in primitive lunar glasses: I. FTIR and EPMA analyses of Apollo 15 green and yellow glasses and revision of the volatile-assisted fire-fountain theory. Geochimica et Cosmochimica Acta 59 (1):201-215. doi:http://dx.doi.org/10.1016/0016-7037(94)00377-X

Gaetani GA, O'Leary JA, Shimizu N, Bucholz CE, Newville M (2012) Rapid reequilibration of H_2O and oxygen fugacity in olivine-hosted melt inclusions. Geology 40 (10):915-918

Hauri EH, Weinreich T, Saal AE, Rutherford MC, Van Orman JA (2011) High Pre-Eruptive Water Contents Preserved in Lunar Melt Inclusions. Science 333 (6039):213-215. doi:10.1126/science.1204626

Le Voyer M, Asimow PD, Mosenfelder JL, Guan Y, Wallace PJ, Schiano P, Stolper EM, Eiler JM (2014) Zonation of H_2O and F Concentrations around Melt Inclusions in Olivines. Journal of Petrology. doi:10.1093/petrology/egu003

Libowitzky E, Rossman GR (1997) An IR absorption calibration for water in minerals. American Mineralogist 82 (11):1111-1115

Lloyd A, Plank T, Ruprecht P, Hauri E, Rose W (2013) Volatile loss from melt inclusions in pyroclasts of differing sizes. Contributions to Mineralogy and Petrology 165 (1):129-153. doi:10.1007/s00410-012-0800-2

Mandeville CW, Webster JD, Rutherford MJ, Taylor BE, Timbal A, Faure K (2002) Determination of molar absorptivities for infrared absorption bands of H2O in andesitic glasses. American Mineralogist, vol 87. doi:10.2138/am-2002-0702

Mercier M, Muro AD, Métrich N, Giordano D, Belhadj O, Mandeville CW (2010) Spectroscopic analysis (FTIR, Raman) of water in mafic and intermediate glasses and glass inclusions. Geochimica et Cosmochimica Acta 74 (19):5641-5656. doi:http://dx.doi.org/10.1016/j.gca.2010.06.020

Ni H, Xu Z, Zhang Y (2012) Hydroxyl and Molecular H_2O Diffusivity in a Haploandesitic Melt. Geochimica et Cosmochimica Acta

Nicholis MG, Rutherford MJ (2009) Graphite oxidation in the Apollo 17 orange glass magma: Implications for the generation of a lunar volcanic gas phase. Geochimica et Cosmochimica Acta 73 (19):5905-5917. doi:http://dx.doi.org/10.1016/j.gca.2009.06.022

Paterson M (1982) The determination of hydroxyl by infrared absorption in quartz, silicate glasses, and similar materials. Bulletin de la Societe Francaise de Mineralogie 105:20-29

Rutherford MJ, Papale P (2009) Origin of basalt fire-fountain eruptions on Earth versus the Moon. Geology 37 (3):219-222. doi:10.1130/g25402a.1

Saal AE, Hauri EH, Cascio ML, Van Orman JA, Rutherford MC, Cooper RF (2008) Volatile content of lunar volcanic glasses and the presence of water in the Moon's interior. Nature 454 (7201):192-195. doi:http://www.nature.com/nature/journal/v454/n7201/suppinfo/nature07047_S1.html

Teng F-Z, Dauphas N, Helz RT, Gao S, Huang S (2011) Diffusion-driven magnesium and iron isotope fractionation in Hawaiian olivine. Earth and Planetary Science Letters 308 (3–4):317-324. doi:http://dx.doi.org/10.1016/j.epsl.2011.06.003

Wade JA, Plank T, Hauri EH, Kelley KA, Roggensack K, Zimmer M (2008) Prediction of magmatic water contents via measurement of H2O in clinopyroxene phenocrysts. Geology 36 (10):799-802. doi:10.1130/g24964a.1

Wetzel DT, Hauri EH, Saal AE, Rutherford MJ (2015) Carbon content and degassing history of the lunar volcanic glasses. Nature Geosci advance online publication. doi:10.1038/ngeo2511 http://www.nature.com/ngeo/journal/vaop/ncurrent/abs/ngeo2511.html#supplementary-information

Zhang Y, Stolper EM (1991) Water diffusion in a basaltic melt. Nature 351 (6324):306-309

Zhang Y, Stolper EM, Wasserburg GJ (1991) Diffusion of water in rhyolitic glasses. Geochimica et Cosmochimica Acta 55 (2):441-456. doi:10.1016/0016-7037(91)90003-n

-

A p p e n d i x I

CHEMICAL ZONATION IN OLIVINE-HOSTED MELT INCLUSIONS

M.E. Newcombe[a], A. Fabbrizio[a, b], Youxue Zhang[c], C. Ma[a], M. Le Voyer[a, d], Y. Guan[a], J. Eiler[a], A. Saal[e], E.M. Stolper[a]

* Previously published as **Online Resource 1** in Newcombe, M. E., et al. "Chemical zonation in olivine-hosted melt inclusions."*Contributions to Mineralogy and Petrology* 168.1 (2014): 1-26.

doi:10.1007/s00410-014-1030-6

Contents

- Effect of overestimating T_{high}

Section S4: Comparison of the 1-stage and 2-stage models

Section S5: Comparison of cooling rates determined by our model with cooling rates expected by conductive cooling.

Section S6: Additional references

Table S1: Sample names and collection locations of melt inclusions

Table S2: Cooling history parameters determined using both 1-stage and 2-stage linear cooling models for all of the melt inclusions listed in Table S1, except those melt inclusions for which the MgO concentration profiles consisted of <5 points

Figures S1 – S17

S1. Further description of the model

S1.1 Forward model of MgO evolution in melt inclusions in response to cooling and crystallization of olivine

In this section, we describe in detail the equations used to calculate the distribution of MgO in an olivine-hosted melt inclusion in response to a given thermal history.

Diffusion of MgO in an (assumed spherical) melt inclusion is described by the radial component of the diffusion equation in spherical polar coordinates:

$$\frac{\partial C}{\partial t} = D\left(\frac{\partial^2 C}{\partial r^2} + \frac{2}{r}\frac{\partial C}{\partial r}\right) \quad \text{(S1)}$$

In equation (S1), C is the concentration of MgO (in wt. %), t is time (in seconds), r is the radial distance measured from the center of the melt inclusion (in meters) and D is the diffusivity of MgO (in m^2s^{-1}). D is assumed to be temperature-dependent, but not concentration- or radius-dependent. The initial condition ($C(r,0) = C_0$) and the boundary conditions ($C(a,t) = C_b$ and $\partial C/\partial r|_{r=0} = 0$, where a is the radius of the melt inclusion and C_b may depend on time) are discussed in the main text (see "Using zonation in melt inclusions to derive thermal histories: Description of the forward model").

By making the substitution $w=Cr$, equation (S1) can be reduced to the one dimensional diffusion equation:

$$\frac{\partial w}{\partial t} = D\frac{\partial^2 w}{\partial r^2} \tag{S2}$$

Equation (S2) can be non-dimensionalized using the following transformations:

$$x = \frac{r}{a} \tag{S3}$$

$$u = \frac{rC}{aC_0} = \frac{xC}{C_0} \tag{S4}$$

$$dt' = \frac{Ddt}{a^2} \tag{S5}$$

Applying transformations (S3) and (S4), equation (S2) becomes

$$\frac{a^2}{D}\frac{\partial u}{\partial t} = \frac{\partial^2 u}{\partial x^2} \tag{S6}$$

Similarly, the initial condition transforms to

$$u(x,0) = x \tag{S7}$$

and the boundary condition at $r=a$ becomes

$$u(x=1,t') = \frac{C_b}{C_0} \tag{S8}$$

Equations (S6)–(S8) are discretized using a forward-time, centered-space (FTCS) explicit scheme:

$$u_i^{j+1} = u_i^j + \frac{\Delta t'}{(\Delta x)^2}\left(u_{i+1}^j + u_{i-1}^j - 2u_i^j\right) \tag{S9}$$

In equation (S9), we adopt the notation $u(i\Delta x, j\Delta t) = u_i^j$. Since D is temperature-dependent (and therefore time-dependent in the cooling rate calculations we have done), $\Delta t'$ is calculated using the geometric average of $D(t)$ and $D(t+\Delta t)$:

$$\Delta t' = \frac{\sqrt{D(t)\cdot D(t+\Delta t)}}{a^2}\Delta t \tag{S10}$$

Once $u(x,t')$ has been calculated, $C(r,t)$ is found via the following transformation:

$$C(r,t) = \frac{uC_0}{x} \tag{S11}$$

S1.2 Calculation of olivine growth rate

As described in the main text (see "Testing the two-stage linear cooling model – 2. Modeling zonation of Al_2O_3"), the amount of olivine crystallized on the walls of the melt inclusion is calculated at each time step using mass balance arguments: The amount of MgO extracted from the melt at each time step is converted into a corresponding volume of olivine of a constant composition. The volume of olivine crystallized is then divided by the surface area of the (assumed spherical) melt inclusion to estimate the distance propagated by the olivine crystallization front during the time step.

The amount of MgO (in wt. %) extracted from the melt at each time step (ΔM) is calculated as follows:

$$\Delta M = \int \Delta C \cdot \mathrm{d}\left(\frac{4\pi r^3}{3}\right) \tag{S12}$$

ΔM calculated in equation (S12) can be converted into olivine growth distance using the following expression:

$$L = \frac{\Delta M}{C_{olivine} - C_0} \cdot \frac{\rho_{melt}}{\rho_{olivine}} \cdot \frac{1}{4\pi a^2} \tag{S13}$$

The first term of equation (S13) converts the mass of MgO extracted from the melt into a mass of olivine produced ($C_{olivine}$ is the mass fraction of MgO (in wt. %) in olivine, which is assumed to be a constant; C_0 is the initial mass fraction of MgO (in wt. %) measured in the melt inclusion). The second term converts this mass of olivine produced into a volume, accounting for the difference between the density of the melt (ρ_{melt}) and the density of the olivine ($\rho_{olivine}$), both of which are assumed to be constant with values of 2700 kg m^{-3} and 3250 kg m^{-3} respectively. The final term of equation (S13) divides the volume of olivine produced by the surface area of the melt inclusion in order to determine the width of the olivine growth rim on the walls of the inclusion (*L*). Knowledge of the width of the olivine growth rim at each time step was then used to calculate the olivine growth rate (*V*):

$$V = \frac{\Delta L}{\Delta t} \tag{S14}$$

S2. Errors introduced by assumptions of the model

S2.1 Assumption that olivine-melt boundary is fixed: Recalculation of MgO profiles in the melt inclusions considering olivine growth

The model described in section S1.1 uses a boundary condition that is fixed at *r=a* and does not consider the effects of olivine growth on the walls of the melt inclusion. Typical modeling results for the natural inclusions studied in the paper show a post-entrapment growth of about 1 μm thick olivine layer (meaning boundary motion of 1 μm) in a melt inclusion of about 100 μm radius. That is, the total effect of the boundary motion is not significant. In each time step, the boundary motion is of the order 0.001 μm. Accounting for the boundary motion would significantly increase the complexity of the programing. In this section we describe another method for calculating the distribution of MgO in the melt inclusions, this time considering the effects of olivine growth. The approach taken for this recalculation of MgO is similar to the calculation of Al_2O_3 evolution in the melt inclusions described in the main text (see "Testing the two-stage linear cooling model – 2. Modeling zonation of Al_2O_3").

As described in section S1.1, we wish to solve the radial component of the spherical diffusion equation (equation S1), with a homogenous concentration of MgO as the initial condition. We define the new boundary condition as follows:

$$D\frac{\partial C}{\partial r}\bigg|_{r=a} = V\left(C_{r=a} - C_{olivine}\right) = -\left(K_d - 1\right)VC_{r=a} \tag{S15}$$

In equation (S15), $C_{r=a}$ is the concentration of MgO (in wt. %) in the melt at the olivine-melt interface, $C_{olivine}$ is the concentration of MgO (in wt. %) in the olivine, and K_d is the olivine-melt partition coefficient ($K_d = C_{olivine}/C_{r=a}$). K_d is known to be dependent on melt composition and temperature (e.g., Roeder and Emslie 1970) and likely changes from ~4 to ~9 during cooling and crystallization of the melt inclusions. However, for simplicity, we assume a constant value of $K_d = 6$ throughout the simulation.

The boundary condition in equation S15 can be non-dimensionalized following transformations (S3)–(S4) and introducing the dimensionless variable *b*, defined as $b = aV / D$:

$$\left.\frac{\partial u}{\partial x}\right|_{x=1} = \left(1 - b\left[K_d - 1\right]\right)u_{x=1} \tag{S16}$$

The numerical scheme is the same as described in section S1.1, apart from the boundary condition at $x = 1$, which becomes:

$$u_{N,j} = \frac{u_{N-1,j}}{1 - \left(1 - b\left[K_d - 1\right]\right)\Delta x} \tag{S17}$$

In equation (S17), $u_{N,j}$ represents the dimensionless concentration of MgO in the melt at the olivine-melt interface.

The results of the recalculation of MgO with boundary condition (S16) are shown in Figure S1 for melt inclusion Siq16. The two methods of calculating MgO are in good agreement. The slight differences between the two calculations that are visible near the inclusion edge are probably primarily due to the inaccuracy of the assumption that K_d has a constant value of 6.

S2.2 Use of Chen and Zhang (2008) thermometer

The largest source of error in our calculation of cooling histories is the choice of relationship between temperature and MgO concentration in the melt at the olivine-melt interface. There are many published parameterizations of the temperature dependence of the MgO concentration of melt in equilibrium with olivine (e.g., Roeder and Emslie 1970; Sugawara 2000; Chen and Zhang 2008; Putirka 2008; Matzen et al. 2011) and also many published olivine-liquid equilibria models (Ford et al. 1983; Beattie 1993; Ghiorso and Sack 1995). We opted for the relatively simple model of Chen and Zhang (2008), which, in addition to simplicity, also has the advantage that the experiments used to determine the temperature dependence of MgO concentration in the liquid at the olivine-melt interface were also used to determine the temperature dependence of the diffusivity of MgO in the melt (which is another important parameter in our model). However, the MgO-temperature parameterization of Chen and Zhang (2008) was determined by fitting the results of olivine dissolution experiments (dissolution of San Carlos olivine with a composition of

$Fo_{90.6}$ into a basaltic melt), and so an implied assumption of this model is that the olivine has a constant composition of $Fo_{90.6}$. In reality, the composition of the host olivine of the Siqueiros melt inclusions decreases from ~Fo_{90} far (i.e., ≳20 μm) from the inclusions to ~Fo_{88} at the olivine-melt interface (as measured by electron microprobe – see Online Resource 2), and the composition of the olivine adjacent to the Galapagos inclusions can be as low as Fo_{82}. If higher resolution analytical techniques were available, it is possible that an even stronger decrease in the forsterite content of the olivine could be observed right at the olivine-melt interface. This assumption in the modeling that the temperature reflects MgO partitioning between the melt and San Carlos olivine is thus an imperfect approximation and results in an underestimation of the temperature of equilibration of the olivine and melt at the outer edges of the melt inclusions (~50°C for the Siqueiros inclusions and up to ~70°C for the Galapagos inclusions).

To assess the potential error in our best-fit cooling rates introduced by using the Chen and Zhang (2008) parameterization rather than a more complex olivine-liquid equilibrium model, we ran a MELTS fractional crystallization calculation on the composition measured in the centre of inclusion Siq16, and we used the results of this calculation to predict the MgO concentration in the melt as olivine crystallization progressed. We found that for a given MgO concentration in equilibrium with olivine, MELTS predicts temperatures that are ~50 °C higher than temperatures predicted by the Chen and Zhang (2008) parameterization. We fit inclusion Siq16 using the MgO-temperature relationship found by MELTS, and compare the results to fitting with the Chen and Zhang MgO-temperature relationship in Figures S2 and S3. We find that the best-fit cooling rates found using the MELTS MgO-temperature relationship are approximately a factor of two higher than the best-fit cooling rates found using the Chen and Zhang (2008) MgO-temperature parameterization (Figure S3). The quality of the fit to the MgO data in melt inclusion Siq16 is the same for both MgO-temperature relationships. Although the choice of MgO-temperature parameterization is a source of uncertainty for our cooling rate model, it does not alter the conclusions of the study.

S2.3 Error in the calculated amount of olivine growth

The assumption of a constant olivine composition of $Fo_{90.6}$ affects not only the estimated temperature of olivine-melt equilibrium, but also affects the calculated mass of olivine growth during cooling and crystallization. As described in section S1.2, the amount of olivine growth is

calculated by mass balance of MgO loss from the melt inclusions. The composition of the growing olivine is an important parameter in this calculation: the more forsteritic the olivine is assumed to be, the less olivine can grow from a given mass of MgO. Since we have slightly overestimated the forsterite content of the growing olivine, we must also have underestimated the mass of olivine growth. Although the olivine growth rate does not affect the derived cooling histories, it does affect the calculated distribution of Al_2O_3 in the melt inclusions. We have used MELTS calculations (described in the previous section) to explore the likely magnitude of this affect for inclusion Siq16. The results are presented in Figures S4 and S5.

S2.4 Choice of T_{high}

As explained in the main text (see "Using zonation in melt inclusions to derive thermal histories"), two-stage linear cooling histories are defined by five parameters: A starting temperature (T_{high}), an intermediate temperature at which the cooling rate changes (T_{mid}), a final temperature (T_{low}), and two cooling rates (q_1 and q_2). In our model, we treat T_{mid}, q_1, and q_2 as free parameters, and T_{high} and T_{low} are calculated from measured MgO concentrations using equation (1). T_{low} is calculated using the lowest measured MgO concentration at the edge of each melt inclusion. Similarly, T_{high} is calculated using the initial concentration of MgO in each melt inclusion (see equation (1)). However, the initial concentration of MgO in the melt inclusions could be chosen in a number of ways, and this results in some uncertainty in the estimation of T_{high}. We considered four choices of initial MgO concentration:

i. **Initial MgO concentration calculated to be in equilibrium with the far-field olivine host:** This choice of initial condition results in high values of T_{high} (up to 1252 °C). The lack of MgO data between the initial concentration of MgO (up to 12.8 wt. % MgO) and the highest measured concentration of MgO in the melt inclusions (up to 9.5 wt. % MgO) results in the inversion problem for this choice of initial condition being very poorly constrained. The misfit between the model and the data is greater when this initial condition is applied than the misfit obtained using the initial conditions described below.

ii. **Initial MgO concentration chosen to match the composition of the matrix glass:** This choice of initial condition also results in high values of T_{high} for the Siqueiros melt inclusions, and therefore a poorly constrained inversion problem. The Galapagos matrix

glasses are more evolved than the melt inclusions, so this choice of initial condition would not be appropriate for the Galapagos melt inclusions.

iii. **Initial MgO concentration chosen as the highest measured MgO concentration in each individual melt inclusion:** This choice of initial condition results in lower values of T_{high} (up to 1171 °C) compared to method **i**. The inversion problem is well constrained with this choice of initial MgO concentration. However, choosing a different starting MgO concentration for each melt inclusion based on its highest measured MgO concentration results in the introduction of a bias in the fitting procedure, because small melt inclusions tend to have lower central concentrations of MgO than large inclusions (see Figure 5 in the main text).

iv. **Initial MgO concentration chosen as the highest MgO concentration measured among all melt inclusions from the same sample locality:** This is our preferred method of estimating the initial concentration of MgO in the melt inclusions and is explained in detail in the main text (see "Using zonation in melt inclusions to derive thermal histories: Description of the forward model").

S2.5 Choice of T_{low}

For the fitting procedure presented in the main text, the lowest temperature considered by the model (T_{low}) is the temperature corresponding to the lowest MgO concentration measured at the edges of each melt inclusion (except where pairs of inclusions were fit together, in which case, the lowest measured MgO in the pair of inclusions was used to calculate T_{low}). This temperature is typically ~1000 °C for the Siqueiros melt inclusions. An alternative way to set this temperature would be to allow the model to run all the way down to a temperature comfortably past the closure temperature for MgO diffusion (MgO diffusion becomes negligible in this system at ~700 °C over a timescale of 1 hour), or even to seawater temperature (~2 °C). We tried these methods of setting T_{low}, and found that it made little difference to the shapes of the model MgO curves (Figures S6 and S7). However, the misfit between the model and the MgO data in the melt inclusions was reduced when we set T_{low} to the temperature corresponding to the lowest MgO concentration measured at the edges of each melt inclusion, so we chose to adopt this approach

for the fitting presented in the main paper. We have tested the effect on the best-fit cooling rates for melt inclusion Siq16 determined by fixing T_{low} to 600 °C, and find that this assumption increases the best-fit value of q_1 by a factor of ~2, and increases the best-fit value of q_2 by a factor of ~3 (Figure S8).

It should be noted that our MgO concentration profiles provide little constraint as to how the melt inclusions cool from ~1000 °C to seawater temperature, and constraint of the cooling history over this temperature range would require much higher spatial resolution data at the edges of the melt inclusions than we are currently able to achieve with the electron microprobe. It is also possible that the assumption of equilibrium between the crystallizing olivine and the adjacent melt at these low temperatures may break down, such that the boundary condition assumed by our model is no longer applicable.

S2.6 Assumption that melt inclusions are cut through their centers

When preparing melt inclusions for this study, care was taken to expose the maximum possible surface area of the melt inclusions during polishing, such that the exposed sections of the melt inclusions passed approximately through their centers. However, for olivine crystals hosting multiple inclusions, it is difficult to cut every melt inclusion through its center, and it is likely that some of the inclusions were under- or over-exposed.

We explore the effect of an off-center cut through a melt inclusion on the resultant profiles of MgO and Al_2O_3 in Figure S9. When a chemically zoned melt inclusion is cut along a plane that is far from the center of the inclusion, it samples more of the diffusive boundary layer. Concentration profiles across such a plane will be relatively depleted in MgO and enriched in Al_2O_3. In the main text (see "Testing the two-stage linear cooling model – 2. Modeling zonation of Al_2O_3"), we calculate the distribution of Al_2O_3 across a pair of melt inclusions hosted in the same olivine crystal, and we find that the smaller inclusion of the pair requires a higher starting concentration of Al_2O_3 than the larger inclusion in order to match the data. Although it is likely in this case that the inclusions trapped different melt compositions (given the differences in Sr/Sr* between the inclusions, and the variability of Al_2O_3 in the Siqueiros inclusions more generally), it is also possible that an off-center cut through the smaller inclusion contributed to its elevated Al_2O_3 concentration.

S3. Inversion tests

We designed a number of inversion tests to answer the following questions:

- When given data from a melt inclusion with a known two-stage linear cooling history, does our inversion technique find the correct cooling history parameters?
- What is the effect of melt inclusion size on the ability of the inversion technique to find the correct cooling history parameters?
- What is the effect of changing the spatial resolution (i.e., the point spacing) of concentration measurements?
- What is the effect of overestimating the starting temperature?

We created synthetic MgO concentration data for melt inclusions with radii of 50 and 150 μm, by running the forward model described in the main text (see "Using zonation in melt inclusions to derive thermal histories: Description of the forward model") with T_{high}=1440 K, T_{mid}=1400 K, T_{low}=1300 K, q_1=600 K hr^{-1}, and q_2=6000 K hr^{-1}. The synthetic profiles were sampled at 2 and 10 μm point spacing.

We inverted the synthetic profiles using the technique described in the main text (see "Using zonation in melt inclusions to derive thermal histories: Inverting the MgO concentration profiles for two-stage linear cooling histories"). Noise was added to the synthetic data to create 100 "noisy" MgO concentration profiles, by assuming normally distributed data with 1σ=0.1 wt. % MgO. A best-fit two-stage linear cooling history was found for each of these noisy profiles. The cooling history parameters for the synthetic data were determined by calculating the median values of q_1, q_2, and T_{mid} found by the parametric bootstrap fitting procedure described in the main text. This process is illustrated in Figure S10 for a synthetic melt inclusion with a radius of 150 μm and a point spacing of 10 μm.

S3.1 Testing the accuracy of the inversion technique

In Figure S11, we present the results of inverting the MgO concentration profile across a model melt inclusion with a radius of 150 µm and a point spacing of 10 µm. The inversion technique returns cooling history parameters that are within 4% of their true values (parameter values returned by inversion: q_1=578.2 K/hr, q_2=6064 K/hr, T_{mid}=1400.3 K; true parameter values: q_1=600 K/hr, q_2=6000 K/hr, T_{mid}=1400 K). The best-fit values of q_1 and q_2 are not normally distributed, and tend to be skewed towards higher cooling rates, particularly for small melt inclusions with fewer data points; this is because, beyond a certain point, increasing the cooling rate to higher values has little effect on the resultant distribution of MgO within the melt inclusions. Due to this asymmetry in the distribution of best-fit parameters, we find that the median of the best-fit parameters is a better proxy for the true parameter values than the mean.

S3.1.1 Effect of melt inclusion size

We have tested the effect of melt inclusion size on the accuracy and precision of the inversion technique. The results are presented in Figure S12 for two model melt inclusions with different radii (50 and 150 µm) that both underwent the same thermal history (T_{high}=1440 K, T_{mid}=1400 K, T_{low}=1300 K, q_1=600 K hr^{-1}, and q_2=6000 K hr^{-1}). MgO concentrations across both melt inclusions were sampled at 10 µm intervals, such that the 150 µm inclusion contained three times as many data points as the 50 µm inclusion. The accuracy of the inversion technique was not greatly affected for the small inclusion: values of q_1, q_2 and T_{mid} determined by the inversion technique were within 6% of their true values. However, the precision of the inversion technique was lower for the 50 µm inclusion (precision can be assessed by the spread of best fits to noisy profiles in Figure S12, and the sizes of the 95% confidence ellipses).

S3.1.2 Effect of spatial resolution of MgO measurements

In this section, we explore the effect of the spacing of MgO concentration measurements in a melt inclusion on the accuracy and precision of our cooling history inversion technique. As explained in the main text (see the "Analytical techniques" section), in the early phases of the study, the electron microprobe beam diameter was set to 5 µm with a step size of 10 µm. In order to improve spatial resolution, later profiles were measured with a focused beam (with a nominal diameter of ~150 nm) and a step size of 1–2 µm.

To test for the effect of spatial resolution on our inversion technique, we ran a forward model for a melt inclusion with a radius of 150 μm with the following cooling history parameters: T_{high}=1440 K, T_{mid}=1400 K, T_{low}=1300 K, q_1=600 K hr^{-1}, and q_2=6000 K hr^{-1}. The resultant MgO concentration profile was sampled with a 2 μm point spacing ('high spatial resolution') and a 10 μm point spacing ('low spatial resolution'). Cooling histories were fit to both the high spatial resolution and the low spatial resolution profiles using our inversion technique, and the results are presented in Figure S13. The reduction of the step size from 10 to 2 μm leads to a significant reduction in the size of the 95% confidence ellipse around the best-fit cooling history parameters. For this reason, in the main text, we focus on the melt inclusions whose MgO concentrations were measured with high spatial resolution.

S3.1.3 Effect of overestimating T_{high}

As discussed above, we have used our forward model to create MgO data for a synthetic melt inclusion with a radius of 150 μm with the following cooling history parameters: T_{high}=1440 K, T_{mid}=1400 K, T_{low}=1300 K, q_1=600 K hr^{-1}, and q_2=6000 K hr^{-1}. We have assessed the effects on our inversion technique of overestimating T_{high} by inverting this synthetic MgO data assuming T_{high}=1480 K (instead of the true value of T_{high}=1440 K). The results of this inversion are shown in Figure S14. When T_{high} is overestimated, q_1 and q_2 are forced to take lower values. The value of q_1 must be low to allow sufficient diffusive relaxation of MgO to reproduce the flat MgO concentration profile across the center of this melt inclusion. The curvature at the edges of the profile must then be produced solely during the second stage of cooling. This forces q_2 to take a value that compromises between the high value required to reproduce the steep gradient near the olivine-melt interface and the lower value required to reproduce the shallowing of this gradient from edge to center.

S4. Comparison of the 1-stage and 2-stage models

Figure S15 compares the best-fit cooling rates from the second stage of the two-stage linear cooling model (q_2) with the cooling rates fit to the single-stage cooling model (q). Overall, the single-stage cooling rate correlates with the cooling rate during the second stage of cooling (q_2) in the two-stage model. For some inclusions (Siq7, Gal-AHA2-27, Gal-STG17, and Gal-STG-48; labeled in red on Figure S15), the two rates agree within error (where the error bars represent two

standard deviations), but for others (Gal-AHA2-24, Siq8, Siq13, Siq15, and Siq16; labeled in black on Figure S15), q_2 is higher than q by up to a factor of ~2. The latter inclusions are the ones for which the shallow central gradient in MgO concentration is most pronounced (Figure 9 of main paper), so they are less well described by the single-stage cooling model (i.e., the fits are poorer, see Figure S15b). In these cases, the single-stage cooling model has been forced to compromise between the low cooling rate required to fit the shallow MgO gradient in the center of the inclusions and the fast rate required to fit the sharp MgO gradient at the edges of the inclusions, explaining why the single stage rate is lower than q_2 (Figure S15c). For the inclusions that are well fit by the single-stage model, q and q_2 are similar (Figure S15c; labeled in red), as are the misfits of the two models (Figure S15b; labeled in red).

There is a bias in our fitting procedure for the single-stage cooling model that results in large melt inclusions being fit by lower cooling rates than small inclusions (Figure S15a). This effect can be understood in the context of the best-fit multi-stage cooling histories, which always have an initial period of slow cooling and a final stage of rapid cooling: In small inclusions, diffusion of MgO from the boundary layer produced during the final period of rapid cooling may reach the center of the inclusion and thereby erase nearly all evidence for the prior period of slow cooling. In large inclusions, however, the shallow central gradient of MgO produced during slow cooling can be preserved during the final stage of rapid cooling, because there may not be enough time for the MgO boundary layer produced at the edges of the melt inclusion during rapid cooling to propagate into the center of the inclusion. This would produce the correlation between single-stage cooling rates and inclusion size observed in Figure S15a for those inclusions not well fit by a single-stage cooling history (labeled in black). Note that this correlation does not exist for those inclusions that are well fit by the single-stage cooling model (labeled in red on Figure S15a), including the two subaerially erupted melt inclusions (Gal-STG-17 and Gal-STG-48), suggesting that the high cooling rates recorded by these two inclusions are not simply an artifact of their small size.

S5. Comparison of cooling rates determined by our model with cooling rates expected for conductive cooling

The results of a simple conductive cooling model are shown in Figure S16. For these calculations, the diffusivity of heat was assumed to be 1×10^{-6} m^2s^{-1}, and we used an analytical expression for diffusion in a semi-infinite medium (Crank 1975). The temperature at the interface between the lava and the seawater was held at a constant value of 2 °C, and the initial temperature of the lava was set to 1200 °C.

The results of this simple calculation show that the range of cooling rates determined for the Siqueiros melt inclusions by our technique (~300 – 10,000 °C/hr) is consistent with conductive cooling of the melt inclusions at distances of a few centimeters from the lava-water interface. The Siqueiros melt inclusions were sampled from pillow-rim glass, which typically extends no more than 1 – 2 cm from the lava-water interface, so the slightly greater distances from the lava-water interface implied by the conductive cooling model may reflect cooling during transport of the host olivine crystal from the interior to the edge of the pillow.

Cooling rates determined from fitting MgO concentration profiles in melt inclusions from a hornito on Santiago Island reach higher values (up to ~22,000 °C/hr) than those determined for the Siquieros melt inclusions. These higher values may reflect the small size of the pyroclasts (i.e., short distances from the melt inclusion to the lava-air interface) during this kind of eruption. The maximum cooling rates recorded by the Santiago inclusions are consistent with the passage of a conductive cooling front during cooling at a distance of 1 – 2 cm from the air-lava interface (Figure S16).

Table S1 Description of samples

Inclusion name	Sample ID	Saal et al. (2002) inclusion ID [a]	Locality	References [b]	EMP point spacing (µm)
Siq7	A25-D20-1	n/a	Siqueiros Fracture Zone	1, 2	2
Siq8	A25-D20-1	n/a	Siqueiros Fracture Zone	1, 2	2 and 10
Siq1-11a	2384-2	n/a	Siqueiros Fracture Zone	1, 2	10
Siq1-11b	2384-2	2-8-1	Siqueiros Fracture Zone	1, 2	10
Siq1-12a	2384-2	n/a	Siqueiros Fracture Zone	1, 2	10
Siq1-12b	2384-2	2-7-2	Siqueiros Fracture Zone	1, 2	10
Siq1-12c	2384-2	n/a	Siqueiros Fracture Zone	1, 2	10
Siq13	2384-9	n/a	Siqueiros Fracture Zone	1, 2	2
Siq15	2384-9	n/a	Siqueiros Fracture Zone	1, 2	2
Siq16	2384-9	n/a	Siqueiros Fracture Zone	1, 2	2
Siq1-19a	2384-2	2-3-1	Siqueiros Fracture Zone	1, 2	10
Siq1-19b	2384-2	2-3-2	Siqueiros Fracture Zone	1, 2	10
Siq1-24a	2384-3	n/a	Siqueiros Fracture Zone	1, 2	10
Siq1-24b	2384-3	3-10-2	Siqueiros Fracture Zone	1, 2	10
Siq1-24c	2384-3	3-10-1	Siqueiros Fracture Zone	1, 2	10
Siq2-47a	A25-D20-5	A-8-2	Siqueiros Fracture Zone	1, 2	10
Siq2-47b	A25-D20-5	A-8-1	Siqueiros Fracture Zone	1, 2	10
Siq2-52a	2384-9	9-1-2-2	Siqueiros Fracture Zone	1, 2	10
Siq2-52b	2384-9	9-1-2-1	Siqueiros Fracture Zone	1, 2	10
Siq2-53a	2384-9	9-1-1	Siqueiros Fracture Zone	1, 2	10
Siq2-53b	2384-9	n/a	Siqueiros Fracture Zone	1, 2	10
Siq3-56a	2384-6	n/a	Siqueiros Fracture Zone	1, 2	10
Siq3-56b	2384-6	6-3	Siqueiros Fracture Zone	1, 2	10
Siq3-65a	A25-D20-1	D-6-2	Siqueiros Fracture Zone	1, 2	10
Siq3-65b	A25-D20-1	D-6-3	Siqueiros Fracture Zone	1, 2	10
Siq3-65c	A25-D20-1	D-6-1	Siqueiros Fracture Zone	1, 2	10
Gal-AHA2-24	AHA D25C	n/a	Fernandina, Galapagos	3	2
Gal-AHA2-27	AHA D25C	n/a	Fernandina, Galapagos	3	2
Gal-STG13	STG06-29-13	n/a	Santiago, Galapagos	3	2
Gal-STG16b	STG06-29-16b	n/a	Santiago, Galapagos	3	2
Gal-STG16c	STG06-29-16c	n/a	Santiago, Galapagos	3	2
Gal-STG17	STG06-29-17	n/a	Santiago, Galapagos	3	2
Gal-STG20	STG06-29-20	n/a	Santiago, Galapagos	3	2
Gal-STG23	STG06-29-23	n/a	Santiago, Galapagos	3	2
Gal-STG48	STG06-29-48	n/a	Santiago, Galapagos	3	2

[a] Inclusion ID corresponds to names given to specific inclusions previously studied in Saal et al. (2002)

[b] References: 1. Saal et al. (2002) 2. Perfit et al. (1996) 3. Koleszar et al. (2009)

Table S2 Fitting results for the single-stage and two-stage cooling models, for all melt inclusions whose MgO concentration profiles have >5 points.

			Single-stage cooling model		Two-stage cooling model		
Inclusion name	**T_{high} (K)**	**T_{low} (K)**	**q (K/hr)**	**1σ (K/hr)**	**q_1 (K/hr)**	**q_2 (K/hr)**	**T_{mid} (K)**
Siq7	1413	1245	907	10.1	271	1195	1358
Siq8	1413	1264	1551	28.5	1113	2983	1324
Siq1-11b	1423	1318	401	14.3	174	1617	1369
Siq1-12b	1423	1268	560	15.4	265	4101	1319
Siq13	1444	1299	3197	76.2	815	7176	1399
Siq15	1444	1302	4239	99.8	1117	10313	1398
Siq16	1444	1280	3353	90.0	292	6305	1412
Siq1-19a	1423	1293	835	42.3	381	19937	1343
Siq1-19b	1423	1316	485	15.3	180	1694	1370
Siq1-24b	1441	1294	808	17.3	501	1497	1364
Siq1-24c	1441	1323	1311	72.3	389	3969	1389
Siq2-47a	1365	1246	662	31.0	507	8423	1267
Siq2-47b	1365	1254	708	37.0	1057	597	1305
Siq2-52a	1444	1355	1311	84.1	124	1603	1431
Siq2-52b	1444	1301	712	22.2	687	754	1327
Siq2-53a	1444	1354	523	26.7	14	723	1433
Siq3-56a	1417	1279	2864	141.7	552	3718	1361
Siq3-56b	1417	1313	2102	112.7	828	2144	1417
Siq3-65a	1413	1301	1119	29.8	693	1297	1372
Siq3-65b	1413	1320	1308	50.5	898	7407	1341

Gal-AHA2-24	1334	1151	155	3.4	64	323	1274
Gal-AHA2-27	1334	1289	4358	764.3	684	4689	1332
Gal-STG13	1402	1353	12720	1753	356	20243	1394
Gal-STG16b	1402	1317	4880	168	724	8342	1379
Gal-STG16c	1402	1303	6144	223	666	7123	1390
Gal-STG17	1402	1312	5889	395.9	140	7146	1394
Gal-STG20	1402	1334	12202	912	494	13473	1398
Gal-STG23	1402	1348	12086	1729	65	22207	1395
Gal-STG48	1402	1303	4360	182.2	609	8106	1379

S6. Additional references

Beattie P (1993) Olivine-melt and orthopyroxene-melt equilibria. Contributions to Mineralogy and Petrology 115 (1):103-111. doi:10.1007/bf00712982

Chen Y, Zhang Y (2008) Olivine dissolution in basaltic melt. Geochimica et Cosmochimica Acta 72 (19):4756-4777. doi:10.1016/j.gca.2008.07.014

Crank J (1975) The Mathematics of Diffusion. 2nd edn. Oxford University Press,

Ford C, Russell D, Craven J, Fisk M (1983) Olivine-liquid equilibria: temperature, pressure and composition dependence of the crystal/liquid cation partition coefficients for Mg, Fe2+, Ca and Mn. Journal of Petrology 24 (3):256-266

Ghiorso MS, Sack RO (1995) Chemical mass transfer in magmatic processes IV. A revised and internally consistent thermodynamic model for the interpolation and extrapolation of liquid-solid equilibria in magmatic systems at elevated temperatures and pressures. Contributions to Mineralogy and Petrology 119 (2):197-212

Koleszar AM, Saal AE, Hauri EH, Nagle AN, Liang Y, Kurz MD (2009) The volatile contents of the Galapagos plume; evidence for H_2O and F open system behavior in melt inclusions. Earth and Planetary Science Letters 287 (3–4):442-452. doi:10.1016/j.epsl.2009.08.029

Matzen AK, Baker MB, Beckett JR, Stolper EM (2011) Fe–Mg partitioning between olivine and high-magnesian melts and the nature of Hawaiian parental liquids. Journal of Petrology 52 (7-8):1243-1263

Perfit MR, Fornari DJ, Ridley WI, Kirk PD, Casey J, Kastens KA, Reynolds JR, Edwards M, Desonie D, Shuster R, Paradis S (1996) Recent volcanism in the Siqueiros transform fault: picritic basalts and implications for MORB magma genesis. Earth and Planetary Science Letters 141 (1–4):91-108. doi:10.1016/0012-821x(96)00052-0

Putirka KD (2008) Thermometers and barometers for volcanic systems. Reviews in Mineralogy and Geochemistry 69 (1):61-120

Roeder P, Emslie R (1970) Olivine-liquid equilibrium. Contributions to Mineralogy and Petrology 29 (4):275-289

Saal AE, Hauri EH, Langmuir CH, Perfit MR (2002) Vapour undersaturation in primitive mid-ocean-ridge basalt and the volatile content of Earth's upper mantle. Nature 419 (6906):451-455. doi:http://www.nature.com/nature/journal/v419/n6906/suppinfo/nature01073_S1.html

Sugawara T (2000) Empirical relationships between temperature, pressure, and MgO content in olivine and pyroxene saturated liquid. Journal of Geophysical Research 105 (B4):8457-8472

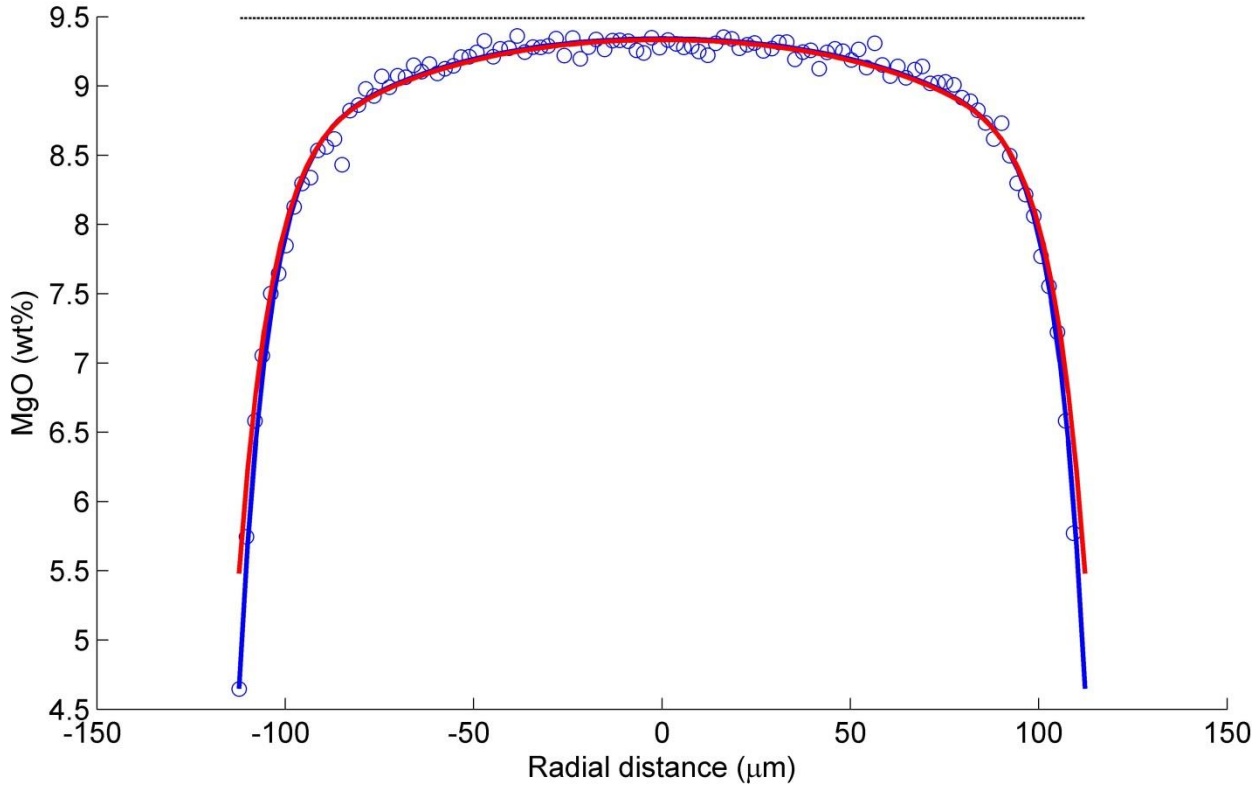

Figure S1 Comparison between two methods of calculating MgO distribution in melt inclusion Siq16. The initial concentration of MgO is assumed to be 9.5 wt. %). The best-fit two-stage linear cooling model (described in section S1.1 and the main text) is plotted in blue. The recalculation of MgO considering olivine growth (see section S1.3) is plotted in red.

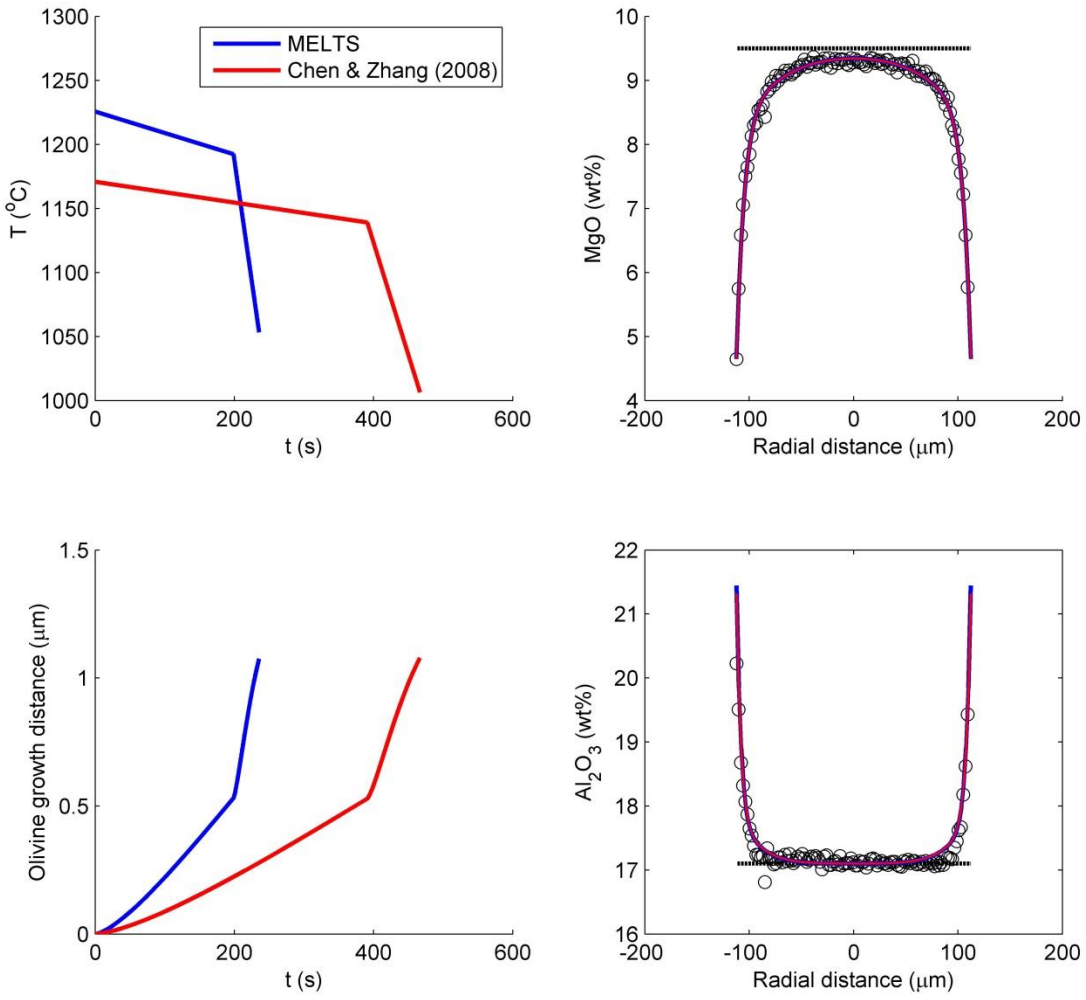

Figure S2 Comparison of best fits to MgO data from melt inclusion Siq16 using the MgO-temperature relationship of Chen and Zhang (2008) (in red) and MELTS (in blue). The MELTS calculation used the central composition of Siq16 as a starting composition and an oxygen fugacity of two log units below the NNO buffer (Saal et al. 2002). The fits to the data were equally good for both models. The MELTS thermometer predicts a higher temperature for a given MgO concentration in the liquid than the Chen and Zhang (2008) thermometer (see discussion in S2.2), and this results in higher cooling rates and a shorter duration of cooling by approximately a factor of two when the MELTS thermometer is used.

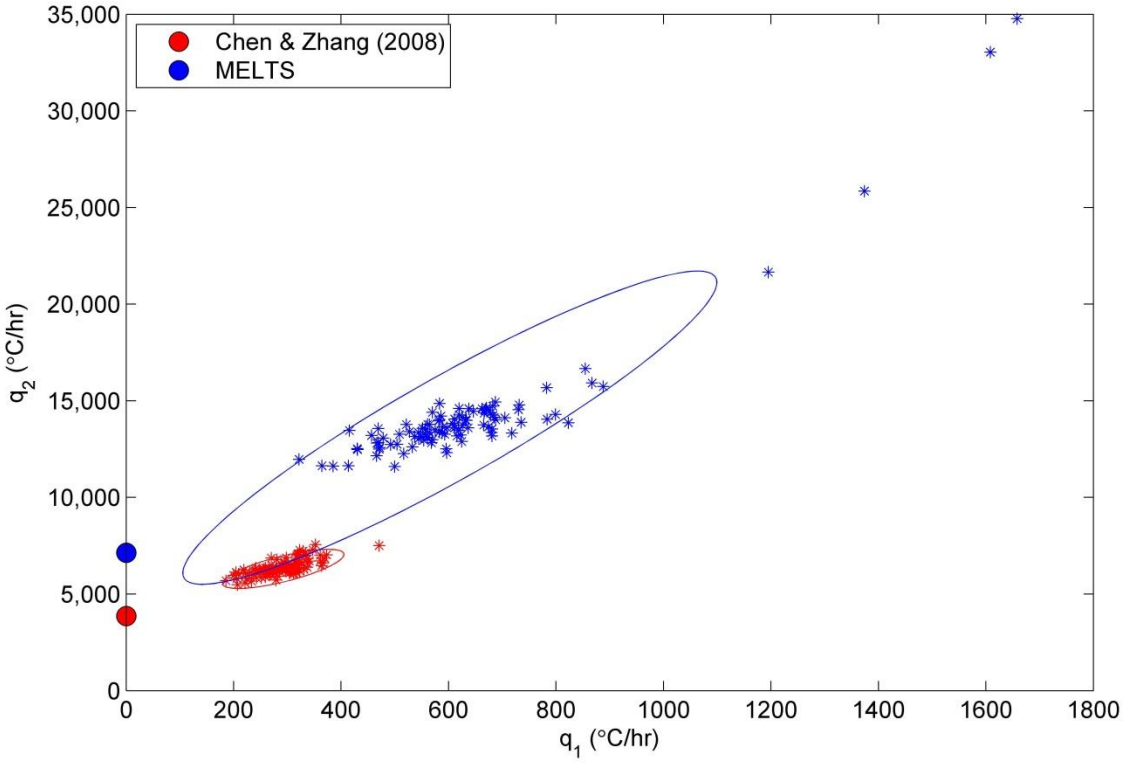

Figure S3 Comparison of best-fit cooling rates for melt inclusion Siq16 using the MgO-temperature relationship of Chen and Zhang (2008) (in red) and MELTS (in blue). Colored circles on the y-axis are results of the single stage cooling model. Small stars indicate the results of fitting MgO data in melt inclusion Siq16 with added noise (from a normal distribution with a standard deviation of 0.1 wt. % MgO). For each of the two thermometers, 100 noisy MgO profiles were fit. Red and blue ellipses are q_1–q_2 95% confidence error ellipses for the best-fit 2-stage cooling histories using the Chen and Zhang (2008) thermometer and MELTS thermometer, respectively. The higher temperatures for a given MgO concentration in the liquid that are predicted by MELTS result in a factor of ~2 increase in best-fit cooling rates compared to the Chen and Zhang (2008) model.

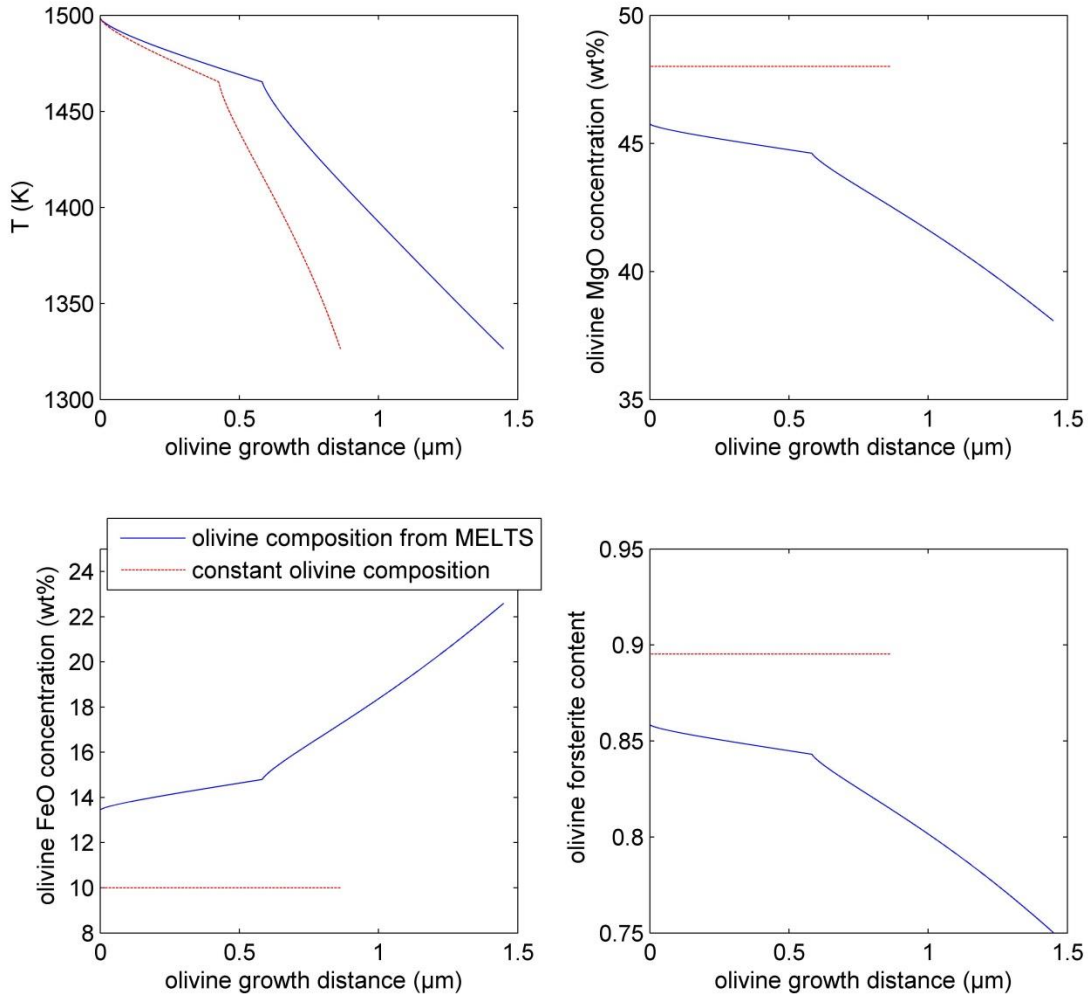

Figure S4 Comparison of the constant olivine composition model (used for the fitting presented in the main text; red lines) with a variable composition olivine model calculated using MELTS (blue lines) for melt inclusion Siq16. The MELTS calculation shown here is the same as the calculation shown in Figures S2 and S3. Using MELTS to calculate the decrease in forsterite content of the olivine as crystallization progresses results in the crystallization of ~50% more olivine than predicted by our constant olivine composition assumption. Although this does not affect the cooling history fitting, it does affect the calculated distribution of Al_2O_3 in the melt inclusions. This effect is explored in Figure S5.

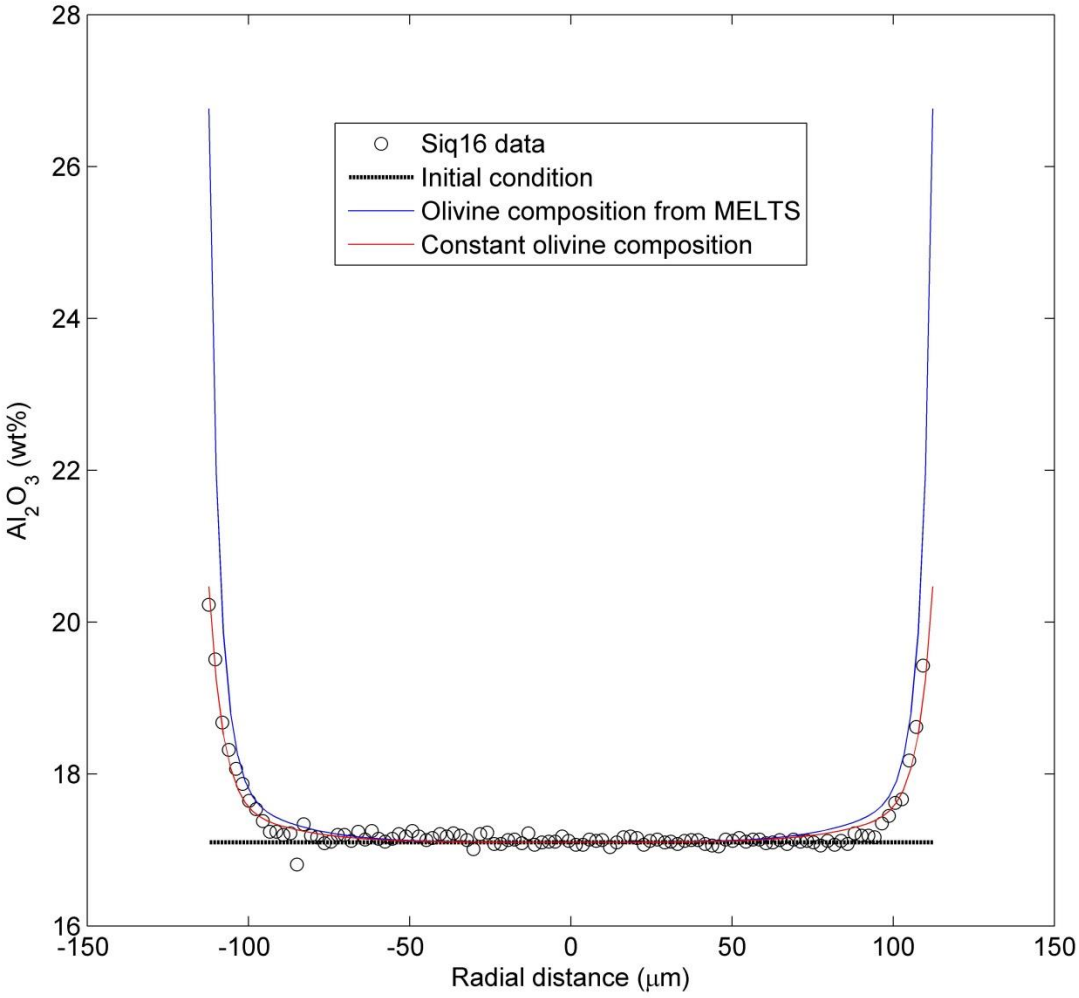

Figure S5 Comparison of the effects of two different models for olivine composition on the fit to Al_2O_3 data from melt inclusion Siq16. Both models follow the best-fit cooling history for Siq16 determined using MELTS (see Figure S2, blue lines). The fit to the Al_2O_3 data is marginally better using a constant composition olivine model. However, it is possible that higher resolution measurements at the olivine-melt interface would reveal a stronger enrichment in Al_2O_3 at the interface than we observed during this study.

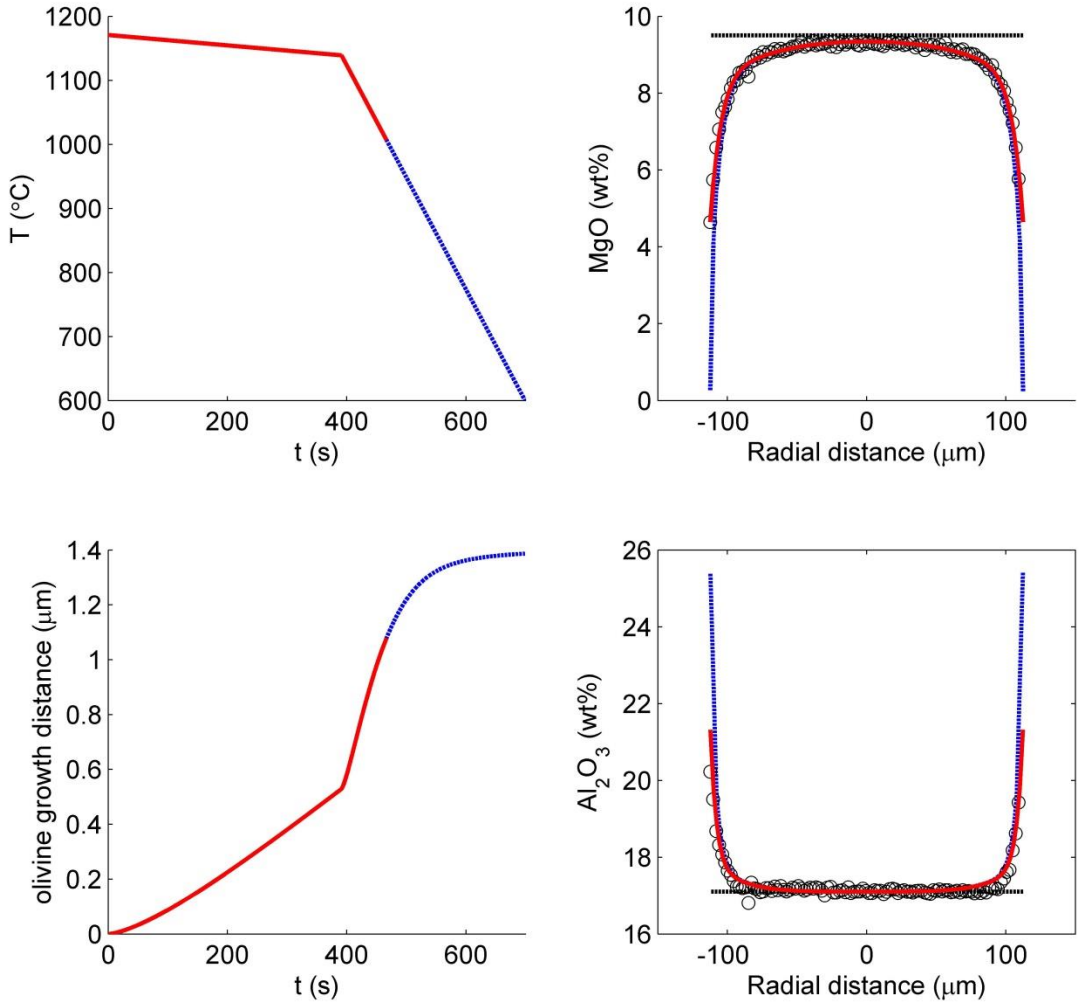

Figure S6 Comparison of two different assumptions for the value of T_{low} (the lowest temperature experienced by the melt inclusion during cooling) for melt inclusion Siq16. The simulation in red fixes T_{low} to be the temperature corresponding to the lowest measured MgO concentration in the melt inclusion (using the thermometer of Chen and Zhang, 2008). This is the assumption applied for the fitting in the main paper, and the curves represent the best-fit cooling history from Table S2. The simulation in blue extends the cooling history (at a fixed cooling rate) to a temperature of 600 °C. This extended cooling history produces ~0.3 μm additional olivine growth. The quality of the match between the model and the MgO and Al_2O_3 data is slightly degraded at the edges of the melt inclusion, although this is a small effect.

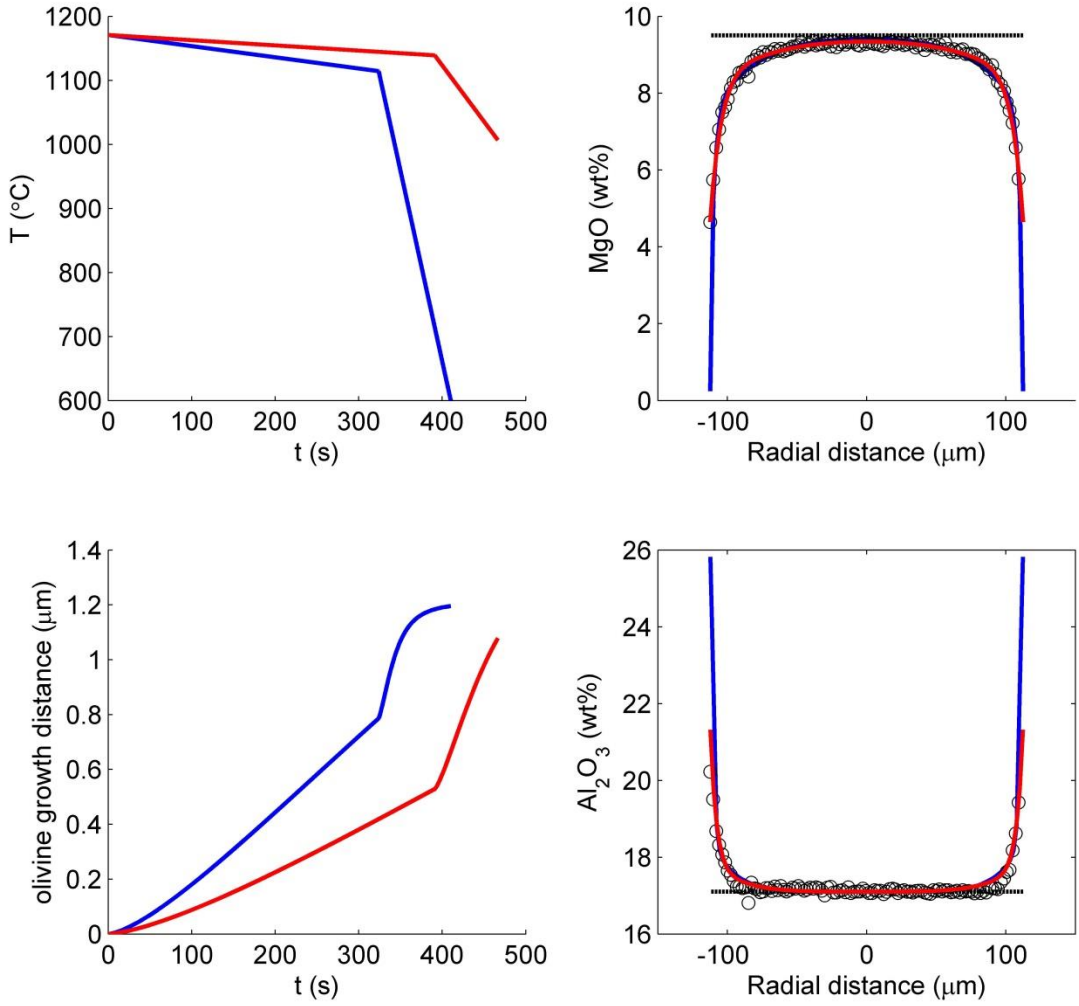

Figure S7 Comparison of two different assumptions for the value of T_{low} (the lowest temperature experienced by the melt inclusion during cooling) for melt inclusion Siq16. The red curves are as on Figure S6 and were calculated by finding the best fit to MgO data in melt inclusion Siq16 fixing T_{low} to the temperature corresponding to the lowest measured MgO concentration in the melt inclusion. The blue curves represent the best fit to the MgO data in Siq16 fixing T_{low} to 600 °C. Although by eye (except at the edges of the melt inclusion) the two models both adequately describe the MgO data, the misfit between the best-fit model and the data is greater when T_{low} is fixed to 600 °C (misfit = 0.2027 for the blue curve, where misfit is defined in the main text—see "The inverse model: using the measured MgO to solve for cooling rate") than it is when T_{low} is fixed to the temperature corresponding to the lowest measured MgO concentration in the melt inclusion (misfit = 0.0060 for the red curve).

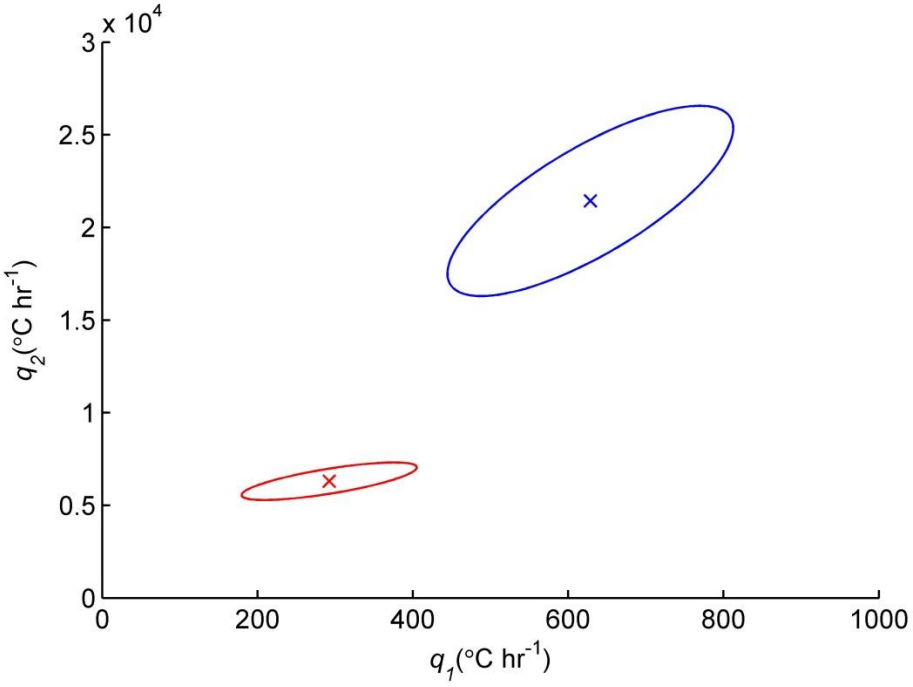

Figure S8 Comparison of q_1-q_2 95% confidence ellipses for melt inclusion Siq16, for different values of T_{low}. The red ellipse is for the case where T_{low} is assumed to be the temperature corresponding to the lowest measured MgO in Siq16 (this is the approach taken in the main paper). The blue ellipse is for the case where T_{low} is fixed to a value of 600 °C. Lowering the value of T_{low} to below the closure temperature for MgO diffusion in the melt inclusion results in an increase in the best-fit cooling rates (by a factor of ~2 for q_1 and a factor of ~3 for q_2). However, this approach slightly degrades the match between the model and the MgO data (see Figure S7). The red cross marks the cooling rates used to create the red curves in Figure S7, and the blue cross marks the cooling rates used to create the blue curves in Figure S7.

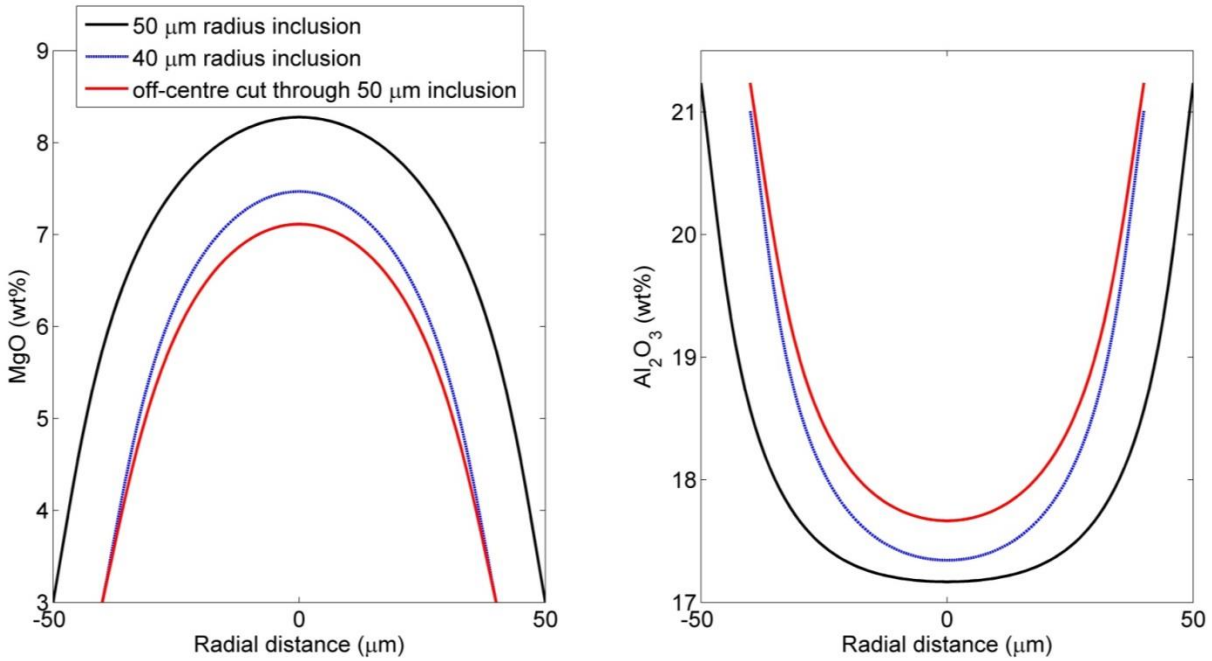

Figure S9 Exploring the effect of an off-center cut through a melt inclusion on its expected MgO and Al_2O_3 concentration profiles. All curves on this figure experienced the same cooling history. The black curves are calculated concentration profiles of MgO and Al_2O_3 for a 50 μm radius inclusion cut through its center. The blue curves are calculated concentration profiles of MgO and Al_2O_3 for a 40 μm radius inclusion cut through its center. The red curves are calculated concentration profiles of MgO and Al_2O_3 for a 50 μm radius inclusion cut along a circular section with a radius of 40 μm. Cutting this melt inclusion along an off-center plane has the effect of lowering its central MgO concentration and raising its central Al_2O_3 concentration. This provides another possible explanation for the discrepancy in initial concentrations of Al_2O_3 required to fit the Al_2O_3 data in pairs of melt inclusions trapped in the same olivine host (see "Testing the two-stage linear cooling model – 2. Modeling zonation of Al_2O_3" in the main text), where we observe that the smaller inclusion in each pair typically requires a higher starting concentration of Al_2O_3.

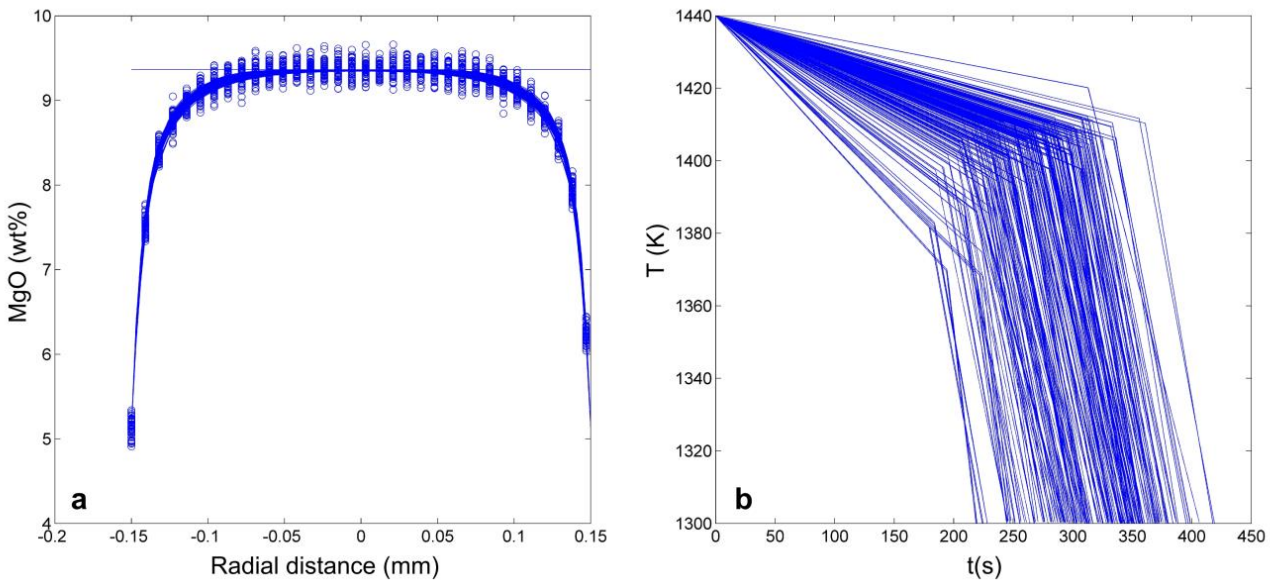

Figure S10 (a) Illustration of the parametric bootstrap inversion technique. 100 noisy MgO concentration profiles across a 150 μm radius melt inclusion are plotted as blue circles. Noisy profiles were created by adding noise (with 1σ=0.1 wt. %) to synthetic data spaced at 10 μm. The best fits to these noisy profiles are plotted as solid blue lines. **(b)** Best-fit two-stage linear cooling histories for the 100 noisy MgO concentration profiles plotted in (a).

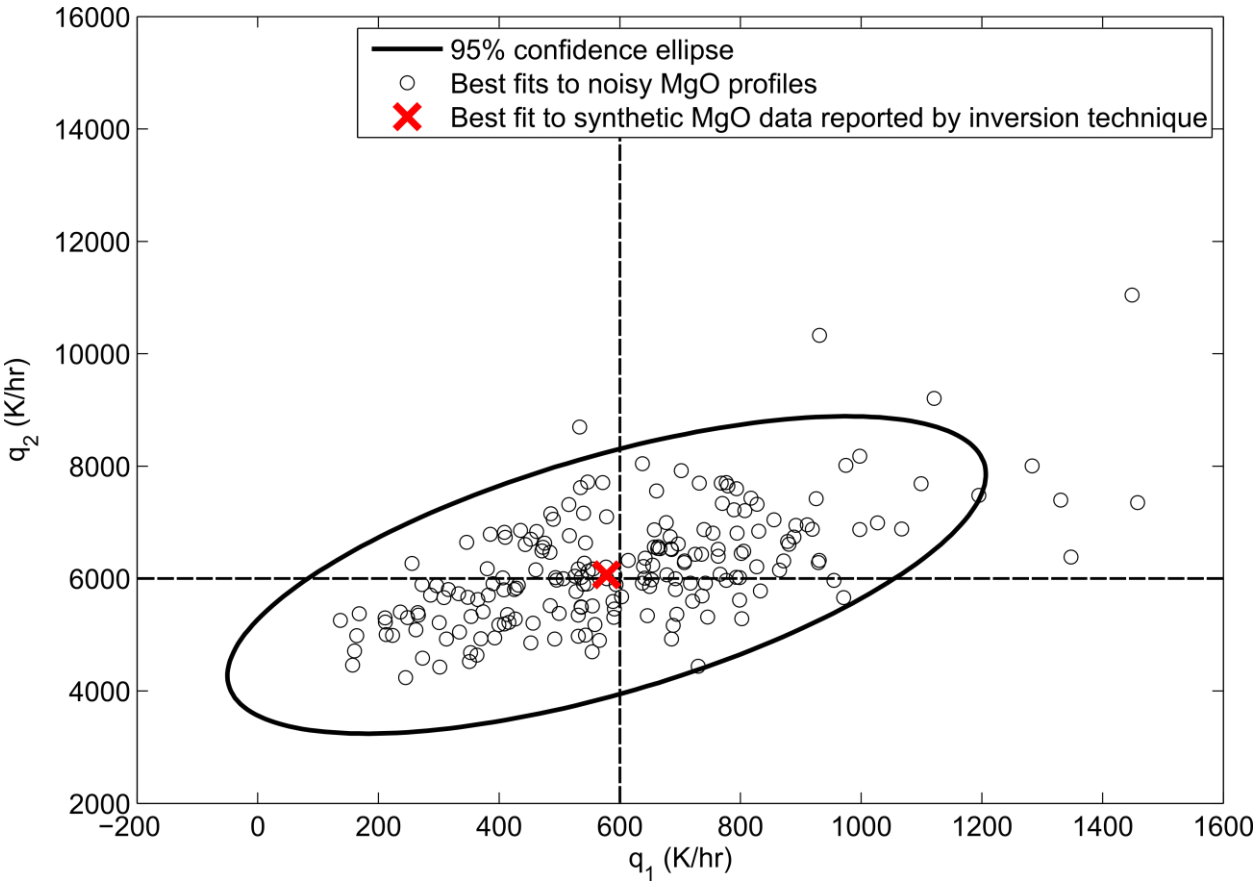

Figure S11 Test of the cooling history inversion technique on a synthetic, 150 μm radius melt inclusion with a known cooling history (T_{mid}=1400 K; q_1=600 K/hr; q_2=6000 K/hr). Best fits to 100 different noisy MgO profiles are plotted as black circles. The 95% confidence ellipse is centered on the median values of q_1 and q_2 (red cross), and these values are output by the inversion technique as the 'overall best-fit' to the original MgO data. The true parameter values are indicated by black dashed lines.

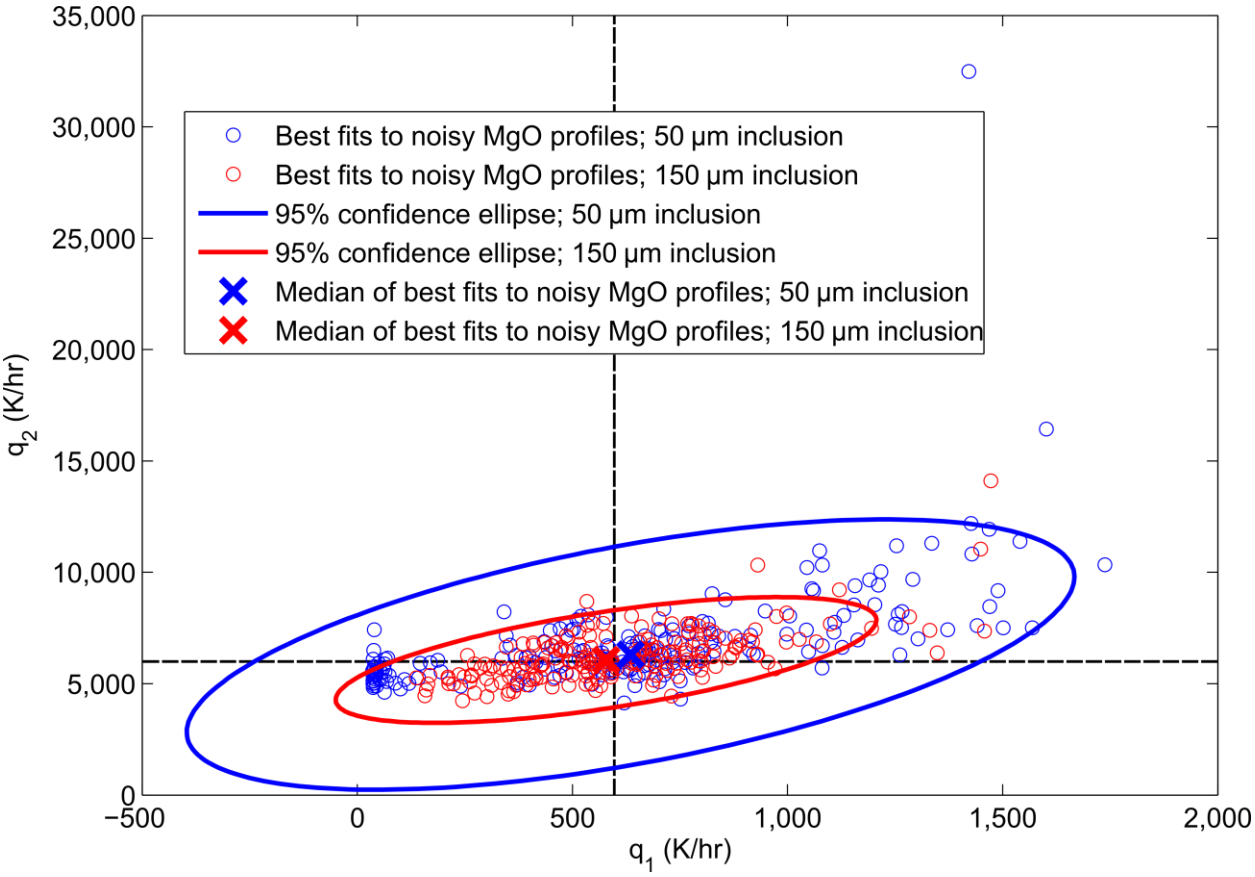

Figure S12 Results of inverting MgO profiles in two modelsynthetic melt inclusions of different sizes with identical, known cooling histories (T_{mid}=1400 K; q_1=600 K/hr; q_2=6000 K/hr – indicated by black dashed lines). The 95% confidence ellipse for the small inclusion (in blue) is larger than the 95% confidence ellipse for the large inclusion (in red), suggesting that cooling history parameters determined from small melt inclusions are less precisely constrained than the parameters determined from large melt inclusions (when MgO measurements are made with the same spatial resolution). However, the accuracy of the technique is not greatly affected in this case: The cooling history parameters for the smaller inclusion are accurate to within 6% and the large inclusion cooling history parameters are accurate to within 4%.

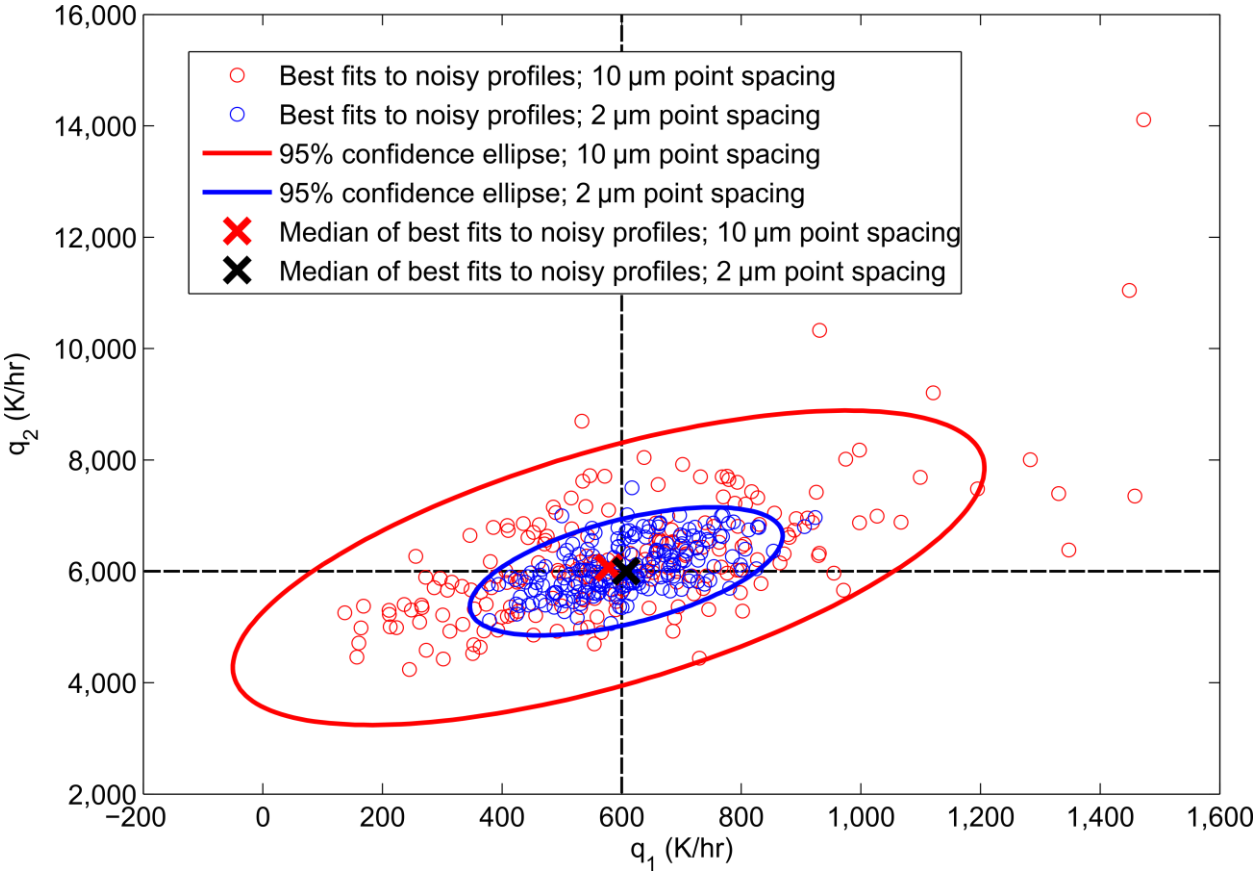

Figure S13 Effect of spatial resolution of MgO concentration measurements on accuracy and precision of inversion technique for synthetic data generated with the following cooling history parameters: T_{high}=1440 K, T_{mid}=1400 K, T_{low}=1300 K, q_1=600 K hr^{-1}, and q_2=6000 K hr^{-1}(cooling rates indicated by black dashed lines). Increasing the spatial resolution of the MgO profile from 10 to 2 μm point spacing results in an increase in the accuracy of the cooling history parameters (from <4 rel. % to <2 rel. %) and also increases the precision of the inversion technique (as demonstrated by the reduction in the size of the 95% confidence ellipse for the high spatial resolution profile).

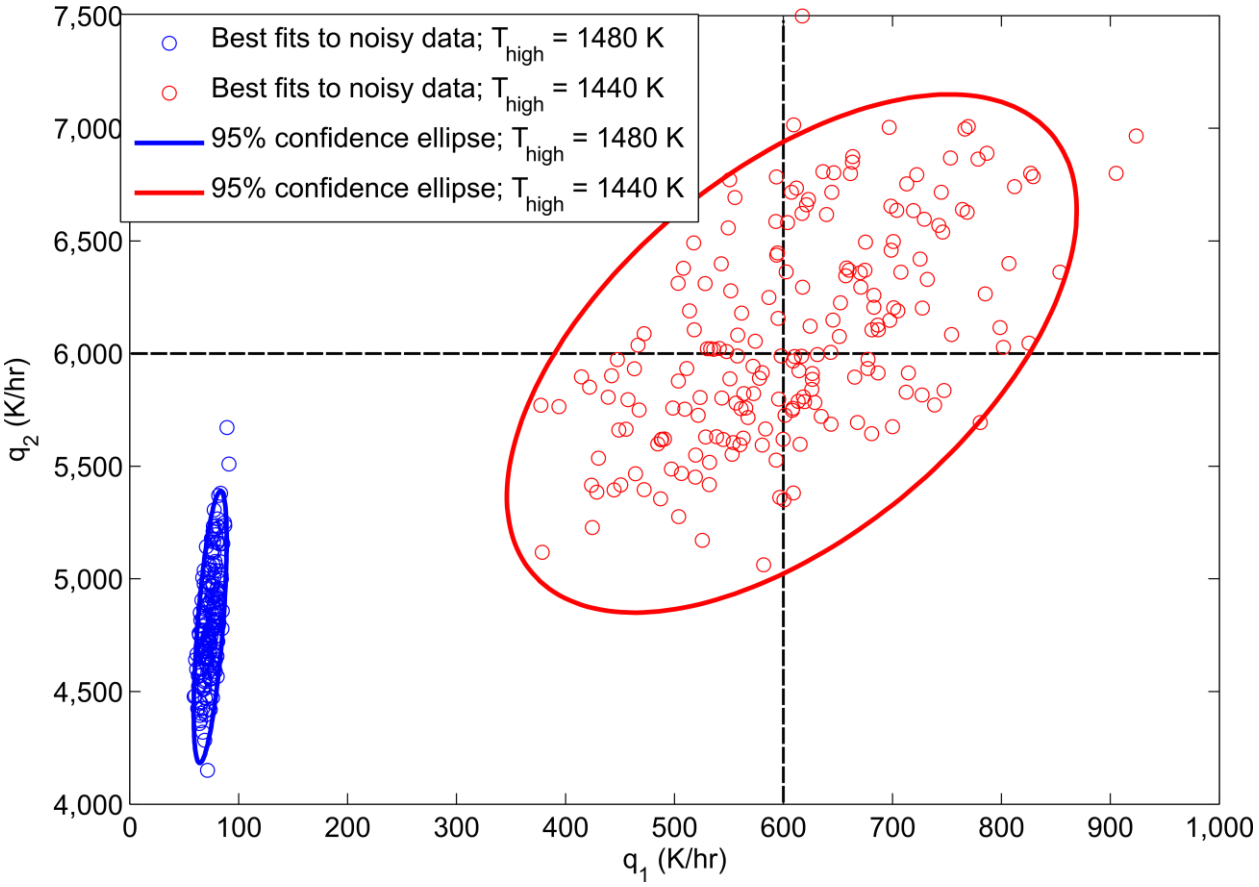

Figure S14 Results of a simulation (with T_{high}=1440 K, T_{mid}=1400 K, T_{low}=1300 K, q_1=600 K hr^{-1}, and q_2=6000 K hr^{-1} – true cooling rates indicated by black dashed lines) to test the effects of overestimating T_{high}. Shown in red are the best fits and the 95% confidence ellipse for an inversion assuming the correct value of T_{high} (i.e., T_{high} = 1440 K). The values of q_1 and q_2 returned by this inversion are within 2 rel. % of their true values. Shown in blue are the best fits and the 95% confidence ellipse for an inversion assuming a value of T_{high} that is 40 K higher than its true value (i.e., T_{high} = 1480 K). Overestimating T_{high} drives q_1 and q_2 to lower values.

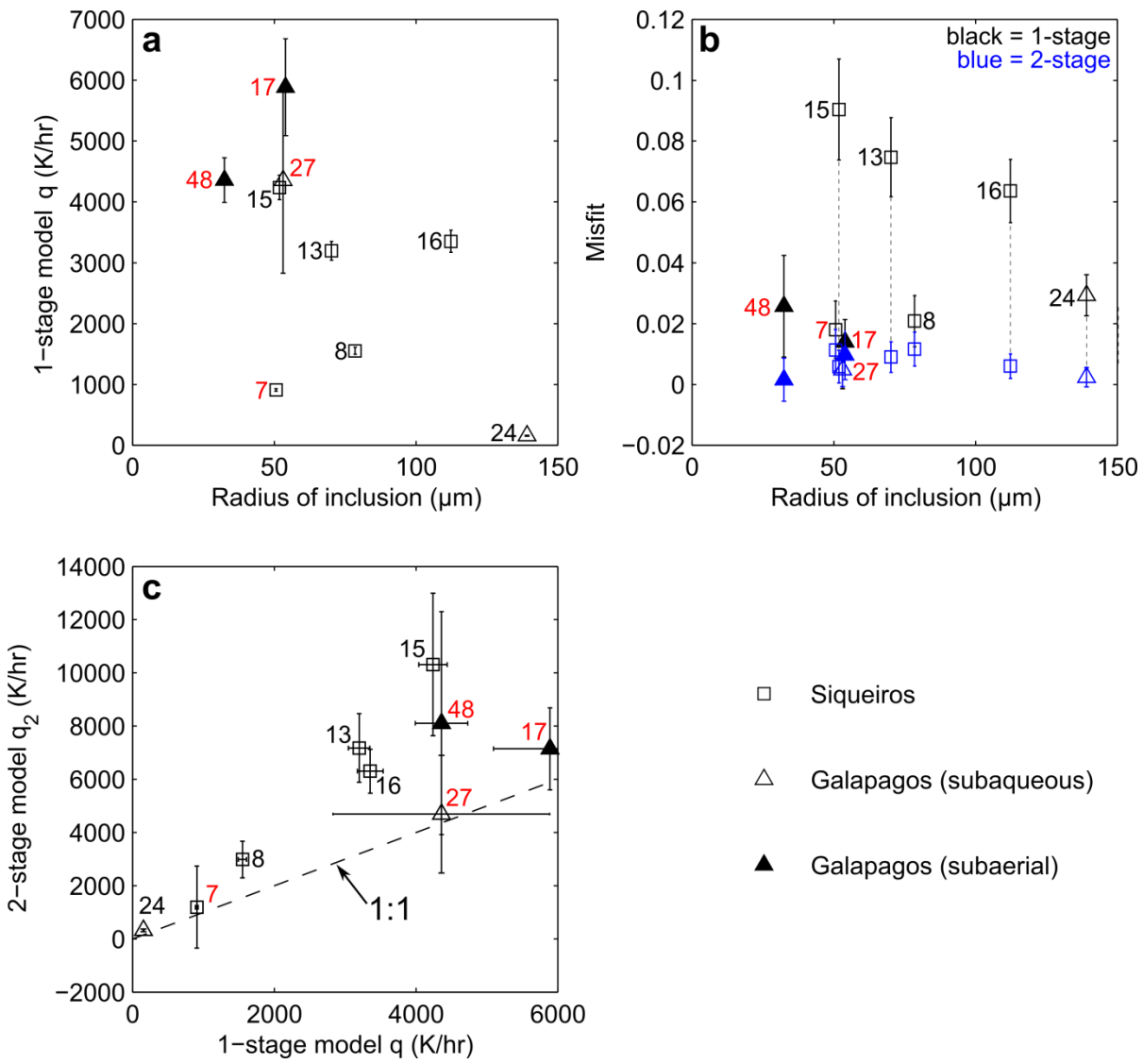

Figure S15 Comparison of best-fit parameters from single-stage and two-stage models for all inclusions with data points spaced 2 μm apart. In each panel, the Siqueiros melt inclusions are plotted as squares and the Galapagos inclusions are plotted as triangles. Each point is labeled with the identification number of the melt inclusion. **(a)** Plot of the cooling rate determined by the single-stage linear cooling model vs. melt-inclusion radius illustrating the negative correlation between cooling rate and inclusion size. Error bars represent ±2σ (where σ is the standard deviation of cooling rates fit to 100 synthetic MgO profiles—see "Inverting the MgO concentration profiles for two-stage cooling histories" in the main text, and Figure S10). **(b)** Plot of the model misfit (see "The inverse model: using the measured MgO to solve for

cooling rate" in the main text for definition of misfit) vs. the melt inclusion radius for fits to both the single-stage linear cooling model (in black) and the two-stage linear cooling model (in blue). Single-stage linear cooling model fits are labeled with the identification number of the melt inclusion and are joined to the two-stage model fits of the same melt inclusion by a thin dashed black line. Error bars represent ±2σ (standard deviation) of the misfits determined by fitting 100 synthetic MgO profiles. **(c)** Relationship between best-fit values of q_2 (the second constant cooling rate in the two-stage linear cooling model) and best-fit values of q (the cooling rate in the single-stage linear cooling model). A 1:1 line is plotted for reference (black dashed line). Melt inclusions for which q and q_2 overlap at 2σ are labeled in red. These inclusions are described well by the single-stage cooling model and the improvement by going to the two-stage model is small. Note that in (b), the misfit of the single-stage cooling model is relatively low for these inclusions. For those melt inclusions whose identification number is written in black, q and q_2 do not overlap at 2σ. These melt inclusions are poorly fit by the single-stage model (they have high misfit values in (b) and the single-stage model underestimates their final cooling rate.

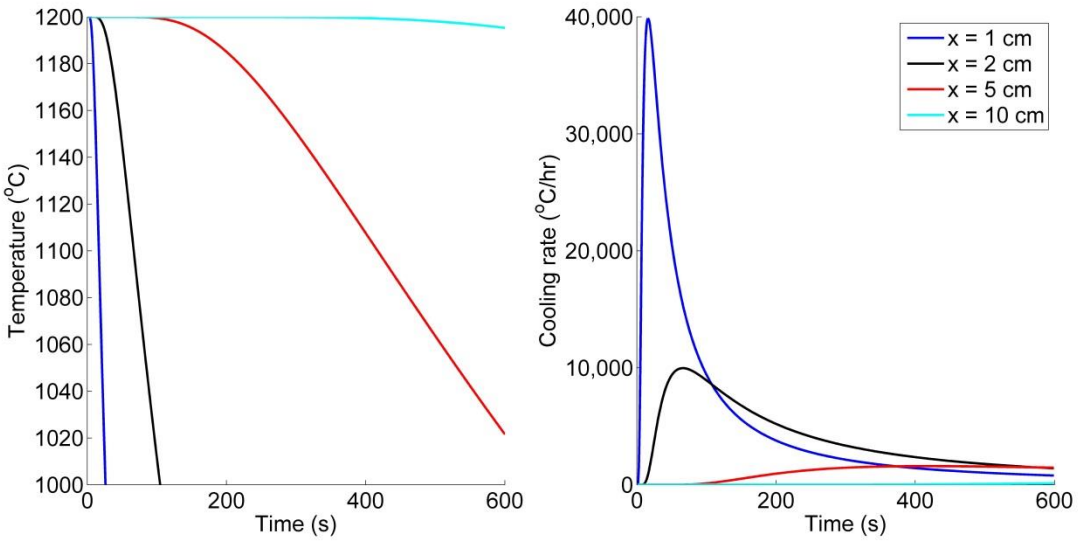

Figure S16 Thermal histories during cooling from 1200 °C to 2 °C calculated using an analytical solution for conductive cooling in a semi-infinite medium with a constant temperature boundary condition (i.e., the lava-water interface is held at 2 °C) (Crank 1975). The best-fit values of q_2 recorded by the melt inclusions (see Table S2) are consistent with conductive cooling at distances of a few centimeters from the lava-water or lava-air interface.

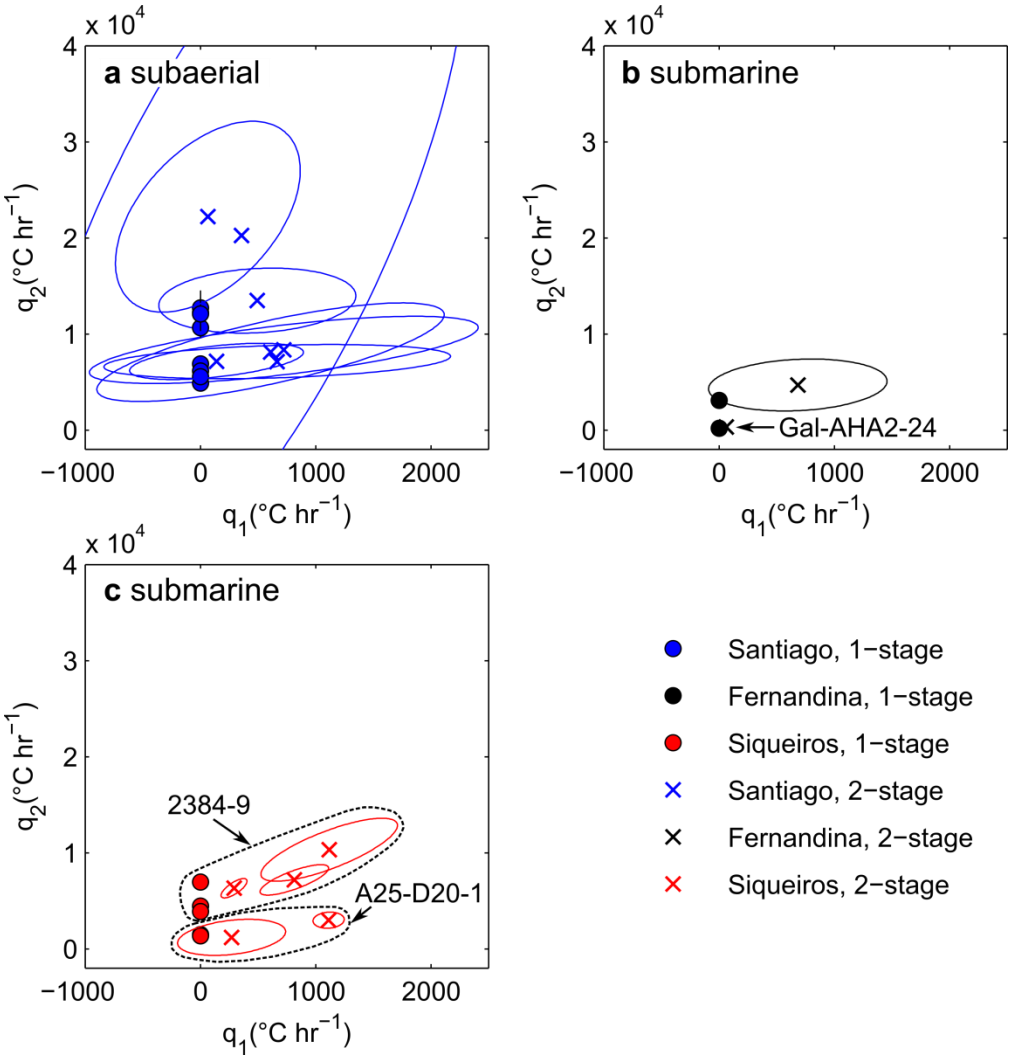

Figure S17 q_1-q_2 95% confidence error ellipses for all of the melt inclusions that were measured with 2µm point spacing. Compare with Figure 10 in the main paper, for which 95% confidence ellipses were calculated for $\log_{10}(q_1)$-$\log_{10}(q_2)$. The median values of q_1 and q_2 are marked by crosses. The colored circles plotted along q_1=0 are the results of the single-stage linear cooling model. The best fit cooling rates determined by the single-stage linear cooling model tend to be similar to but systematically low relative to the best-fit values for q_2 (colored squares), and the relative order of best-fit cooling rates is successfully predicted by the single-stage model. **(a)** Subaerially quenched Santiago melt inclusions. These inclusions tend to be well-described by single-stage cooling histories (e.g., Gal-STG-17 on Fig. 9), so their q_1-q_2 error ellipses for the 2-stage cooling model are relatively poorly constrained, with some best fit cooling rates extending to arbitrarily high values. This asymmetry in the distribution of best fit cooling histories causes the 95% confidence ellipses to extend to unphysical negative cooling rates. As presented

in the main paper, best fit values of q_1 and q_2 for these inclusions are better described by a lognormal distribution. (**b)** Submarine Fernandina melt inclusions. Symbols as in (a). Note that the cooling history for Gal-AHA2-24 is so well-constrained that its error ellipse is barely visible at this scale. **(c)** Siqueiros melt inclusions. All samples in this panel are from one of two locations (see Table S1): Siq7 and Siq8 are from dredge A25-D20-1; Siq13, Siq15, and Siq16 were collected during an Alvin submersible dive, and the thermal histories of melt inclusions from these different locations are grouped together.

A p p e n d i x I I

CHEMICAL ZONATION IN OLIVINE-HOSTED MELT INCLUSIONS

M.E. Newcombe[a,], A. Fabbrizio[a, b], Youxue Zhang[c], C. Ma[a], M. Le Voyer[a, d], Y. Guan[a], J. Eiler[a], A. Saal[e], E.M. Stolper[a]

* Previously published as **Online Resource 3** in Newcombe, M. E., et al. "Chemical zonation in olivine-hosted melt inclusions."*Contributions to Mineralogy and Petrology* 168.1 (2014): 1-26.

doi:10.1007/s00410-014-1030-6

Here we present additional supporting materials for the article "Chemical zonation in olivine-hosted melt inclusions". In this appendix, we provide further discussion of the calibration of our nanoSIMS data, and include a table of compositions of glass standards used to calibrate the data (Table S3-1), and two sets of calibration curves for H_2O, S, F, and Cl that were made during two separate analytical sessions on the nanoSIMS at Caltech (Figures S3-1–S3-8). We also include concentration profiles of H_2O, S, F, and Cl across melt inclusions Siq7 and Siq16 (Figures S3-9–S3-10).

Overview of calibration method

OH, Cl, F, and S profiles were measured across five Siqueiros melt inclusions during two analytical sessions (5^{th} – 8^{th} July, 2011, and 25^{th} – 27^{th} July, 2011). Glass standards containing known amounts of H_2O, S, F, and Cl (Table S3-1) were measured typically 3–6 times during each analytical session, and these measurements were used to build two sets of calibration curves (i.e., one set of calibration curves for each session). The calibration curves used during the first analytical session are shown in Figures S3-1–S3-4, and those used for the second analytical session are shown in Figures S3-5–S3-8.

All measurements of standards and samples in Figures S3-1–S3-10 and Figure 5 have been blank-corrected: The average ratios of $^{16}O^{1}H/^{18}O$, $^{32}S/^{18}O$, $^{35}Cl/^{18}O$, and $^{19}F/^{18}O$ measured on the analytical blank (GRR997; Mosenfelder et al. (2011)) during each analytical session were subtracted from the ratios measured on the standards and samples. Calibration curves were created from blank-corrected ratios using least-squares linear regression through the origin.

Volatile concentration data in melt inclusions Siq7 and Siq16

Volatile concentrations were measured in melt inclusions Siq7, Siq8, Siq13, Siq15, and Siq16 in linear profiles that extended across the entire diameter of the inclusions. Analyses were spaced ~3–5 μm apart. Data from Siq8 is shown in Figure 5 of the main paper. Concentration profiles across Siq13 and Siq15 were highly scattered (likely due to problems with charging on the sample surface) and are not shown here. Below, we discuss concentration profiles measured in melt inclusions Siq7 and Siq16.

Volatile concentration profiles across melt inclusion Siq7 (Figures S3-11) show similar trends to inclusion Siq8 (discussed in the main paper): F and possibly H_2O are observed to decrease towards the edges of the melt inclusion, and S is observed to increase towards the edges of the melt inclusion. Cl concentrations are below the calculated detection limit of 2.7 ppm, though there does seem to be a slight increase in relative Cl concentration towards the edges of the melt inclusion. Background levels of volatiles, especially water, were high during this analytical session. A number of different factors may have contributed to this: The low beam current (~3.5 pA) used to achieve high spatial resolution may have resulted in a higher contribution of counts from the background. Also, this analytical session was short (three days), so there was limited time for the nanoSIMS pump to reduce volatile contamination inside the sample chamber. Although care was taken to avoid contact with organics during sample preparation, the sample itself may have been contaminated with volatile material, which likely contributed to the high background. Despite these issues, measured concentrations of H_2O, S, and F are all well above their calculated detection limits (see caption to Figure S3-9).

Concentration profiles across melt inclusion Siq16 show trends that are broadly consistent with those observed in Siq8 (discussed in the main paper): Cl and S are enriched at the edges of the melt inclusion, and H_2O and F are depleted at the edges of the melt inclusion (see Figures S3-14). In this inclusion, the zones of depletion of H_2O and F at the edges of the inclusion are narrower than the equivalent concentration profiles in melt inclusion Siq8. F exhibits complex

behavior in Siq16, with a concentration profile from edge to center that increases, reaches a maximum and then decreases again. This behavior is similar to concentration profiles of CaO and FeO in this inclusion, which we interpreted as uphill diffusion. Uphill diffusion could responsible for the behavior of F in Siq16. Alternatively, the shape of this profile could be a result of rapid olivine crystallization in response to cooling (which would enrich F at the edges of the melt inclusion and could create the broad minimum in F concentration across the center of the inclusion) followed by loss of F into the surrounding olivine at temperatures too low for rapid olivine growth.

Sample no.	CFA47	ALV981-R23	alv1645	wok16-2	1396-hawaii	StHs6/80-G	1833-1
SiO_2	61.74	49.22	50.21	50.77	51.09	63.70	51.82
TiO_2	0.42	1.27	1.20	1.49	2.54	0.70	1.63
Al_2O_3	17.96	15.76	15.04	15.66	13.35	17.80	15.19
FeO	2.86	8.77	9.18	8.81	10.92	4.37	9.10
MnO	0.17	0.17	0.18	0.17	0.16	0.08	0.19
MgO	0.39	8.38	8.23	7.08	6.49	1.97	4.50
CaO	1.85	11.99	12.20	10.74	10.97	5.28	8.85
Na_2O	5.31	2.79	2.64	3.37	2.20	4.44	3.19
K_2O	7.93	0.05	0.05	0.20	0.45	1.29	0.56
P_2O_5	0.06	0.09	0.08	0.17	0.24	0.16	0.24
Total	98.68	98.49	99.01	98.46	98.40	99.79	95.26
ref.	*1*	*1*	*1*	*1*	*1*	*2*	*1*
H_2O	n.a.	n.a.	1030	6490	831	250	21400
ref.			*1*	*1*	*1*	*2*	*1*
S	n.a.	1100	n.a.	n.a.	n.a.	n.a.	n.a.
ref.		*3*					
F	2483	130	n.a.	n.a.	n.a.	320	n.a.
ref.	*4*	*5*				*2*	
Cl	4850	60	30	119	100	231	721
ref.	*6*	*1*	*1*	*1*	*1*	*2*	*1*

Table S3-1 Compositions of glass standards used to calibrate nanoSIMS data. References: *1* Le Voyer et al. (2013); *2* Jochum et al. (2006); *3* Bouvier et al. (2008); *4* Witter and Kuehner (2004); *5* Mosbah et al. (1991); *6* Metrich and Clocchiatti (1989)

Calibration curves for first analytical session: 5th–8th July, 2011

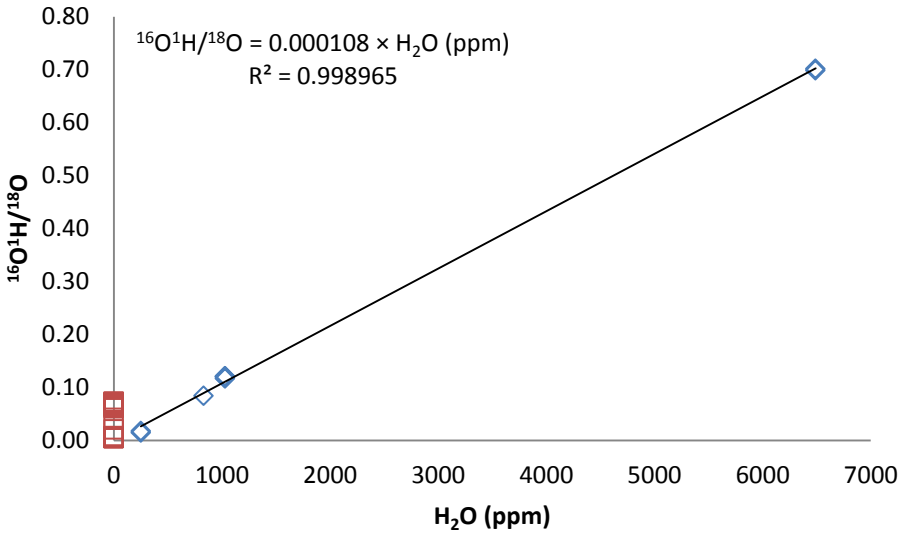

Figure S3-1 Calibration curve for water analyses. Blue diamonds are blank-corrected measurements of glass standards, and pink squares on the y-axis demarcate the range of blank-corrected $^{16}O^{1}H/^{18}O$ measured in sample Siq8. The black line is a least squares linear regression to the data forced through the origin, and the equation of the line and its coefficient of determination (R^2) are written above the plot. Standards were analyzed on the 6th, 7th, and 8th of July, and these analyses were grouped to create a single calibration curve for samples analyzed on the 6th, 7th, and 8th of July.

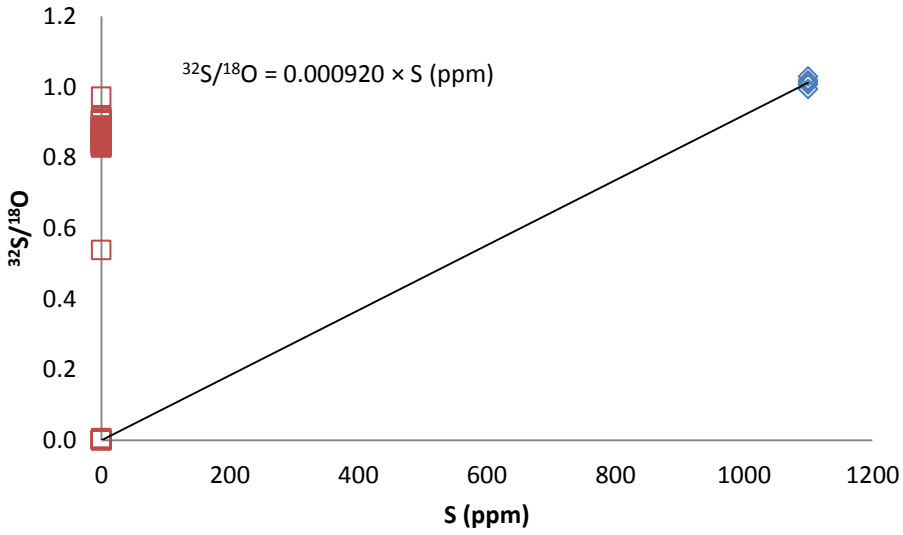

Figure S3-2 Calibration curve for sulfur analyses. Blue diamonds are blank-corrected measurements of glass standard ALV981-R23; pink squares on the y-axis demarcate the range of blank-corrected $^{32}S/^{18}O$ measured in sample Siq8. Standard ALV981-R23 was analyzed on the 6th, 7th and 8th of July, and these analyses were grouped to create a single calibration curve for samples analyzed on the 6th, 7th and 8th of July, which was created by drawing a line through the mean of these analyses through the origin. Five replicate analyses of ALV981-R23 were reproducible within 3 rel. % (2 standard deviations).

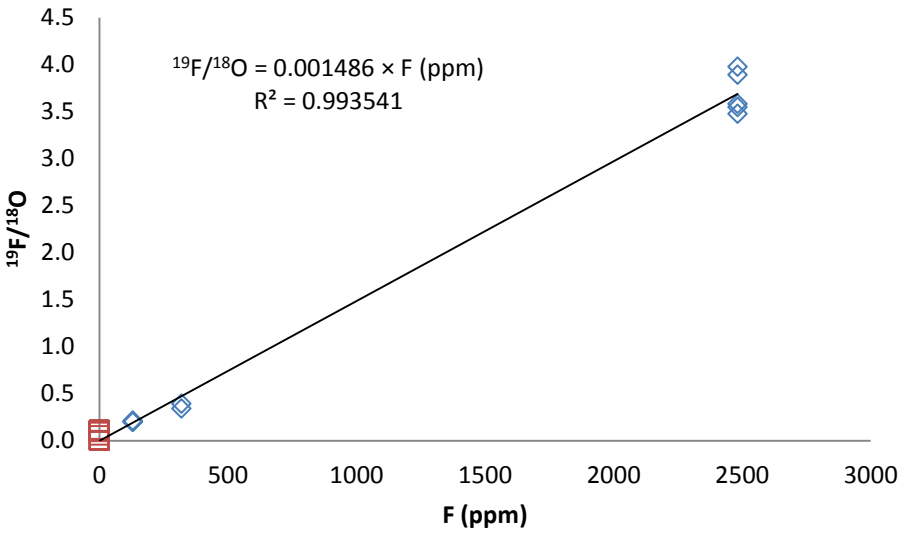

Figure S3-3 Calibration curve for fluorine analyses. Blue diamonds are blank-corrected measurements of glass standards, and pink squares on the y-axis demarcate the range of blank-corrected $^{19}F/^{18}O$ measured in sample Siq8. The black line is a least squares linear regression to the data forced through the origin, and the equation of the line and its coefficient of determination (R^2) are written on the plot. Standards were analyzed on the 6th, 7th, and 8th of July, and these analyses were grouped to create a single calibration curve for samples analyzed on the 6th, 7th, and 8th of July.

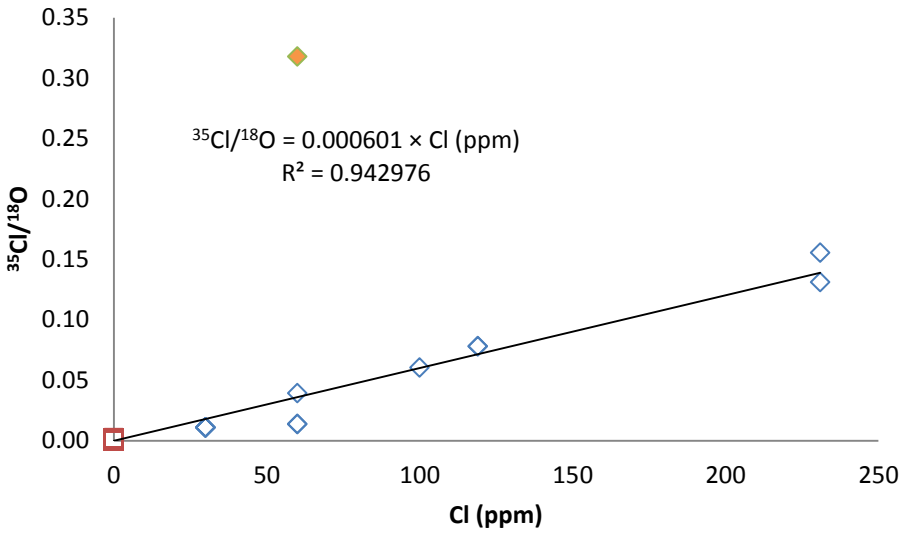

Figure S3-4 Calibration curve for chlorine analyses. Blue diamonds are blank-corrected measurements of glass standards; the orange diamond was excluded from the calibration; pink squares on the y-axis demarcate the range of blank-corrected $^{35}Cl/^{18}O$ measured in sample Siq8. The black line is a least squares linear regression to the data forced through the origin, and the equation of the line and its coefficient of determination (R^2) are written on the plot. Standards were analyzed on the 6th, 7th, and 8th of July, and these analyses were grouped to create a single calibration curve for samples analyzed on the 6th, 7th, and 8th of July.

Calibration curves for second analytical session: 25th–27th July, 2011

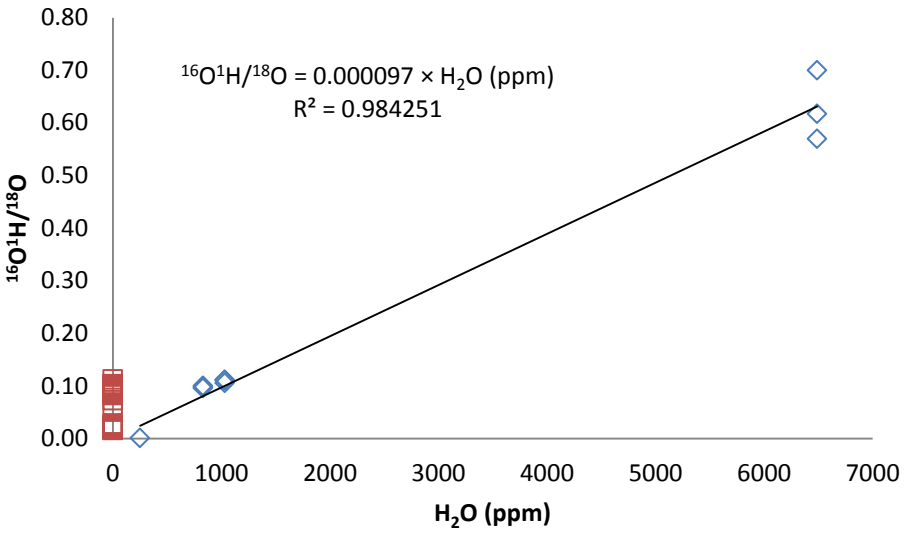

Figure S3-5 Calibration curve for water analyses. Blue diamonds are blank-corrected measurements of glass standards; pink squares on the y-axis demarcate the range of blank-corrected $^{16}O^{1}H/^{18}O$ measured in sample Siq7. The black line is a least squares linear regression to the data forced through the origin, and the equation of the line and its coefficient of determination (R^2) are written on the plot. Standards were analyzed on the 25th and 26th July, and these analyses were grouped to create a single calibration curve for samples analyzed on the 26th and 27th July.

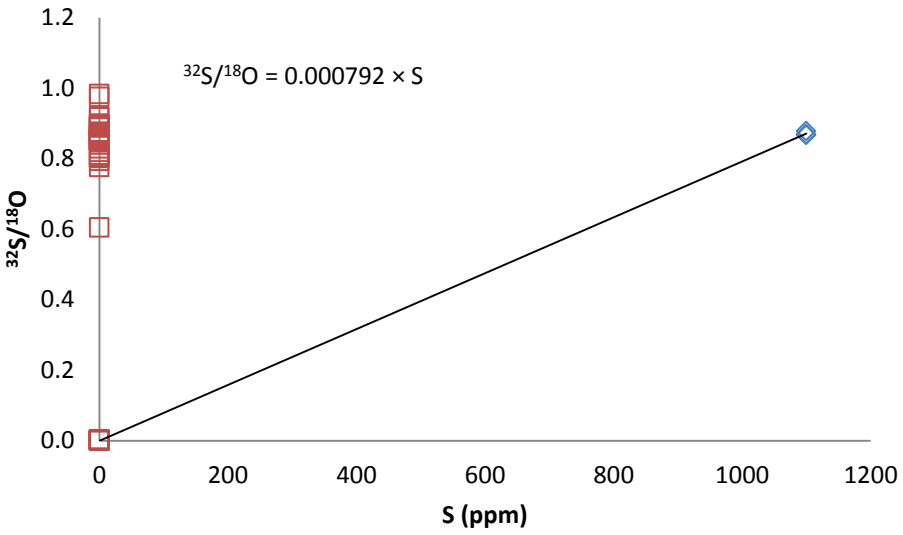

Figure S3-6 Calibration curve for sulfur analyses. Blue diamonds are blank-corrected measurements of glass standards; pink squares on the y-axis demarcate the range of blank-corrected $^{32}S/^{18}O$ measured in sample Siq7. Standard ALV981-R23 was analyzed on the 26th July, and these analyses were grouped to create a single calibration curve for samples analyzed on the 26th and 27th July, which was created by drawing a line through the mean of these analyses through the origin. Three replicate analyses of ALV981-R23 were reproducible within 2 rel. % (2 standard deviations).

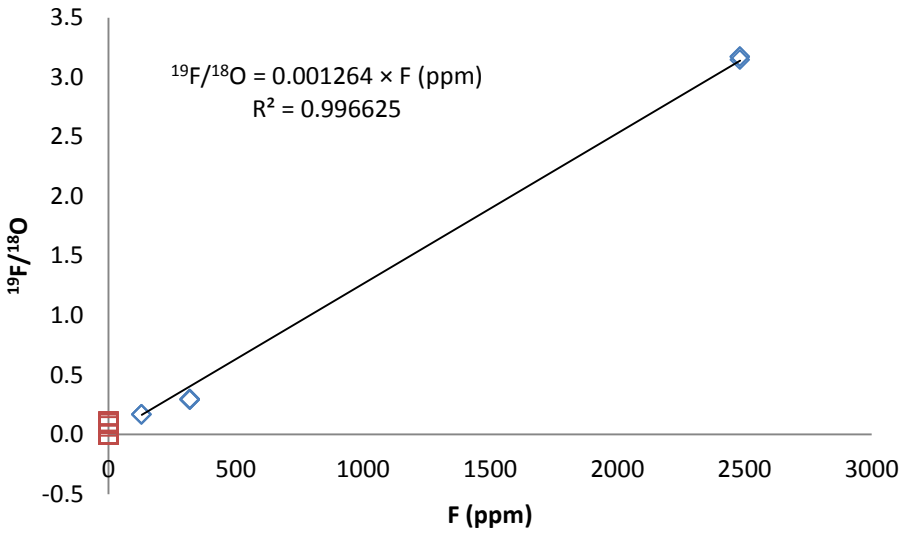

Figure S3-7 Calibration curve for fluorine analyses. Blue diamonds are blank-corrected measurements of glass standards; pink squares on the y-axis demarcate the range of blank-corrected $^{19}F/^{18}O$ measured in sample Siq7. The black line is a least squares linear regression to the data forced through the origin, and the equation of the line and its coefficient of determination (R^2) are written on the plot. Standards were analyzed on the 25th and 26th July, and these analyses were grouped to create a single calibration curve for samples analyzed on the 26th and 27th July.

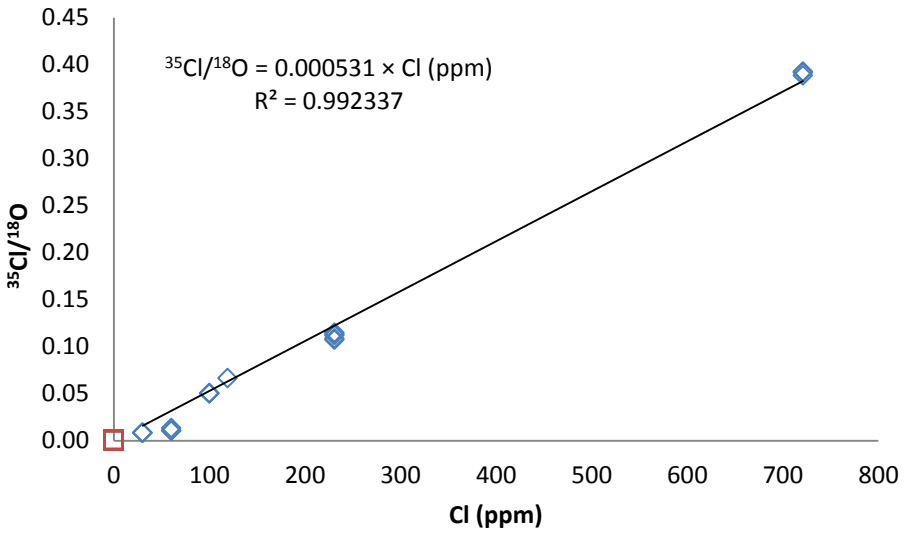

Figure S3-8 Calibration curve for chlorine analyses. Blue diamonds are blank-corrected measurements of glass standards; pink squares on the y-axis demarcate the range of blank-corrected $^{35}Cl/^{18}O$ measured in sample Siq7. The black line is a least squares linear regression to the data forced through the origin, and the equation of the line and its coefficient of determination (R^2) are written on the plot. Standards were analyzed on 25th and 26th July, and these analyses were grouped to create a single calibration curve for samples analyzed on 26th and 27th July.

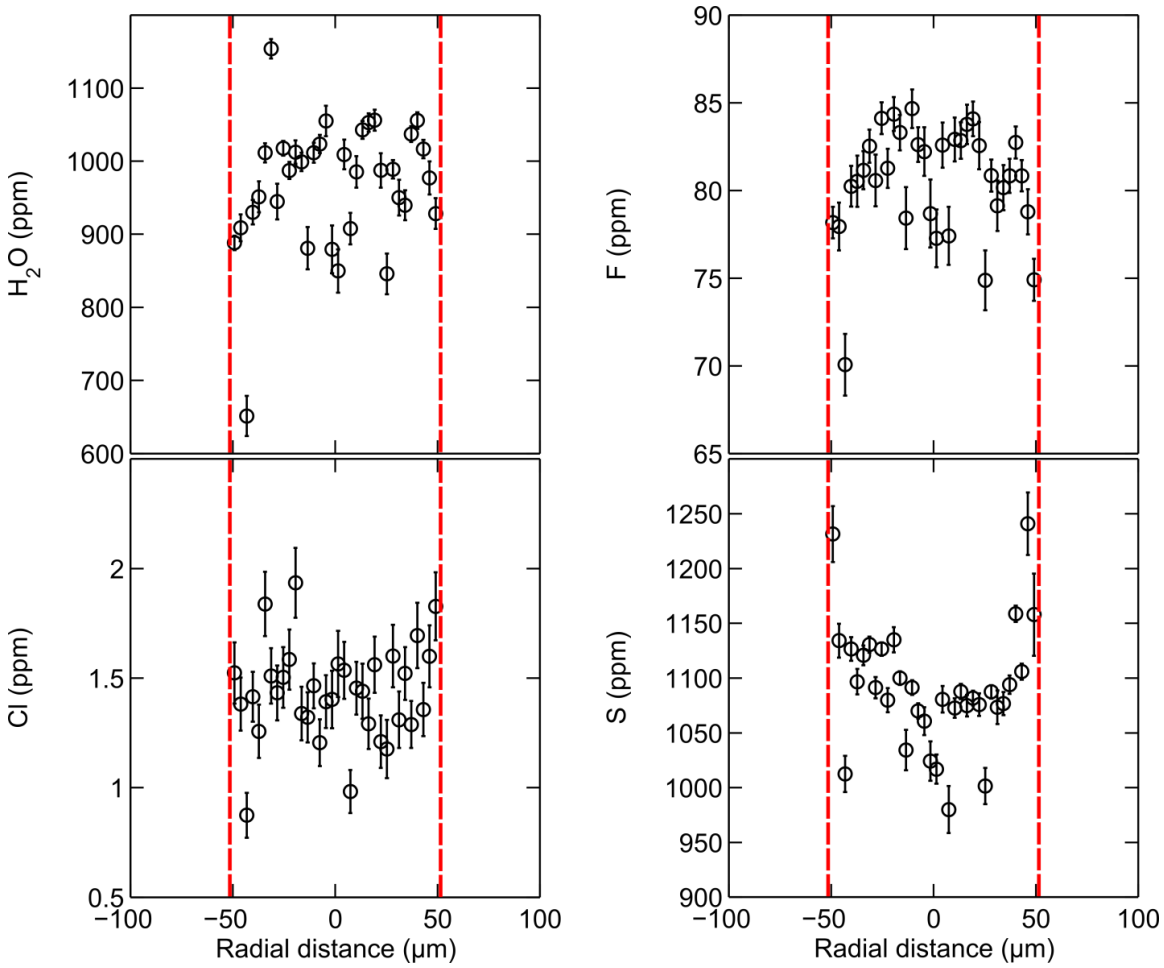

Figure S3-9 Concentrations of H_2O, S, F and Cl in melt inclusion Siq7. Data collected on 27th July 2011. Concentrations calculated using calibration curves in Figures S3-5–S3-8. Red dashed lines indicate the edges of the melt inclusion. 100 cycles of data were collected at each point, and data points are plotted at the mean values of these 100 cycles. Error bars are two times the standard error of the mean. Three replicate analyses of GRR997 (Mosenfelder et al. 2011) were used to assess the detection limits at 99% confidence for H_2O, Cl, F, and S, following equation (7) of Long and Winefordner (1983). The detection limits were 445 ppm for H_2O, 2.3 ppm for F, 5.7 ppm for S, and 2.7 ppm for Cl. Note that all Cl analyses are below the nominal detection limit of 2.7 ppm.

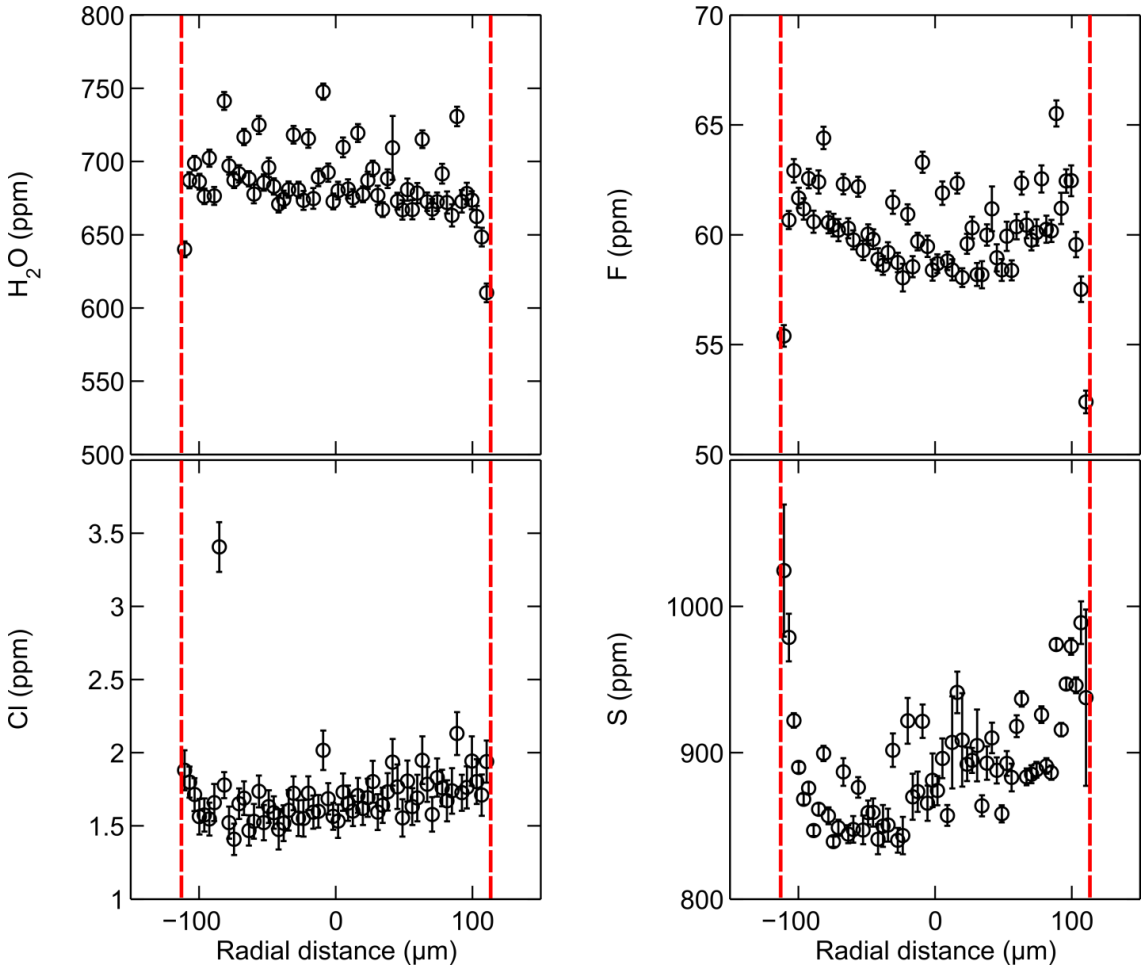

Figure S3-12 Concentrations of H_2O, S, F and Cl in melt inclusion Siq16. Data collected on 6th July 2011. Concentrations calculated using calibration curves in Figures S3-1–S3-4. Red dashed lines indicate the edges of the melt inclusion. 100 cycles of data were collected at each point, and data points are plotted at the mean values of these 100 cycles. Error bars are two times the standard error of the mean. One H_2O data point plots off the scale of the figure (at 1233 ppm) and is likely contaminated (the same point is anomalously high in Cl). Four replicate analyses of GRR997 (Mosenfelder et al. 2011) were used to assess the detection limits at 99% confidence for H_2O, Cl, F, and S, following equation (7) of Long and Winefordner (1983). The detection limits were 74 ppm for H_2O, 1.8 ppm for F, 0.9 ppm for S, and 0.4 ppm for Cl.

References

Bouvier A-S, Métrich N, Deloule E (2008) Slab-Derived Fluids in the Magma Sources of St. Vincent (Lesser Antilles Arc): Volatile and Light Element Imprints. Journal of Petrology 49 (8):1427-1448. doi:10.1093/petrology/egn031

Jochum KP, Stoll B, Herwig K, Willbold M, Hofmann AW, Amini M, Aarburg S, Abouchami W, Hellebrand E, Mocek B (2006) MPI-DING reference glasses for in situ microanalysis: New reference values for element concentrations and isotope ratios. Geochemistry, Geophysics, Geosystems 7 (2)

Le Voyer M, Asimow PD, Mosenfelder J, Guan Y, Wallace PJ, Schiano P, Stolper EM, Eiler JM (2013) Zonation of H_2O, Cl, and F concentrations around melt inclusions in olivines. Submitted to Journal of Petrology

Long GL, Winefordner JD (1983) Limit of Detection A Closer Look at the IUPAC Definition. Analytical Chemistry 55 (7):712A-724A. doi:10.1021/ac00258a724

Metrich N, Clocchiatti R (1989) Melt inclusion investigation of the volatile behaviour in historic alkali basaltic magmas of Etna. Bulletin of Volcanology 51 (3):185-198

Mosbah M, Metrich N, Massiot P (1991) PIGME fluorine determination using a nuclear microprobe with application to glass inclusions. Nuclear Instruments and Methods in Physics Research Section B: Beam Interactions with Materials and Atoms 58 (2):227-231

Mosenfelder JL, Le Voyer M, Rossman GR, Guan Y, Bell DR, Asimow PD, Eiler JM (2011) Analysis of hydrogen in olivine by SIMS: Evaluation of standards and protocol. Am Miner 96 (11-12):1725-1741. doi:10.2138/am.2011.3810

Witter JB, Kuehner SM (2004) A simple empirical method for high-quality electron microprobe analysis of fluorine at trace levels in Fe-bearing minerals and glasses. Am Miner 89 (1):57-63

Appendix III

THE PETROCHEMISTRY OF JAKE_M: A MARTIAN MUGEARITE

E.M. Stolper[1], M.B. Baker[1], M.E. Newcombe[1], M.E. Schmidt[2], A.H. Treiman[3], A. Cousin[4,5], M.D. Dyar[6], M.R. Fisk[7], R. Gellert[8], P.L. King[9], L. Leshin[10], S. Maurice[5], S.M. McLennan[11], M.E. Minitti[12], G. Perrett[8], S. Rowland[13], V. Sautter[14], R.C. Wiens[4], and the MSL Science Team.

[1]Caltech, Pasadena, CA 91125;
[2]Brock Univ., St. Catharines, ON L2T 3V8, Canada;
[3]Lunar & Planet. Inst., Houston, TX 77058;
[4]LANL, Los Alamos, NM 87545;
[5]Institut de Recherches en Astrophysique et Planétologie, 31028 Toulouse, France;
[6]Mt. Holyoke College, South Hadley, MA 01075;
[7]Oregon State Univ., Corvallis, OR 97331;
[8]Univ. Guelph, Guelph, ON N1G 2W1, Canada;
[9]Res. School Earth Sci., ANU, Acton ACT 0200, Australia;
[10]RPI, Troy, NY 12180;
[11]SUNY, Stony Brook, NY 11794;
[12]APL, The Johns Hopkins Univ., Baltimore, MD 20723;
[13]Univ. Hawaii, Honolulu, HI 96822;
[14]LMCM, 75005 Paris, France

*Published as Stolper, E. M., et al. "The petrochemistry of Jake_M: A Martian mugearite." *Science* 341.6153 (2013): 1239463.

DOI: 10.1126/science.1239463

The Petrochemistry of Jake_M: A Martian Mugearite

E.M. Stolper[1], M.B. Baker[1], M.E. Newcombe[1], M.E. Schmidt[2], A.H. Treiman[3], A. Cousin[4,5], M.D. Dyar[6], M.R. Fisk[7], R. Gellert[8], P.L. King[9], L. Leshin[10], S. Maurice[5], S.M. McLennan[11], M.E. Minitti[12], G. Perrett[8], S. Rowland[13], V. Sautter[14], R.C. Wiens[4], and the MSL Science Team.

[1]Caltech, Pasadena, CA 91125; [2]Brock Univ., St. Catharines, ON L2T 3V8, Canada; [3]Lunar & Planet. Inst., Houston, TX 77058; [4]LANL, Los Alamos, NM 87545; [5]Institut de Recherches en Astrophysique et Planétologie, 31028 Toulouse, France; [6]Mt. Holyoke College, South Hadley, MA 01075; [7]Oregon State Univ., Corvallis, OR 97331; [8]Univ. Guelph, Guelph, ON N1G 2W1, Canada; [9]Res. School Earth Sci., ANU, Acton ACT 0200, Australia; [10]RPI, Troy, NY 12180; [11]SUNY, Stony Brook, NY 11794; [12]APL, The Johns Hopkins Univ., Baltimore, MD 20723; [13]Univ. Hawaii, Honolulu, HI 96822; [14]LMCM, 75005 Paris, France;

Abstract: Jake_M, the first rock analyzed by the APXS instrument on the Curiosity rover, differs significantly in chemical composition from other known martian igneous rocks: It is alkaline (>15% normative nepheline) and relatively fractionated. Jake_M is similar compositionally to terrestrial mugearites, a rock type typically found at ocean islands and continental rifts. By analogy with these comparable terrestrial rocks, Jake_M could have been produced by extensive fractional crystallization of a primary alkaline or transitional magma at elevated pressure, with or without elevated water contents. The discovery of Jake_M suggests that alkaline magmas may be more abundant on Mars than on Earth and that Curiosity could encounter even more fractionated alkaline rocks (e.g., phonolites and trachytes).

Introduction:

Rock "Jake_M" (JM; named for JPL engineer Jake Matijevic) was the first sample imaged using the Mars Hand Lens Imager (MAHLI) and analyzed on sols 46 and 47 with the Alpha Particle X-ray Spectrometer (APXS) on the Mars Science Laboratory (MSL) (*1, 2*). Although the rock is an isolated fragment lacking field context (encountered ~282 m from the Bradbury landing site), its dark color and apparently fine-grained texture suggested prior to analysis that it was a relatively homogeneous (on a mm-to-cm scale) igneous rock and thus an appropriate sample with which to initiate the APXS analytical program and to analyze with ChemCam (*3*) using Laser-induced Breakdown Spectroscopy (LIBS). We report here chemical analyses of JM and an interpretation of their meaning for its petrogenesis.

Results and Discussion:

Petrography:

JM is roughly pyramidal in shape (~50 cm on each of its three base edges and ~50 cm tall; Fig. 1). The rock is dark gray and thinly coated by light-toned reddish-brown dust. Its upper surfaces have rounded hollows likely due to wind erosion and <1–3 mm pits that could be vesicles. The lowest ~2 cm of the rock has smoother surfaces that may reflect primary layering or the effects of wind erosion. Near-vertical fractures (~10 cm long) project upward from the base. Feldspar microphenocrysts have been tentatively identified in MAHLI images (*4*), but individual mineral grains could not otherwise be distinguished in optical images, perhaps due to the dust cover and/or polish by wind. Compositional variations among the 14 individual locations (see Fig. 1 and Supplementary Materials, Fig. S1) analyzed by LIBS using ChemCam show that the rock is heterogeneous on a length scale of ~0.5 mm. The heterogeneities observed by LIBS analyses suggest the presence of plagioclase (broadly consistent with oligoclase), Ca-rich pyroxene, olivine, and Fe-Ti-rich oxide(s) [(*3*); see also Supplementary Materials, Figs. S1–S4].

Bulk composition and classification:

The three APXS analyses (Table 1) were collected on two different spots; the listed uncertainties on the average (calculated after normalizing each analysis to 100 wt. %, excluding SO_3, Cl, and trace elements) are due to variations between the three analyses that may partially reflect real differences between the two analyzed spots. The surface of JM was not brushed or abraded prior to analysis; in the Supplementary Materials we compare the JM analyses to both unbrushed (i.e., "as is") and physically abraded rock surfaces analyzed by the Mars Exploration Rovers (MERs). The CIPW norms (*5*) (Table 1) are based on the average JM composition and were calculated using molar Fe^{3+}/(total Fe) ratios of 0 and 0.15. Although this range of Fe^{3+}/(total Fe) ratios brackets the ratios

expected in basaltic melts at the estimated fO_2 values of basaltic shergottites (e.g., *6*), recent modeling suggests that mantle melting at higher fO_2s may have occurred early in the planet's history (*7*). However, even for a Fe^{3+}/total Fe value of 0.3, normative nepheline is still ~15 wt. %.

Based on either its calculated norm or inspection of its major-element composition, JM has a basaltic composition, and it is likely an igneous rock (although we cannot tell whether it is from a lava flow, an intrusion, a pyroclastic flow, or a volcaniclastic sediment deposited after minimal fractionation or alteration of primary igneous rocks). Moreover, with its ~16–17 % normative nepheline (Table 1) and its position on an alkali-silica diagram (Fig. 2), JM is an alkaline rock [with an alkalinity index (*8*) significantly higher than other known martian rocks]. It is also evolved (likely due to crystal fractionation) relative to most other known martian igneous rocks (Fig. 3): it has a low MgO content (4.4 wt. %), albitic normative plagioclase (oligoclase, ~An_{15}), a molar $Mg/(Mg+Fe_{total})$ ratio of ~0.43, ~40 ppm Ni, and ~270 ppm Cr (Ni and Cr values are from the two long-duration analyses listed in Table 1). Based on its MgO content, JM is more fractionated than most other martian rocks—of the analyses plotted in Fig. 3, only the basaltic shergottite Los Angeles (*9*), the rocks Wishstone and Champagne analyzed by the MERs (*10*), and the two estimated soil-free Pathfinder rock compositions (*11, 12*) have similar or lower MgO contents.

For terrestrial igneous rocks, chemical composition is generally not the sole criterion for classification. For JM, we have no other information and although it plots slightly above the nominal mugearite field on the alkali-silica diagram (this field is shown as the blue polygon in Fig. 2), the composition of the normative plagioclase (i.e., oligoclase; broadly consistent with the ChemCam results), the substantial normative nepheline and orthoclase, and the fact that it overlaps compositionally with many terrestrial rocks that

have historically been called mugearites (Figs. 2b, S5) leads us to classify JM as a mugearite (*13*). Mugearites are a well-defined and widely distributed (though relatively uncommon) intermediate (i.e., fractionated) member of the terrestrial alkali-olivine basalt, hawaiite, mugearite, benmoreite, trachyte-phonolite magma series found in locations such as ocean islands and continental rifts (*14-16*). They generally contain normative nepheline, but nepheline as a phenocryst phase is relatively rare (*14*) so the absence of a nepheline signature in the ChemCam results is not inconsistent with JM's normative composition. Note that although JM actually plots in the nominal phonotephrite field in Fig. 2, in other respects the compositional comparison of JM to terrestrial rocks that have been called phonotephrites is no better (and arguably worse) than to rocks called mugearites (Fig. S5, S6).

Comparison to other martian igneous rocks:

Although there is overlap in some oxide concentrations, taken as a whole, the JM composition is distinct from all other known martian igneous rocks (Figs. 2, 3). In particular, compared to JM's Na_2O and K_2O contents of ~7 and ~2.1 wt. %, respectively (Table 1), all martian meteorites and martian igneous rocks analyzed by Pathfinder and the MERs are significantly lower in sodium and potassium: the highest previously analyzed Na_2O contents are only ~4–5 wt. % (Backstay, Humboldt Peak, NWA 7034 meteorite, Wishstone, Champagne, and one of the estimated soil-free Pathfinder compositions; see Fig. 3f); the highest K_2O contents of relatively unaltered martian rocks (*17*) are only ~1 wt. % (Backstay, Humboldt Peak, Madeline English, and the soil-free Pathfinder compositions; Fig. 3g). There is, however, evidence from the nakhlite meteorites of K-rich martian liquids: (i) the presence of K-rich kaersutite in melt inclusions (*18*); (ii) highly fractionated glassy mesostasis in the nakhlites (*19*); and (iii) K-rich bulk melt inclusion compositions (*20*). Most martian meteorites and analyzed martian igneous rocks have higher MgO and FeO* contents and lower Al_2O_3 contents

than JM [Figs. 3c, d; see also (*21*)]; although there are exceptions for individual elements (e.g., the soil-free Pathfinder compositions, Wishstone, Champagne, and Los Angeles for MgO; Backstay, Wishstone, Champagne, and NWA 7034 for FeO*; and Wishstone and Champagne for Al_2O_3), no known martian rock overlaps JM in all three of these elements. The Ni (22-59 ppm) and Cr (~270 ppm) contents of JM are among the lowest values for an unbrushed rock surface found on Mars to date; moreover, since martian dust is typically enriched in Ni by ~10 times JM values (*22*), JM probably contains even lower Ni than is suggested by the APXS analyses.

Although some Gusev samples are alkaline [i.e., they plot above the alkaline-subalkaline boundary curve in Fig. 2 (*23*) and have normative nepheline; e.g., Humboldt Peak] or transitional (i.e., they plot near the boundary curve and have only small amounts of either normative nepheline or hypersthene; e.g., Backstay, NWA 7034), no relatively unaltered samples are as alkali-rich relative to the alkaline-subalkaline boundary curve in Fig. 2 or as rich in normative nepheline as JM. Note that despite their positions in Fig. 2, Wishstone and Champagne are *not* nepheline normative. This is due to their extremely high bulk P_2O_5 contents of 5.2–5.3 wt. %; only if P_2O_5 were ~1 wt. %, a value more typical of Gusev Crater rocks, would these rocks be as strongly nepheline normative as their positions on Fig. 2 might suggest. [See also (*24*) for a discussion of how changing the normative phosphate-bearing mineral from apatite to Ca-merrillite affects the proportions of the other normative components.]

Comparison to terrestrial compositions:

As shown by a comparison between JM and lavas from Tenerife (one of the Canary Islands), there is an excellent correspondence between JM and fractionated alkaline basaltic rocks on Earth (Figs. 3, S5–S8). JM lies on or near the oxide-MgO trends for Tenerife for all oxides except TiO_2. As is the case for JM, when compared with Tenerife

lavas with the same MgO content, nearly all of the martian rocks plotted in Fig. 3 have substantially lower TiO_2 contents than the Tenerife lavas, and this low TiO_2 appears to be a characteristic of martian rocks generally. Nevertheless, even the TiO_2 content of JM is not outside the range of fractionated terrestrial alkaline igneous rock compositions (Fig. S7a), and both JM and non-alkaline martian rocks overlap with terrestrial tholeiites in TiO_2-MgO space (Fig. S7b). Although JM is slightly elevated in total alkalis relative to the Tenerife trend (Fig. 2) and at the upper end of a field defined by mugearite lavas (reflecting JM's high Na_2O content; Figs. 3f, S5f), terrestrial alkaline suites span a wide range of total alkali contents at a given silica (or MgO) content, with some being lower than JM [e.g., St. Helena, (*25*)] and others being higher [e.g., Tristan da Cunha, (*25*)].

The chemical similarity between JM and terrestrial igneous rocks is surprising given that the chemical compositions of SNC meteorites and of igneous rocks analyzed using APXS on the surface of Mars (after correction for or removal by brushing or abrasion of surface-correlated components such as dust) differ systematically in many respects from those of terrestrial igneous rocks [(e.g., *26, 27*); see also (*21*)]. These distinctions remain even when martian meteorites are compared with Fe-rich terrestrial lavas (*28*). However, even JM's Fe/Mn ratio is within the range of comparable terrestrial igneous rocks [Fig. S8; terrestrial and martian bulk rock and olivine and pyroxene Fe/Mn ratios have historically been considered diagnostic of each planet, (*29-32*)]. Overall, were JM found on Earth, we would be hard pressed to tell from its whole-rock chemical composition that it is martian. In the discussion below, we use the fact that JM plots essentially on the alkaline rock series from Tenerife (Figs. 2, 3) as an aid to understanding one possible model for its petrogenesis.

Based on the differences in S and Cl contents from undisturbed *vs*. physically abraded martian rock surfaces, it is likely that much of the S and Cl in the APXS analysis of JM

reflects a surficial component such as dust [after abrasion, SO_3 and Cl contents of Gusev crater rocks/outcrops generally drop by ~40–90%, (*10*)]. However, there are haüyne-bearing terrestrial lavas, historically called "tahitites" (*33*), with major-element compositions broadly similar to JM and with elevated S and Cl contents. Analyses of such haüyne-bearing lavas (containing 50–58 wt. % SiO_2 on a volatile-free basis) from the Georoc database (*25*) have 0.6–2.4 wt. % SO_3 and up to 0.8 wt. % Cl [and some phonolitic lavas from Tenerife contain haüyne, (e.g., *34*)]. Thus, although it cannot be quantified at this time, it is possible that non-negligible amounts of the S and Cl in the JM analysis are indigenous to the magma from which it formed rather than a secondary, surface-correlated feature.

Petrogenesis of JM:

Hypotheses for the origins of igneous rocks rarely rely on isolated chemical compositions but are constrained by field relations, petrography, and the compositional trends defined by related rocks. We lack these data for JM, but we are able to say with some confidence what its compositional features would signify if it formed by processes similar to those that have produced comparable terrestrial rocks. Although an infinite number of petrogenetic models could be constructed to account for a single rock composition such as JM, we emphasize again the strong compositional correspondence between JM and terrestrial mugearites (including its position close to the liquid-line-of-descent of Tenerife magmas). This correspondence provides a plausible context for interpreting the composition of JM and is at least permissive that the petrogenetic processes responsible for the compositional trends observed in these terrestrial lavas could be applicable to the evolution of JM.

Evolved terrestrial alkaline rocks including mugearites are generally produced by extensive crystal fractionation of alkaline or transitional magmas. Although in some cases

this fractionation appears to occur in the upper mantle based on the presence of peridotite xenoliths in some mugearites and related rocks (*35-37*), it more commonly occurs in crustal magma chambers or at even shallower depth within a volcanic edifice (e.g., *15, 16, 38*). With this in mind, we used MELTS (*39, 40*) to simulate fractional crystallization of a primitive Tenerife melt composition over a range of pressures (1–6000 bar), water concentrations (0–3 wt. %), and oxygen fugacities (QFM–1 to QFM+2).

A crucial constraint on the fractionation required to explain the trend of Tenerife magmas is the monotonic increase in the Al_2O_3 contents of the observed rocks with decreasing MgO content (at least down to 2 wt. % MgO). As shown by MELTS calculations (Fig. 4), this monotonic change all the way down to 2 wt. % MgO cannot be produced by fractionation from a dry primitive basanite at 1 bar—under these conditions, plagioclase saturation is reached at ~7.8 wt. % MgO, long before sufficient fractionation has occurred to produce residual liquids with MgO contents in the 2 % range. As a result, residual liquids with MgO contents like those of JM (4–5 wt. %) contain only 14–15 wt. % Al_2O_3 (i.e., less than the ~15–19 wt. % Al_2O_3 in JM and terrestrial mugearites; Fig. S5). In order to produce residual melts with monotonically increasing Al_2O_3 contents at these MgO contents, plagioclase crystallization must be suppressed—it is well known that elevated water contents and elevated total pressure individually or together can suppress plagioclase crystallization (*41-44*). MELTS calculations confirm this: Starting with the primitive basanite at 4 kbar dry, the MELTS calculations predict that plagioclase saturation is indeed delayed relative to 1 bar crystallization, only being reached at liquid MgO contents of ~4.8 wt. % (Fig. 4); in contrast, and as expected, clinopyroxene saturates earlier in the fractionation sequence relative to the calculated trend at 1 bar (Fig. 4). With the addition of 1 wt. % H_2O to the parental basanite at 4 kbar, plagioclase crystallization is even further suppressed; Fig. 4 shows that the model fractionation sequence only reaches plagioclase saturation at ~2 wt. % MgO and that clinopyroxene

appearance is also somewhat delayed relative to the 4 kbar anhydrous calculation. Note that the points along the model liquid-lines-of-descent that mark the appearance of Fe-rich spinel are little affected over the ranges in pressure and water content investigated here (Figs. 4, S11). These calculations were all done at an fO_2 fixed relative to the QFM buffer [i.e., at QFM+1, an fO_2 consistent with estimates from Fe-Ti oxides in Tenerife volcanics (*38*)]; under more oxidizing or reducing conditions Fe-rich spinel would appear earlier or later in the calculated liquid-line-of-descent.

Although the 4 kbar dry simulation of the Tenerife parental basanite suppresses plagioclase crystallization sufficiently to account for the high Al_2O_3 contents of JM and rocks from Tenerife with 4–5 wt. % MgO, the simulated fractionation trend provides a poor fit to the more evolved lavas from Tenerife (Fig. 4), which would require even further suppression of plagioclase crystallization to account for their even higher Al_2O_3 contents. In contrast, the 4 kbar simulation with 1 wt. % H_2O in the parent magma reproduces the observed trend in Al_2O_3 all the way down to ~2 wt. % MgO (Fig. 4), reproduces reasonably well the trends of all of the other oxides (Fig. S11), and matches the water contents measured in melt inclusions from Tenerife lavas with phonolitic compositions (*45*). The simulation at 4 kbar with 1 wt. % H_2O in the parental basanite magma, which reaches the MgO content of JM after ~57% crystallization and with ~2.3 wt. % H_2O in the JM-like residual melt, provides the best fit to the overall Tenerife trend (see Fig. S12, which illustrates the degree to which the calculated liquid-lines-of-descent reproduce the compositional trend of the lavas as pressure and initial water content vary). Similar calculations by Beier et al. (*46*) using lavas from Sete Cidades volcano, Sao Miguel (in the Azores) produced comparable results, requiring 0.5 wt. % H_2O in the parent liquid and fractionation at 5 kbar to reproduce the overall observed liquid-line-of-descent.

The point of these simulations and their comparisons to JM and to the overall Tenerife liquid-line-of-descent (Figs. 4, S11) is not whether a precise match can be achieved. As good as they are, MELTS calculations are no substitute for experiments in determining a fractionation path and its sensitivity to pressure, water content, other volatiles, and oxygen fugacity [e.g., the calculated best-fit liquid-line-of-descent does not include amphibole and yet amphibole is present in the more fractionated Tenerife lavas (*38*)]. Moreover, it is unreasonable to suppose that JM's bulk composition represents exactly a liquid composition or that the parent magma would be identical in all respects to one from Tenerife (indeed, as pointed out above, the Na_2O and TiO_2 contents of JM and the Tenerife trend do not match perfectly). The point of the comparison is simply that the overall trend of the Tenerife liquid-line-of-descent is captured reasonably well *only* if plagioclase crystallization is suppressed relative to low-pressure, dry conditions and that several kilobars of pressure (corresponding to up to a few tens of kilometers depth within Mars) and water contents in the parent magma of order 1 wt. % H_2O do this successfully. If the pressure were less than ~1 kbar, the fits worsen because under these conditions not enough water is able to dissolve in the melt to suppress plagioclase crystallization sufficiently to reproduce the monotonic enrichment with fractionation observed in Al_2O_3 among the most highly evolved rocks from Tenerife. Nevertheless, as stated above, the 4 kbar anhydrous trend provides a reasonable fit to the JM compositions, and thus we cannot say with any confidence that the fractionation of JM requires ~1 wt. % H_2O in the parental magma; indeed, although the model 1 bar trend at 4–5 wt. % MgO is low in Al_2O_3 relative to JM, if we allowed for moderate plagioclase accumulation in JM or increased uncertainties in JM's stated composition, even fractionation under these conditions could not be ruled out. However, we can say with reasonable certainty that terrestrial magmas that are compositionally similar to JM require fractionation at both elevated pressure and water content. One way to resolve this for JM would be if more evolved alkaline lavas are discovered on Mars and if these, like comparable terrestrial

magmas, have even higher Al_2O_3 contents than JM. If so, this would strengthen the requirement for a moderate pressure, hydrous liquid-line-of-descent to explain JM since it would be difficult to match such elevated Al_2O_3 contents at low pressure or without dissolved water. Although they are not definitive, the pits on the surface of JM (Fig. 1) may be wind-eroded vesicles, and this would be consistent with hydrous fractionation. Likewise, the inferred water content of JM (~2 wt. % if we accept the analogy with Tenerife magmas) is also consistent with previous efforts to constrain the petrogenesis of martian magmas, which have concluded that they contained up to several wt. % dissolved H_2O (*47-49*). Measurements of water in amphiboles in Chassigny (*50*) also suggest that the mantle source region of Chassigny may have been relatively wet. In contrast, however, Filiberto and Treiman (*51*) have argued that magmas parental to the martian meteorites were chlorine-rich and water-poor, i.e., <0.3 wt. % H_2O. Although extensive work has been done on the partitioning of Cl between silicate melts and H_2O-rich fluids (e.g., *52, 53*), it is not clear from available experimental data (e.g., *54*) whether Cl suppresses plagioclase crystallization to a similar degree as H_2O.

In order to explore whether any known martian igneous rocks could represent acceptable parent liquids for JM, we also performed MELTS calculations on Backstay, Humboldt Peak, and NWA 7034. In these cases, because there is no suite of lavas to constrain the liquid-line-of-descent as in the case of the Tenerife calculations, we only used MELTS simulations to determine whether parent liquids corresponding to these known martian igneous rocks could fractionate to produce a residual liquid corresponding to JM, and if so, what conditions would be required. None of the martian rock compositions have high enough alkali contents to produce a close match to JM under any conditions (Supplementary Materials; Figs. S13–S24). However, if we arbitrarily increased the alkali contents by an amount such that on fractionation the modeled alkali contents of the fractionated liquids matched those of JM at an MgO content of ~4–5 wt. %, the alkali-

enriched Backstay composition could produce a reasonable approximation of JM after a few tens of percent crystal fractionation (although we note that the required arbitrary increases in alkalis are not trivial).

Origins of alkaline magmas on Mars:

We have no constraints on conditions required on Mars to produce the parental alkaline or transitional liquids from which JM is presumed to have evolved by extensive crystal fractionation. On Earth, such parental magmas have been attributed to a variety of conditions and processes, including melting of lherzolite + CO_2 ± H_2O at elevated pressures (e.g., *55, 56, 57*); melting of metasomatized lithospheric mantle (e.g., *58, 59, 60*); and melting of pyroxenites and amphibolites (e.g., *60, 61, 62*). Models for the origin of previously described alkaline and transitional martian magmas have called upon melting of a more alkali-rich mantle source [relative to that of the shergottites, (*63*)] and/or hydrous fractional crystallization of transitional magmas at pressures of a few kilobars (*64*).

Ratios of moderately volatile alkalis to refractory lithophile elements in martian rocks have been used to infer that the primitive martian mantle was richer in Na and K than the terrestrial mantle by as much as a factor of two (e.g., *65, 66-69*). On this basis alone, although few alkaline martian rocks have been documented thus far, it would not be surprising if alkaline magmas derived from relatively alkali-rich sources (either primitive martian mantle or mantle that has been metasomatized by low-degree melts of relatively primitive mantle) were more common on Mars than they are on Earth [on Earth, alkaline lavas are rare from a planetary perspective, representing an estimated < 1 vol. % of terrestrial igneous rocks, (e.g., *70*)]. Note that based on trace-element and radiogenic-isotope ratios, the average sources of most shergottite meteorites are inferred to have been depleted and in some cases highly depleted (i.e., melts have been extracted from

these source regions prior to the melting events that produced the shergottites). This depletion of their sources could explain the low alkali (and alumina) contents characteristic of the shergottites. If the liquids extracted during these earlier depletion events were enriched in alkalis (i.e., because they formed as partial melts of relatively primitive martian mantle) and were emplaced into the crust and lithospheric mantle, they could have enriched and metasomatized portions of the martian mantle. Melting of such enriched sources might then have produced the magmas parental to alkaline rocks such as JM. The overall K-rich nature of analyzed rocks from the MSL mission thus far (*71*) could reflect the presence of such an enriched region in the mantle underlying Gale Crater.

Acknowledgments: Paula Antoshechkin provided insight concerning several aspects of MELTS and Sarah Lambart ran early MELTS calculations and provided initial compilations of terrestrial alkaline lavas. We would also like to thank two anonymous referees for constructive reviews of the manuscript and the Mars Science Laboratory Project engineering and management teams for their efforts in making the mission such a success. This work was supported by grants from the National Science Foundation, the National Aeronautics and Space Administration, the Canadian Space Agency, and the Centre National d'Études Spatiales.

Figure Captions:

Fig. 1. Raw image of Jake_Matijevic taken by the Left Mastcam (0046ML0212000000E1) with overlain MAHLI at 26.9, 6.9, and 4.4 cm offsets from the front of the lens. The MAHLI projection on the left was taken at 4.4 cm (0047MH0011002000E1). Shadowing by the turret reduced the contrast in the inset MAHLI images, causing color differences with the Mastcam image. The filled red circles labeled JM1 and JM2 indicate the locations of the two APXS spots (1.7 cm diameter). ChemCam raster spots are represented by yellow open circles; actual spot sizes are ~0.45 mm. Credit: NASA/JPL-Caltech/MSSS.

Fig. 2. Alkali-silica diagram. Compositional boundaries and rock names are from (*72*); the mugearite field is shown in blue. The dashed curve shows the alkaline/subalkaline boundary curve from Irvine and Baragar (*23*). (a) Colored symbols (see legend) show the three JM analyses (Table 1), normalized to 100 wt. % without SO_3, Cl, and trace elements; basaltic martian meteorites [the shergottite "Los Angeles" (*9, 73*) and the basaltic breccia NWA 7034 (*74*) are shown as distinct symbols]; martian rocks analyzed by the MERs (*10, 75-77*) and interpreted as igneous (including volcaniclastics); and the two soil-free Pathfinder compositions calculated by Wänke et al. (*11*) and Foley et al. (*12*). Errors bars associated with the NWA 7034 and Pathfinder compositions reflect either 1σ uncertainties (NWA 7034) or the projection methods used to calculate a "soil-free" composition (Pathfinder). Note that NWA 7034 maybe a polymict breccia (*78, 79*). Larger filled colored circles labeled "Adirondack" through "Champagne" in the legend denote specific Mars surface rocks analyzed by the MERs. (b) Comparison of the three JM analyses (Table 1) with lavas from Tenerife in the Canary Islands (*25*) and with terrestrial lavas that have been called mugearites, including some from Tenerife (*25*). Only Georoc (*25*) analyses with oxides sums between 97 and 102.5 wt. % are plotted and all have been normalized to 100 wt. % on a volatile-free (including sulfur and chlorine) basis.

Fig. 3. Oxide-MgO variation diagrams (wt. %) comparing Tenerife lavas, the three Jake_M compositions (Table 1), and various martian igneous rock compositions (see caption to Fig. 2 for references and filters applied to the Tenerife lava compositions). (a) SiO_2-MgO; (b) TiO_2-MgO; (c) Al_2O_3-MgO; (d) FeO*-MgO; where FeO* denotes all Fe as FeO; (e) CaO-MgO; (f) Na_2O-MgO; (g) K_2O-MgO; (h) P_2O_5-MgO. Error bars as in Fig. 2.

Fig. 4. (a) Al_2O_3-MgO and (b) CaO-MgO variation diagrams comparing Tenerife lavas, the three Jake_M composition, and colored curves showing three MELTS fractional crystallization calculations described in the text (1 bar, anhydrous; 4 kbar, anhydrous; 4 kbar, 1 wt. % water in the parental liquid composition; all three calculations were done at fO_2 = QFM+1 where QFM is the quartz-fayalite-magnetite buffer). Phase abbreviations: pl = plagioclase, Fe-sp = magnetite-rich spinel, cpx = clinopyroxene, ol = olivine, Cr-sp = chromite-rich spinel; arrows point to the appearance of phases along

the MELTS-modeled liquid-lines-of-descent. Compositions of the Tenerife lavas are from (*25*, see caption to Fig. 2); starting composition for the MELTS modeling is the average of Tenerife lavas with 12–13.5 wt. % MgO and is reported in the Supplementary Materials along with further details of the MELTS calculations.

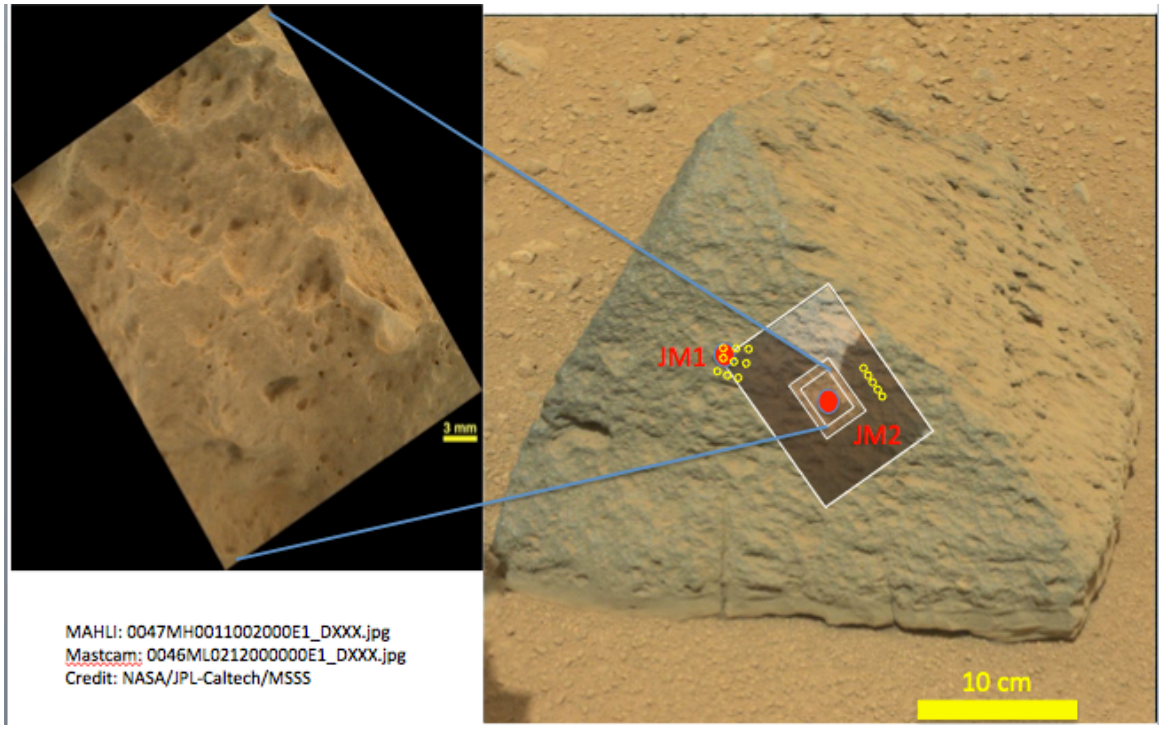
3 mm
JM1
JM2
10 cm
MAHLI: 0047MH0011002000E1_DXXX.jpg
Mastcam: 0046ML0212000000E1_DXXX.jpg
Credit: NASA/JPL-Caltech/MSSS

Fig. 1.

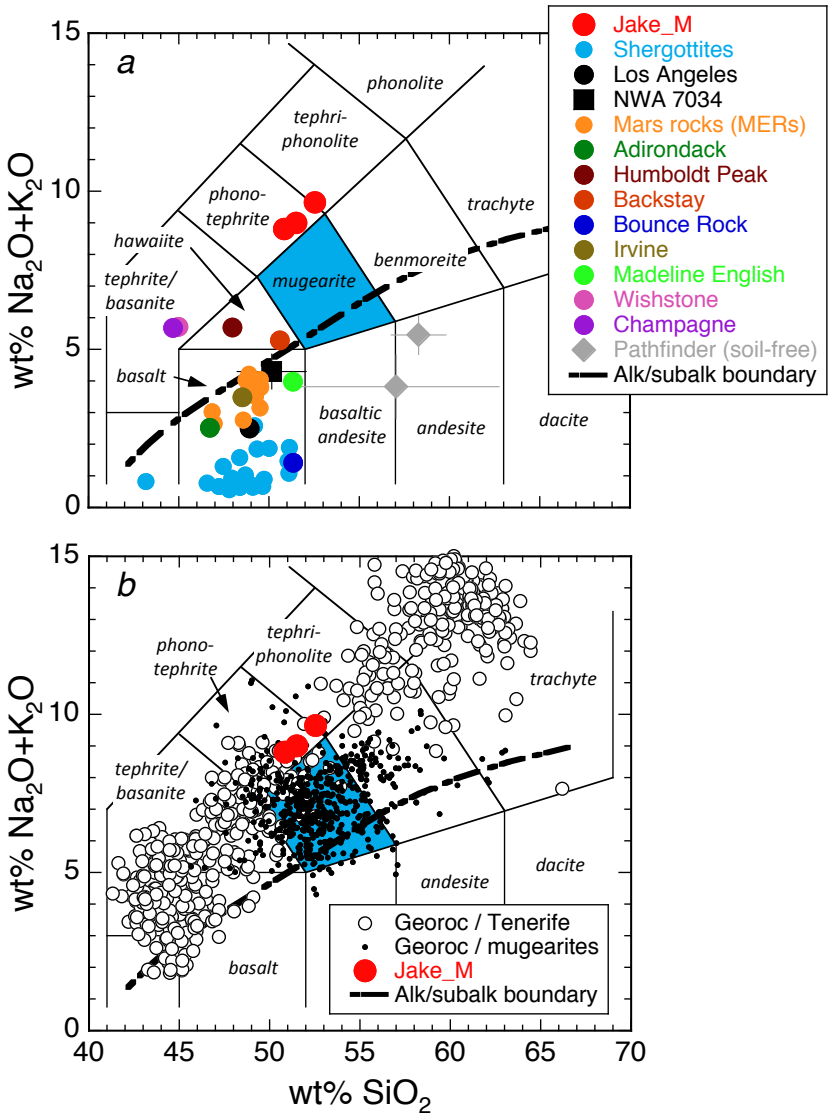
a
b
phonolite
tephri-
phonolite
phono-
tephrite
trachyte
hawaiite
tephrite/
basanite
mugearite
benmoreite
basalt
basaltic
andesite
andesite
dacite
Jake_M
Shergottites
Los Angeles
NWA 7034
Mars rocks (MERs)
Adirondack
Humboldt Peak
Backstay
Bounce Rock
Irvine
Madeline English
Wishstone
Champagne
Pathfinder (soil-free)
Alk/subalk boundary
Georoc / Tenerife
Georoc / mugearites
wt% Na2O+K2O
wt% SiO2
0
5
10
15
40
45
50
55
60
65
70

Fig. 2.

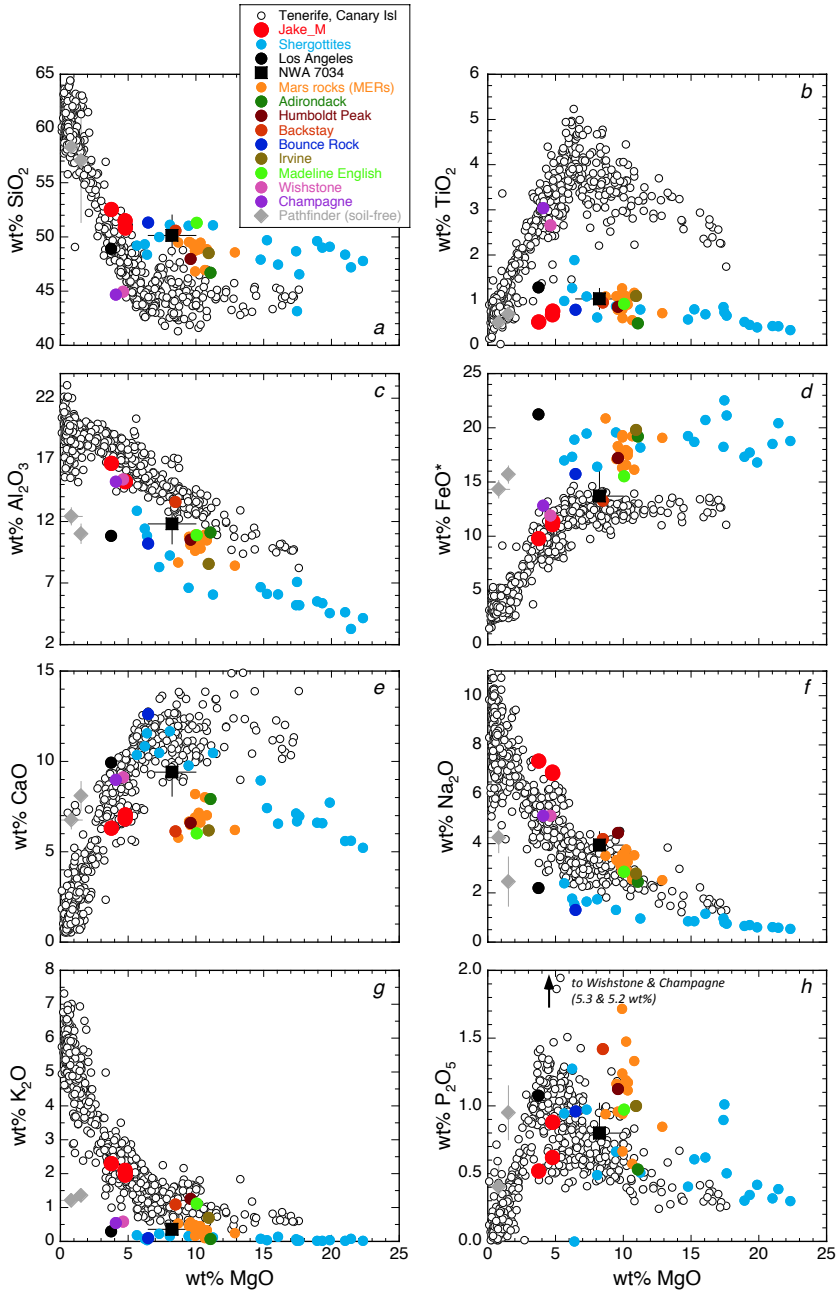
Tenerife, Canary Isl
Jake_M
Shergottites
Los Angeles
NWA 7034
Mars rocks (MERs)
Adirondack
Humboldt Peak
Backstay
Bounce Rock
Irvine
Madeline English
Wishstone
Champagne
Pathfinder (soil-free)
wt% SiO2
wt% TiO2
wt% Al2O3
wt% FeO*
wt% CaO
wt% Na2O
wt% K2O
wt% P2O5
wt% MgO
wt% MgO
a
b
c
d
e
f
g
h
to Wishstone & Champagne
(5.3 & 5.2 wt%)

Fig. 3

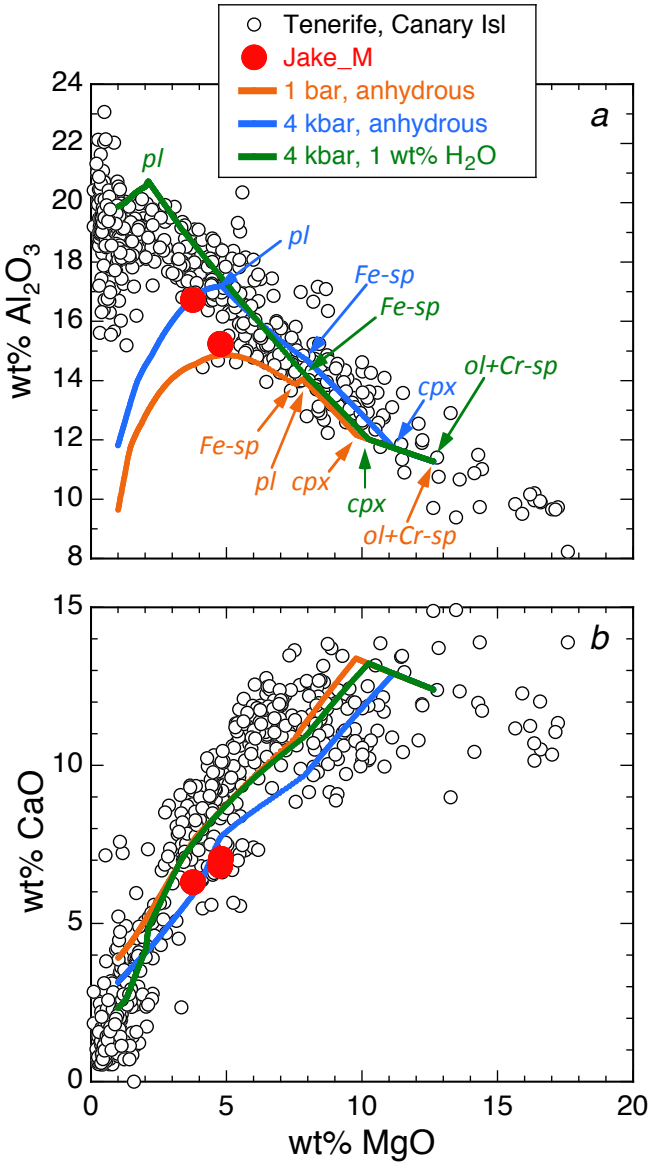
Tenerife, Canary Isl
Jake_M
1 bar, anhydrous
4 kbar, anhydrous
4 kbar, 1 wt% H2O
a
b
wt% Al2O3
wt% CaO
wt% MgO
pl
Fe-sp
ol+Cr-sp
cpx

Fig. 4.

Table 1. Composition and CIPW norms of Jake_M

wt%	JM1	JM2	JM2n	Average	Norm	0 Fe^{3+}	0.15 Fe^{3+}
SiO_2	50.7(6)	49.3(9)	48.9(5)	51.6(9)	Pl	32.3	34.4
TiO_2	0.50(3)	0.65(6)	0.73(3)	0.65(12)	Or	12.5	12.5
Al_2O_3	16.1(5)	14.6(7)	14.6(2)	15.7(9)	Ne	17.4	16.2
Cr_2O_3	0.03(1)	0.09(3)	0.04(1)	0.04(1)	Cpx	20.0	19.8
FeO	9.44(7)	10.61(11)	10.94(9)	10.8(8)	Ol	14.9	11.6
MnO	0.14(1)	0.17(2)	0.21(1)	0.18(4)	Ilm	1.2	1.2
MgO	3.6(4)	4.6(7)	4.60(12)	4.4(6)	Mt		2.6
CaO	6.09(7)	6.54(11)	6.78(8)	6.7(4)	Ap	1.6	1.6
Na_2O	7.1(3)	6.6(5)	5.59(14)	7.0(3)	Chr	0.06	0.06
K_2O	2.22(4)	2.01(6)	1.89(3)	2.12(17)	%An	15.2	14.2
P_2O_5	0.50(7)	0.60(12)	0.85(4)	0.68(19)	Mg# $_{ol}$	43.0	49.7
SO_3	2.46(9)	3.05(16)	2.81(8)		Mg# $_{cpx}$	43.0	49.7
Cl	0.88(3)	1.03(5)	0.95(3)		$(Mg\#)^{ol}$	68.0	71.6
Total	99.80	99.80	99.90				
Ni (ppm)	22(17)	n.d.	59(17)				
Zn (ppm)	216(13)	341(25)	318(15)				
Br (ppm)	88(8)	94(11)	107(7)				
Temp	–3 °C	–2 °C	–55 °C				
Duration	30 min	12 min	30 min				

1 and 2 after JM indicate the two locations analyzed on the rock (see Fig. 1), 2n indicates the nighttime analysis on spot 2. Values in parentheses for JM1, JM2, and JM2n are assessments of 2σ uncertainty based on counting statistics and data reduction in terms of the least units cited, i.e., 50.7(6) = 50.7±0.6; for further details see (*2*); n.d. = not detected. The average represents the unweighted mean of the three compositions each normalized to 100% excluding SO_3, Cl, and trace elements; values in parentheses are the standard deviations. Norm = normative minerals in wt. %; the column labeled 0 Fe^{3+} shows the calculated CIPW norm assuming that all Fe in the average bulk composition is Fe^{2+}; the column labeled 0.15 Fe^{3+} shows the calculated CIPW norm assuming Fe^{3+}/(total Fe) = 0.15; normative constituents: Pl = plagioclase (sum of normative anorthite and albite); Or = orthoclase; Ne = nepheline; Cpx = sum of normative diopside and hedenbergite; Ol = sum of normative forsterite and fayalite; Ilm = ilmenite; Mt = magnetite; Ap = apatite; Chr = chromite; %An = $100\times Ca/(Ca+Na)_{molar}$ in the normative plagioclase; Mg# $_{ol}$ and Mg# $_{cpx}$ = $100\times Mg/(Mg+Fe)_{molar}$ in normative olivine and high-Ca pyroxene, respectively; $(Mg\#)^{ol}$ = $100\times Mg/(Mg+Fe)_{molar}$ of the liquidus olivine calculated using an ol-liq $K_{D,Fe^{2+}\text{-}Mg}$ of 0.34 (*80, 81*).

Supplementary Materials for

The Petrochemistry of Jake_M: A Martian Mugearite

E.M. Stolper[1], M.B. Baker[1], M.E. Newcombe[1], M.E. Schmidt[2], A.H. Treiman[3], A. Cousin[4,5], M.D. Dyar[6], M.R. Fisk[7], R. Gellert[8], P.L. King[9], L. Leshin[10], S. Maurice[5], S.M. McLennan[11], M.E. Minitti[12], G. Perrett[8], S. Rowland[13], V. Sautter[14], R.C. Wiens[4], and the MSL Science Team.
correspondence to: ems@gps.caltech.edu

Includes:

Materials and Methods
Supplementary Text
Figs. S1 to S24

Supplementary Text

Here we present supporting materials for the article: The Petrochemistry of Jake_M: A Martian Mugearite. In particular, we provide a more complete discussion and supporting figures (S1–S4) for the LIBS analyses. We also compare Jake_M (JM) to terrestrial igneous rocks and show the close compositional resemblance of JM to terrestrial mugearites and phonotephrites (Figs. S5, S6). We compare the composition of JM to the compositions of terrestrial lavas in terms of TiO_2 *vs*. MgO (Fig. S7) and Fe/Mn *vs*. MgO (Fig. S8). Data from (*10, 75, 76*) are also used to demonstrate how the SO_3 and Cl contents of "unbrushed" or "as is" rocks analyzed by the Mars Exploration Rovers (MERs) compare to the sulfur and chlorine contents of the "unbrushed" JM analyses (Fig. S9). We also compare unbrushed and physically abraded compositions from the same outcrops (both normalized to 100 wt. % on a SO_3- and Cl-free basis) analyzed by the Spirit rover to the three normalized JM analyses (Fig. S10) to demonstrate that, for a given rock/outcrop, the major element spread in the unbrushed and abraded analyses, once renormalized, is comparable to the spread in the three JM analyses. Additionally, we provide a more detailed discussion of the MELTS calculations as well as a complete set of oxide-MgO variation diagrams (for SiO_2, TiO_2, Al_2O_3, FeO*, CaO, Na_2O, K_2O, and P_2O_5) showing the Tenerife Island lavas, JM, and selected MELTS fractionation paths (Fig. S11). A contoured misfit map (Fig. S12) shows the extent to which MELTS calculations at different pressures and with varying initial water contents match the overall fractionation trend of the Tenerife lavas. A similar set of figures shows MELTS fractional crystallization calculations (in oxide-MgO space) and misfit contour maps where the starting compositions were various known martian rocks (surface rocks from Gusev Crater, and the NWA 7034 meteorite), both with and without arbitrarily increased Na_2O and K_2O contents (Figs. S13–S24). The purpose of these calculations was to test whether known martian rock compositions could be viable parental liquids for JM. At the end of the Supplement, we list all MSL science team members and their institutional affiliations.

We note that in two previously presented abstracts of oral presentations that discussed the petrogenesis of JM (*82, 83*), the JM composition was compared to lavas from St. Helena, and not those from Tenerife. These two abstracts were based on a preliminary APXS data reduction of the raw JM analyses. Following a re-calibration of the APXS data, the composition of JM changed slightly and although the average of the new and old analyses overlap at 2σ, the St. Helena fractionation trend was not as good a match to the revised JM composition as it had been to the previous composition. For this reason, the compositions of St. Helena lavas have been replaced in this work by lavas from Tenerife Island. Nevertheless, it is important to stress that both terrestrial suites are alkaline and

that the most successful MELTS calculations for both suites require moderate pressures and water contents.

Materials and Methods

Three APXS analyses of JM were obtained on two unbrushed areas ~1.7 cm in diameter (JM1 and JM2) and separated by ~7 cm (Fig. 1): JM1 was analyzed once during the day and JM2 was analyzed twice (at night and during the day). Results of the three analyses are listed in Table 1. The surface of JM was not brushed or abraded prior to analysis, so the APXS analyses include surface-correlated contributions, including adhering dust that likely contributes to the observed S and Cl. Note that Na and Mg would be the major elements most affected in the APXS analyses by surface-correlated components since most emitted X-rays for Na and Mg originate in the outer ~2 to 3 μm of the target (*71, 84*). However, experience with the MERs indicates that the characteristics of rock compositions are typically not obscured by surface components, and the levels of S in JM are lower than in most unbrushed analyses from the Exploration rovers (see The effect of surface components on Jake_M's composition below), so the level of surface contamination and alteration are likely relatively minor (*85*). Moreover, successive LIBS shots on a single location gave no evidence of a surface coating or crust, but suggested instead a thin dust layer that was penetrated within 1–2 laser shots (*3*). Individual LIBS shots involved a spot size of ~0.45 mm and a penetration depth of ~0.5 μm (*86, 87*). Although the differences between the JM1 and JM2n analyses (the two long-duration analyses; Table 1) are small in an absolute sense, none of the concentrations except Cr_2O_3 overlap at the 2σ level. This suggests heterogeneity on a cm scale—not unsurprising in a polymineralic igneous rock—and consistent with the observed variations between the LIBS analyses (albeit on a different length scale).

ChemCam Analyses

Fourteen locations were analyzed by ChemCam (*86, 87*) on JM with two sets of measurements (*3, 88*): a 5-point line-scan with points separated by ~6 mm on sol 45 while the target was at a distance of 3.8 m, and a 3×3 raster (total of 9 LIBS points separated by 7 mm horizontally and ~10 mm vertically) on sol 48 while the target was at a distance of 3.2 m (Figs. 1, S1). Thirty laser shots [spot size around 420-440 μm; (*89*)] were directed at each analysis location, each providing a spectrum at successive depths to a maximum depth of ~15 μm inside the rock (*87*). The 420 spectra obtained from the fourteen LIBS analysis locations show that JM is heterogeneous at scales > ~0.5 mm (and likely smaller), with the thirty spectra from each analysis location defining a separate compositional cluster in multi-dimensional component space. Four distinct end-member compositions were determined by subjecting 392 spectra (the first two spectra at each analysis location were excluded since they are most affected by surface dust) to an

independent component analysis (ICA) algorithm. ICA involves a linear transformation that minimizes the statistical dependence between components, allowing spectra to be compared in the phase space of the most strongly varying components (*90, 91*). Different components can represent the spectral signature of a single element. Plots displaying ICA results show the correlation coefficients of the represented elements in arbitrary units. Figure S2 shows the Ti component versus the Ca component obtained from ICA. Most of the 28 spectra from each analysis location cluster together showing that for these elements the composition does not vary significantly with depth. We observe two main end members corresponding to analysis locations 1 and 2 (labeled JM_1 and JM_2 in Fig. S2). JM_2 is strongly associated with Ti, whereas JM_1 shows the lowest Ca. The other two end members are also labeled in Fig. S2: JM_10 is enriched in alkali elements (Fig. S3), whereas JM_14 shows higher Ca.

Figure S3 presents the four end members in the ultra-violet (UV) and part of the visible and near infrared (VNIR) spectral ranges. For this figure, the spectra from each analysis location were averaged over depth, which is justified in most cases given the similarity of most analysis points. Ti line intensities are low in JM_1 and JM_10. JM_1 and JM_2 (in red and green, respectively) also show weak Ca lines compared to JM_10 and JM_14 (in blue and black, respectively). JM_1 and JM_14 show stronger Mg signals than JM_2. This location (JM_2) shows almost no Mg, Al, and Ca, and is interpreted to be a mixture that includes Fe-Ti oxide(s). JM_10 is enriched in Al and alkalis relative to JM_2 and JM_14. Preliminary elemental compositions in wt. % were obtained via the partial-least-square (PLS) technique discussed by Lasue et al. (*92*); these compositions are consistent with three major types of minerals: plagioclase, pyroxene, and olivine. PLS also shows that JM-2 does not contain a significant fraction of these three phases—its higher Fe and Ti are consistent with a substantial fraction of Fe-Ti oxide(s) in the analyzed volumes of each laser shot.

While most of the JM analysis locations are homogeneous with depth, a comparison of the thirty successive spectra at each analysis location shows that some locations exhibit significant heterogeneity with increasing depth. The location showing the greatest heterogeneity with depth is JM_14. Figure S4a shows that successive spectra at this location have increasing MgO and CaO along a linear trend. The first two shots (Fig. S4a) are contaminated by dust, and then the trend (shots 3–30) suggests a mixture of groundmass (?) and plagioclase and high-Ca pyroxene with the proportion of pyroxene increasing with depth. The presence of groundmass is suggested by CIPW normative components such as orthoclase, pyroxene, magnetite and ilmenite in the composition from shot number 4. A CIPW norm calculation of the 30^{th} laser shot composition contains > 50% diopside+hedenbergite but the analysis is potentially consistent, within uncertainties, with other Ca-rich pyroxene compositions. Figure S4b shows the same

location for other elements, indicating that they are decreasing in a manner consistent with progressive profiling into a region that is dominated by a high-Ca pyroxene grain but with other contributions to the spectra. This result indicates that JM contains mineral grains that are at least nearly as large as the laser beam diameter. Other locations generally show less variation with depth, although JM_4 initially shows a composition enriched in CaO and MgO, which becomes richer in alkalis at greater depth. This trend suggests that in this case, first a pyroxene was sampled, and then the fine-grained matrix.

Further Compositional Comparisons of Jake_M to Terrestrial Lavas

Figures S5 and S6 compare the three JM analyses (normalized to 100% minus SO_3, Cl, and trace elements) to rock compositions culled from the Georoc database that had been labeled either as mugearites or phonotephrites. With the exception of TiO_2-MgO and Na_2O-MgO, the JM compositions plot broadly near the centers of the remaining oxide-MgO mugearite fields (Fig. S5). For TiO_2 and Na_2O, JM lies near/on the lower and upper boundaries of the range of mugearite compositions, respectively. Similarly, the JM compositions lie at the extreme ranges of Na_2O (upper bound) and TiO_2 (lower bound) of rocks called phonotephrites (Fig. S6). But unlike the mugearites, JM's K_2O content is much lower than typical phonotephrites. It is largely for these reasons that, although JM plots in the phonotephrite field in the total alkali-silica diagram in Fig. 2 (although near the phonotephrite/mugearite boundary), we prefer to refer to it as a mugearite, since it has a stronger overall affinity to terrestrial rocks that have been given this designation.

As noted in the main text, martian rocks are depleted in TiO_2 relative to alkaline lavas from the island of Tenerife. However, Fig. S7 shows that, although they are low, the TiO_2 contents of JM, basaltic shergotittes (martian meteorites) and martian rocks analyzed by the Mars Exploration Rovers, are not outside of the range of both terrestrial alkaline lavas and terrestrial tholeiites. In Fig. S7a, the JM compositions plot at the lower end, but nevertheless within the range of TiO_2 contents in alkaline lavas with similar MgO and SiO_2 contents. Likewise, JM, basaltic shergotittes, and Mars surface rocks are not outside of the TiO_2-MgO field defined by terrestrial tholeiites (Fig. S7b).

Although bulk rock Fe/Mn ratios have historically been one of the criteria used to distinguish martian from terrestrial rocks, (e.g., *29, 30*), Fig. S8 shows that the long-duration nighttime analysis of JM has Fe/Mn and MgO values that place it on the trend of Tenerife lavas in Fe/Mn-MgO space. High-precision Fe/Mn measurements (*93, 94*) of Hawaiian and Icelandic lavas with MgO contents of ~7–28 wt. % have values between ~58 and 70; these values are largely independent of MgO and are substantially above the JM value of 53. Fe/Mn values of Tenerife lavas with > ~7–8 wt. % MgO, although displaying greater variation (~90% of the lavas with >8 wt. % MgO have Fe/Mn of 60–80), nevertheless overlap the high-precision measurements on Hawaiian and Icelandic

basalts (greater scatter in Fe/Mn among the Tenerife rocks largely reflects lower precision of the MnO measurements). However, at lower magnesium contents (< ~7–8 wt. % MgO), Fe/Mn values in the Tenerife lavas are positively correlated with MgO and drop dramatically reaching values as low as 10–15 at MgO < 1 wt. %. This drop in Fe/Mn reflects the appearance and fractionation of titanomagnetite (± ilmenite) at MgO contents < ~7–8 wt. % and is consistent with the MELTS models in which Fe-rich spinel appears in the liquid-line-of-descent at ~7–8 wt. % MgO (Fig. 4, S11). Although not plotted, we note that lavas from St. Helena show a similar monotonic decrease in Fe/Mn with decreasing magnesium content once bulk rock MgO values fall below ~7–8 wt. %. Note that the martian rocks plotted in Fig. S8 have Fe/Mn values that are essentially independent of MgO content (~4–22 wt. %) and thus for MgO concentrations > ~6–7 wt. %, Fe/Mn values (~30–45) are substantially below the terrestrial ratios. However, because Fe/Mn values are not positively correlated with MgO at low MgO contents, more evolved (i.e., less magnesian) martian rocks intersect the Tenerife trend, suggesting that Fe/Mn is not a robust discriminant for evolved martian and terrestrial lavas.

The Effect of Surface Components on Jake_M's Composition

As discussed in the main text and in the Materials and Methods section above, the surface of Jake_M was not cleaned (i.e., mechanically brushed or physically abraded) prior to the three APXS analyses and thus a major fraction of the S and Cl in the analyses may reflect a surface component such as dust. Figure S9 compares SO_3 and Cl contents in JM with those from rocks analyzed by the MERs. With respect to S, the JM concentrations are lower than in most of the martian rock analyses collected from undisturbed (i.e., "as is") surfaces; in fact only a few rocks have lower S contents (e.g., Backstay, Irvine, Esperanza, and Humboldt Peak). Cl contents in the analyses of JM are roughly at the mid-point of the range of Cl concentrations in "as is" rock analyses (~0.4–1.6 wt. % Cl). Figure 10 shows that the spread in SiO_2, Al_2O_3, FeO*, CaO and MgO concentrations among the three normalized JM analyses is comparable to the spread observed in analyses of "as is" *vs*. abraded rock/outcrop surfaces once each analysis had been normalized on a SO_3- and Cl-free basis. This suggests that if we had analyses of JM from an abraded surface, they would not be sufficiently different from the compositions in Table 1 (once all had been renormalized without S and Cl) to substantively change any of the conclusions of this study.

MELTS Modeling of Liquid-lines-of-descent: Tenerife

AlphaMELTS 1.2 (*39, 40*) was used to model fractional crystallization of a primitive Tenerife composition (all in wt. %: SiO_2 44.231; TiO_2 3.186; Al_2O_3 11.317; Cr_2O_3 0.098; FeO* 12.431; MnO 0.181; MgO 12.672; CaO 12.430; Na_2O 2.253; K_2O 0.801; P_2O_5 0.401), over a range of pressures (1 bar and 1, 2, 3, 4, and 6 kbar) and starting water concentrations (0, 0.1, 0.5, 1, 2, and 3 wt. %). The effect of oxygen fugacity (fO_2) on the

liquid-lines-of-descent was also explored; however, a fixed fO_2 of QFM+1 is shown in Figs. S11 and S12. This fO_2 is consistent with estimates from Fe-Ti oxides in Tenerife volcanics (*38*); under more oxidizing or reducing conditions Fe-rich spinel would appear earlier or later in the calculated liquid-line-of-descent. For each fractional crystallization calculation, the oxides were plotted against MgO and cubic spline functions were fit to the discrete model points. The Tenerife lavas and a subset of MELTS calculations are shown in Fig. S11. For each of the 36 MELTS calculations, a misfit parameter was calculated by summing the absolute values of the differences between the MELTS curves in SiO_2-, Al_2O_3-, FeO*-, and CaO-MgO space and the Tenerife lava compositions; i.e., for each Tenerife lava, the MgO concentration was used to calculate an SiO_2, Al_2O_3, FeO*, and CaO content based on cubic spline fits to a given MELTS calculation and the absolute value of these differences were summed for all of the lavas with MgO contents between 1 and 12.685 wt. %. The sum of the differences was then divided by the number of Tenerife data points in this composition range (445). Some of the calculated liquid-lines-of-descent at pressures > 1 kbar and water concentrations < 2 wt. % became saturated in orthopyroxene at low MgO concentrations (MgO < 2.5 wt. %). Orthopyroxene is not expected in evolved alkaline magmas, (e.g., *16*) and has not been observed in the Tenerife lavas (e.g., *95*), so the crystallization of this phase was suppressed for the calculations shown in Figs. S11 and S12 [we note that MELTS is known to overstabilize orthopyroxene and thus its presence in these calculated evolved liquid compositions is likely an artifact (*96*)].

Figure S12 shows a contour plot of misfit over the tested range of pressures and water concentrations. The best fit over this range of pressures and water concentrations is in the middle of the darkest blue region at a pressure of 4 kbar and a starting water concentration of 1 wt. %. As illustrated by the MgO variation diagrams in Fig. S11, a good match to the Tenerife data requires the suppression of plagioclase crystallization such that the Al_2O_3 concentrations in the most evolved melts can be enriched to ~20 wt. %. Although the "best-fit" requires elevated pressure and water contents, as discussed in the main text, the suppression of plagioclase can be achieved by increasing the pressure of crystallization either with or without added water (increasing pressure and water content is more effective than pressure alone).

MELTS Modeling of Liquid-lines-of-descent: Martian Starting Liquid Compositions

We explored the possibility that JM might represent a residual liquid from fractional crystallization of known martian rock compositions. We tried a variety of starting liquid compositions, including the shergottite EETA 79001A (*9*), NWA 7034 (*74*), and four compositions measured by the Spirit rover in Gusev crater: Adirondack, Humphrey, Humboldt Peak, and Backstay. For these starting compositions, we again used MELTS to calculate liquid-lines-of-descent over a range of pressures (1 bar and 1, 2, 3, and 4 kbar)

and starting water concentrations (0, 0.1, 0.5, 1, 2, and 3 wt. %). We tried calculations over a range of fO_2 conditions from QFM−1 to QFM+3 (*6, 7, 97*). However, all of the results shown in Figs. S13–S24 were calculated at QFM−1. The misfit between the calculated liquid-lines-of-descent and JM was computed using a similar method to that described above for Tenerife, the only difference being that the calculated concentrations of SiO_2, Al_2O_3, FeO*, and CaO were this time compared to the three analyses of JM instead of the large Tenerife dataset. The results of the Backstay, NWA 7034, and Humboldt Peak calculations are discussed below.

Although none of the martian compositions considered in this study have high enough concentrations of alkalis to be viable parental liquids for JM (Figs. S13, S17, and S21), fractional crystallization of Backstay is able to match the concentrations of SiO_2, Al_2O_3, FeO*, and CaO in JM reasonably well (Fig. S13). A contoured misfit plot using Backstay as the starting composition (Fig. S14) shows that the best-fit conditions are 4 kbar and 3 wt. % water in the starting composition. These conditions yield a best-fit match to JM that is comparable to the best-fit to JM achieved by starting with the primitive Tenerife composition (again considering only SiO_2, Al_2O_3, FeO*, and CaO). However, all of the melts comprising the best-fit liquid-line-of-descent calculated using Backstay are hyperthene normative (i.e., normative nepheline = 0), in striking contrast to the ~16–17 wt. % normative nepheline in the JM bulk composition (Table 1).

Fractional crystallization of NWA 7034 and Humboldt Peak give poorer fits to JM (in terms of SiO_2, Al_2O_3, FeO*, and CaO) than Backstay, with misfits ranging from 7.5–12 for NWA 7034 (Fig. S18) and 10.5–12 for Humboldt Peak (Fig. S22). However, unlike Backstay, NWA 7034 and Humboldt Peak produced fractionated model liquids in the compositional region of JM (~4.4 wt. % MgO) that are nepheline normative, although the calculated abundances of normative nepheline (< 1 wt. %, NWA 7034; ~6 wt. % Humboldt Peak) are substantially less than that calculated for JM (~16–17 wt. %). In addition to having insufficient alkalis, both NWA 7034 and Humboldt Peak have concentrations of Al_2O_3 that are too low and concentrations of FeO* that are too high for either of these starting compositions to be parental to JM under the conditions considered in this study.

In order to assess whether a known martian composition enriched in alkalis could provide a viable parent for JM, we re-calculated the liquid-lines-of-descent from Backstay, NWA 7034, and Humboldt Peak with arbitrarily increased concentrations of Na_2O and K_2O. The addition of extra alkalis had the effect of decreasing the Al_2O_3 and SiO_2 concentrations of the residual liquids at a given MgO concentration, which increased the combined misfit for SiO_2, Al_2O_3, FeO*, and CaO between the calculated liquid-lines-of-descent and JM (Figs. S16, S20, and S24). The best-fit conditions for the Backstay

starting composition shifted to a higher pressure and a lower water concentration as a result of increasing the alkali concentration of the melt. This could reflect the role of Na_2O and K_2O as network modifiers in silicate liquids (*98*).

In conclusion, of the martian starting compositions considered in this study, fractional crystallization of Backstay provides the best match to the SiO_2, Al_2O_3, FeO*, and CaO concentrations in JM. However, concentrations of K_2O and Na_2O for all previously analyzed martian rocks, including Backstay, are too low to explain the alkali-rich nature of JM. A Backstay-like melt arbitrarily enriched in alkalis could on fractionation produce a melt similar to JM in most elements via fractional crystallization. The best-fit crystallization conditions are at pressures of 3 kbar or higher for all starting melt compositions.

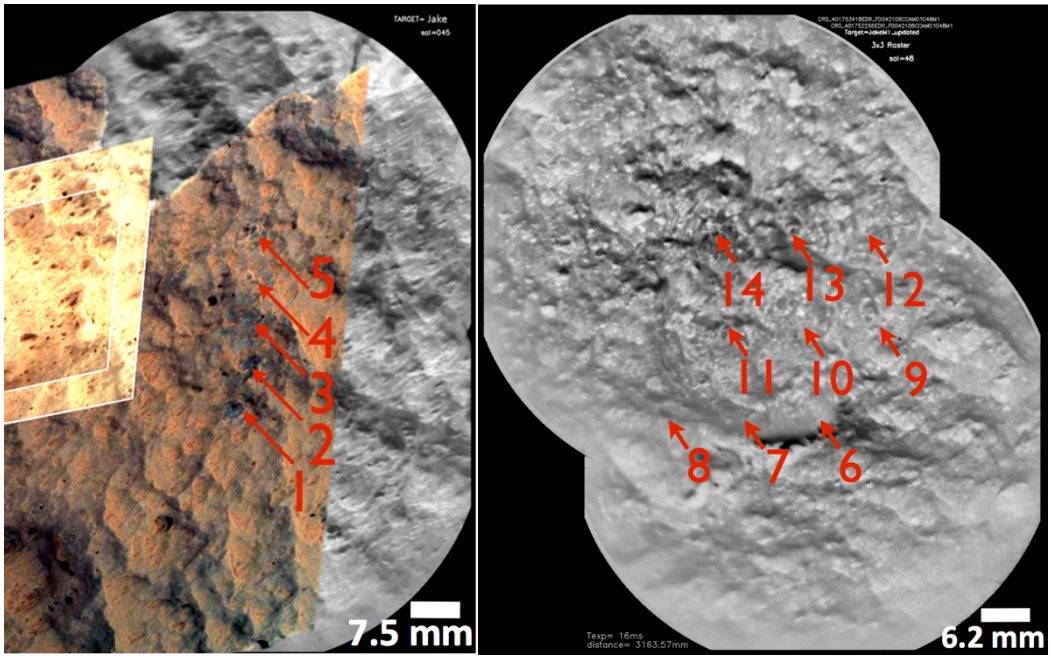

Fig. S1.

RMI mosaics of the 2 rasters performed on Jake_M. The mosaic on the left is coupled with Mahli colors. Credit : NASA/JPL-Caltech/ LANL/IRAP/MSSS/IAS/LTP- Nantes.

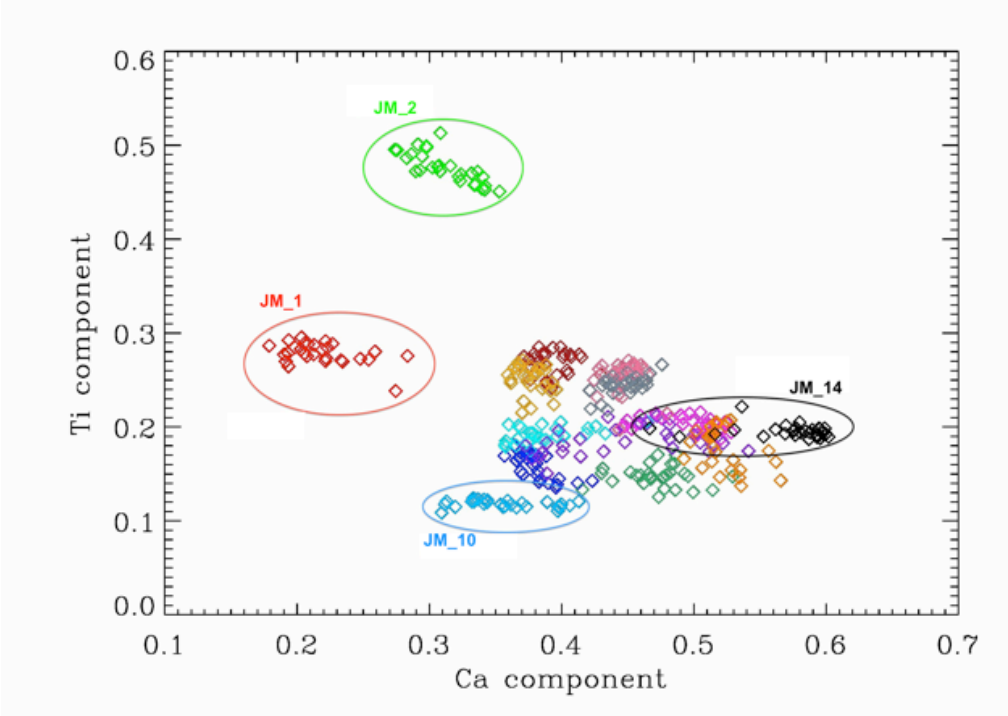

Fig. S2.

ICA (*91*) plot showing Ti component *vs*. Ca component for all the 392 spectra obtained on Jake_M (dust spectra removed). Observations at locations 1, 2, 10, and 14 represent compositional end-members. Units along the axes give relative separation of a given ICA component.

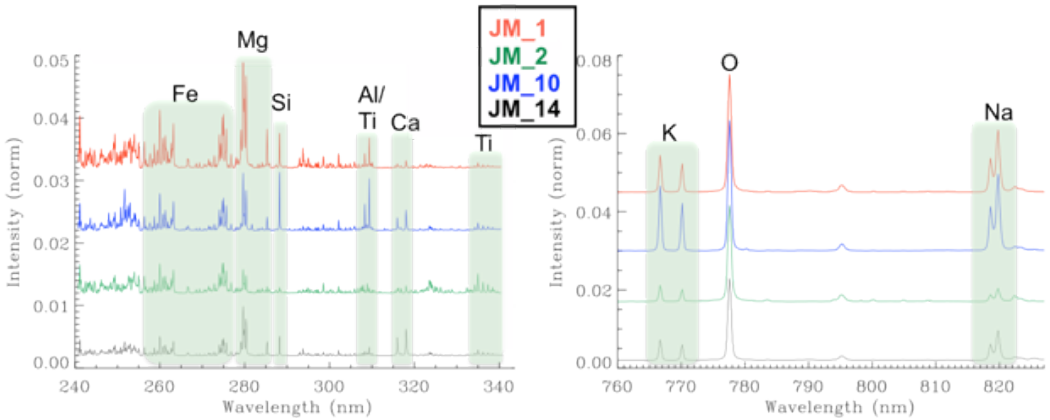

Fig. S3.

Spectra averaged over depth for the four analysis locations that are show end-member compositions from Jake_M. Left panel: UV range; Right panel: Part of the VNIR range showing the K and Na lines.

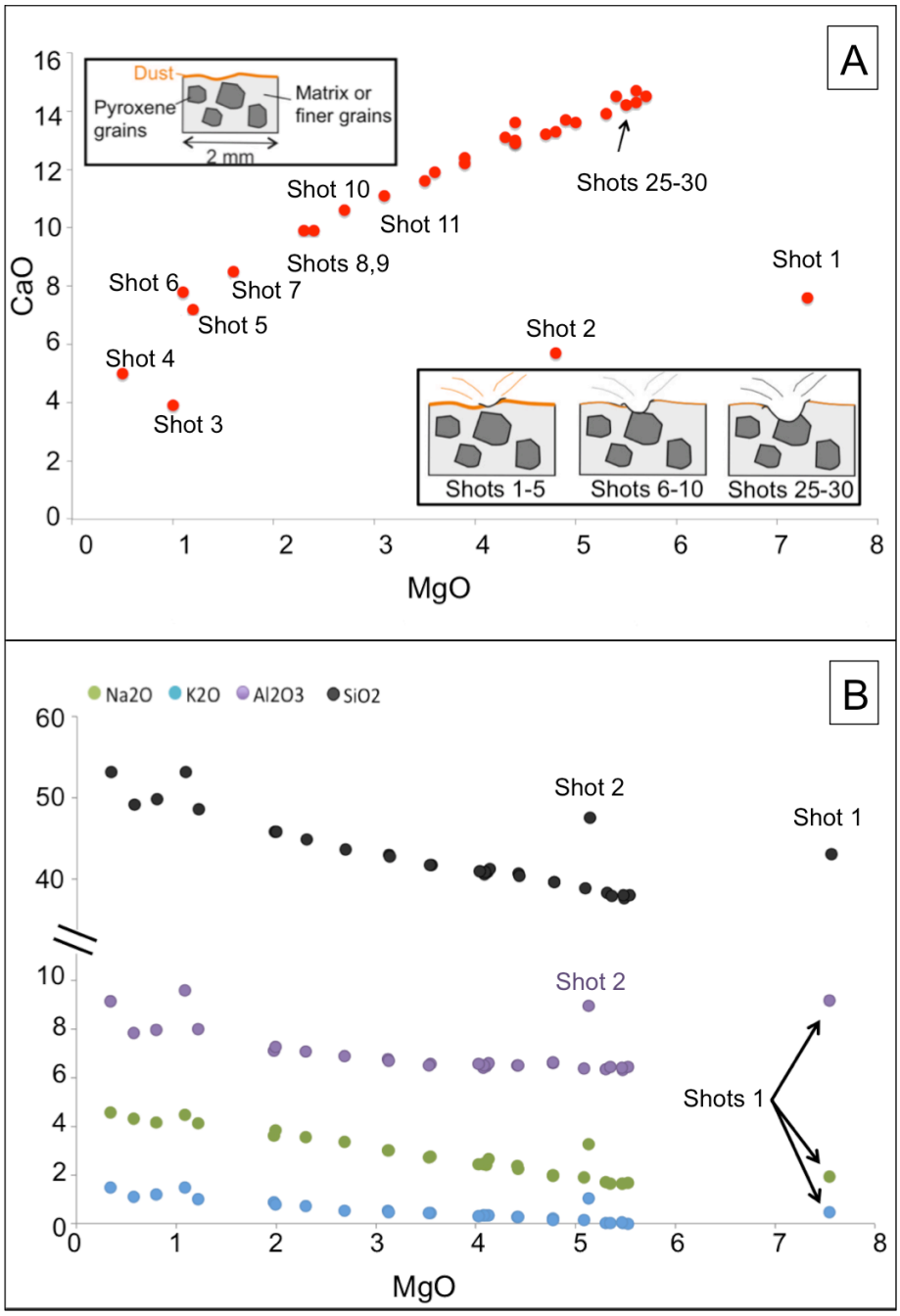

Fig. S4.

(A) CaO *vs*. MgO determined by PLS for ChemCam location 14 on Jake_M. The first two shots show the effect of surface dust; shots 3–30 suggest a mixture dominated by plagioclase and a high-Ca pyroxene with the proportion of pyroxene increasing with depth. (B) SiO_2, Al_2O_3, K_2O, and Na_2O *vs*. MgO in wt. % determined by PLS for ChemCam location 14 on Jake_M. The first two shots show the effect of surface dust. All these elements are decreasing while Mg increases, which is consistent with an interpretation of a Ca-rich pyroxene at depth.

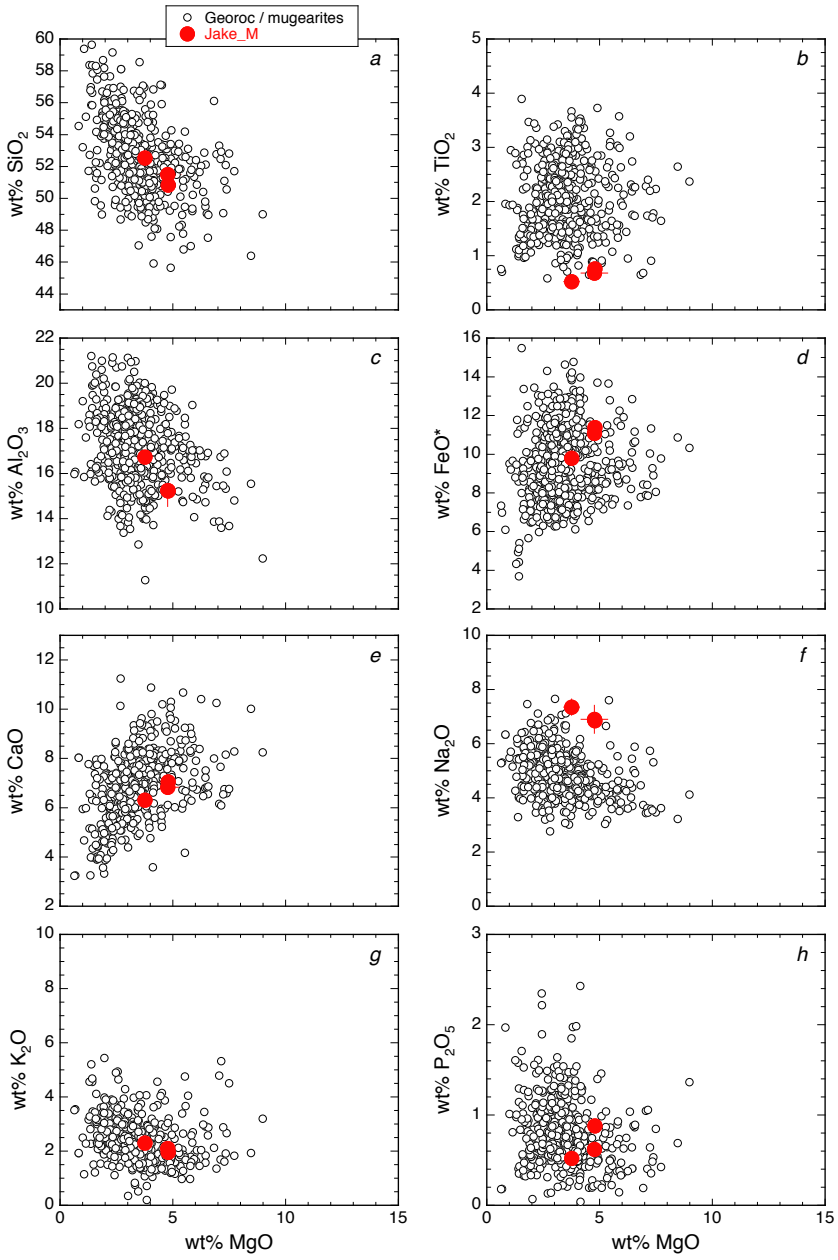

Fig. S5.
Comparison of the three Jake_M analyses (Table 1) to terrestrial rocks labeled mugearites in the Georoc database (*25*); all analyses normalized to 100% on a H_2O-, CO_2-, S-, and Cl-free basis. (a) SiO_2-MgO, (b) TiO_2-MgO, (c) Al_2O_3-MgO, (d) FeO*-MgO, (e) CaO-MgO, (f) Na_2O-MgO, (g) K_2O-MgO, (h) P_2O_5-MgO; FeO* = all Fe as FeO.

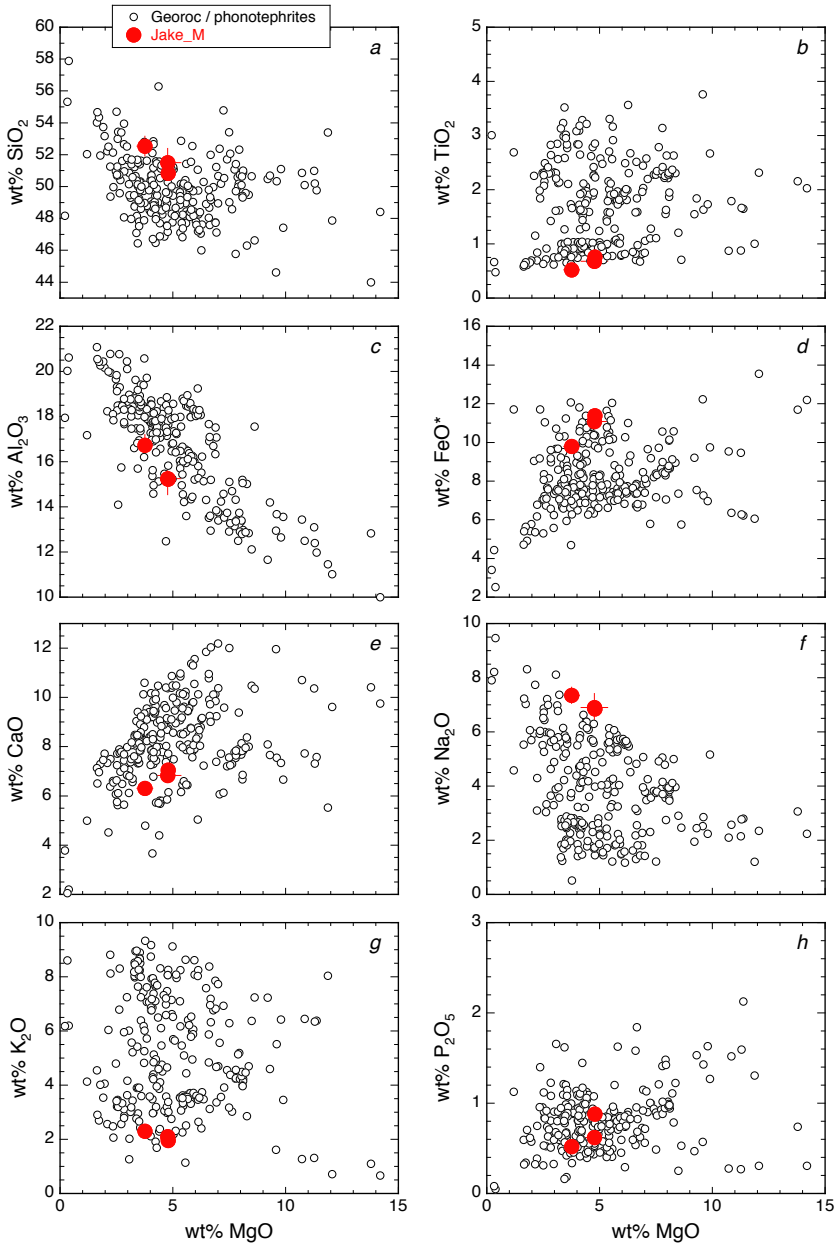

Fig. S6.
Comparison of the three Jake_M analyses (Table 1) to terrestrial rocks labeled phonotephrites in the Georoc database (*25*); all analyses normalized to 100% on a H_2O-, CO_2-, S-, and Cl-free basis. (a) SiO_2-MgO, (b) TiO_2-MgO, (c) Al_2O_3-MgO, (d) FeO*-MgO, (e) CaO-MgO, (f) Na_2O-MgO, (g) K_2O-MgO, (h) P_2O_5-MgO; FeO* = all Fe as FeO.

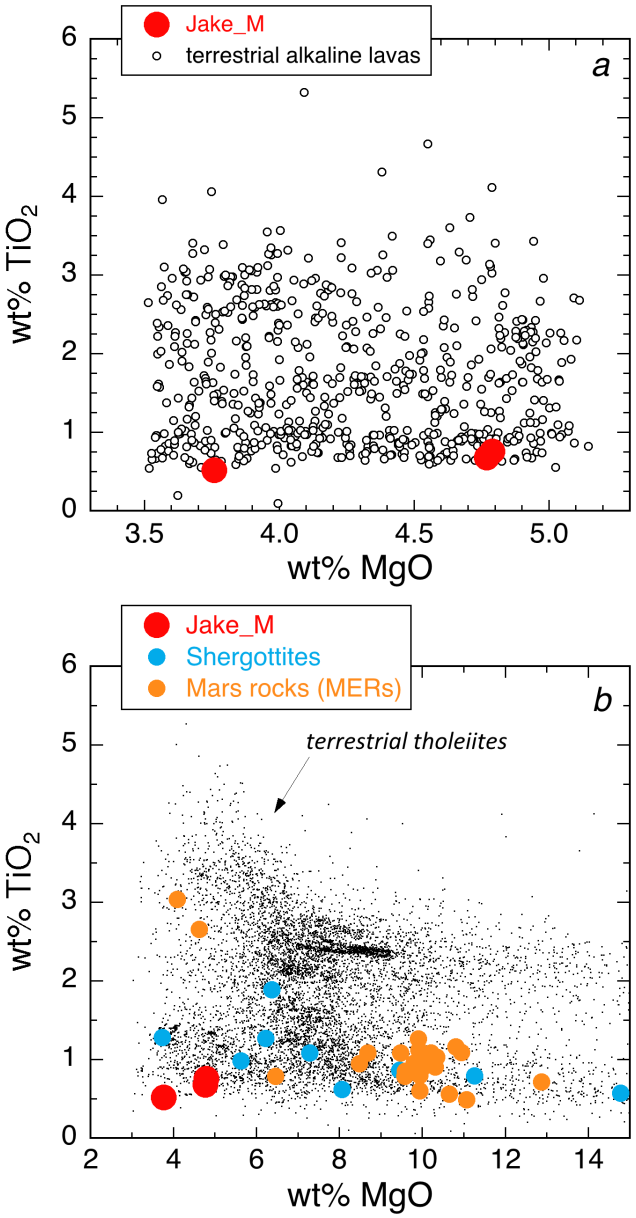

Fig. S7.
(a) TiO_2 *vs*. MgO comparison between terrestrial alkaline rocks (*25*) [those lying above the alkaline-subalkaline boundary (*23*) in Na_2O+K_2O *vs*. SiO_2 space] with 50–55 wt. % SiO_2 and 3.5–5 wt. % MgO and Jake_M (Table 1). (b) TiO_2 *vs*. MgO comparison between terrestrial tholeiitic rocks (i.e., compositions that plot below the alkaline-subalkaline boundary) with 47–53 wt. % SiO_2 and 3–15 wt. % MgO (*25*) and Jake_M (Table 1), shergottites (*9*), and martian rocks analyzed by the Mars Exploration Rovers (*10, 75-77*). The two high TiO_2 martian rocks are Wishstone and Champagne (*10*). All analyses in (a) and (b) have been normalized to 100 wt. % on a volatile-free basis with all Fe as FeO; terrestrial lavas were culled from the Georoc database (*25*) prior to normalization.

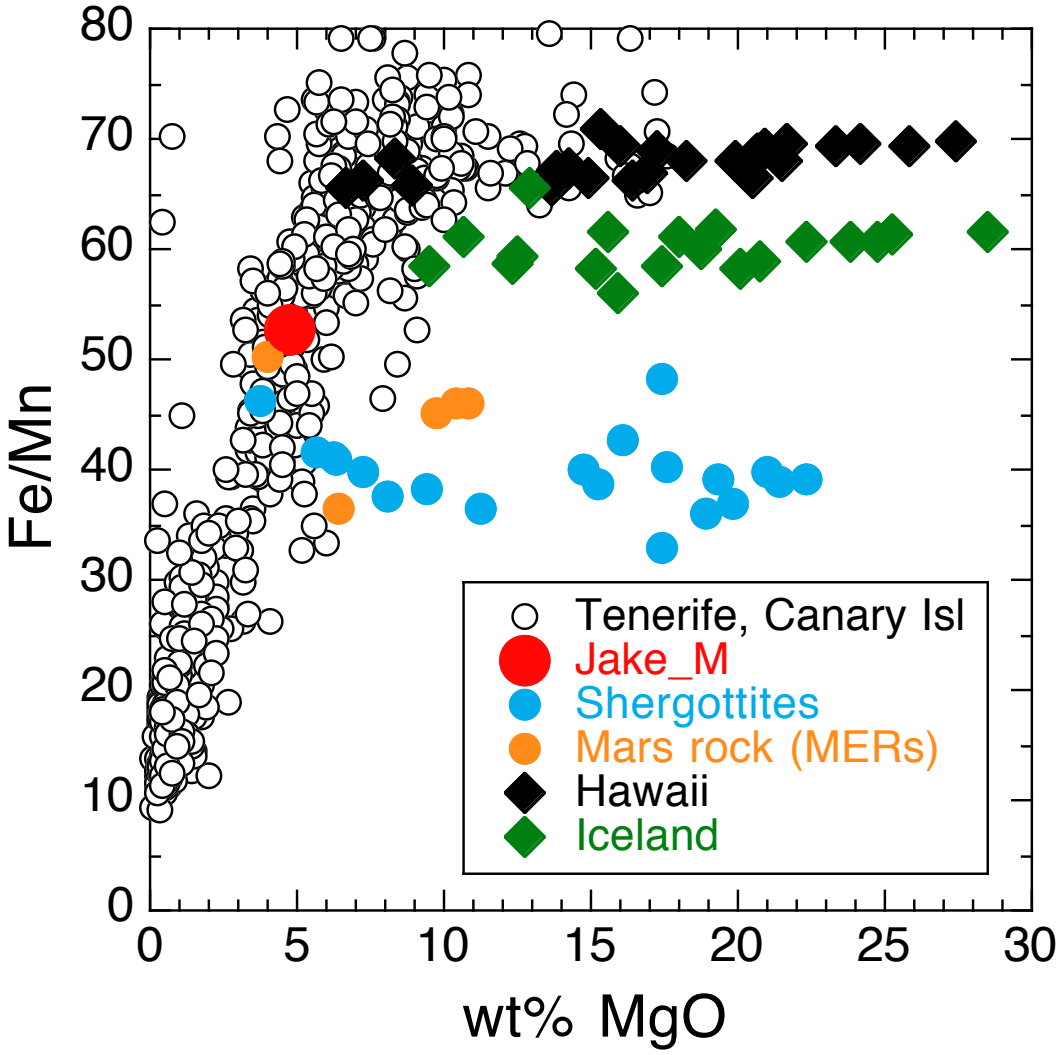

Fig. S8.
Fe/Mn (by weight) *vs*. MgO for Tenerife lavas (*25*), Jake_M (JM2n, Table 1), shergottites (*9, 73*), "abraded" Mars surface rock compositions analyzed by the Mars Exploration Rovers (*10, 76*) and high-precision Fe/Mn measurements on Hawaiian and Icelandic basalts (*93, 94*). The 13 Tenerife lavas with Fe/Mn > 80 are not plotted and most likely represent analytical errors (high Fe/Mn correlates with low, i.e., ≤0.1 wt. %, MnO values). One-sigma errors for the Hawaiian and Icelandic lavas are smaller than the size of the symbols.

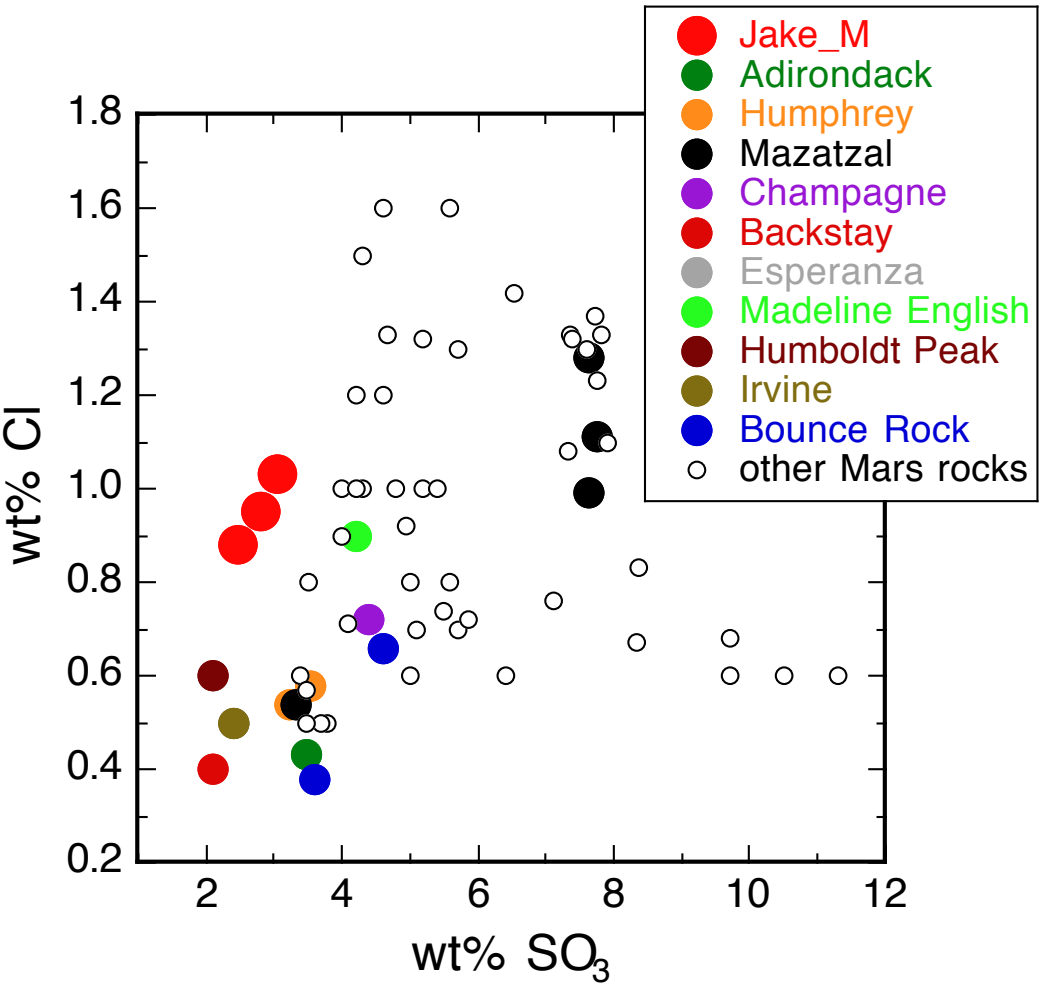

Fig. S9.
SO_3 *vs*. Cl (both in wt. %) in unbrushed and unabraded (i.e., "as is") rocks analyzed by the MERs (*10, 75, 76*) and in Jake_M (Table 1); note that Esperanza plots beneath Irvine.

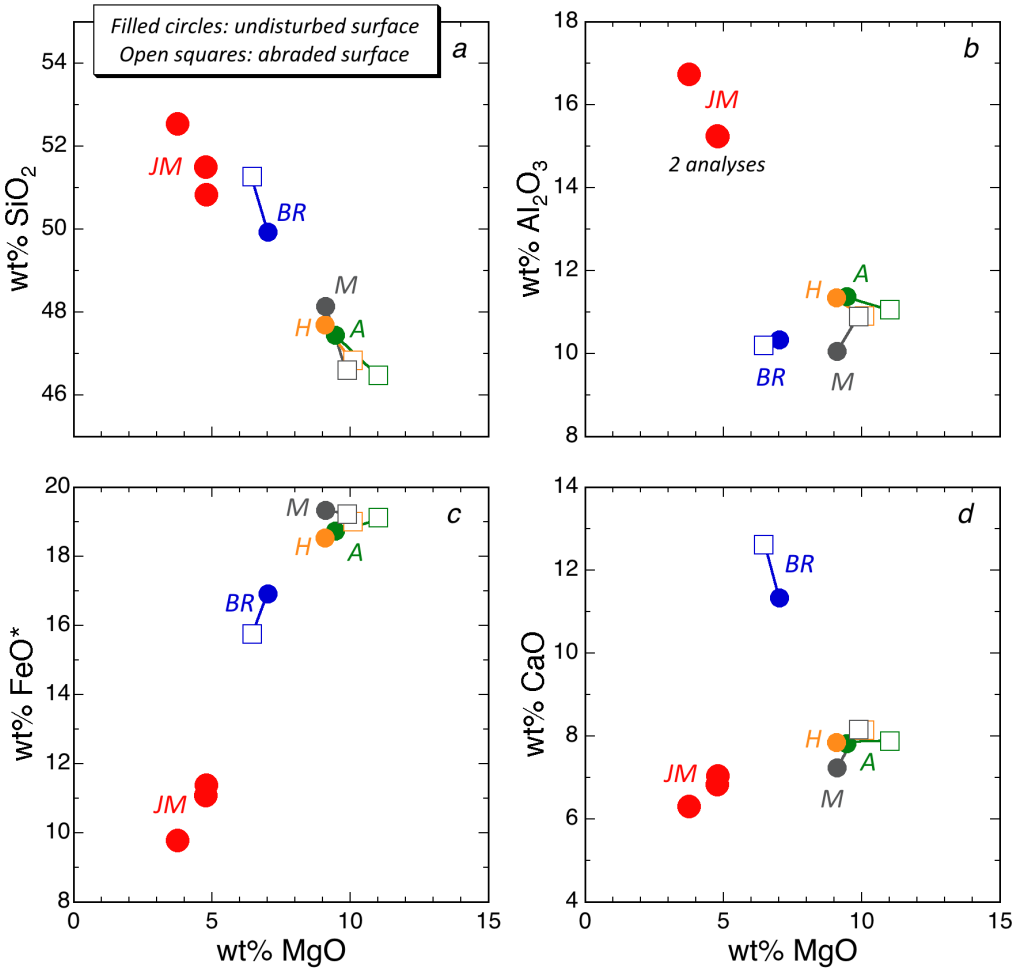

Fig. S10.
Oxide-MgO (all in wt. %) in JM (large filled circles; Table 1) and in unbrushed and unabraded, i.e., "as is" rock analyses (smaller filled circles) and physically abraded rock analyses (open squares) by the MERs (*10, 76*). All analyses have been normalized to 100 wt. % on a SO_3- and Cl-free basis; tie lines connect "as is" and abraded analyses of the same rock/outcrop. Abbreviations: JM = Jake_M; BR = Bounce Rock; M = Mazatzal; H = Humphrey; A = Adirondack. In the case of Mazatzal and Humphrey, multiple analyses have been averaged after being normalized. (a) SiO_2-MgO; (b) Al_2O_3-MgO; (c) FeO*-MgO, where FeO* = all Fe as FeO; (d) CaO-MgO.

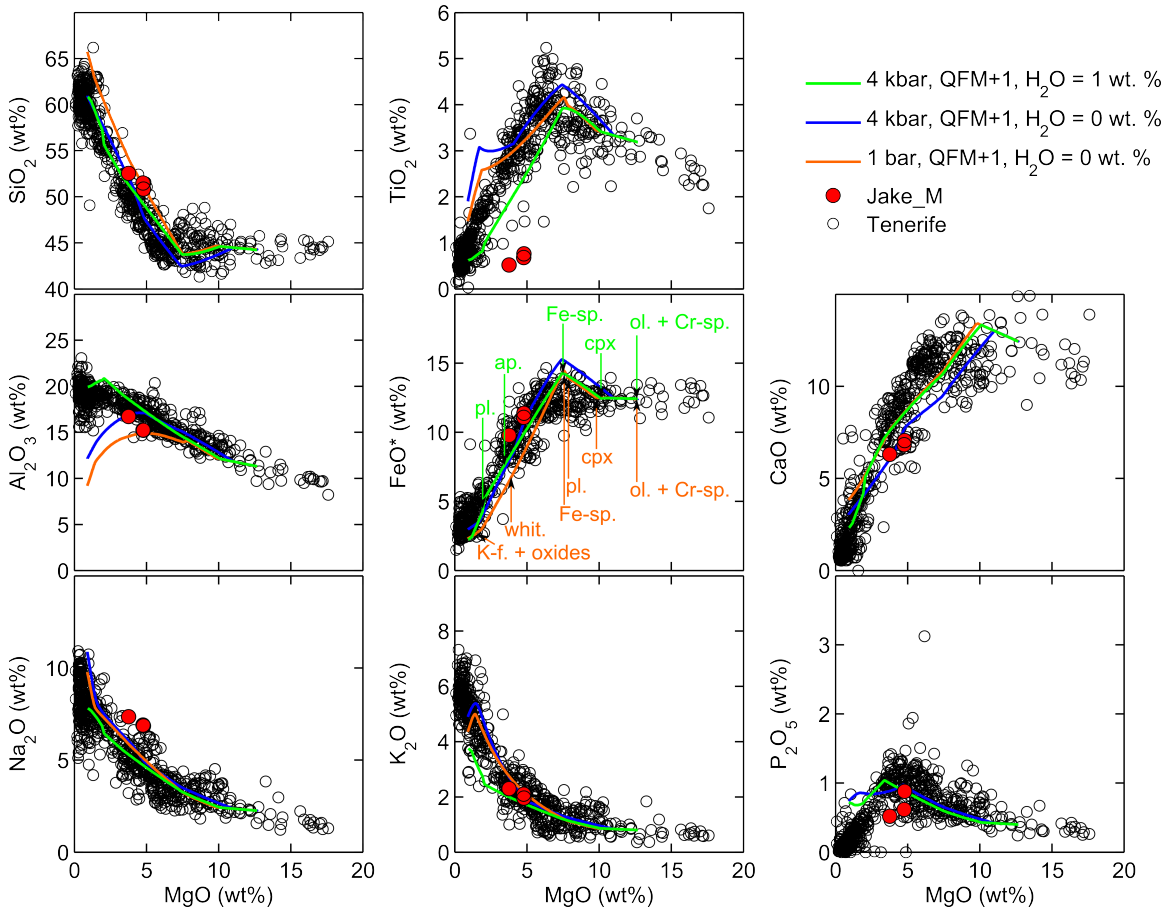

Fig. S11.
Oxide-MgO variation diagrams showing the compositions of Tenerife lavas (*25*), Jake_M (Table 1), and the results of selected MELTS fractional crystallization calculations. The best-fit MELTS calculation (4 kbar, QFM+1, H_2O = 1 wt. %) is plotted in green (Fig. S12 shows how the mismatch between a given MELTS calculation and the Tenerife lavas varies as a function of pressure and initial water content). For comparison, the calculation at 4 kbar, QFM+1 and 0 wt. % water is shown in blue and the calculation at 1 bar, QFM+1 and 0 wt. % water is shown in orange. Colored arrows indicate the entry of phases in the calculated fractional crystallization sequence: ol. = olivine; cpx = clinopyroxene; pl. = plagioclase; Fe-sp. = Fe-rich spinel; K-f. = K-feldspar; whit. = whitlockite; ap. = apatite; oxides = ilmenite.

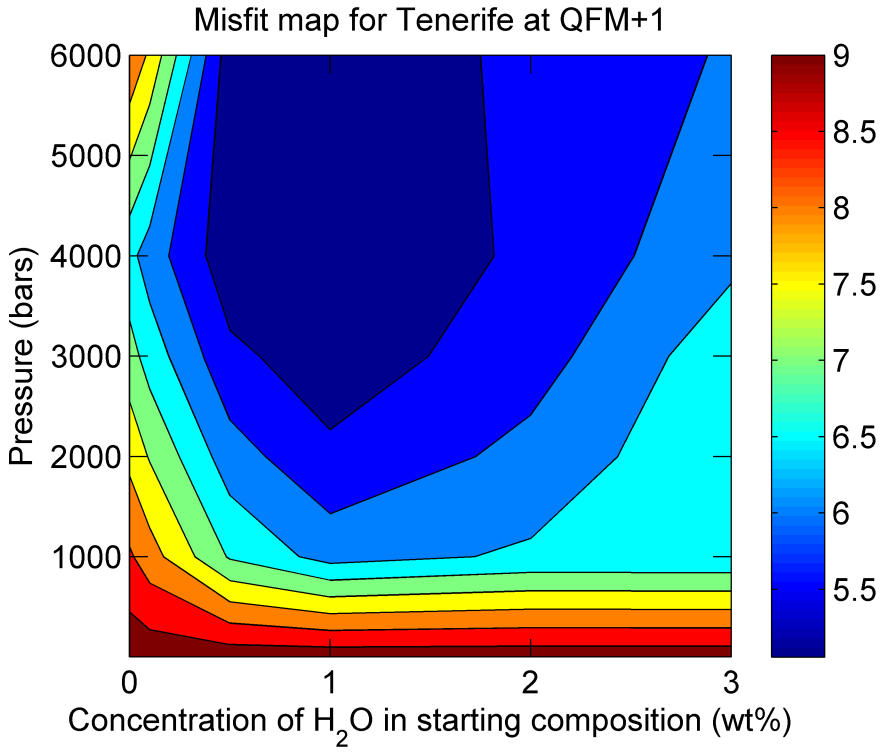

Fig. S12.
Contour plot of misfit between Tenerife data and MELTS fractional crystallization calculations. Calculations performed at QFM+1, at pressures of 1, 1000, 2000, 3000, 4000 and 6000 bars, and water concentrations of 0, 0.1, 0.5, 1, 2 and 3 wt. %. For each of the 36 MELTS calculations, the misfit was calculated by summing the absolute values of the differences between the MELTS curves in SiO_2-, Al_2O_3-, FeO*-, and CaO-MgO space and Tenerife lava compositions with MgO contents between 1 and 12.685 wt. %. The sum of the differences was then divided by the number of Tenerife data points (445) within this MgO concentration range. Note that this misfit parameter does not directly compare with the ones that follow (in Figs. S14, S16, S18, S20, S22, and S24), which are calculated against the three measured Jake_M compositions rather than the whole Tenerife suite. Colored vertical scale bar indicates the degree of misfit; red = large (i.e., worse fit to the Tenerife data) and blue = small (i.e., better fit to the Tenerife data).

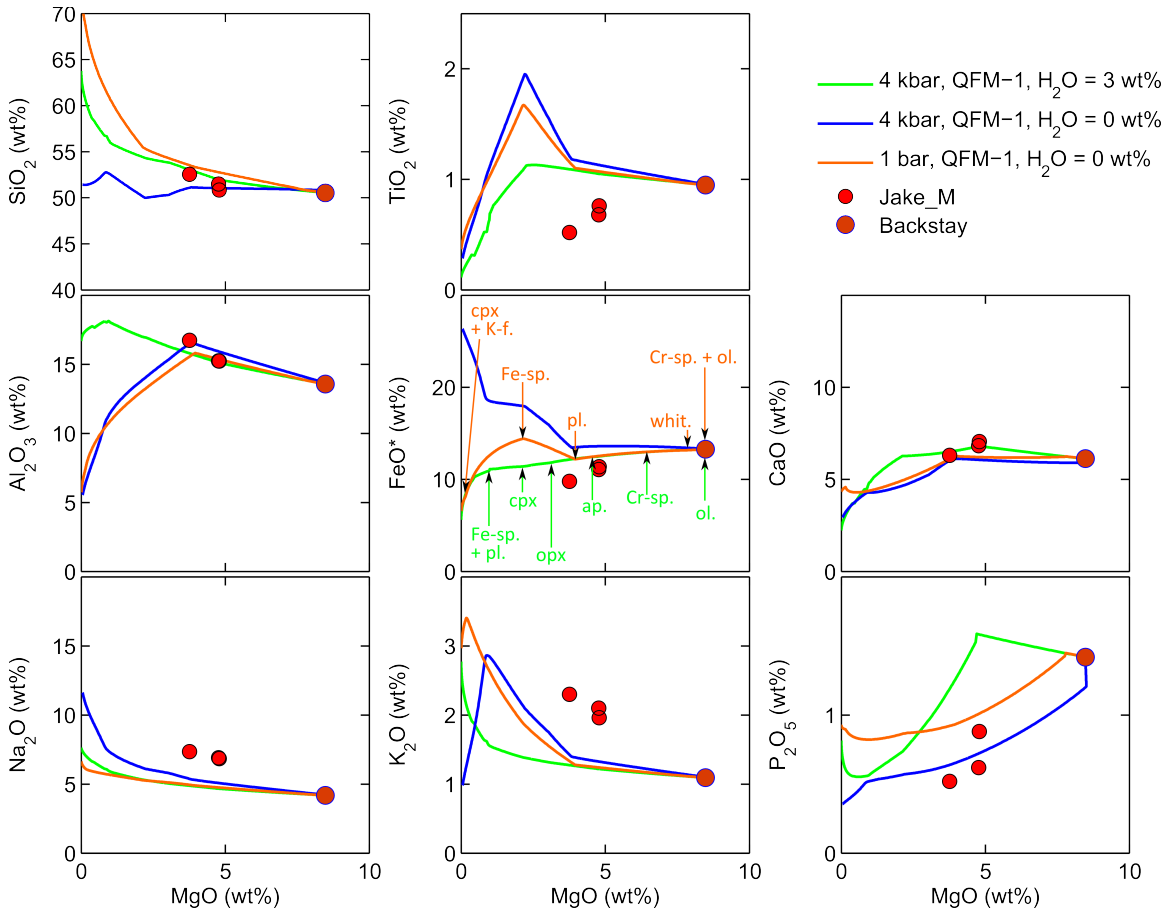

Fig. S13.
MgO variation diagrams for Backstay, Jake_M, and MELTS fractional crystallization calculations at QFM−1. The best-fit calculation (4 kbar and 3 wt. % water) is plotted in green. For comparison, the calculation at 4 kbar and 0 wt. % water is shown in blue, and the calculation at 1 bar and 0 wt. % water is shown in orange. Colored arrows indicate the entry of phases in the calculated fractional crystallization sequence: ol. = olivine; Cr-sp. = Cr-spinel; whit. = whitlockite; ap. = apatite; pl. = plagioclase; opx = orthopyroxene; cpx = clinopyroxene; Fe-sp. = Fe-rich spinel; K-f. = K-feldspar.

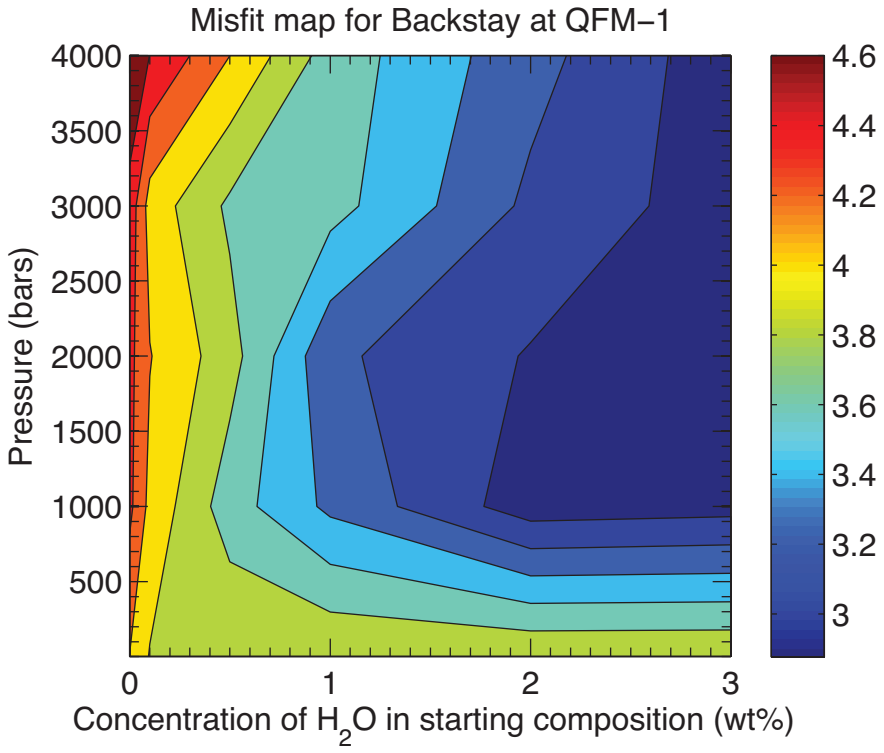

Fig. S14.
Contour plot of misfit between Jake_M and MELTS fractional crystallization calculations at QFM–1 using Backstay as the starting composition. Calculations performed at pressures of 1, 1000, 2000, 3000 and 4000 bars, and water concentrations of 0, 0.1, 0.5, 1, 2 and 3 wt. %. For each of the 30 MELTS calculations, the misfit was calculated by summing the differences between the MELTS curves in SiO_2-, Al_2O_3-, FeO*-, and CaO-MgO space and the three measured Jake_M compositions. The sum of the differences was then divided by three. Note that the misfit in this figure and subsequent figures is not directly comparable to the misfit plotted in Fig. S12, which is calculated against the whole Tenerife suite rather than Jake_M. Colored vertical scale bar indicates the degree of misfit; red = large (i.e., worse fit to Jake_M) and blue = small (i.e., better fit to Jake_M).

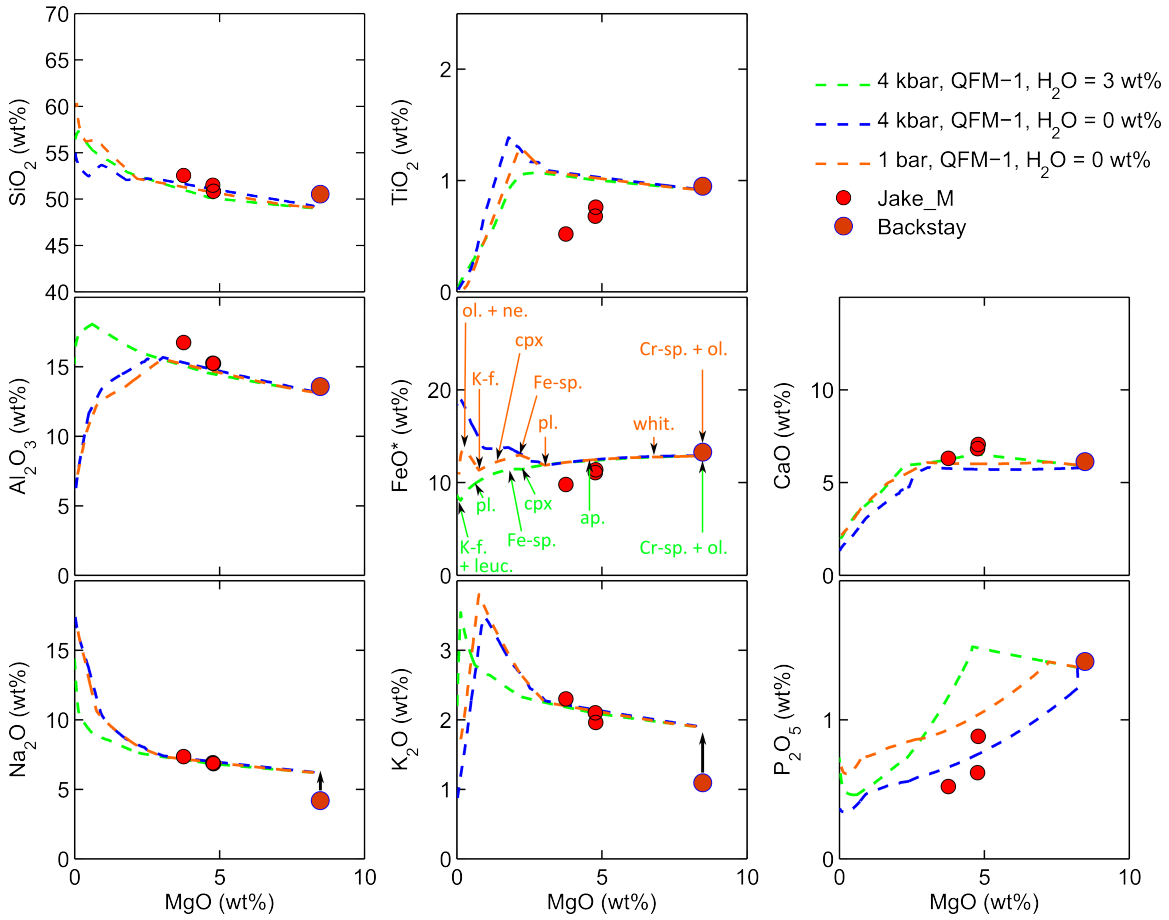

Fig. S15.
MgO variation diagrams for Backstay (with added Na_2O and K_2O so as to match the alkali content of Jake_M), Jake_M, and MELTS fractional crystallization calculations at QFM–1. The best-fit calculation (4 kbar and 3 wt. % water) is plotted in green (note that for the modified and unmodified Backstay composition, the best-fit models occur at the extremes of our investigated pressures and water contents and thus may not represent true minima in pressure-H_2O space). For comparison, the calculation at 4 kbar and 0 wt. % water is shown in blue, and the calculation at 1 bar and 0 wt. % water is shown in orange. Colored arrows indicate the entry of phases in the calculated fractional crystallization sequence: ol. = olivine; Cr-sp. = Cr-spinel; whit. = whitlockite; ap. = apatite; Fe-sp. = Fe-rich spinel; cpx = clinopyroxene; K-f. = K-feldspar; leuc. = leucite. Note that renormalization to 100 wt. % following the addition of alkalis to the Backstay starting composition causes a small decrease in the concentrations of all of the other elements, such that the starting point for the MELTS fractional crystallization calculations is offset from Backstay in all panels. Black arrows in the Na_2O and K_2O variation diagrams emphasize the amount by which Backstay has been enriched in alkalis to create this new starting composition.

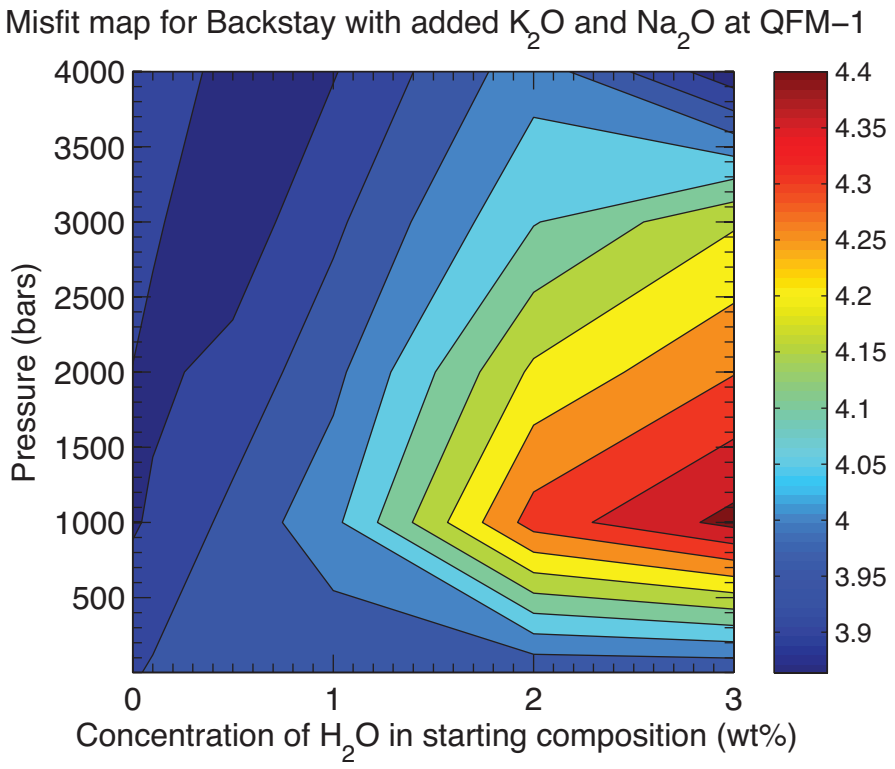

Fig. S16.
Contour plot of misfit between MELTS fractional crystallization calculations at QFM–1, starting with a Backstay composition with added Na_2O and K_2O. Calculations performed at pressures of 1, 1000, 2000, 3000 and 4000 bars, and water concentrations of 0, 0.1, 0.5, 1, 2 and 3 wt. %. For each of the 30 MELTS calculations, the misfit was calculated by summing the differences between the MELTS curves in SiO_2-, Al_2O_3-, FeO*-, and CaO-MgO space and the three measured Jake_M compositions. The sum of the differences was then divided by three. Note that the misfit in this figure and subsequent figures is not directly comparable to the misfit plotted in Fig. S12, which is calculated against the whole Tenerife suite rather than Jake_M. Colored vertical scale bar indicates the degree of misfit; red = large (i.e., worse fit to Jake_M) and blue = small (i.e., better fit to Jake_M).

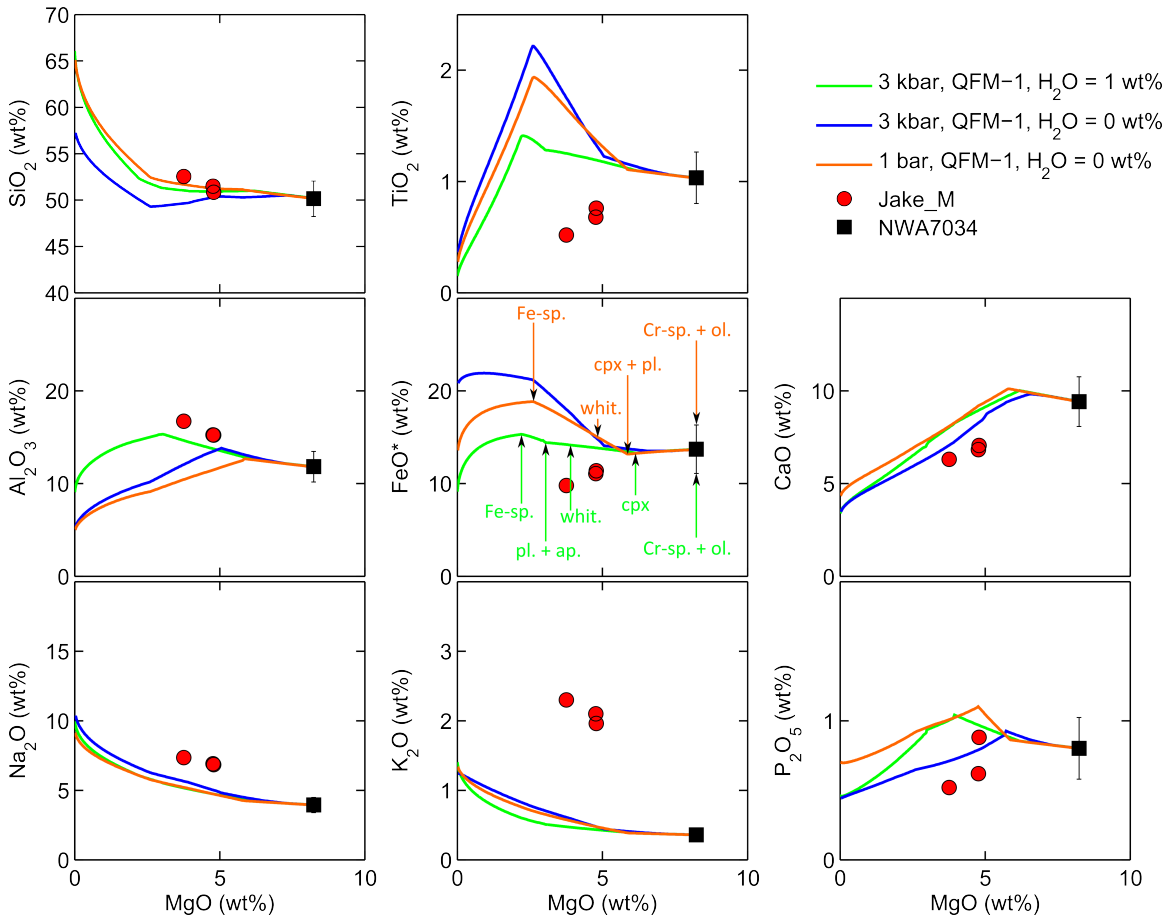

Fig. S17.
MgO variation diagrams for NWA 7034, Jake_M, and MELTS fractional crystallization calculations at QFM−1. The best-fit calculation (3 kbar and 1 wt. % water) is plotted in green. For comparison, the calculation at 3 kbar and 0 wt. % water is shown in blue, and the calculation at 1 bar and 0 wt. % water is shown in orange. Colored arrows indicate the entry of phases in the calculated fractional crystallization sequence: ol. = olivine; Cr-sp. = Cr-spinel; cpx = clinopyroxene; pl. = plagioclase; whit. = whitlockite; ap. = apatite; Fe-sp. = Fe-rich spinel. Error bars on the composition of NWA 7034 are one standard deviation of 225 microprobe analyses of plumose groundmass (*74*).

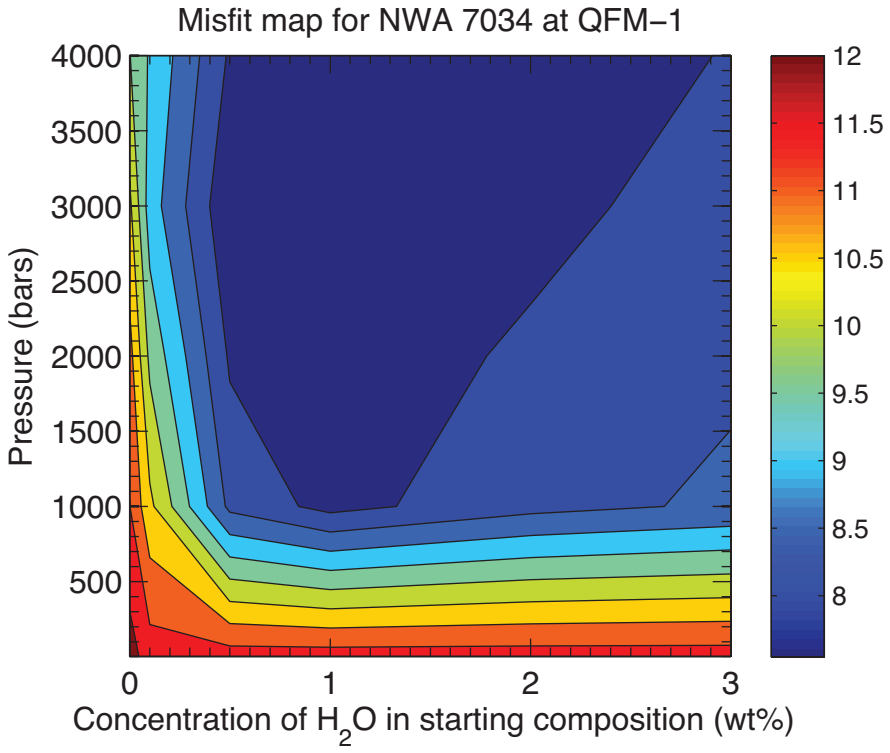

Fig. S18.
Contour plot of misfit between Jake_M and MELTS fractional crystallization calculations at QFM–1 using NWA 7034 as the starting composition. Calculations performed at pressures of 1, 1000, 2000, 3000 and 4000 bars, and water concentrations of 0, 0.1, 0.5, 1, 2 and 3 wt. %. For each of the 30 MELTS calculations, the misfit was calculated by summing the differences between the MELTS curves in SiO_2-, Al_2O_3-, FeO*-, and CaO-MgO space and the three measured Jake_M compositions. The sum of the differences was then divided by three. Note that the misfit in this figure and subsequent figures is not directly comparable to the misfit plotted in Fig. S12, which is calculated against the whole Tenerife suite rather than Jake_M. Colored vertical scale bar indicates the degree of misfit; red = large (i.e., worse fit to Jake_M) and blue = small (i.e., better fit to Jake_M).

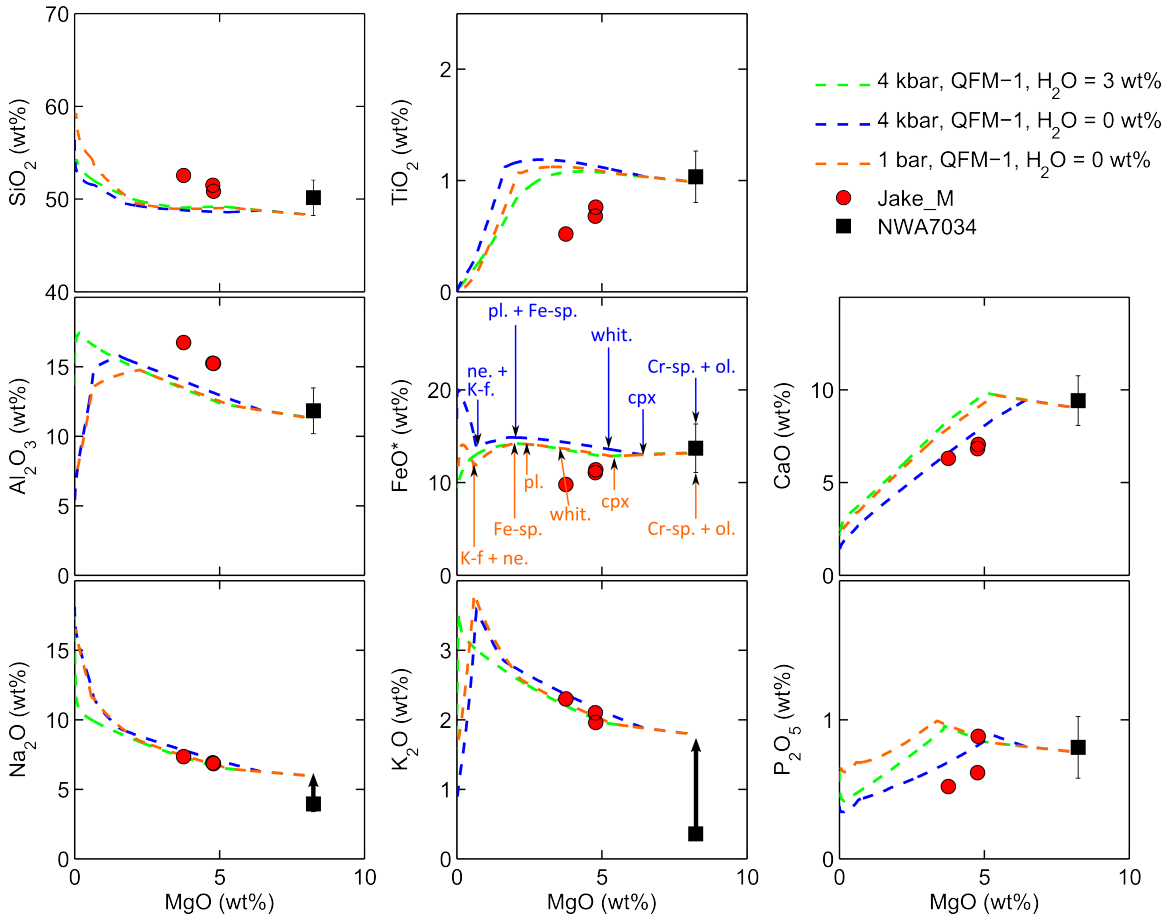

Fig. S19.
MgO variation diagrams for NWA 7034 (with added Na_2O and K_2O so as to match the alkali content of Jake_M), Jake_M, and MELTS fractional crystallization calculations at QFM–1. The best-fit calculation (4 kbar and 0 wt. % water) is plotted in blue and represents the minimum with respect to the investigated region of pressure-H_2O space. For comparison, the calculation at 4 kbar and 3 wt. % water is shown in green, and the calculation at 1 bar and 0 wt. % water is shown in orange. Colored arrows indicate the entry of phases in the calculated fractional crystallization sequence: ol. = olivine; Cr-sp. = Cr-spinel; cpx = clinopyroxene; whit. = whitlockite; pl. = plagioclase; ap. = apatite; Fe-sp. = Fe-rich spinel; K-f. = K-feldspar; ne. = nepheline. Note that renormalization to 100 wt. % following the addition of alkalis to the NWA 7034 starting composition causes a small decrease in the concentrations of all of the other elements, such that the starting point for the MELTS fractional crystallization calculations is offset from NWA 7034 in all panels. Black arrows in the Na_2O and K_2O variation diagrams emphasize the amount by which NWA 7034 has been enriched in alkalis to create this new starting composition. Error bars on the composition of NWA 7034 are one standard deviation of 225 microprobe analyses of plumose groundmass (*74*).

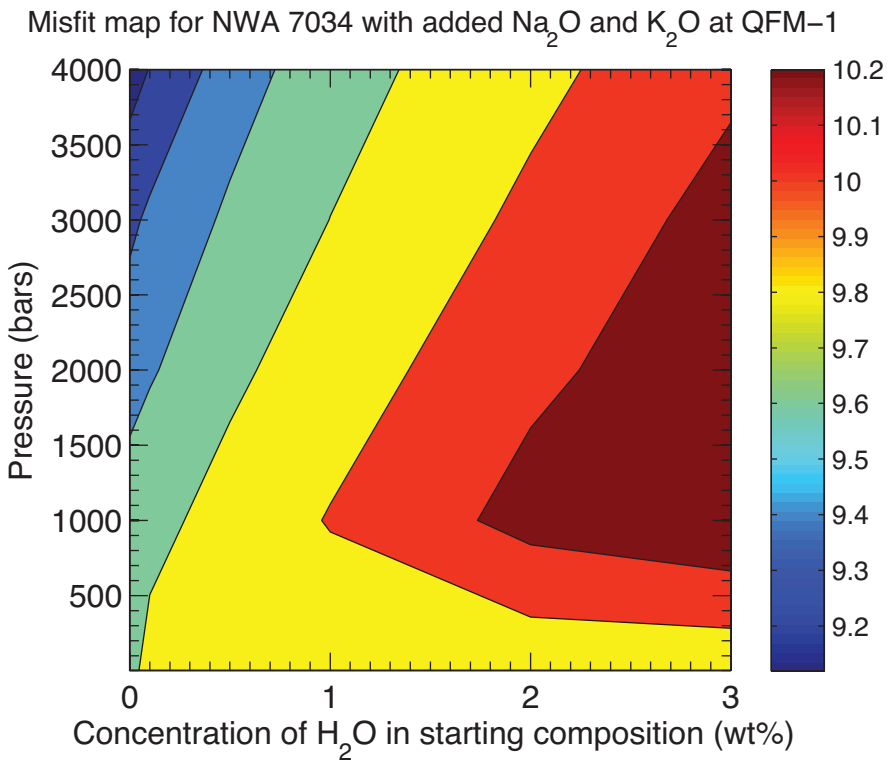

Fig. S20.
Contour plot of misfit between Jake_M and MELTS fractional crystallization calculations at QFM–1 using NWA 7034 with added Na_2O and K_2O as the starting composition. Calculations performed at pressures of 1, 1000, 2000, 3000 and 4000 bars, and water concentrations of 0, 0.1, 0.5, 1, 2 and 3 wt. %. For each of the 30 MELTS calculations, the misfit was calculated by summing the differences between the MELTS curves in SiO_2-, Al_2O_3-, FeO*-, and CaO-MgO space and the three measured Jake_M compositions. The sum of the differences was then divided by three. Note that the misfit in this figure and subsequent figures is not directly comparable to the misfit plotted in Fig. S12, which is calculated against the whole Tenerife suite rather than Jake_M. Colored vertical scale bar indicates the degree of misfit; red = large (i.e., worse fit to Jake_M) and blue = small (i.e., better fit to Jake_M).

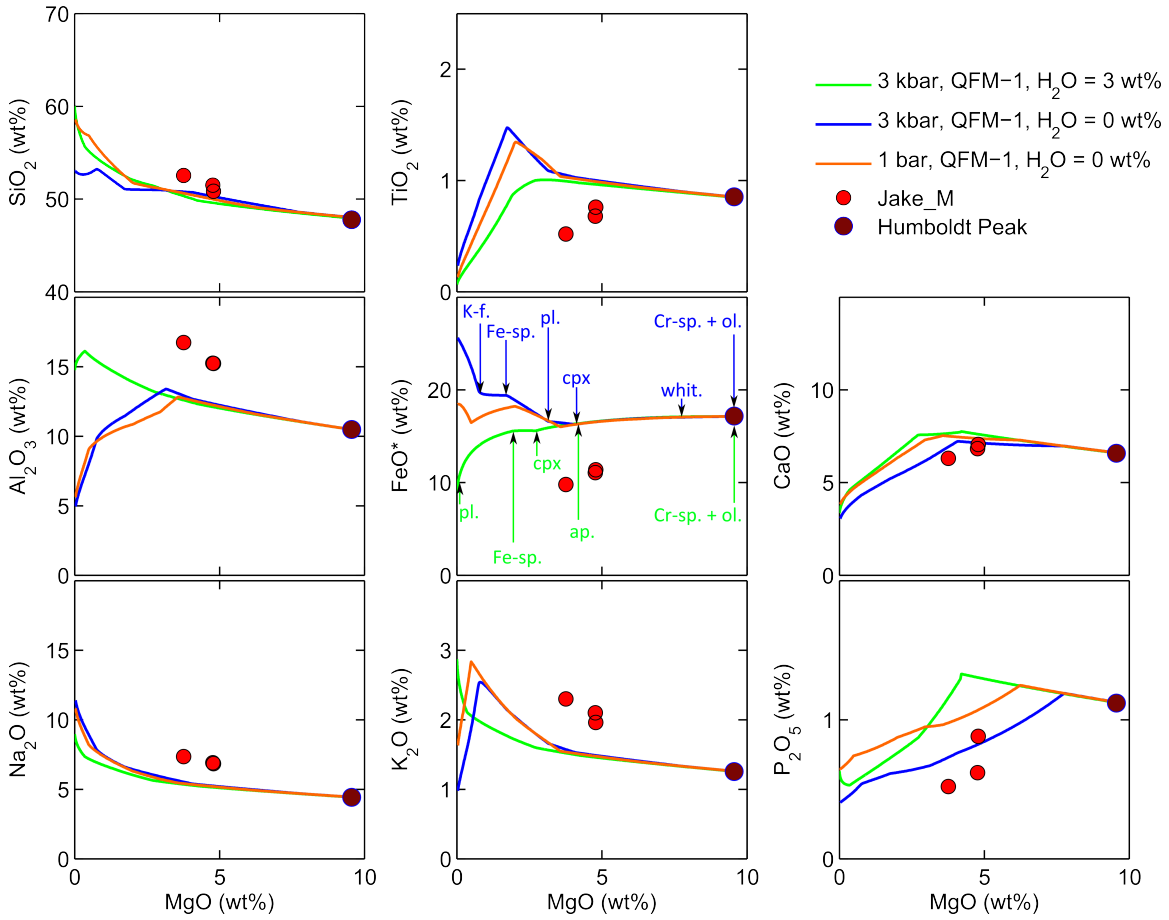

Fig. S21.
MgO variation diagrams for Humboldt Peak, Jake_M, and MELTS fractional crystallization calculations at QFM−1. The best-fit calculation (3 kbar and 0 wt. % water) is plotted in blue. For comparison, the calculation at 3 kbar and 3 wt. % water is shown in green, and the calculation at 1 bar and 0 wt. % water is shown in orange. Colored arrows indicate the entry of phases in the calculated fractional crystallization sequence ol. = olivine; Cr-sp. = Cr-spinel; whit. = whitlockite; ap. = apatite; pl. = plagioclase; cpx = clinopyroxene; Fe-sp. = Fe-rich spinel; K-f. = K-feldspar.

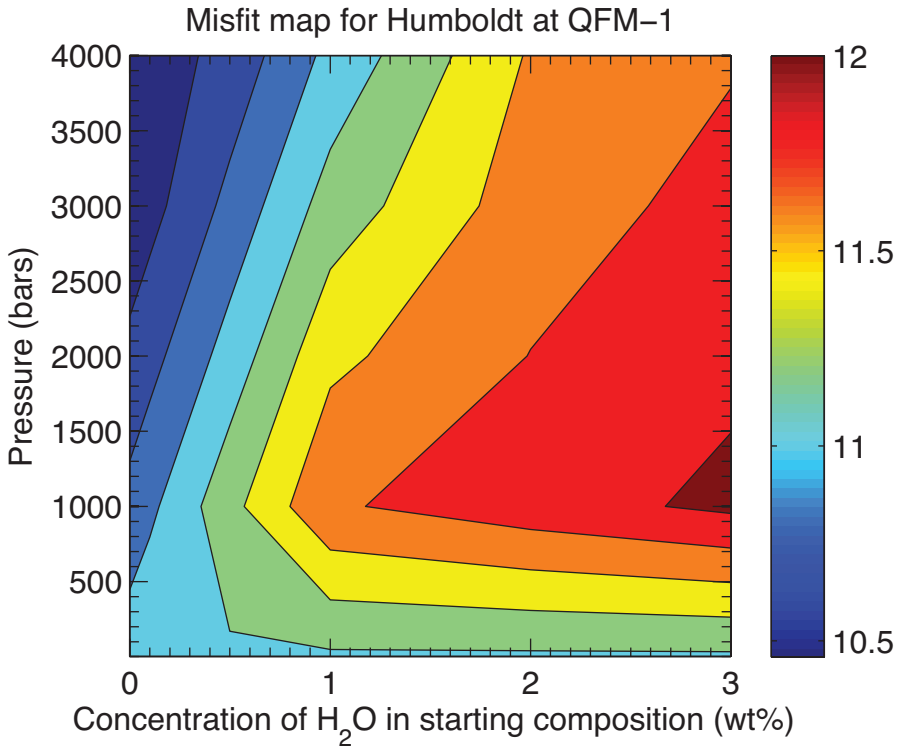

Fig. S22.
Contour plot of misfit between Jake_M and MELTS fractional crystallization calculations at QFM–1 using Humboldt Peak as the starting composition. Calculations performed at pressures of 1, 1000, 2000, 3000 and 4000 bars, and water concentrations of 0, 0.1, 0.5, 1, 2 and 3 wt. %. For each of the 30 MELTS calculations, the misfit was calculated by summing the differences between the MELTS curves in SiO_2-, Al_2O_3-, FeO*-, and CaO-MgO space and the three measured Jake_M compositions. The sum of the differences was then divided by three. Note that the misfit in this figure and subsequent figures is not directly comparable to the misfit plotted in Fig. S12, which is calculated against the whole Tenerife suite rather than Jake_M. Colored vertical scale bar indicates the degree of misfit; red = large (i.e., worse fit to Jake_M) and blue = small (i.e., better fit to Jake_M).

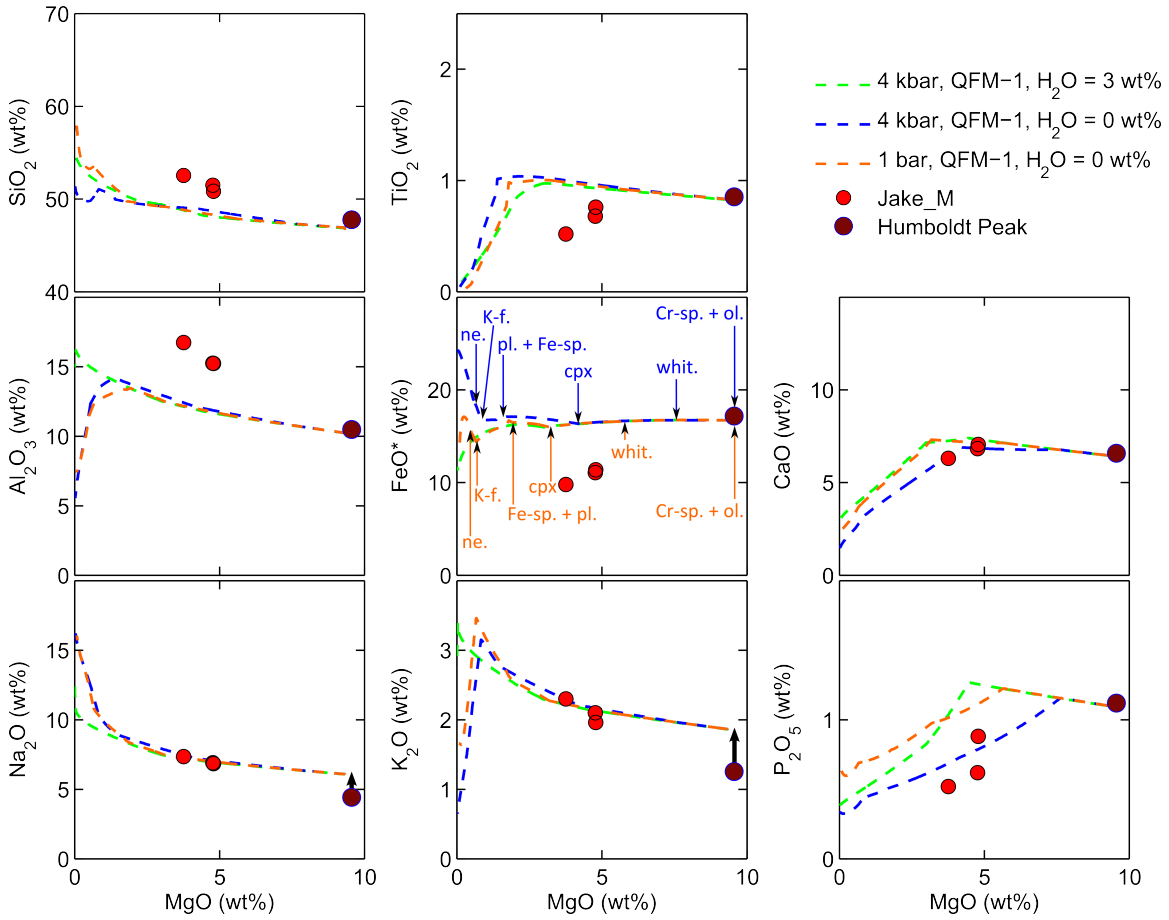

Fig. S23.
MgO variation diagrams for Humboldt Peak (with added Na_2O and K_2O so as to match the alkali content of Jake_M), Jake_M, and MELTS fractional crystallization calculations at QFM–1. The best-fit calculation (4 kbar and 0 wt. % water) is plotted in blue. For comparison, the calculation at 4 kbar and 3 wt. % water is shown in green, and the calculation at 1 bar and 0 wt. % water is shown in orange. Colored arrows indicate the entry of phases in the calculated fractional crystallization sequence: ol. = olivine; Cr-sp. = Cr-spinel; whit. = whitlockite; ap. = apatite; cpx = clinopyroxene; pl. = plagioclase; Fe-sp. = Fe-rich spinel; opx = orthopyroxene; ne. = nepheline; K-f. = K-feldspar. Note that renormalization to 100 wt. % following the addition of alkalis to the Humboldt Peak starting composition causes a small decrease in the concentrations of all of the other elements, such that the starting point for the MELTS fractional crystallization calculations is offset from Humboldt Peak in all panels. Black arrows in the Na_2O and K_2O variation diagrams emphasize the amount by which Humboldt Peak has been enriched in alkalis to create this new starting composition.

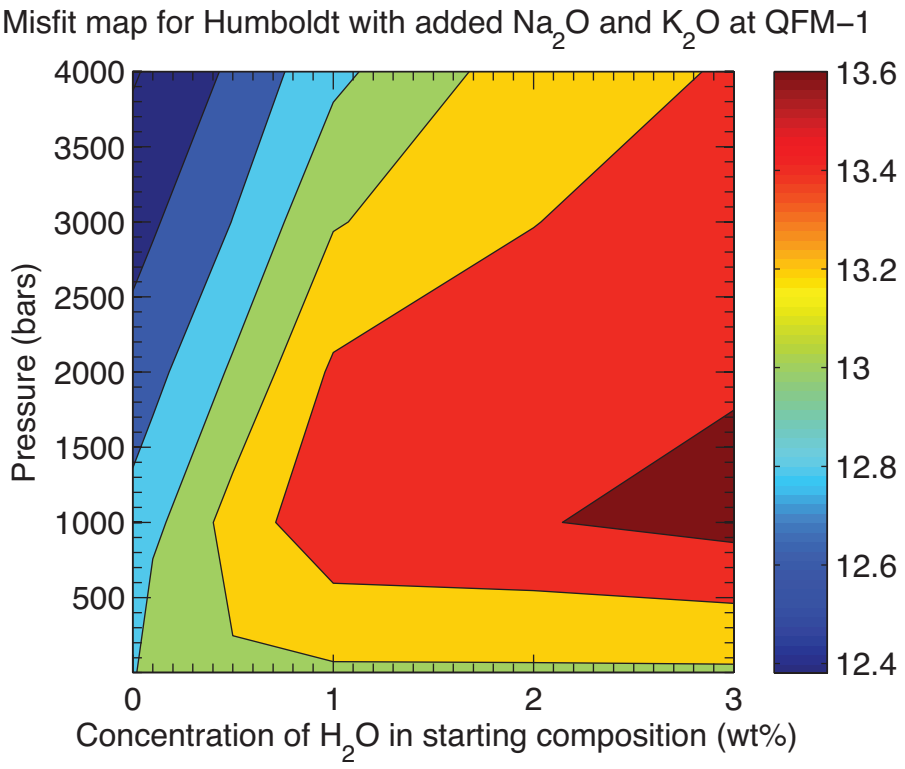

Fig. S24.
Contour plot of misfit between Jake_M and MELTS fractional crystallization calculations at QFM–1 using Humboldt Peak with added Na_2O and K_2O as the starting composition. Calculations performed at pressures of 1, 1000, 2000, 3000 and 4000 bars, and water concentrations of 0, 0.1, 0.5, 1, 2 and 3 wt. %. For each of the 30 MELTS calculations, the misfit was calculated by summing the differences between the MELTS curves in SiO_2-, Al_2O_3-, FeO*-, and CaO-MgO space and the three measured Jake_M compositions. The sum of the differences was then divided by three. Note that the misfit in this figure and subsequent figures is not directly comparable to the misfit plotted in Fig. S12, which is calculated against the whole Tenerife suite rather than Jake_M. Colored vertical scale bar indicates the degree of misfit; red = large (i.e., worse fit to Jake_M) and blue = small (i.e., better fit to Jake_M).

Mars Science Laboratory (MSL) Science Team

Aalto University
Osku Kemppinen

Applied Physics Laboratory (APL) at Johns Hopkins University
Nathan Bridges, Jeffrey R. Johnson, Michelle Minitti

Applied Research Associates, Inc. (ARA)
David Cremers

Arizona State University (ASU)
James F. Bell III, Lauren Edgar, Jack Farmer, Austin Godber, Meenakshi Wadhwa, Danika Wellington

Ashima Research
Ian McEwan, Claire Newman, Mark Richardson

ATOS Origin
Antoine Charpentier, Laurent Peret

Australian National University (ANU)
Penelope King

Bay Area Environmental Research Institute (BAER)
Jennifer Blank

Big Head Endian LLC
Gerald Weigle

Brock University
Mariek Schmidt

Brown University
Shuai Li, Ralph Milliken, Kevin Robertson, Vivian Sun

California Institute of Technology (Caltech)
Michael Baker, Christopher Edwards, Bethany Ehlmann, Kenneth Farley, Jennifer Griffes, John Grotzinger, Hayden Miller, Megan Newcombe, Cedric Pilorget, Melissa Rice, Kirsten Siebach, Katie Stack, Edward Stolper

Canadian Space Agency (CSA)
Claude Brunet, Victoria Hipkin, Richard Léveillé, Geneviève Marchand, Pablo Sobrón Sánchez

Capgemini France
Laurent Favot

Carnegie Institution of Washington
George Cody, Andrew Steele

Carnegie Mellon University
Lorenzo Flückiger, David Lees, Ara Nefian

Catholic University of America
Mildred Martin

Centre National de la Recherche Scientifique (CNRS)
Marc Gailhanou, Frances Westall, Guy Israël

Centre National d'Etudes Spatiales (CNES)
Christophe Agard, Julien Baroukh, Christophe Donny, Alain Gaboriaud, Philippe Guillemot, Vivian Lafaille, Eric Lorigny, Alexis Paillet, René Pérez, Muriel Saccoccio, Charles Yana

Centro de Astrobiología (CAB)

Carlos Armiens-Aparicio, Javier Caride Rodríguez, Isaías Carrasco Blázquez, Felipe Gómez Gómez , Javier Gómez-Elvira, Sebastian Hettrich, Alain Lepinette Malvitte, Mercedes Marín Jiménez, Jesús Martínez-Frías, Javier Martín-Soler, F. Javier Martín-Torres, Antonio Molina Jurado, Luis Mora-Sotomayor, Guillermo Muñoz Caro, Sara Navarro López, Verónica Peinado-González, Jorge Pla-García, José Antonio Rodriguez Manfredi, Julio José Romeral-Planelló, Sara Alejandra Sans Fuentes, Eduardo Sebastian Martinez, Josefina Torres Redondo, Roser Urqui-O'Callaghan, María-Paz Zorzano Mier

Chesapeake Energy
Steve Chipera

Commissariat à l'Énergie Atomique et aux Énergies Alternatives (CEA)
Jean-Luc Lacour, Patrick Mauchien, Jean-Baptiste Sirven

Concordia College
Heidi Manning

Cornell University
Alberto Fairén, Alexander Hayes, Jonathan Joseph, Steven Squyres, Robert Sullivan, Peter Thomas

CS Systemes d'Information
Audrey Dupont

Delaware State University
Angela Lundberg, Noureddine Melikechi, Alissa Mezzacappa

Denver Museum of Nature & Science
Julia DeMarines, David Grinspoon

Deutsches Zentrum für Luft- und Raumfahrt (DLR)
Günther Reitz

eINFORMe Inc. (at NASA GSFC)
Benito Prats

Finnish Meteorological Institute
Evgeny Atlaskin, Maria Genzer, Ari-Matti Harri, Harri Haukka, Henrik Kahanpää, Janne Kauhanen, Osku Kemppinen, Mark Paton, Jouni Polkko, Walter Schmidt, Tero Siili

GeoRessources
Cécile Fabre

Georgia Institute of Technology
James Wray, Mary Beth Wilhelm

Géosciences Environnement Toulouse (GET)
Franck Poitrasson

Global Science & Technology, Inc.
Kiran Patel

Honeybee Robotics
Stephen Gorevan, Stephen Indyk, Gale Paulsen

Imperial College
Sanjeev Gupta

Indiana University Bloomington
David Bish, Juergen Schieber

Institut d'Astrophysique Spatiale (IAS)
Brigitte Gondet, Yves Langevin

Institut de Chimie des Milieux et Matériaux de Poitier (IC2MP)
Claude Geffroy

Institut de Recherche en Astrophysique et Planétologie (IRAP), Université de Toulouse
David Baratoux, Gilles Berger, Alain Cros, Claude d'Uston, Olivier Forni, Olivier Gasnault, Jérémie Lasue, Qiu-Mei Lee, Sylvestre Maurice, Pierre-Yves Meslin, Etienne Pallier, Yann Parot, Patrick Pinet, Susanne Schröder, Mike Toplis

Institut des Sciences de la Terre (ISTerre)
Éric Lewin

inXitu
Will Brunner

Jackson State University
Ezat Heydari

Jacobs Technology
Cherie Achilles, Dorothy Oehler, Brad Sutter

Laboratoire Atmosphères, Milieux, Observations Spatiales (LATMOS)
Michel Cabane, David Coscia, Guy Israël, Cyril Szopa, Samuel Teinturier

Laboratoire de Géologié de Lyon : Terre, Planète, Environnement (LGL-TPE)
Gilles Dromart

Laboratoire de Minéralogie et Cosmochimie du Muséum (LMCM)
François Robert, Violaine Sautter

Laboratoire de Planétologie et Géodynamique de Nantes (LPGN)
Stéphane Le Mouélic, Nicolas Mangold, Marion Nachon

Laboratoire Génie des Procédés et Matériaux (LGPM)
Arnaud Buch

Laboratoire Interuniversitaire des Systèmes Atmosphériques (LISA)
Fabien Stalport, Patrice Coll, Pascaline François, François Raulin

Lightstorm Entertainment Inc.
James Cameron

Los Alamos National Lab (LANL)
Sam Clegg, Agnès Cousin, Dorothea DeLapp, Robert Dingler, Ryan Steele Jackson, Stephen Johnstone, Nina Lanza, Cynthia Little, Tony Nelson, Roger C. Wiens, Richard B. Williams

Lunar and Planetary Institute (LPI)
Laurel Kirkland, Allan Treiman

Malin Space Science Systems (MSSS)
Burt Baker, Bruce Cantor, Michael Caplinger, Scott Davis, Brian Duston, Kenneth Edgett, Donald Fay, Craig Hardgrove, David Harker, Paul Herrera, Elsa Jensen, Megan R. Kennedy, Gillian Krezoski, Daniel Krysak, Leslie Lipkaman, Michael Malin, Elaina McCartney, Sean McNair, Brian Nixon, Liliya Posiolova, Michael Ravine, Andrew Salamon, Lee Saper, Kevin Stoiber, Kimberley Supulver, Jason Van Beek, Tessa Van Beek, Robert Zimdar

Massachusetts Institute of Technology (MIT)
Katherine Louise French, Karl Iagnemma, Kristen Miller, Roger Summons

Max Planck Institute for Solar System Research
Fred Goesmann, Walter Goetz, Stubbe Hviid

Microtel

Micah Johnson, Matthew Lefavor, Eric Lyness

Mount Holyoke College
Elly Breves, M. Darby Dyar, Caleb Fassett

NASA Ames
David F. Blake, Thomas Bristow, David DesMarais, Laurence Edwards, Robert Haberle, Tori Hoehler, Jeff Hollingsworth, Melinda Kahre, Leslie Keely, Christopher McKay, Mary Beth Wilhelm

NASA Goddard Space Flight Center (GSFC)
Lora Bleacher, William Brinckerhoff, David Choi, Pamela Conrad, Jason P. Dworkin, Jennifer Eigenbrode, Melissa Floyd, Caroline Freissinet, James Garvin, Daniel Glavin, Daniel Harpold, Paul Mahaffy, David K. Martin, Amy McAdam, Alexander Pavlov, Eric Raaen, Michael D. Smith, Jennifer Stern, Florence Tan, Melissa Trainer

NASA Headquarters
Michael Meyer, Arik Posner, Mary Voytek

NASA Jet Propulsion Laboratory (JPL)
Robert C, Anderson, Andrew Aubrey, Luther W. Beegle, Alberto Behar, Diana Blaney, David Brinza, Fred Calef, Lance Christensen, Joy Crisp, Lauren DeFlores, Bethany Ehlmann, Jason Feldman, Sabrina Feldman, Gregory Flesch, Joel Hurowitz, Insoo Jun, Didier Keymeulen, Justin Maki, Michael Mischna, John Michael Morookian, Timothy Parker, Betina Pavri, Marcel Schoppers, Aaron Sengstacken, John J. Simmonds, Nicole Spanovich, Manuel de la Torre Juarez, Ashwin Vasavada, Christopher R. Webster, Albert Yen
NASA Johnson Space Center (JSC)
Paul Douglas Archer, Francis Cucinotta, John H. Jones, Douglas Ming, Richard V. Morris, Paul Niles, Elizabeth Rampe

Nolan Engineering
Thomas Nolan

Oregon State University
Martin Fisk

Piezo Energy Technologies
Leon Radziemski

Planetary Science Institute
Bruce Barraclough, Steve Bender, Daniel Berman, Eldar Noe Dobrea, Robert Tokar, David Vaniman, Rebecca M. E. Williams, Aileen Yingst

Princeton University
Kevin Lewis

Rensselaer Polytechnic Institute (RPI)
Laurie Leshin

Retired
Timothy Cleghorn, Wesley Huntress, Gérard Manhès

Salish Kootenai College
Judy Hudgins, Timothy Olson, Noel Stewart

Search for Extraterrestrial Intelligence Institute (SETI I)
Philippe Sarrazin

Smithsonian Institution
John Grant, Edward Vicenzi, Sharon A. Wilson

Southwest Research Institute (SwRI)
Mark Bullock, Bent Ehresmann, Victoria Hamilton, Donald Hassler, Joseph Peterson, Scot Rafkin, Cary Zeitlin

Space Research Institute
Fedor Fedosov, Dmitry Golovin, Natalya Karpushkina, Alexander Kozyrev, Maxim Litvak, Alexey Malakhov, Igor Mitrofanov, Maxim Mokrousov, Sergey Nikiforov, Vasily Prokhorov, Anton Sanin, Vladislav Tretyakov, Alexey Varenikov, Andrey Vostrukhin, Ruslan Kuzmin

Space Science Institute (SSI)
Benton Clark, Michael Wolff

State University of New York (SUNY) Stony Brook
Scott McLennan

Swiss Space Office
Oliver Botta

TechSource
Darrell Drake

Texas A&M
Keri Bean, Mark Lemmon

The Open University
Susanne P. Schwenzer

United States Geological Survey (USGS) Flagstaff
Ryan B. Anderson, Kenneth Herkenhoff, Ella Mae Lee, Robert Sucharski

Universidad de Alcalá
Miguel Ángel de Pablo Hernández, Juan José Blanco Ávalos, Miguel Ramos

Universities Space Research Association (USRA)
Andrea Jones, Myung-Hee Kim, Charles Malespin, Ianik Plante

University College London (UCL)
Jan-Peter Muller

University Nacional Autónoma de México (UNAM)
Rafael Navarro-González

University of Alabama
Ryan Ewing

University of Arizona
William Boynton, Robert Downs, Mike Fitzgibbon, Karl Harshman, Shaunna Morrison

University of California Berkeley
William Dietrich, Onno Kortmann, Marisa Palucis

University of California Davis
Dawn Y. Sumner, Amy Williams

University of California San Diego
Günter Lugmair

University of California San Francisco
Michael A. Wilson

University of California Santa Cruz
David Rubin

University of Colorado Boulder
Bruce Jakosky

University of Copenhagen
Tonci Balic-Zunic, Jens Frydenvang, Jaqueline Kløvgaard Jensen, Kjartan Kinch, Asmus Koefoed, Morten Bo Madsen, Susan Louise Svane Stipp

University of Guelph
Nick Boyd, John L. Campbell, Ralf Gellert, Glynis Perrett, Irina Pradler, Scott VanBommel

University of Hawai'i at Manoa
Samantha Jacob, Tobias Owen, Scott Rowland

University of Helsinki
Evgeny Atlaskin, Hannu Savijärvi

University of Kiel
Eckart Boehm, Stephan Böttcher, Sönke Burmeister, Jingnan Guo, Jan Köhler, César Martín García, Reinhold Mueller-Mellin, Robert Wimmer-Schweingruber

University of Leicester
John C. Bridges

University of Maryland
Timothy McConnochie

University of Maryland Baltimore County
Mehdi Benna, Heather Franz

University of Maryland College Park
Hannah Bower, Anna Brunner

University of Massachusetts
Hannah Blau, Thomas Boucher, Marco Carmosino

University of Michigan Ann Arbor
Sushil Atreya, Harvey Elliott, Douglas Halleaux, Nilton Rennó, Michael Wong

University of Minnesota
Robert Pepin

University of New Brunswick
Beverley Elliott, John Spray, Lucy Thompson

University of New Mexico
Suzanne Gordon, Horton Newsom, Ann Ollila, Joshua Williams

University of Queensland
Paulo Vasconcelos

University of Saskatchewan
Jennifer Bentz

University of Southern California (USC)
Kenneth Nealson, Radu Popa

University of Tennessee Knoxville
Linda C. Kah, Jeffrey Moersch, Christopher Tate

University of Texas at Austin
Mackenzie Day, Gary Kocurek

University of Washington Seattle
Bernard Hallet, Ronald Sletten

University of Western Ontario
Raymond Francis, Emily McCullough

University of Winnipeg
Ed Cloutis

Utrecht University
Inge Loes ten Kate

Vernadsky Institute
Ruslan Kuzmin

Washington University in St. Louis (WUSTL)
Raymond Arvidson, Abigail Fraeman, Daniel Scholes, Susan Slavney, Thomas Stein, Jennifer Ward

Western University
Jeffrey Berger

York University
John E. Moores

References

1. J. P. Grotzinger *et al.*, Mars Science Laboratory: First 100 sols of geologic and geochemical exploration from Bradbury Landing to Glenelg. *44th Lunar and Planetary Science Conference*, 1259 (2013).
2. R. Gellert *et al.*, Initial MSL APXS activities and observations at Gale Crater, Mars. *44th Lunar and Planetary Science Conference*, 1432 (2013).
3. A. Cousin *et al.*, ChemCam analysis of Jake Matijevic, Gale Crater. *44th Lunar and Planetary Science Conference*, 1409 (2013).
4. M. E. Minitti *et al.*, Mars Hand Lens Imager (MAHLI) observations of rocks at Curiosity's field site. *44th Lunar and Planetary Science Conference*, 2186 (2013).
5. W. Cross, J. P. Iddings, L. V. Pirsson, H. S. Washington, *Quantitative Classification of Igneous Rocks*. (University of Chicago Press, 1903), pp. 286.
6. M. Wadhwa, Redox conditions on small bodies, the Moon and Mars. *Reviews in Mineralogy and Geochemistry* **68**, 493 (2008).
7. J. Tuff, J. Wade, B. J. Wood, Volcanism on Mars controlled by early oxidation of the upper mantle. *Nature* **498**, 342 (2013).
8. J. M. Rhodes, Geochemical stratigraphy of lava flows sampled by the Hawaiian Scientific Drilling Project. *Journal of Geophysical Research* **101**, 11 (1996).
9. C. Meyer, The Martian meteorite compendium. *(*http://curator.jsc.nasa.gov/antmet/mmc/index.cfm), (2012).
10. R. Gellert *et al.*, Alpha particle X-ray spectrometer (APXS): Results from Gusev crater and calibration report. *Journal of Geophysical Research* **111**, E02S05 (2006).
11. H. Wänke, J. Brückner, G. Dreibus, R. Rieder, I. Ryabchikov, Chemical composition of rocks and soils at the Pathfinder site. *Space Science Reviews* **96**, 317 (2001).
12. C. N. Foley, T. E. Economou, R. N. Clayton, W. Dietrich, Calibration of the Mars Pathfinder alpha proton X-ray spectrometer. *Journal of Geophysical Research* **108**, 8095 (2003).
13. A. Harker, *The Tertiary Igneous Rocks of Skye*. Memoirs of the Geological Survey of the United Kingdom (Glascow, 1904), pp. 481.
14. I. D. Muir, C. E. Tilley, Mugearites and their place in alkali igneous rock series. *Journal of Geology* **69**, 186 (1961).
15. I. S. E. Carmichael, F. J. Turner, J. Verhoogen, *Igneous Petrology*. (McGraw-Hill, 1974), pp. 739.
16. M. Wilson, *Igneous Petrogenesis*. (Unwin Hyman, London, 1989), pp. 466.
17. R. V. Morris *et al.*, Iron mineralogy and aqueous alteration from Husband Hill through Home Plate at Gusev Crater, Mars: results from the Mössbauer instrument on the Spirit Mars Exploration Rover. *Journal of Geophysical Research* **113**, E12S42 (2008).
18. V. Sautter, A. Jambon, O. Boudouma, Cl-amphibole in the nakhlite MIL 03346: Evidence for sediment contamination in a Martian meteorite. *Earth and Planetary Science Letters* **252**, 45 (2006).
19. J. M. D. Day, L. A. Taylor, C. Floss, H. Y. McSween Jr., Petrology and chemistry of ML 03346 and its significance in understanding the petrogenesis of nakhlites on Mars. *Meteoritics and Planetary Science* **41**, 581 (2006).
20. A. H. Treiman, The parent magma of the Nakhla (SNC) meteorite, inferred from magmatic inclusions. *Geochimica et Cosmochimica Acta* **57**, 4753 (1993).
21. H. Y. McSween Jr., G. J. Taylor, M. B. Wyatt, Elemental composition of the Martian crust. *Science* **324**, 736 (2009).
22. A. S. Yen *et al.*, Nickel on Mars: Constraints on meteoritic material at the surface. *Journal of Geophysical Research* **111**, E12S11 (2006).
23. T. N. Irvine, W. R. A. Baragar, A guide to the chemical classification of the common volcanic rocks. *Canadian Journal of Earth Sciences* **8**, 523 (1971).
24. T. Usui, H. Y. McSween Jr., B. C. Clark III, Petrogenesis of high-phosphorus Wishstone Class rocks in Gusev Crater, Mars. *Journal of Geophysical Research* **113**, E12S44 (2008).
25. Georoc database, (http://georoc.mpch-mainz.gwdg.de/georoc/).
26. H. Y. McSween Jr., What have we learned about Mars from SNC meteorites. *Meteoritics* **29**, 757 (1994).
27. A. Ruzicka, G. A. Synder, L. A. Taylor, Comparative geochemistry of basalts from the Moon, Earth, HED asteroid, and Mars: Implications for the origin of the Moon. *Geochimica et Cosmochimica Acta* **65**, 979 (2001).
28. J. Filiberto, Similarities between the Shergottites and terrestrial ferropicrites. *Icarus* **197**, 52 (2008).
29. E. Stolper, H. Y. McSween Jr., J. F. Hays, A petrologic model of the relationships among achondritic meteorites. *Geochimica et Cosmochimica Acta* **43**, 589 (1979).

30. H. Wänke, G. Dreibus, Chemical composition and accretion history of terrestrial planets. *Philosophical Transactions of the Royal Society of London A* **325**, 545 (1988).
31. J. Karner, J. J. Papike, C. K. Shearer, Olivine from planetary basalts: Chemical signatures that indicate planetary parentage and those that record igneous setting and process. *American Mineralogist* **88**, 806 (2003).
32. J. Karner, J. J. Papike, C. K. Shearer, Comparative planetary mineralogy: Pyroxene major- and minor-element chemistry and partitioning of vanadium between pyroxene and melt in planetary basalts. *American Mineralogist* **91**, 1574 (2006).
33. A. Lacroix, Les lavas à haüyne d'Auvergne et leurs enclaves homoeogènes. *Comptes Rendus* **CLXIV**, 581 (1917).
34. J. Andújar, F. Costa, J. Martí, J. A. Wolff, M. R. Carroll, Experimental constraints on pre-eruptive conditions of phonolitic magma from caldera-forming El Abrigo eruption, Tenerife (Canary Islands). *Chemical Geology* **257**, 173 (2008).
35. J. F. G. Wilkinson, R. A. Binns, Hawaiite of high pressure origin from northeastern New South Wales. *Nature* **222**, 553 (1969).
36. A. J. Stolz, Garnet websterites and associated ultramamfic inclusions from a nepheline mugearite in the Walcha area, New South Wales, Australia. *Mineralogical Magazine* **48**, 167 (1984).
37. D. H. Green, A. D. Edgar, P. Beasley, E. Kiss, N. G. Ware, Upper mantle source for some hawaiites, mugearites and benmoreites. *Contributions to Mineralogy and Petrology* **48**, 33 (1974).
38. G. J. Ablay, M. R. Carroll, M. R. Palmer, J. Martí, R. S. J. Sparks, Basanite-phonolite lineages of the Teide-Pico volcanic complex, Tenerife, Canaray Islands. *Journal of Petrology* **39**, 905 (1998).
39. P. M. Smith, P. D. Asimow, Adiabat_1ph: A new public front-end to the MELTS, pMELTS, and pHMELTS models. *Geochemistry, Geophysics, Geosystems* **6**, Q02004 (2005).
40. M. S. Ghiorso, R. O. Sack, Chemical mass transfer in magmatic processes. IV. A revised and internally consistent thermodynamic model for the interpolation and extrapolation of liquid-solid equilibria. *Contributions to Mineralogy and Petrology* **119**, 197 (1995).
41. H. S. Yoder, C. E. Tilley, Origin of basaltic magmas: An experimental study of natural and synthetic rock systems. *Journal of Petrology* **3**, 342 (1962).
42. D. C. Presnall *et al.*, Liquidus phase relations on the join diopside-forsterite-anorthite from 1-atm to 20 kbar: Their bearing on the generation and crystallization of basaltic magma. *Contributions to Mineralogy and Petrology* **66**, 203 (1978).
43. D. H. Eggler, Water-saturated and undersaturated melting relations in a Paricutin andesite and an estimate of water content in the natural magma. *Contributions to Mineralogy and Petrology* **34**, 261 (1972).
44. P. J. Wyllie, Magmas and volatile components. *American Mineralogist* **64**, 469 (1979).
45. G. J. Ablay, G. G. J. Ernst, J. Marti, R. S. J. Sparks, The ~2ka subplinian eruption of Montana Blanca, Tenerife. *Bulletin of Volcanology* **57**, 337 (1995).
46. C. Beier, K. M. Haase, T. H. Hansteen, Magma evolution of the Sete Cidades volcano, São Miguel, Azores. *Journal of Petrology* **47**, 1375 (2006).
47. J. C. Dann, A. H. Holzheid, T. L. Grove, H. Y. McSween Jr., Phase equilibria of the Shergotty meteorite: Constraints on pre-eruptive water contents of martian magmas and fractional crystallization under hydrous conditions. *Meteoritics and Planetary Science* **36**, 793 (2001).
48. H. Nekvasil, J. Filiberto, F. M. McCubbin, D. H. Lindsley, Alkalic parental magmas for chassignites? *Meteoritics and Planetary Science* **42**, 979 (2007).
49. M. C. Johnson, M. J. Rutherford, P. C. Hess, Chassigny petrogenesis: Melt compositions, intersive parameters, and water contents of Martian (?) magmas. *Geochimica et Cosmochimica Acta* **55**, 349 (1991).
50. F. M. McCubbin *et al.*, Hydrous magmatism on Mars: A source of water for the surface and subsurface during the Amazonian. *Earth and Planetary Science Letters* **292**, 132 (2010).
51. J. Filiberto, A. H. Treiman, Martian magmas contained abundant chlorine, but little water. *Geology* **37**, 1087 (2009).
52. D. R. Baker, M. Alletti, Fluid saturation and volatile partitioning between melts and hydrous fluids in crustal magmatic systems: The contribution of experimental measurements and solubility models. *Earth-Science Reviews* **114**, 298 (2012).
53. M. R. Carroll, J. D. Webster, Solubilities of sulfur, noble gases, nitrogen, chlorine, and fluorine in magmas. *Reviews in Mineralogy* **30**, 231 (1994).
54. P. J. Wyllie, O. F. Tuttle, Experimental investigations of silicate systems containing two volatile components. Part III. The effects of SO_3, P_2O_5, HCl, and Li_2O, in addition to H_2O, on the melting temperatures of albite and granite. *American Journal of Science* **262**, 930 (1964).
55. A. D. Edgar, in *Alkaline Igneous Rocks,* J. G. Fitton, B. G. J. Upton, Eds. (Geological Society of London, 1987), pp. 29–52.
56. D. H. Green, T. J. Falloon, W. R. Taylor, in *Magmatic Processes: Physiochemical Principles,* B. O. Mysen, Ed. (The Geochemical Society, 1987), pp. 139–154.
57. R. Dasgupta, M. M. Hirschmann, Partial melting experiments of peridotite + CO_2 at 3 GPa and genesis of alkalic ocean island basalts. *Journal of Petrology* **48**, 2093 (2007).

58. F. E. Lloyd, D. K. Bailey, Light element metasomatism of the continental mantle: The evidence and the consequences. *Physics and Chemistry of the Earth* **9**, 389 (1975).
59. M. Menzies, V. Rama Murthy, Mantle metasomatism as a precursor to the genesis of alkaline magmas—isotopic evidence. *American Journal of Science* **280-A**, 622 (1980).
60. S. Pilet, M. B. Baker, E. M. Stolper, Metasomatized lithosphere and the origin of alkaline lavas. *Science* **320**, 916 (2008).
61. S. Keshav, G. H. Gudfinnsson, G. Sen, Y. W. Fei, High-pressure melting experiments on garnet clinopyroxenite and the alkalic to tholeiitic transition in ocean-island basalts. *Earth and Planetary Science Letters* **223**, 365 (2004).
62. T. Kogiso, M. M. Hirschmann, D. J. Frost, High-pressure partial melting of garnet pyroxenite: possible mafic lithologies in the source of ocean island basalts. *Earth and Planetary Science Letters* **216**, 603 (2003).
63. M. E. Schmidt, T. J. McCoy, The evolution of a heterogeneous Martian mantle: Clues from K, P, Ti, Cr, and Ni variations in Gusev basalts and shergottite meteorites. *Earth and Planetary Science Letters* **296**, 67 (2010).
64. H. Y. McSween Jr. *et al.*, Alkaline volcanic rocks from the Columbia Hills, Gusev crater, Mars. *Journal of Geophysical Research* **111**, E09S91 (2006).
65. G. Dreibus, H. Wänke, Volatiles on Earth and Mars: A comparison. *Icarus* **71**, 225 (1987).
66. G. J. Taylor *et al.*, Bulk composition and early differentiation of Mars. *Journal of Geophysical Research* **111**, E03S10 (2006).
67. K. Lodders, B. Fegley Jr., An oxygen isotope model for the composition of Mars. *Icarus* **126**, 373 (1997).
68. S. M. McLennan, Large-ion lithophile element fractionation during the early differentiation of Mars and the composition of the Martian primitive mantle. *Meteoritics and Planetary Science* **38**, 895 (2003).
69. A. H. Treiman, Chemical compositions of martian basalts (shergottites): Some inferences on basalt formation, mantle metasomatism, and differentiation in Mars. *Meteoritics and Planetary Science* **38**, 1849 (2003).
70. J. D. Winter, *An Introduction to Igneous and Metamorphic Petrology*. (Prentice Hall, 2010), pp. 702.
71. M. E. Schmidt *et al.*, APXS of first rocks encountered by Curiosity in Gale Crater: Geochemical diversity and volatile element (K and Zn) enrichment. *44th Lunar and Planetary Science Conference*, 1278 (2013).
72. R. W. Le Maitre, Ed., *Igneous Rocks: A Classification and Glossary of Terms*, (Cambridge University Press, ed. 2nd, 2002), pp. 236.
73. H. Chennaoui Aoudjehane *et al.*, Tissint martian meteorite: a fresh look at the interior, surface, and atmosphere of Mars. *Science* **338**, 785 (2012).
74. C. B. Agee *et al.*, Unique meteorite from early Amazonian Mars: Water-rich basaltic breccia Northwest Africa 7034. *Science* **339**, 780 (2013).
75. D. W. Ming *et al.*, Geochemical properties of rocks and soils in Gusev crater, Mars: Results of the Alpha particle X-ray spectrometer from Cumberland Ridge to Home Plate. *Journal of Geophysical Research* **113**, E12S39 (2008).
76. R. Rieder *et al.*, Chemistry of rocks and soils at Meridiani Planum from the Alpha Particle X-ray Spectrometer. *Science* **306**, 1746 (2004).
77. S. W. Squyres *et al.*, Pyroclastic activity at Home Plate in Gusev Crater, Mars. *Science* **316**, 738 (2007).
78. R. H. Hewins *et al.*, Northwest Africa 7533, an impact breccia from Mars. *44th Lunar and Planetary Science Conference*, 2385 (2013).
79. M. Humayun, B. Zanda, R. H. Hewins, C. Göpel, Composition of Northwest Africa 7533: Implications for the origin of martian soils and crust. *44th Lunar and Planetary Science Conference*, 1429 (2013).
80. A. K. Matzen, M. B. Baker, J. R. Beckett, E. M. Stolper, Fe-Mg partitioning between olivine and high-magnesian melts and the nature of Hawaiian parental liquids. *Journal of Petrology* **52**, 1243 (2011).
81. J. Filiberto, R. Dasgupta, Fe^{+2}-Mg partitioning between olivine and basaltic melts: Applications to genesis of olivine-phyric Shergottites and conditions of melting in the Martian interior. *Earth and Planetary Science Letters* **304**, 527 (2011).
82. E. M. Stolper *et al.*, The petrochemistry of Jake_M: A martian mugearite. *44th Lunar and Planetary Science Conference*, 1685 (2013).
83. E. M. Stolper *et al.*, The petrochemistry of Jake_M: A martian mugearite. *Mineralogical Magazine* **77**, 2269 (2013).
84. J. Brückner *et al.*, in *The Martian Surface: Composition, Mineralogy, and Physical Properties,* J. F. Bell III, Ed. (Cambridge University Press, Cambridge, 2008), pp. 58–102.
85. J. A. Hurowitz *et al.*, In situ and experimental evidence for acidic weathering of rocks and soils on Mars. *Journal of Geophysical Research* **111**, E02S19 (2006).
86. S. Maurice *et al.*, The ChemCam instrument suite on the Mars Science Laboratory (MSL) rover: Science objectives, and mast unit description. *Space Science Reviews* **170**, 95 (2012).
87. R. C. Wiens *et al.*, The ChemCam instrument suite on the Mars Science Laboratory (MSL) rover: Body unit and combined system tests. *Space Science Reviews* **170**, 167 (2012).

88. E. Lewin *et al.*, Modal mineralogy of igneous rocks with ChemCam at Gale crater. *44th Lunar and Planetary Science Conference*, 3102 (2013).
89. S. Maurice *et al.*, Laser Induced Spectroscopy (LIBS) spot size stand-off distances with ChemCam. *43rd Lunar and Planetary Science Conference*, 2899 (2012).
90. P. Comon, Independent component analysis, a new concept? *Signal Processing* **36**, 287 (1994).
91. O. Forni *et al.*, Component separation of OMEGA spectra with ICA. *36th Lunar and Planetary Science Conference*, 1623 (2005).
92. J. Lasue *et al.*, Partial least squares sensitivity analysis and improvements for ChemCam LIBS data anlysis on Mars. *44th Lunar and Planetary Science Conference*, 2230 (2013).
93. L. Qin, M. Humayun, The Fe/Mn ratio in MORB and OIB determined by ICP-MS. *Geochimica et Cosmochimica Acta* **72**, 1660 (2008).
94. M. Humayun, L. Qin, M. D. Norman, Geochemical evidence for excess iron in the mantle beneath Hawaii. *Science* **306**, 91 (2004).
95. W. I. Ridley, The petrology of the Las Canada volcanoes, Tenerife, Canary Islands. *Contributions to Mineralogy and Petrology* **26**, 124 (1970).
96. M. M. Hirschmann, M. S. Ghiorso, L. E. Wasylenki, P. D. Asimow, E. M. Stolper, Calculation of peridotite partial melting from thermodynamic models of minerals and melts. I. Review of methods and comparison with experiments. *Journal of Petrology* **39**, 1091 (1998).
97. C. D. K. Herd, Basalts as probes of planetary interior redox state. *Reviews in Mineralogy and Geochemistry* **68**, 527 (2008).
98. Y. Bottinga, D. F. Weill, The viscosity of magmatic silicate liquids: a model calculation. *American Journal of Science* **272**, 438 (1972).